Internal Deformation in Hybrid-materials

Internal magneto-active configuration and macroscopic deformations

Zur Erlangung des Grades eines Doktors der Naturwissenschaften (Dr. rer. nat.)
Genehmigte Dissertation von Henrik Schmidt aus Würzburg
Tag der Einreichung: 09. Februar 2021, Tag der Prüfung: 14. April 2021

1. Gutachten: Prof. Dr. Hans-Jürgen Butt
2. Gutachten: Prof. Dr. Regine von Klitzing
Darmstadt-D17

TECHNISCHE UNIVERSITÄT DARMSTADT

Physics Department
Institute for Condensed Matter Physics
Soft Matter at Interfaces

Internal Deformation in Hybrid-materials
Internal magneto-active configuration and macroscopic deformations

Accepted doctoral thesis by Henrik Schmidt

1. Review: Prof. Dr. Hans-Jürgen Butt
2. Review: Prof. Dr. Regine von Klitzing

Date of submission: 09. Februar 2021
Date of thesis defense: 14. April 2021

Darmstadt-D17

For Family & Friends

"You can kill the dreamer, but you can’t kill the dream."

Martin Luther King Jr.

Erklärungen laut Promotionsordnung

§8 Abs. 1 lit. c PromO

Ich versichere hiermit, dass die elektronische Version meiner Dissertation mit der schriftlichen Version übereinstimmt.

§8 Abs. 1 lit. d PromO

Ich versichere hiermit, dass zu einem vorherigen Zeitpunkt noch keine Promotion versucht wurde. In diesem Fall sind nähere Angaben über Zeitpunkt, Hochschule, Dissertationsthema und Ergebnis dieses Versuchs mitzuteilen.

§9 Abs. 1 PromO

Ich versichere hiermit, dass die vorliegende Dissertation selbstständig und nur unter Verwendung der angegebenen Quellen verfasst wurde.

§9 Abs. 2 PromO

Die Arbeit hat bisher noch nicht zu Prüfungszwecken gedient.

Darmstadt, 09. Februar 2021

H. Schmidt

Abstract

Hybridmaterialien zeigen im Vergleich zu ihren Bestandteilen verbesserte oder neue Eigenschaften. Magnetische Hybridmaterialien bestehen im allgemeinem aus einem magnetischem Füllmaterial, welches in einem nicht magnetischen Trägermaterial (Trägermatrix) eingebettet ist. Ist das Trägermaterial ein Elastomer, werden diese Materialien auch magneto-rheologische Elastomere (MRE) genannt. In den meisten Fällen bestehen MREs aus magnetischen Partikeln, die in eine Polymermatrix eingebettet wurden. Werden MREs einem magnetischen Feld ausgesetzt, zeigen sie zwei Reaktionen: Die Magnetostriktion und den magnetorheologischen (MR) Effekt. Magnetostriktion ist die Fähigkeit des Materials, seine Form durch das Anlegen eines Magnetfeldes zu ändern, wohingegen der MR Effekt die Variation der Steifigkeit des Materials im Magnetfeld beschreibt. Um einen starke Magnetostriktion zu erzielen, müssen sich die Partikel im MRE unter dem Einfluss eines Magnetfeldes umordnen. Deshalb ist es für eine Optimierung dieser Fähigkeit wichtig, den Zusammenhang zwischen Formveränderung und Partikelbewegung im MRE zu verstehen.
Diese Arbeit baut auf den früheren Arbeiten von Huang und Puljiz *et al.* auf [69, 133, 135]. Die MRE-Proben wurden ähnlich wie in [133, 135] als Schichtsystem aus Polymer [Polydimethylsiloxan (PDMS)] und Partikeln hergestellt. Dies vereinfachte eine Partikel-Positionierung. Um die Anzahl der unbekannten Parameter gering zu halten, wurden zunächst Proben mit zwei paramagnetischen Nickel-Partikeln, die in einem Abstand von ungefähr einem Partikel Durchmesser zueinander plaziert wurden, hergestellt. Danach wurde die Komplexität der Proben durch die Hinzugabe von weiteren Partikeln sukzessive gesteigert. Da die magnetisch Kraft zwischen den beiden Partikeln nicht nur durch die Feldstärke sondern auch durch die Partikelposition relativ zur Feldorientierung geändert werden kann, wurden die Proben einem homogenen, schrittweise rotierenden Magnetfeld von $180\,mT$ ausgesetzt. Durch das optische Aufnehmen der Partikeltrajektorien wurde der Partikelabstand für die dazugehörige Magnetfeldorientierung bestimmt. Die beiden Partikel zeigten einen neuen magneto-aktiven Zustand, der sich dadurch auszeichnet, dass kleine Veränderungen in der Magnetfeldorientierung eine große Änderung des Partikelabstands hervorriefen. Dieser magneto-aktive Zustand hängt vom ursprünglichem Partikelabstand, dem Young's Modul der PDMS-Matrix und der Magnetfeldstärke ab. Er tritt nur für ein definiertes Verhältniss zwischen den drei Größen, also nur für ein bestimmtes Verhältnis zwischen elastischer und magnetischer Kraft auf.
Um den Einfluss weiterer Partikel zu untersuchen, wurde zunächst die Partikelanzahl in einer linearen Anordnung bis auf vierzehn erhöht. Dabei zeigte sich, dass keine durchgängige Partikelkette ensteht, sondern ein Zerfall in unterschiedlich große Partikelgruppen stattfindet. Ob Partikel in Kontakt kamen, korrelierte dabei stark mit ihrem Abstand zu den benachbarten Partikeln. Auch Matrix vermittelte Wechselwirkungen konnten belegt werden und spielten eine Rolle.
In Partikelgittern von fünf auf fünf Partikeln wurden Partikelgruppen mit mehr als fünf Partikeln detektiert. Für magnetische Feldrichtungen entlang der Gitterachsen konnte der Einfluss von Gitterfehlern gezeigt werden. Es ergab sich ein Zusammenhang zwischen der durchschnittlichen Größe der Partikelgruppen und der Fläche, welche die Randpartikel umrahmten. Dabei galt, je

größer die Partikelgruppen desto kleiner die Fläche.
Abschließend wurden magnetische Hohlkugeln und magnetisch aktive Membrane hergestellt, die eine dicht gepackte Partikel-Monolage beinhalteten. Die Hohlkugeln zeichneten sich durch große und in ihrer Richtung steuerbare Deformationen aus. Die Membrane fungierten als Tropfenselektor und wiesen im Vergleich zur reinen PDMS-Matrix eine deutlich erhöhte Steifigkeit auf.

Abstract

Magnetic-hybrid materials generally consist of non-magnetic carrier materials interspersed with a magnetic filler material. If the carrier material is an elastomer they are called more specifically magnetorheologic elastomer (MREs). Under an applied magnetic field, those materials can respond in two ways: The magnetostriction and the magnetorheological (MR) effect. Magnetostriction is the ability to deform when subjected to a magnetic field. The MR effect is the alternation of mechanical properties like tensile strain under an applied magnetic field. To obtain strong magnetostrictive effects, the particles inside the MRE have to rearrange in position and orientation under the influence of a magnetic field. To be applicable e.g. as an actuator, it is of utter importance to understand the link between particle movement and macroscopic deformation.
This work extends the previous studies of Huang and Puljiz *et al.* [69, 133, 135]. Similar to [133, 135] the sample were prepared as layer system of polymer layers [polydimethylsiloxan (PDMS)] and particles. This facilitated particle positioning. At first, MRE samples comprising two paramagnetic nickel particles with initial inter-particle distance of roughly one particle diameter were prepared in order to keep the amount of unknown parameters small. Subsequently, the sample complexity was increased by introducing more particles into the system. As the magnetic forces not only depends on the distance between the particles but also on their position relative to the external field, the system was exposed to a slowly, stepwise rotating magnetic field of $180\,mT$. Resolving the particle attachment and detachment and measuring the angles between particle axis and external field for all corresponding magnetic field orientations, I identified a strong magneto-active configuration. This strong magneto-active configuration is characterized by a large inter-particle distance change generated by a small alternation of the external magnetic field orientation. It is sensitive to the initial inter-particle distance, Young's modulus of the matrix, and magnetic field strength and thus, was only stable in a defined parameter range, i.e. for a defined ratio between elastic and magnetic forces.
To determine the influence of additional particles, the particle number in this linear arrangement was successively increased up to fourteen particles. Particles did not form a continuous particle chain but particle groups of different particle numbers. Thereby, the distance to neighbor particles determined whether particles were able to get into contact or not. Also matrix mediated interaction was observed.
In addition, in five by five particle lattices, particle groups of more than five particles formed. For magnetic fields orientated along the lateral lattice direction the influence of lattice irregularities was shown. Furthermore, a correlation between the mean particle number per group and the area the rim particles surround, existed. It was an inverse correlation, i.e. the larger the mean particle number per group the smaller the area.
Concluding, magnetically hollow spheres and magneto-active membranes comprising a dense packed monolayer of particles, were prepared. The hollow spheres showed large and direction changable deformations. The membrane was used as drop size selector and showed a significantly larger stiffness as the pure PDMS matrix.

Contents

1 Introduction

Within material science, the research on combined materials, or hybrid-materials, is of great significance. One can distinguish between blends and composites. In contrast to blends, composite's constituents show two or more distinct physical or chemical phases [84]. The distinct phases are on the one hand the matrix material and on the other hand the second phase, the filler material. Thus, composites consist of two or more different constituents, resulting in a material that shows altered and or enhanced structural or functional properties e.g. superior mechanical properties. These improved properties are non-attainable by one of the composite parts alone.
The practical benefits of a hybrid material can be seen for example in widely used catheters used in healthcare. They are made from a hybrid material where silica particles were added to the silicon rubber matrix to improve its mechanical properties like tensile strength and wettability [142]. Apart from the aim to create materials with enhanced features a significant amount of research does focus on materials that alter their properties when stimulated externally [62, 65]. External stimulation can be but is not limited to optical, electronic, chemical, and magnetic [48]. Every stimulation has its advantages and disadvantages. This thesis focuses solely on magnetic stimulation due to fact that relatively high magnetic field strengths can be achieved with minor technical effort and that stimulation takes place contactless.
The history of magnetic hybrid-materials starts with the creation of so-called magnetic slurries (1948) [138]. Today a more common name is magnetorheological fluids (MRF). They are usually fabricated by combining a carrier fluid, magnetically polarizable particles and a stabilizer [65]. The most familiar MRFs are the ferrofluids which are in principle in their thermodynamic equilibrium [128]. In the case of ferrofluids, a suspension of surface-treated ferromagnetic particles (7 - 10 vol.%) with an average diameter in the nanometer range are dispersed in a more or less viscous carrier fluid [125, 126, 150]. Therefore, they combine rheological and magnetical properties which can be stimulated by relatively low magnetic fields of around 50 mT [125, 126]. By applying a magnetic field the viscosity and shape can be selectively changed. To date MRFs are used in electrical machines, damping systems, bearings, or positioning systems [35, 123, 126, 149].
The actual response to the external stimulation happens on the particle level. Since the particles can be considered as thermally induced magnetic dipoles (high magnetic moments) a relatively small magnetic field gradient can already induce forces that outweigh the gravitation force and change the ferrofluid's shape. Also, the viscosity variation can be traced back to the particle level. On one hand, the particles experience due to their magnetic moment a rotation in the magnetic

field that counteracts the mechanical rotation when the fluid is sheared. On the other hand, the particles form chain-like agglomerates that break during shearing. Therefore, the response depends on the MRF's characteristics such as the density of magnetic particles, magnetic field strength (H), temperature(T), type of carrier fluid etcetera [65].
To be useful MRFs need to fulfill some fundamental requirements: The magnetic particles should not agglomerate. The same applies to the sedimentation or segregation of the particles which should not occur and if it does, in a way that the particles can easily be dispersed again. By using nano-particles or coating the particle's surface, thermal energy and steric repulsion provide for the ferrofluids stabilization [125, 126]. Another aspect that needs to be considered is the possibility of leakage as the carrier material is a somewhat viscose fluid. Hence suitable confinements are essential. Confinement can happen by enclosures or by fixing the position of the fluid with an external magnetic field. To date, MRFs are still an actual topic in research [5, 105, 118, 169].
To circumvent some of the restrictions, like the enclosure to avoid leakage of MRFs, and disadvantages, like segregation or sedimentation (stability) of MRFs, other magneto-active composites evolved. Among those are magneto-rheological elastomer (MRE), magneto-rheological grease, magneto-rheological polymer gels, and magneto-rheological plastomers [3]. One of the first magneto-active elastomers to emerge were in 1983 the MREs [145], where the carrier fluid was replaced by an elastomer, functioning as carrier matrix. Since the elastomer results from a solution of cross-linkable monomers that form a chemical network it counts as a solid and therefore prevents embedded particles from sedimentation or segregation. Additionally, the mechanical stability of the elastomer prohibits leakage in comparison to MRFs and thus MREs do not need any confinement.

1.1 Magnetostriction and magnetic field-stiffening

Being magneto-active, MREs show two main responses to external magnetic fields, magnetic field-stiffening (magnetorheological or MR-effect) and magnetostriction [67]. The magnetorheological effect is the response of MREs to change their mechanical properties e.g. increase of shear and tensile strength, when subjected to a magnetic field [14, 25, 42, 130]. Magnetostriction on the other hand is the deformation of MREs induced by a magnetic field [44, 46]. This effect is already known since 1847 as Joule experienced the deformation of an iron bar [50]. Due to their in comparison to an iron bar soft matrix magnetostriction is by far more pronounced in MREs [44, 46, 67]. Thus MREs are widely used for applications, such as transducers, actuators, sensors, biomedical systems, and vibration damping [10, 11, 91, 103].

Apart from the change in matrix material (silicone rubber, natural rubber, polyurethane, hydrogels) [10, 11, 31] and magnetic filler particles (volume fraction, size, magnetization, shape) [14, 25, 26, 44, 46, 55, 102, 154, 164, 173], the underlying microscopic particle structure affects the two main responses of MREs [67]. Concerning the microscopic particle structure, one differs between isotropic and anisotropic particle distribution [11]. Isotropic MREs are fabricated under the absence of a magnetic field by dispersing the magnetic filler particles in the uncured elastomer matrix [13, 152, 154, 164]. Thus, the particles are randomly distributed. If the particles are not randomly distributed but structured e.g. aligned and in a chain-like arrangement, the MREs are called anisotropic. This is achieved by curing the MREs under an applied magnetic field. Depending on the time the sample is influenced by the magnetic field and the particles magnetization different particle configuration form [14, 23, 24, 33, 55, 69, 96, 157]. Apart from the isotropic and anisotropic particle distribution, it is possible to directly pattern the particle configuration [134, 135, 179]. Not only microscopic but macroscopic structuring of magneto-active structures has been enabled by molding technique [53] and 3D printing [7–9, 147]. While all those microscopic and macroscopic structuring affect the magnetostriction and magneto-rheology in their way, the responses of MREs to external magnetic fields start on the particle level. Still, the macroscopic responses need to be related to the particle microstructure and internal particle movements.

To connect the magnetorheological effect with the actual particle movement, x-ray tomographic measurement, were conducted by the Odenbach group [130, 152–155, 168, 173]. For these measurements, magneto-active elastomer samples, consisting of a polydimethylsiloxan (PDMS) based matrix with dispersed carbonyl iron particles or NdFeB-particles [152–154], are exposed to a magnetic field of 250 mT. Subsequently, a horizontally aligned X-ray beam penetrates the sample and is projected on a X-ray image intensifier [155]. The X-ray image is transformed into visible light and detected with a CCD camera. Digitization and processing follow and thus an image with 10 μm spatial resolution is obtained [155]. By taking 1440 radiographic images in 0.25° steps and assembling them, a 3D tomographic image of the sample is received and the particle position in a 3D sample subjected to a magnetic field was determined [152]. A comparison with the particle position before the magnetic loading ensured the evaluation of particle paths. Furthermore, the Odenbach group could link the MR effect, a significant enhancement of the Young's modulus under an applied magnetic field, to a change in the internal structure e.g. the transition of the particle microstructure (orientation and position) from isotropic to anisotropic (aligned and in a chain-like arrangement) [152–154]. Zhang, *et al.* [179] reported a change in the MR-effect when subjected to a magnetic field depending on the lattice configured of the particles. To summarize the previous paragraph, the MR-effect of MREs depends on following main parameters [10, 22, 152–154, 178]:

1. MRE microstructure
2. Particle concentration
3. Matrix stiffness
4. Preloading and strain

Concerning the magnetostriction of MREs, a differentiation between isotropic and anisotropic MREs has to be made. Anisotropic MREs show in general higher magnetostriction but also dependence on the orientation of particle chains concerning the external magnetic field direction was observed [38, 60, 109]. Further, the aspect ratio of the MRE (shape), the particle volume fraction and sample strain affect the magnitude of the magnetostriction [44, 60, 109]. Diguet, *et al.* [44] reported a maximum in magnetostriction for a certain particle volume fraction. Additionally, a strong dependence on the prestress was measured. For a prestress in form of compression they observed an elongation of the MRE under applied magnetic field [38]. In contrast, if changing the prestress to a tensile value, the MREs contracted when subjected to a magnetic field [38]. Apart from microscopic structuring, macroscopic structuring with 3D printing can create many different deformation shapes [95]. To date, the influence of particle patterning, like Zhang *et al.* [179] performed for the MR-effect, has not been investigated for the magnetostriction effect. First experiments resolved the particle movement of up to four particles and thus the change in inter-particle distance [134, 135].
Complementary to the experimental research on MREs, many theoretical models and simulations have evolved over the years to depict MREs's responses. While some incorporate a discrete particle distribution other use a continuum approach [54, 66, 72, 74, 139, 162]. Thus, one can find models that describe the macroscopic behaviour of MREs containing chains [42], zick zack chains [66] and lattice structures [72, 74]. Some have already been validated by experiments. Simulations and theoretical description of the actual particle displacement under the application of a magnetic field can be found as well [16, 17, 85, 88, 113, 116, 134, 136, 137, 160, 163]. Due to the continuous advancement in the synthesis of different MREs, whether they differ in the matrix material or particle distribution, theories and models need to be adapted to reproduce the actual response. In general, theories and models are based on two different strategies to depict the relation of elastic to magnetic forces e.g use a continuum approach or the actual particle distribution.
To summarize the previous sections:

- Composites consist of two or more different materials showing a physical or chemical phase and show compared to the single constituent enhanced properties. Especially composites that can be stimulated by an external magnetic field, magneto-active materials, are of

great interest due to their strong responses when subjected to an external magnetic field. Compared to electric or chemical stimulation, magnetic stimulation takes place contactless and magnetic field strengths required to generate material responses are producible with small permanent magnets.

- One of the first magneto-active materials were MRFs which used a liquid as carrier material. To overcome some disadvantages of the MRFs like leakage or segregation, composites with an exchange carrier material such as magneto-rheological elastomer (MRE), magneto-rheological grease, magneto-rheological polymer gels and magneto-rheological plastomers etc. emerged.
- Most applications make use of the MRE's reaction when subjected to a magnetic field. In the case of MREs, one differentiates between magnetostriction, the ability to deform under applied magnetic field, and magneto-rheology, the change of mechanical properties when influenced by a magnetic field.
- Experiments, theoretical models, and simulations observed a strong dependence on the underlying particle microstructure of both effects. The particle microstructure is mainly divided into isotropic and anisotropic particle distribution. An isotropic particle distribution is achieved by just dispersing particles in the uncured carrier material e.g. a polymer. An anisotropic particle arrangement arises when a magnetic field is applied during the curing process.
- New fabrication methods like 3D printing [9, 95, 132, 147, 156] are used to structure MREs macroscopically or creating magnetic domains, thus creating ever more targeted responses.

1.2 Integration in the state of the art

To integrate the presented work in the framework of previous studies some of the above-mentioned work is discussed here in more detail. This should give the reader a better overview of which subjects have already been addressed and where knowledge still is lacking. MREs undergo a reversible shape change (magnetostriction) and/or mechanical property change when exerted to a magnetic field and can be used as dampers, actuators, etc.. The kind and magnitude of the response, as well as the needed stimulation, are of utter importance regarding the MRE's practicality. The response is related to parameters such as concentration and microstructure of the filler particles, matrix stiffness, magnetic field strength, etc. The impact of those parameters on the macroscopic level is relatively well studied. In contrast, the fundamental relation

between macroscopic and internal mechanism is much less understood. How do the internal particle movements depend on the microscopic particle distribution? How does the relation of elastic to magnetic force influence particle movements? What macroscopic responses (elongation, contraction) do the internal particle movements induce?

The relation between macroscopic responses and internal particle mechanism needs to be addressed and understood to allow the tailored design of MREs for the specifically required functionality. Considerable contribution to comprehend the MRE's particle level mechanisms and their connection to macroscopic responses was done in the following studies [6, 16, 17, 19–21, 69, 86–89, 111, 113–115, 130, 133–135, 137, 152–154, 173, 179]. Zhang, *et al.* [179] showed that MREs patterned with particles placed on a 3D body-centered cubic lattice show a decreasing magnetic induced shear modulus. X-ray tomographic measurements by the Odenbach group added knowledge by evaluating internal particle movements and structural changes on the particle level. Subsequently, these internal changes could be linked to magnethorheological effects. But X-ray tomographic measurements are time intensive since a single 3D image consists of a multitude of radiographic images. As a result, the time resolution is quite low. Due to the low time resolution and high particle amount in the MREs, the tracking of particles requires high analytical effort. High polydispersities of particle size and shape facilitate the tracking process. Nevertheless, usually, an overall particle movement is evaluated instead of single-particle paths. Furthermore, modeling the magneto-mechanical response is quite well-advanced, too [29]. Models that are based on the internal structure [30, 66, 72, 74] exist connecting the particle distribution (chains, planes, isotropic) with the magneto-mechanical response.

Concerning the magnetostriction of MREs, theoretical studies exist, that relate the underlying microscopic structure to the macroscopic deformation as well [54, 72–74]. For example, Ivaneyko, *et al.* [73] showed by mimicking different particle distribution that MREs elongate. This model is only valid for small particle movements, though, and thus in general not applicable for soft polymers where the internal deformations usually are quite large. Alternatively, computational simulations were conducted to comprehend the particle movement. To this end, the energy of the system was split into an elastic and magnetic contribution. On the one hand, the matrix was simulated as a mesh with underlying elasticity models, e.g Neo-Hookean or Mooney-Rivlin to provide the elastic contribution. On the other hand, the magnetic mutual particle interactions were considered based on experimentally determined particle magnetization. Consequently, internal particle movement induced magnetostriction could be simulated. Thus computational simulations provided important results that assisted greatly with the understanding of MRE's deformation process [86, 87, 89, 114, 115].

Experiments that confirm or reject theoretical and computational models are by far rarer for the

magnetostrictive response than for the MR-effect. They are mostly based on the investigation of the difference between anisotropic and isotropic MREs and in the case of anisotropic MREs, on the distinction between the various orientations and shapes of chain structures [38, 44, 60, 109]. These experiments could report elongations or contractions of versatile magnitude, depending on the particle structure, prestress, particle volume fraction, etc.. But they did not analyze how internal particle movement contributed to the external deformation, nor how the initial inter-particle distance might affect particle movement. For isotropic MREs the development of particle chains was reported by Stepanov, *et al.* [160] and linked to the magnetostriction. But the overall particle configuration change was not related to single particle movement. Particle tracking and evaluation of the inter-particle distance was done for up to four magnetic particles [134]. Puljiz, *et al.* fabrication method reduced the MREs to a 2D system as particles were placed on one solidified PDMS layer and allowed to adapt the initial inter-particle distance [134]. Thus, the relation between magnetic and elastic force could be adjusted more precisely and ensure the particles were prevented from touching under the applied magnetic field. The applied magnetic field was homogeneous and the field orientation, lying in the particle plane, was rotated. Particle tracking of a two-particle system and determination of the inter-particle distance showed an oscillating trend. For most of the field orientations, the particle distance decreased. Adding one or two particles and thus creating a triangle or square, the influence of mutual magnetic and elastic interaction was observed. A theoretical calculation fitted quite well with the experimental data. In a subsequent study, the initial inter-particle distance was diminished [135]. Consequently, while the magnetic field strength was increased step-wise, the particle snapped into contact at a certain critical field strength. Theoretical calculation predicts a hysteresis if the magnetic field would be reduced step-wise, see Biller *et al.* [16, 17]. This is because touching particles have a locally increase magnetization and as a result particle separation occurs at weaker external magnetic field strength than required to bring them into contact [17, 135]. However, experiments could not resolve the separation event. The present work develops this point further.

1.3 Aim of this thesis

To make the use of MREs deformations more applicable, a focused stimulation and form of the deformation response are important. Hence, data on the internal dynamics of MREs is needed. As the internal dynamic depends on the precise determination of the ratio between elastic and magnetic forces, particle displacement and its dependence on the magnetic field, MREs

constituents, and particle microstructure have to be addressed.
First, a high spatial and temporal resolution of the particle needs to be achieved. So far a high spatial resolution was only accomplished by x-ray tomographic measurements on larger probes requiring a significant amount of time for every image. Measurements, which are quite similar to the ones performed for this thesis, provided high spatial resolution in 2D and are temporal much faster than x-ray tomographic measurements [134, 135]. Apart from few studies where the orientation of the magnetic field was adapted [69, 134], the particle displacement was conducted by changing the magnetic field strength. Since the magnetic interaction does not only depend on the magnetization of the particles but also on their position relative to the external field, the orientation of the external magnetic field enables a simple modification of the magnetic force. Linking the particle displacement to the magnetic field orientation gives rise to deformations based on a different stimulation variation apart from the magnetic field strength. Since these particle movements can be induced by constant magnetic fields in the hundred milli Tesla range, the magnetic fields required to induce particle movement can be realized without great technical effort by permanent magnets. As a result, no currents are needed and changes to the magnetic field orientation can be easily done. These changes to the magnetic field orientation should induce strong deformations of the MRE. For this dissertation, the possibility of strong internal and external deformations induced by changes in the orientation of a magnetic field of constant strength was studied.
To obtain strong magnetostrictive effects, the particles inside the MRE must rearrange in position and orientation under the influence of a magnetic field. Those rearrangements are facilitated by softer elastomer carrier materials and especially if particles are enabled to snap into contact, huge internal deformation of the matrix accompanies the particle displacement. Hence, the issue of mechanical matrix instability arises and destruction of the carrier material through repeated particle displacement becomes an issue. This thesis would like to address the dependence of the particle displacement on the matrix stiffness and to evaluate the reproducibility of the particle displacement. If it is possible to create a strong particle displacement along with long mechanical endurance of the carrier material, it will benefit MREs applicability.
It is already known that the particle microstructure influences the MREs responses. While isotropic particle distribution [152], chain-like [38] and lattice formation [179] were investigated, the dependence of the displacement on the initial inter-particle distance, particle mutual magnetization and particle distribution has hardly been addressed by experiments, yet [134]. Due to this thesis, it will be explored how the initial inter-particle distance and particle distribution influence the magneto activity to see whether particles are forming structures like chains [160] or not. The structure formation will then be linked to particle displacement and thereby to the amount of

macroscopic deformation. Thus, the following questions will be answered: Can discrete particle distribution with defined inter-particle distance enhance the deformation of MREs?
Concluding, experiments were conducted to evaluate the difference between internal deformation, induced by particle interaction and external deformation, induced by particle movement in the magnetic field. This gives indications which deformations, best to exploit concerning the actual application the MRE, should be used in and how these deformations depend on the internal particle structure, relation of elastic to magnetic force, and the magnetic history. Furthermore, in this context, dis-/advantages of the used fabrication method compared to the common one, where particles are just dispersed inside the carrier material will be presented. A simple way to macroscopically structure MREs will be shown. This bridges the gap to the 3D-printed MREs which are produced at the expense of high technical effort. Additionally, the developed fabrication process provides a simple method to tailor the MRE's response to its technical requirement.
At this point, it should be mentioned that the in this thesis investigated samples are more strictly speaking magnetorheological polymer gels than MREs. But since polymer gels are fabricated by adding unlinked polymers to the MREs, they are, apart from a weaker carrier matrix, physically identical. Hence, in the following, they will be synonymously called MRE. To address the mentioned issues, the presented work is structured as follows: In chapter 2 MREs constituent parts will be introduced. The focus lies on the materials that are used to fabricate the measured samples. Since the MREs responses are connected to the materials, a short overview of the most commonly used materials will be given. Subsequently, the magnetic and elastic forces that arise by applying a magnetic field are described in chapter 3. In this chapter, I also present two theoretical models that were constructed by collaborators and fit quite well with experimental results. In chapter 4 the magnetic and optical setup for investigating the MRE samples is explained. Additionally, the different sample fabrication methods as well as the in situ measurement of the Young's modulus of the matrix are included. Chapter 5 discusses the result of MRE with discrete particle distribution. Subsequently, chapter 6 discusses the results of magnetic coated spheres and PDMS membranes with a 2D magnetic layer. Concluding, in chapter 7 the main results of this thesis, an outlook for future experiments and issues that need to be addressed will be summarized.

2 MRE's constituent parts

MREs consist of magnetic filler elements, typically magnetic particles, included in an elastic matrix, mostly polymers. Filler particles come in various shapes and magnetic properties. They can be spherical [38, 69], irregularly shaped [152] or with surface roughness and edges [134]. Their magnetic characteristics can be hard or soft magnetic, differing in magnetic hysteresis losses, coercivity, remanence, saturation magnetization, etc.. Filler particles can be ferromagnetic or (super-)paramagnetic particles, with a magnetic net magnetization with an applied field or without. The matrix material also influences the behaviour of the MRE. MRE's mechanical properties are strongly connected to the elasticity and viscosity of the matrix material. Other properties can be added if e.g. an electric conducting matrix material is chosen. It is apparent, that for the magnetic filler material as well as for the matrix material various options exist. Depending on the chosen options the MRE can exhibit diverse responses. The production process of MREs also influences their behaviour e.g anisotropic MREs show different responses than isotropic MREs. Materials investigated in this theses will be characterized in the following sections. In section 4.1 used production processes are described.

2.1 Particles

Magnetic particles as filler element are readily available in a wide range of shapes and magnetic attributes. For this thesis nickel particles, a paramagnetic material, was selected as filler element. In a paramagnetic material the internal magnetic moments are randomly orientated and therefore average macroscopically to zero, i.e. it has no macroscopic magnetic moment without an applied field. The nickel particles were purchased from Alfar Aesar ($-100 + 325$ mesh, purity 99.8 %). Those particles have a size distribution from 50 to $300\,\mu m$ and were already used in prior research work [134, 135]. Magnetic characterization was previously done via a vibrating sample magnetometer (VSM) [134]. In these measurements, a cylindrical volume sample of the material in powder form was used. A different approach was chosen this time. For this purpose, just one particle was investigated with a superconducting quantum interference device (SQUID-Quantum Design MPMS XL). SQUID measurements were performed by Dirk Sindersberger at the OTH Regensburg [151]. A particle with high sphericity was used and compared to VSM measurements no back calculation from a volume magnetic moment of the powder to the magnetization of a

single particle was required. This minimizes errors caused by the assumption of a homogeneous particle distribution (inhomogeneities through enclosed air neglected) and local magnetic field inhomogeneities in the volume samples.
To ensure a stable location for the particle within the SQUID it was encapsulated in a resin ball. First, half of the resin sphere was cast in a silicone mold and the particle positioned while crosslinking was still ongoing. Thus the particle attached nicely to the surface of the hemisphere. Filling the mold up with resin created a spherical shape. After crosslinking, the resin didn't allow optical detection anymore and particle presence was checked using a Mates CMOS-MagView magnetic field camera. An external magnetic field was ramped up from zero to $7\,T$ and back to $-7\,T$. In the range of $-1\,T$ to $1\,T$ the step size was $10\,mT$, thereafter $100\,mT$ steps up to $3\,T$ and finally in $1\,T$ steps. To obtain the actual magnetic behaviour of the particle the diamagnetic background of the resin as well as the particle's demagnetization field had to be evaluated. The diamagnetic background can be extracted from the slope of the magnetization at fields over the magnetic saturation point of the particle and has to be subtracted from measured magnetization. The particles demagnetization field can be calculated by assuming a spherical particle shape with:

$$\vec{H}_d = \frac{\gamma_d \vec{M}_p}{4\pi}. \tag{2.1}$$

For a sphere the demagnetization factor γ_d equals $\frac{4}{3}\pi$ and $\vec{M}_p$ is the magnetization of the particle [75]. This field has to be subtracted from the applied field. Thus, the SQUID measurements result in the trend depicted in figure Fig. 2.1 a). Taking the magnetization at zero field after one sweep, a remanence of 5.7 kA/m was extracted. The non-alternating magnetization at high magnetic fields determines the saturation volume magnetization. The saturation volume magnetization is extracted by fitting the curve with:

$$\vec{M}_p(H) = M_s(\zeta \vec{H}), \tag{2.2}$$

where $\vec{H}$ denotes the magnetic field strength inside the particle, ζ a dimensionless fitting parameter and M_s the saturation volume magnetization. The magnetic field strength inside the particle is given by subtracting the demagnetization field $\vec{H}_d$ from the applied magnetic field strength $\vec{H}_e$. By fitting the SQUID measurement with the equation Eq. 2.2 the saturation volume magnetization was determined with $(314.2 \pm 0.5)\,kA/m$, see Fig. 2.1 a). Comparing these results with the VSM measurement of Puljiz, *et al.* [134, 135], the SQUID measurement reveals a saturation volume magnetization that is only approximately 6% lower than the VSM results. Whereas the relative permeability $\mu_r = 6.4$ found by the SQUID measurement shows a difference of 120% to the VSM measurement. Inherent to the measurement system, the SQUID measurement provides

a more precise magnetization than the VSM measurements because the SQUID measures the magnetic moment of a single particle with known volume whereas the VSM measures a volume sample of unknown particle distribution. Hence, in this thesis more accurate values for the particle magnetization are used than in previous studies [134, 135]. The SQUID measurement also demonstrates that the purchased nickel particles are superparamagnetic with a relatively high volume saturation magnetization and low magnetic hysteresis loss. Specifying the particle diameter its volume can be calculated under the assumption of spherical shape. Thus, the particle magnetization $\vec{M}_p$ is determined from $\vec{M}_p = \frac{\vec{m}}{V_p}$, with $\vec{m}$ the magnetic moment of the particle and V_p the particle volume. Additionally, tomographic measurements from Ulrich Bröckel (Umwelt Campus Birkenfeld) revealed, a slightly non-sphericality and surface roughness of the particles Fig. 2.1 b). Those result in measurement artifacts and some deviation with simulations which will be remarked with occurrence. Otherwise, slightly non-sphericality and surface roughness are neglected for the purpose of this thesis because the resulting deviation from the volume of a spherical particle with the same diameter is minor and thus also the magnetic characteristics.

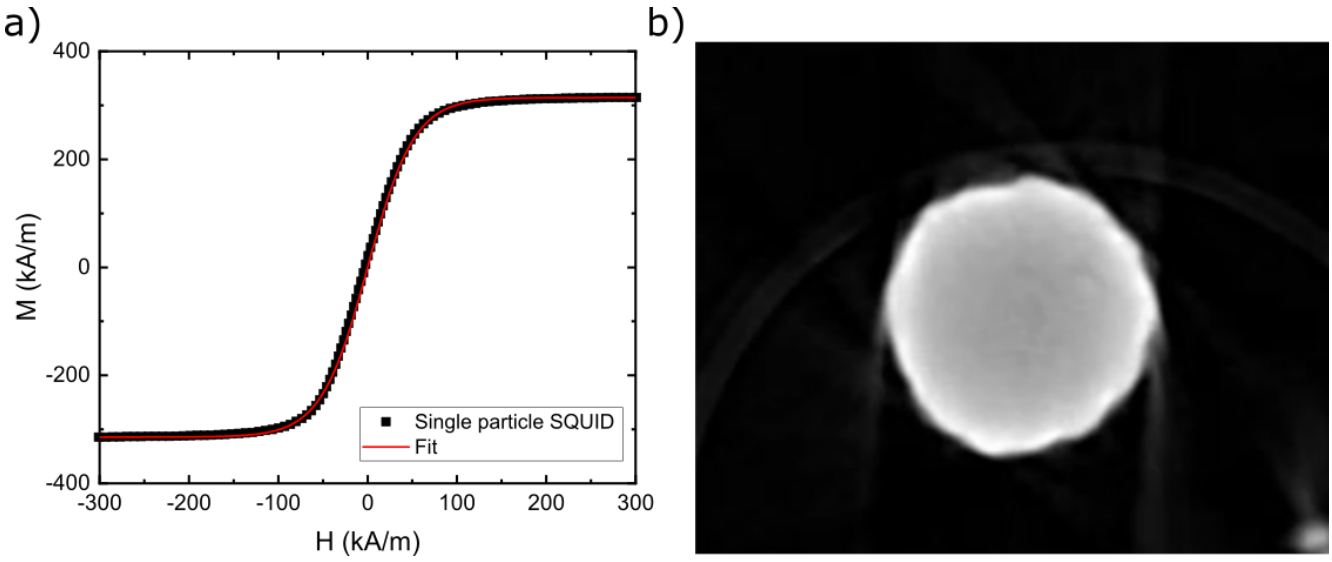

Figure 2.1: a) the magnetization curve of a nickel particle with diameter of $218\,\mu m$ measured by SQUID. The diamagnetic background of the resin was subtracted and the the demagnetization field taken into account. A remanence of $5.7\,kA/m$ and saturation volume magnetization of $314.2\,kA/m$ was extracted. b) Tomographic scan of a nickel particle. The particle was surrounded by air and enclosed by a glass tube.[Adapted from [151], 2021, ©Springer Nature, CC BY 4.0, [151]]

2.2 Matrix-material

The carrier matrix-material of MREs is an elastomer. Concerning the mechanical properties, the term elastomer is used for cross-linked polymeric materials, including polymer gels, that recover to nearly their original dimension after being extended or compressed [39]. Chemical cross-linking and components used to produce elastomers will be covered in the remainder of this chapter. But first, a very brief introduction to rubber chemistry with a special focus on polydimethylsiloxan (PDMS), an elastomer that was used as a carrier matrix in this work, is given.

2.2.1 Chemistry of macromolecules

On the chemical level, an elastomer is a three dimensional chemical network of a polymer and is characterized mostly through its mechanical properties, which will be explained in more detail in chapter 3. A polymer is a macromolecule consisting of repeating identical units, so-called monomers, which are covalently bonded. To name just a few polymers: PDMS, polyvinylalcohol (PVA), polyethylenterephthalat, polydiphenylsiloxan [100]. If those polymer molecules are only connected through entanglement, Van der Waals forces, or hydrogen bonds, a physical network is formed which easily can be destroyed [100]. In contrast, an elastomer is a three dimensional chemical network formed by covalent bonding of polymer chains to each other. The points where those chains bond are so-called crosslinks. The bonding can either be self-induced or by using a crosslinking agent. Elastomers get their elasticity from their three dimensional polymer networks. The elasticity strongly depends on the network density and the amount and order of the crosslinks. Furthermore, the network can not be destroyed by solvents but only swollen with e.g. water (hydrogels) or polymers (polymergel) etc.. Using PDMS as an example the chemical reaction taking place during a crosslinking will be explained.

2.2.2 Polydimethylsiloxane

PDMS is a silicon-based organic polymer consisting of repeating monomers units with chemical formula $[SiO(CH_3)_2]$ [174]. Three ways are known to chemically connect silicones [1, 166]:

- Addition crosslinking
- Cosslinking with peroxides
- Condensation crosslinking

The kind of chemical connection process taking place depends on the functional groups of the polymer and the crosslinking agent. If the polymer contains a vinyl group (red circle Fig. 2.2) and the crosslinking agent a silyl (SiH) group (blue circle Fig. 2.2), addition crosslinking takes place. To start the process a catalyst has to be present. Most common are platinum complexes. For cross-linked PDMS, vinyl terminated PDMS polymers (Fig. 2.2 polymer) of variable chain length are usually crosslinked by methylhydrosiloxane–dimethylsiloxane copolymer (Fig. 2.2 crosslinking agent) [106]. Adding a platinum catalyst, the silyl (SiH) groups of the crosslinking agent and vinyl groups of the polymer bond by hydrosilylation reaction Fig. 2.3 [28]. At the same time, secondary crosslinking reactions do take place at a much slower pace. They hardly affect the cured network though and can be neglected. For a detailed description of those secondary processes, the reader is referred to [28]. The time until the network is cured strongly depends on the ratio of polymer to crosslinking agent, temperature, and catalyst amount. Moderators or inhibitors can additionally be deployed to control the working time. Once the network is cured the Young's modulus stays constant.
The cross-linked PDMS is widely used in research and for applications due to its low cost, simple production, optical transparency in the visible range, low shrinking rate, ability to replicate structures and adaptable Young's modulus [81]. A common, readily available two component PDMS kit is SYLGARD^{TM} 184 from Dow Corning Corporation. As reported, the Young's modulus strongly depends on the mixing ratio between polymer and crosslinking agent [93]. A stoichiometric ratio exists for the mixing ratio between polymer and crosslinking agent at which the volume density of cross links reaches its maximum and with it, the Young's modulus. Every deviation of this stoichiometric ratio leads to an excess of one of the components and softens the cross-linked PDMS by reducing the volume density of cross-links [93]. The generation of cross-links not only depends on the number of functional groups but also on the diffusion length of the functional groups. Hence, the stiffness is affected by the curing temperature as it controls the diffusion of

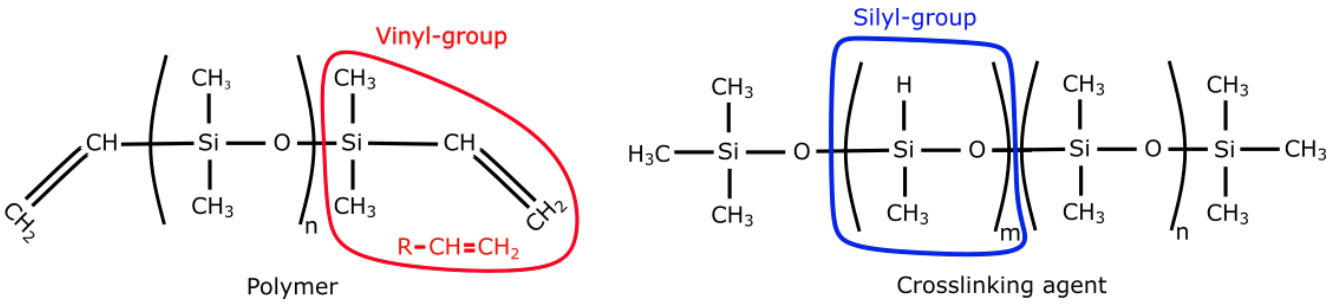

Figure 2.2: The two components mixed to create a PDMS network are schematically depicted. On the left side, marked with polymer, the chemical structure of a vinyl terminated polydimethylsiloxanepolymer is shown. The functional vinyl-group is encircled (red). On the right side, marked with crosslinking agent, the chemical structure of a methylhydrosiloxane–dimethylsiloxane copolymer is sketched. The functional silyl-group is encircled (blue).

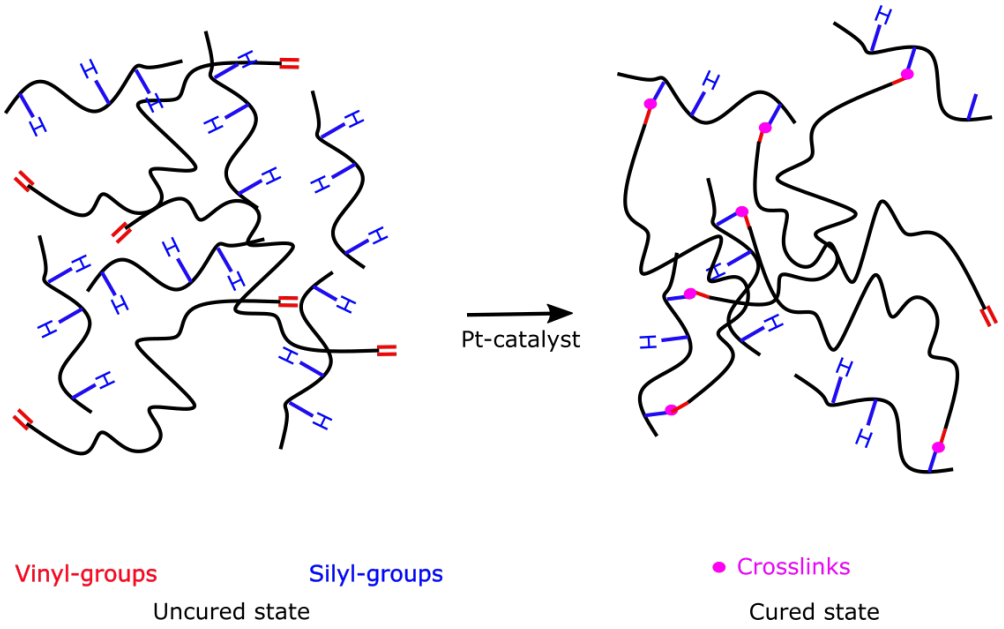

Figure 2.3: The image is adapted from [2]. It shows schematically the PDMS before and after curing. On the left side the uncured components, polymer, and crosslinking agent are depicted. The vinyl-group is indicated by two red lines and the silyl-group by the blue H. After adding the platinum catalyst the hydrosilylation reaction takes place. On the right the cured chemical network is visible. The covalent bonds (crosslinks) are marked with purple circles.

the functional groups [81].

In the presented work investigated PDMS samples are based on mixing a polymer and a crosslinking agent. The exact description of the chemical components and their mixing ratios will be addressed in chapter 4.1. An important subtlety needs to be mentioned already here: The cross-linked PDMS network is swollen by adding a non-functionalized polymer before curing, effectively diluting the prepolymer solution. This enables to create cross-linked PDMS matrices with much lower Young's modulus than achievable with readily available two-component PDMS kits. The swelling also strongly changes the curing dynamic and will be explained in the following. The transition from the still viscoelastic liquid solution of polymer chains to a solidified viscoelastic polymer network, is called sole-gel process (de Gennes *et al.* [40] and Stauffer *et al.* [159]). It was first proposed by Stauffer and Aharony [158] that the point (percolation point) at which this transition starts can be described by the percolation law. The percolation law predicts the growth of branched polymers and can define the number of cross-links per volume required to establish a viscoelastic solid. From a physical point of view, a drastic change of properties occurs at the percolation point. Defining p as the percentage of reacted bonds and p_c the percentage of reacted bonds at the percolation point, one gets the distinction: For $p < p_c$ the polymer is a viscoelastic liquid and for $p > p_c$ an viscoelastic solid [167]. Since the bonding amount directly connects to the ratio r of the functional groups, in the case of PDMS the ratio of silyl groups to vinyl groups, a

critical mixing ratio r_c exists. In the vicinity of the percolation point the shear modulus G is quite sensitive to the mixing ratio and follows a power law [167]:

$$G = G_0 \frac{(r - r_c)^t}{r_c}, \tag{2.3}$$

with G_0 a prefactor and t the exponent depending on the chemical components used. In the case of a swollen PDMS this dependency remains [69]. Hereby the mixing ratio of the polymer and crosslinking agent (prepolymer) stays the same but the concentration of the swelling agent is adapted. Thus, a power law dependency of the shear modulus on the mixing ratio between the prepolymer and swelling agent evolves. The addition of a swelling agent decreases the fraction of bondings as the number of functional ends getting into contact is decreased even if the stoichiometric ratio of the prepolymer was kept constant.
In summary: A polymer is a macromolecule consisting of repeating identical atomic structures so-called monomers. To create an elastomer, polymer chains need to be bonded, covalently. Thus, they form a chemical network giving the elastomere its enhanced elasticity compared to a solution of unbounded polymer chains. PDMS follow the so called additive crosslinking process. The vinyl groups on the polymer chain bond covalently to silyl groups on the crosslinking chain under a hydrosilylation reaction. To start the reaction a platinum catalyst usually is used. In the course of this work the mixture of the polymer and crosslinking agent will be referred to as prepolymer. The stiffness of the resulting elastomere strongly depends on the mixing ratio of the prepolymer. Near the percolation point, the transition between liquid and solid, the shear modulus of the elastomer follows a power law dependency on the prepolymer mixing ratio. Consequently, the shear modulus is quite sensitive to the mixing ratio at this point. Two methods exist to effectively alter the Young's modulus. Either the prepolymer mixing ratio can be varied or a non-functionalized polymer can be added to the prepolymer functioning as a swelling agent. For a fixed prepolymer mixture the shear modulus then follows a power law near the percolation point, depending on the mixing ratio of prepolymer to swelling agent.

3 Theoretical background

MREs consist of different matrix and filler materials. Their macro-and microscopic responses to an external magnetic field therefore can differ significantly. To reflect their responses, theoretical models and simulations need to grasp the underlying physics quite accurately. The following sections focus on the materials introduced in chapter 2, namely, PDMS and nickel particles.
Since the particles can be assumed as rigid and the matrix as non-magnetic both materials can be looked at independently concerning their physics. Thus, when a magnetic field is applied only the particles react to it. The following section distinguishes particles in a homogeneous and inhomogeneous magnetic field. Thereby the magnetic dipole-dipole force, the mutual force between magnetized particles will be derived. As the particles are connected to the matrix material any movement induced by the magnetic forces initiates an answer of the matrix. The answer of the matrix is governed by the viscoelastic behaviour of PDMS which will be introduced. A way to describe the responses of PDMS is the Kelvin-Voigt model. It links the mechanical attributes of the material like elastic modulus (Young's modulus) and viscosity with its deformation under applied stress.
Finally, the key elements of the work of Puljiz *et al.* [134, 135] and Metsch *et al.* [116] are introduced. Both are chosen as in the course of a cooperation their simulation and theoretical models were partly validated with the presented experimental work. Thus, they provide a suitable theoretical basis for further understanding the particle dynamics in the later experimentally investigated MRE samples.

3.1 Linear elasticity

Matter reacts differently to external forces depending upon its state. While solids conserve their shape unlimited in the absence of an applied external force, fluids tend to take the shape of their vessels. Subjected to stress the solid can deform. Elastic deformation is reversible, meaning the solid recovers its original shape after the stress is lifted. To quantify the resistance the solid opposes to the deformation a so-called modulus is introduced. Depending on the kind of deformation different moduli can be defined. If the material is elongated, the resistance is given by the elastic modulus E (Young's modulus), if the material is isotropically compressed, by the compression modulus (bulk modulus) K_b and if the material is sheared, by the shear modulus

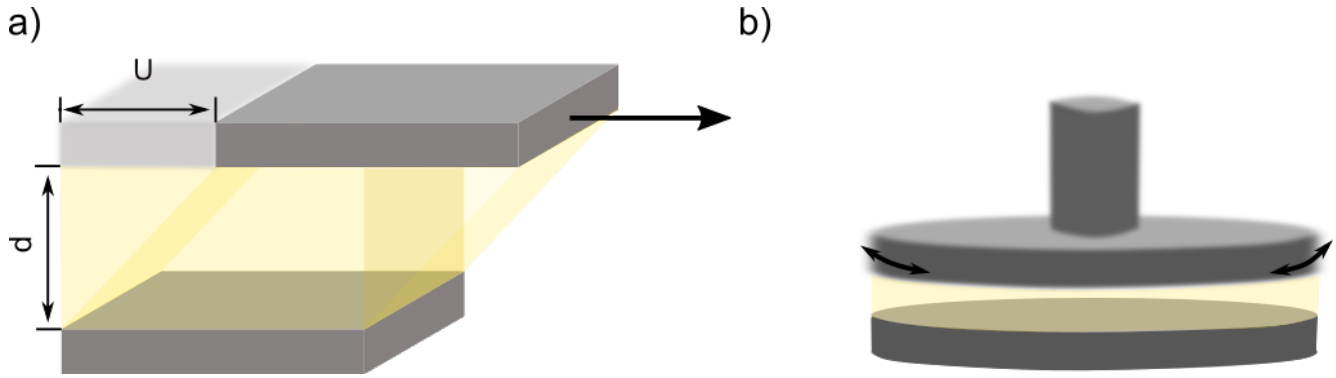

Figure 3.1: a) adapted from [144]. The elastic material depicted in yellow is simply sheared by the movement of the upper plate while the lower plate stays fixed (plates are depicted in gray). A strain is generated with $\gamma = \frac{U}{d}$. b) the configuration of a rheometer with a plate to plate geometry is shown. The lower plate stays fixed while the upper plate is rotated with an angular frequency of ω. Thus the elastic material (yellow) is shear deformed and by measuring the needed torque to uphold the deformation the stress is determined. With the strain and stress finally, the storage G' and loss modulus G'' are extracted.

G. These moduli allow further distinction between hard (large modulus) and soft solids (small modulus) [127]. Every solid ruptures or shows plastic deformation above a certain stress, called yield stress.

In contrast, fluids try to evade the applied stress by flowing. The flowing resembles a permanent and irreversible deformation. To quantify the resistance the fluids oppose to the flow the viscosity is introduced. While elastic materials have a so-called memory effect viscous fluids undergo an irreversible shape change [127].

Starting with the ideal mechanical models: Taking an isotropic elastic solid, the response to stress under infinitesimal simple shear deformation is described by the constitutive equation, the Hooke's law [127]:

$$\sigma = G\gamma. \tag{3.1}$$

Herein, σ denotes the applied stress, G the shear modulus, and $\gamma = \frac{U}{d}$ the strain, Fig. 3.1 a). The Hooke's law gives the proportionality between stress and strain. It also states that the material recovers its original shape after the stress is lifted. Hence, the elasticity can be related to the so-called memory effect, meaning the material has a memory of its original state. For viscous fluids, however, the stress σ and shear rate $\dot{\gamma} = \frac{\partial \gamma}{\partial t}$ are connected through the shear viscosity η, described by Newton's law:

$$\sigma = \eta\dot{\gamma}. \tag{3.2}$$

In contrast to elastic solids, Newtonian fluids obeying this law do not exhibit a memory. They deform irreversibly.

As Maxwell remarked already in 1867 all fluids are viscoelastic. Not only fluids but a lot of

materials possess mechanical characteristics of both kinds (elastic and viscous). They are called viscoelastic materials due to their elastic and viscous properties. Whether their response is dominated by their elastic or viscous properties depends usually on the strength of the applied stress and the time the material is subjected to this stress. Further classification into viscoelastic fluids and viscoelastic solids is done. Viscoelastic fluids still end up deformed irreversible, provided the viscoelastic fluids are subjected to the stress long enough. When applying a sudden shear rate of $\dot{\gamma}$ for a time $t < \tau$ the viscoelastic fluid behaves elastically and for a time $t > \tau$ viscous. The time $\tau = \frac{\eta}{G}$ (viscoelastic relaxation time) at which the material transitions from the viscous to the elastic regime is defined by the ratio between viscosity and elasticity.
Viscoelastic solids show a transition the other way around. If the exposure to stress is shorter than τ it behaves like a viscous fluid and like an elastic solid, if the exposure is longer. The crosslinked PDMS used as matrix material is by definition [83] a polymergel and considered a viscoelastic solid. An elastomer consists of polymer chains that form permanent crosslinks in form of chemical covalent bonds, thereby creating a solid chemical network [127]. A polymer gel additionally contains free uncrosslinked molecules effectively swelling the chemical network (elastomer) [83]. The swelling occurs by adding a fluid before or after the chemical network did form. Depending on the kind of added fluid the gel is designated differently, e.g. when adding water the material is called hydrogel, when adding a polymer, polymergel.
For viscoelastic materials, the viscoelastic relaxation time τ defines transitions from the viscous to the elastic regime or vice versa. It is also the typical time the material needs to recover its equilibrium state after stress release. For small deformations, the material is in the linear elastic regime and the stress is linearly proportional to the strain. In the nonlinear regime, when the material is strongly deformed, the stress is non-linear proportional to the strain. In the linear regime, the shear modulus is constant and the viscosity does not vary. In the nonlinear regime, the shear modulus usually increases with the shear rate while the viscosity usually decreases. Limited to the linear regime, the Kelvin-Voigt model describes the mechanical response of a viscoelastic solid such as polymer gels.
The Kelvin-Voigt model combines a viscous and elastic part where the elasticity of the material is resembled by a spring while the dashpot accounts for the viscous damping with viscosity η. More specifically, it models the material's stress-strain behaviour by coupling a spring and a dashpot parallel Fig. 3.2 a) [127]. As both elements are in parallel the stress sums up to:

$$\sigma = G\gamma + \eta\dot{\gamma}. \tag{3.3}$$

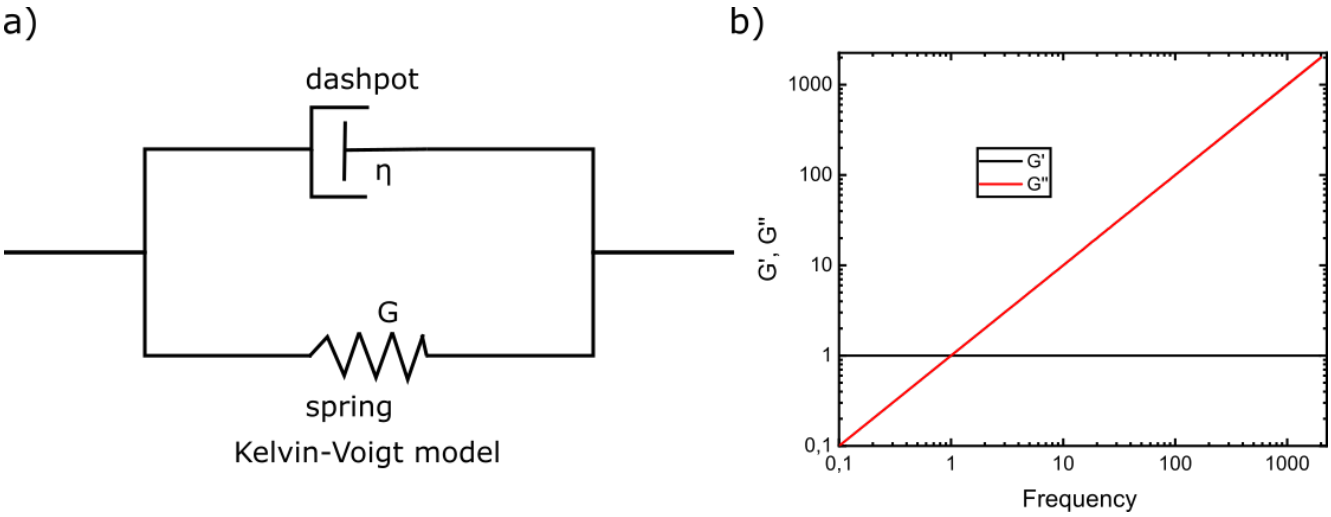

Figure 3.2: a) The Kelvin-Voigt model is illustrated by a dashpot with viscosity η and spring with elasticity G. Herein, the spring accounts for the elasticity of the material while the dashpot stands for internal friction and dissipation. b) an exemplary frequency dependence for the storage and loss modulus, G' respectively G", of a Kelvin-Voigt material. The storage modulus remains constant while the loss modulus increases linearly with the frequency.

Herein, the spring is modeled as a perfect Hookean solid and the dashpot as an ideal Newtonian fluid. Considering a stress pulse of $\sigma = \sigma_0$ applied at time t_0 the strain over time t is given by:

$$\gamma(t) = \frac{\sigma_0}{G}\left[1 - \exp\left(\frac{-t}{\tau}\right)\right]. \tag{3.4}$$

For $t \to \infty$, $\gamma \to \frac{\sigma_0}{G}$ which is a quite realistic prediction.
Applying a dynamical strain in form of a sinusoidal deformation, the strain is given by:

$$\gamma(\omega, t) = \gamma_0 \exp\left(i\omega t\right), \tag{3.5}$$

with an amplitude γ_0 and an angular frequency ω. The linear viscoelastic behaviour is then given by a dynamic complex shear modulus $G^*(\omega)$ in the form of:

$$\sigma(\omega, t) = G^*(\omega)\gamma(\omega, t) \quad \text{with} \quad G^* = G' + iG''. \tag{3.6}$$

Hereby G', also called storage modulus, is the real part of G^* and accounts for the elasticity while G'', also called loss modulus, is the imaginary part of G^* and accounts for the viscous part. In the limit of vanishing frequency, G' becomes G as used in the static case.
To describe the behaviour of a real material more accurately, more complex models can be constructed by generalizing the Kelvin-Voigt model. Therefore, the amount of N different Kelvin-Voigt elements are connected in row. The generalized linear viscoelastic constitutive equation

then is [92]:

$$n_0\sigma + n_1\dot{\sigma} + n_2\ddot{\sigma} + n_3\dddot{\sigma} + \ldots = m_0\gamma + m_1\dot{\gamma} + m_2\ddot{\gamma} + m_3\dddot{\gamma} + \ldots, \tag{3.7}$$

with n, m coefficients yet to be determined with the arrangement of springs and dashpots. Considering the sinusoidal strain in Eq. 3.5, the complex shear modulus can be described in the form:

$$G^* = \frac{m_0 + m_1(i\omega) + m_2(i\omega)^2 + m_3(i\omega)^3 + \ldots}{n_0 + n_1(i\omega) + n_2(i\omega)^2 + n_3(i\omega)^3 + \ldots}. \tag{3.8}$$

For the single Kelvin-Voigt model, Eq. 3.3, the coefficients are set with $m_0 = G$, $m_1 = \eta$, $n_0 = 1$ and $n_1 = 0$ and equation Eq. 3.8 further simplifies to $G^* = G + (i\omega\eta)$. Hence, for a material that can be described by the single Kelvin-Voigt model the storage and loss modulus are $G' = G$ and $G'' = \omega\eta$. An exemplary trend for the storage and loss modulus of a Kelvin-Voigt material is depicted in Fig. 3.2 b).

To determine the storage and loss modulus G', G'' commercial rheometers are available. A common geometry for rheometers is the plate to plate geometry. The sample is clamped between two plates of identical diameter and an oscillating shear is applied while the stress is measured Fig. 3.1 b). In section 4.3.3 the storage modulus of an actual MRE sample is once determined with a commercial rheometer (plate to plate geometry) and once in situ using the Kelvin-Voigt model as a basis.

Two last parameters need to be introduced. The first one is the previously mentioned elastic or Young's modulus E. Applying thermodynamic relations between stress and strain the relationship between the previously introduced shear and Young's modulus can be defined as [127]:

$$E = G(2(1 + \nu)). \tag{3.9}$$

Herein, ν denotes the Poisson ratio. ν takes in the case of an incompressible material (volume is conserved during deformation) the value of 0.5 and therefore $E = 3G$. The second parameter is the elastic and dissipative energy created by the deformation of the material. The maximum elastic energy density W that is stored when the material is deformed with γ_0 is defined as:

$$W = G'\frac{\gamma_0^2}{2}, \tag{3.10}$$

and is recovered when the strain is lifted. The dissipative energy lost during a complete cycle $0 \to \gamma_0 \to 0$ is defined as:

$$W_{diss} = \pi G''\gamma_0^2. \tag{3.11}$$

To understand the basic mechanical behaviour of viscoelastic material under applied stress the Kelvin-Voigt model is sufficient. For the samples investigated in this work, the Kelvin-Voigt model is only applicable to a certain extent, though, as the deformations generated inside the material can be quite high. The linear viscoelasticity of the Kelvin-Voigt model is in general only applicable for small deformations. Furthermore, while the mechanic response under constant stress is depicted quite realistically, the Kelvin-Voigt model is less accurate concerning the relaxation behaviour. To this end, a short introduction to hyperelastic material models follows. Hereby the focus lies on the Mooney-Rivlin model. In contrast to the Kelvin-Voigt model, it describes the material behaviour for nonlinear stress-strain relation when large deformations are present.

3.1.1 Nonlinear elasticity: The hyperelastic material models

For high deformations, linear material models lack accuracy. In general hyperelastic material models are used for high deformations of elastic materials as those models can predict nonlinear elasticity, meaning nonlinear stress-strain material behaviour. In the following, the transition of linear to non-linear elasticity will be explained.
Considering an isotropic material under multi-axial loading the Hookean law Eq. 3.1 becomes [45]:

$$\boldsymbol{\sigma} = 2\mu\boldsymbol{\gamma} + \lambda(\text{tr}\,\boldsymbol{\gamma})\mathbf{1}. \tag{3.12}$$

Herein, $\boldsymbol{\sigma}, \boldsymbol{\gamma}$ denote the stress respectively the strain tensor, (tr) the trace, μ and λ the Lamé coefficients and $\mathbf{1}$ the identity matrix [45]. Equation Eq. 3.12 is the constitutive equation of isotropic linear elasticity. The Lamè coefficients are given by [45]:

$$\lambda = \frac{E\nu}{(1-2\nu)(1+\nu)} \quad \text{and} \quad \mu = \frac{E}{2(1+\nu)}. \tag{3.13}$$

E is the Young's modulus and ν the Poisson ratio. Considering equation Eq.3.9, it is apparent that the Lamè coefficient μ is the same as the shear modulus G. Applying simple shear strain (compare Fig. 3.1 a)) the equation Eq. 3.12 becomes Eq. 3.1.
Considering the elastic energy density W Eq. 3.10 it can also be written in the tensor form as [45]:

$$W = \frac{1}{2}\boldsymbol{\gamma}\!:\!\boldsymbol{\sigma} = \frac{1}{2}\gamma_{ij}\sigma_{ji}, \tag{3.14}$$

with γ_{ij}, σ_{ji} the components of the strain respectively stress tensor. The elastic energy density W is effectively the area under the stress-strain curve. After mathematical transformation the elastic energy can be divided in a deviatoric W_d (shape change) and volumetric term W_V (volume

change). The deviatoric part is dependent on the shear modulus while the volumetric part is dependent on the bulk modulus K_b.
A hyperelastic material is still elastic and returns to its original shape after the load (stress or strain) is removed. In contrast to linear elastic materials, the stress-strain relation is not depending on a constant factor such as shear or elastic modulus but must be derived from a strain energy density function. Since the process of shape change is still reversible (elastic) a potential for the material can be defined [129]. This potential is the so-called strain energy density function W. It gives a measure for the elastic deformation energy [129]. Two conditions need to be fulfilled: The potential becomes zero for zero deformation and the material is isotropic. Introducing new quantities to describe the material deformation one gets apart from the strain so-called principal stretches with $\lambda_{stretch} = \gamma + 1$. Then the strain energy density function W becomes [129]:

$$W = f(I_1, I_2, I_3), \tag{3.15}$$

and is only dependent on the invariants $I_{1,2,3}$ which are given in terms of the principal stretches $\lambda_{stretch}$. Rivlin [146] specified the constitutive equation of the potential Eq. 3.15 in form of a power series [64]:

$$W = \sum_{i+j+k=1}^{\infty} C_{ijk}(I_1 - 3)^i (I_2 - 3)^j (I_3 - 1)^k. \tag{3.16}$$

The potential can be split into a dilatory and isochoric (constant volume) part [76].

$$W = \sum_{i+j=1}^{\infty} C_{ij}(I_1 - 3)^i (I_2 - 3)^j + \sum_{k=1}^{\infty} \frac{1}{D_k}(J_v^2 - \ln J_v - 1)^k, \tag{3.17}$$

and $J_v = \frac{\Delta V}{V}$ being the volume ratio (Jacobi determinant) and C_{ij}, D_k material constants. Apparent, the energy density function for hyperelastic materials is a polynomial function accounting for nonlinearity in the stress-strain relation. Concerning the incompressibility as a further material defining requirement, one can set the material to be incompressible by choosing $I_3 = 1$. Thus the dilatory part becomes zero and taking only the first terms of the sum, i.e., $i = 1$ and $j = 1$, the potential reduces to [64]:

$$W = W_V = C_{10}(I_1 - 3) + C_{01}(I_2 - 3), \tag{3.18}$$

with C_{10} and C_{01} as material constants and $I_{1,2}$ as invariants. This simplified equation Eq. 3.18 is called the Mooney-Rivlin model. It describes the mechanical behaviour of hyperelastic materials and is named after the work of Mooney [119] and Rivlin [146]. Depending on the material the

potential Eq. 3.15 has to be adapted to describe the actual behaviour of the material. The adaption is carried out by choosing the invariants or boundary conditions adequately e.g. by choosing $C_{01} = 0$ Eq. 3.18 becomes the neo-Hookean hyperelastic material model. The neo-Hookean model gives the stress-strain response of an elastic material for moderate strains. For consistency with the linear elastic model $C_{10} = \frac{G}{2}$. To provide a description as precise as possible Eq. 3.17 has to be modified for different hyperelastic materials.

3.2 Magnetic force

The field of electrostatics and magnetostatics exhibit many similarities and can be constructed very similarly. Electrostatic point charges with strength q generate electrical fields with field strength $\vec{E}$. The electric field of a point charge at the distance $\vec{r}$ is given by [97]:

$$\vec{E} = \frac{q}{4\pi\epsilon_0 \left|r\right|^3}\hat{r}, \tag{3.19}$$

where, $|r|$ denotes the norm of $\vec{r}$, $\hat{r}$ the unit vector in the direction of $\vec{r}$ and ϵ_0 the vacuum permittivity. Bringing two point charges close to each other an attractive or repulsive force acts between them. The magnitude of the force is proportional to the magnitude of charges and with the inverse square of the distance between both charges (Coulomb's law).
An electrical dipole can be described with a dumbbell model [97], where two opposite point charges are sitting at the end of a very small dumbbell with position $\vec{a}/2$ and $-\vec{a}/2$. Taking the dipole limit, i.e., $a \to 0$, $q \to \infty$ and $qa^2 \to 0$, the dipole moment $\vec{p}$ is obtained as $qa \to \vec{p}(\neq 0)$. In order to obtain the electric field of an electric dipole, the dipole limit is applied to the electrostatic potential Θ_p of the two opposite point charges which is given by [97]:

$$\Theta_p = \frac{q}{4\pi\epsilon_0}\left(\frac{1}{\left|\vec{r} - \frac{\vec{a}}{2}\right|} - \frac{1}{\left|\vec{r} + \frac{\vec{a}}{2}\right|}\right). \tag{3.20}$$

Therefore, the electrostatic potential is Taylor expanded with relation to $\vec{r}$ and higher quadratic terms in $|a|$ are neglected. Applying the dipole limit, the electric field strength $\vec{E_p} = -\nabla\Theta_p$ of the electric dipole becomes [97]:

$$\vec{E_p} = \frac{\vec{1}}{4\pi\epsilon_0}\frac{3\hat{r}(\hat{r}\cdot\vec{p}) - \vec{p}}{\left|r\right|^3}. \tag{3.21}$$

Subjecting matter to an electric field, electric dipole moments are induced inside the material

with volume V. Depending on the material's electric susceptibility χ_e the polarization $\vec{P}$ of the material can be determined either by:

$$\vec{P} = \epsilon_0 \chi_e \vec{E}, \tag{3.22}$$

or by:

$$\vec{P} = \frac{\vec{p}}{V}. \tag{3.23}$$

The electric field inside the material is then defined by $\vec{D} = \epsilon_0 \vec{E} + \vec{P} = \epsilon_0(1 + \chi_e)\vec{E}$.
In contrast to the electrostatic case no monopoles but only dipoles exist in the magnetostatic case. Comparable to the electrostatic a magnetic field strength $\vec{H}$ and a magnetic dipole moment $\vec{m}$ can be defined for magnetic dipoles [68]. When exerting a material to a magnetic field it is polarized due to small dipoles that are induced inside the material. The so called magnetization $\vec{M}$ is on one hand proportional to the volume V and on the other hand proportional to the magnetic field strength $\vec{H}$. One can write:

$$\vec{M} = \frac{\vec{m}}{V}, \tag{3.24}$$

and

$$\vec{M} = \chi \vec{H}, \tag{3.25}$$

with χ the magnetic susceptibility. The linear relation between magnetization M and magnetic field strength $\vec{H}$ of equation Eq. 3.25 is only valid in a certain range of magnetic field strength (see Fig. 2.1). χ is a characteristic parameter and enables to categorize materials into three different classes:

1. $\chi < 0$: Diamagnetic
2. $\chi > 0$: Paramagnetic
3. $\chi = \infty$: Ferromagnetic

While every material exhibits a diamagnetic background where the internally induced magnetic field is directed opposing the applied field, only materials with intrinsic magnetic moment can show para- or ferromagnetism [170]. Whether materials are paramagnetic or ferromagnetic is defined by whether they exhibit a macroscopic magnetic field without applied field or not. Materials that show only a net magnetic moment under applied magnetic field are called paramagnetic. Ferromagnetic materials exhibit a macroscopic net magnetic moment without being subjected to an external magnetic field and are usually used for permanent magnets. Compared to paramagnetic materials they display in general higher magnetic hysteresis losses, higher coercivity (magnetic field required

to demagnetize the material), higher remanence (magnetization after magnetic field is removed) and higher saturation magnetization, the state when the magnetization does not increase anymore with the external magnetic field. Since the nickel particles used for measurements in this work are paramagnetic the following does focus on paramagnetic spherical particles in magnetic fields. Assuming a spherical paramagnetic particle and subjecting it to a homogeneous magnetic field it gets magnetized and generates a magnetic dipole moment. As deduced from Eq. 3.24 and Eq. 3.25, the magnetization $\vec{M}$ for a particle, in the following $\vec{M}_p$, is related to the magnetic field strength $\vec{H}$. In Eq. 3.25 $\vec{H}$ denotes the magnetic field strenght inside a particle. This field usually differs from the external applied field $\vec{H}_e$ as the particle's magnetization generates a so call demagnetization field. The demagnetization field for a spherical particle can be calculated with $\vec{H}_d = \frac{\gamma_d \vec{M}_p}{4\pi}$ (see equation Eq. 2.1). Thus, the magnetic field strength inside a spherical particle becomes:

$$\vec{H} = \vec{H}_e - \vec{H}_d \quad \text{with} \quad \vec{H}_d = \frac{\vec{M}_p}{3}. \tag{3.26}$$

Substituting Eq. 3.25, 2.1 into 3.26 the magnetization dependency of a spherical particle on the external magnetic field strength is given with:

$$\vec{M}_p = \frac{\chi}{1 + \frac{\chi}{3}} \vec{H}_e, \tag{3.27}$$

In order to determine the magnetization of a particle experimentally usually the magnetic moment is measured for various external magnetic field strengths. Subsequently, the magnetization is calculated with $\vec{M}_p = \vec{m}/V_p$, with m the magnetic moment of the particle and V_p the particle volume. The SQUID measurement presented in section 2.1 is an example for determining the magnetization of a single particle, experimentally. In that case the magnetization dependence on the external field $\vec{M}_p(H_e)$ was measured and the magnetization dependence on the internal field $\vec{M}_p(H)$ had to be calculated. For visualization the different magnetic fields are sketched in Fig. 3.3 a).

Due to this magnetization, paramagnetic particles experience a force when subjected to a magnetic field. Starting with a homogeneous magnetic field the magnetic dipole moment experiences a torque Γ until it is orientated along the external field direction [68]. This torque is given by:

$$\vec{\Gamma} = \vec{m} \times \vec{B} \quad \text{with} \quad \vec{B} = (1 + \chi)\mu_0 \vec{H}_e. \tag{3.28}$$

$\vec{m}$ denotes the magnetic dipole moment, $\vec{B}$ the magnetic flux density, $\vec{H}_e$ the magnetic field strength of the applied magnetic field and μ_0 the magnetic permeability of free space. Since the particle is paramagnetic and its magnetic orientation is not fixed in one direction by anisotropies,

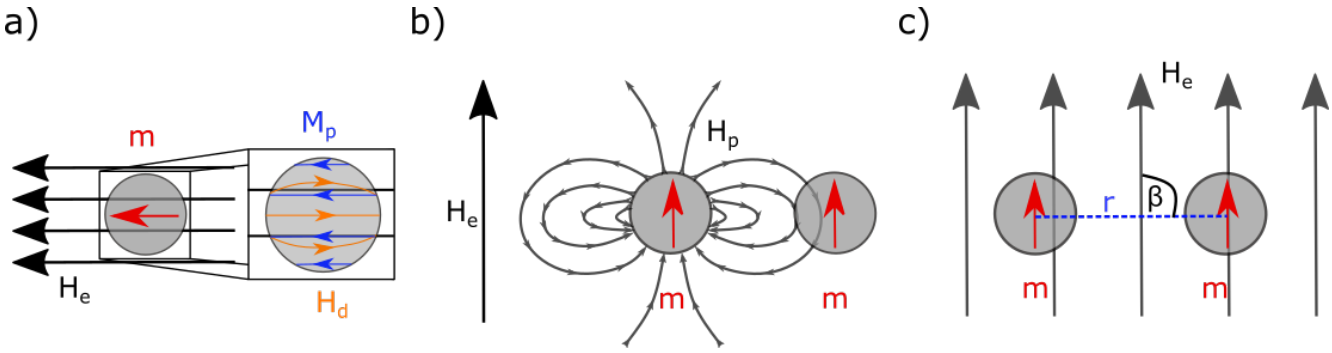

Figure 3.3: a) Fields in- and outside a magnetized particle. The external field $\vec{H}_e$ magnetizes the particle. In return, the magnetization $\vec{M}_p$ creates a demagnetization field $\vec{H}_d$ in the opposite direction of the applied magnetic field. b) The external magnetic field $\vec{H}_e$ induces magnetic dipole moments $\vec{m}$ inside the particles. As a result the particles exhibit a magnetic dipole field $\vec{H}_p$. For simplicity, the magnetic dipole field $\vec{H}_p$ of only one particle is depicted. b) The dipole-dipole force acting mutually on the particles can be defined by the angle β between the particle axis $\vec{r}$ and the external magnetic field direction $\vec{H}_e$.

the magnetic moment aligns to the applied magnetic field without a rotation of the particle. If the magnetic field is inhomogeneous the particle additionally experiences a force in the direction of highest field strength. This force can be calculated by:

$$\vec{F_m} = \nabla(\vec{m} \cdot \vec{B}) = \frac{1}{\mu_0}\chi V_p(\vec{B} \cdot \nabla)\vec{B}. \tag{3.29}$$

Besides interacting with the external magnetic field a magnetic particle can interact with adjacent magnetic particles. This mutual particle interaction is a result of the induced magnetic dipole moments. Due to its magnetic dipole moment $\vec{m_1}$ the particle generates a magnetic field of its own which can be calculated by [75]:

$$\vec{H}_p = \frac{1}{4\pi}\frac{3\hat{r}(\hat{r} \cdot \vec{m_1}) - \vec{m_1}}{|r|^3}, \tag{3.30}$$

with $\hat{r}$ the unit distance vector and $|r|$ the distance norm. Adding a second identical particle with the distance $|r|$ to the first particle it is subjected to this field Fig. 3.3 b). Since here the magnetic field in question is inhomogeneous a force $\vec{F_{12}}$ arises acting on the second particle with magnetic moment $\vec{m_2}$. Inserting the dipole field of the particle Eq. 3.30 into the force that is acting on a particle subjected to a inhomogeneous field Eq. 3.29 becomes [58]:

$$\vec{F_{12}} = \mu_0 \nabla(\vec{m_2} \cdot \vec{H}_p). \tag{3.31}$$

After mathematical transformation Eq. 3.31 becomes [177]:

$$\vec{F_{12}} = \frac{3\mu_0 \left|m_1\right| \left|m_2\right|}{4\pi \left|r\right|^4} [\hat{r} \left(\hat{m_1} \cdot \hat{m_2}\right) + \hat{m_1} \left(\hat{r} \cdot \hat{m_2}\right) + \hat{m_2} \left(\hat{r} \cdot \hat{m_1}\right) - 5 \left(\hat{r} \cdot \hat{m_2}\right) \left(\hat{r} \cdot \hat{m_1}\right) \hat{r}] \,. \tag{3.32}$$

Under the conditions that both particle are identical in size and follow a paramagnetic behaviour, their magnetic moments are of same magnitude and aligned along the external magnetic field direction. Hence it is valid to set $\vec{m_1} = \vec{m_2} = \vec{m}$. Then Eq. 3.32 further simplifies to [99]:

$$\vec{F_{12}} = \frac{3\mu_0 \left|m\right|^2}{4\pi \left|r\right|^4} \left[(2\cos\,\beta)\hat{m} + (1 - 5\cos^2\,\beta)\hat{r}\right], \tag{3.33}$$

with $\hat{m}$ and $\hat{r}$ the unity vectors in direction of the magnetic moment respectively the connecting centerline of the magnetic dipoles (Fig. 3.3 c) blue dashed line) and β the angle between this centerline and the orientation of the external magnetic field Fig. 3.3 c). By using the projection of $\hat{m}$ on $\hat{r}$ equation Eq. 3.33 becomes:

$$\vec{F_{12}} = \frac{3\mu_0 \left|m\right|^2}{4\pi \left|r\right|^4} \left[(1 - 3\cos^2\beta)\hat{r}\right], \tag{3.34}$$

This is the magnetic dipole-dipole force along the particle axis. The "magic angle" of $\beta_m = 54.7°$ can be defined where the force switches from attraction to repulsion. Apart from the strong distance dependency with the inverse fourth power, the magnetic dipole-dipole force is determined by the value of the magnetic dipole moments. As the dipole moment is linked to the particle volume, the dipole-dipole force is influenced by the particle sizes as well. Equating the size of a particle with its diameter a size dependency of the third power of the particle diameter is given. Hence, the dipole-dipole force will be more sensitive to an inter-particle distance change than a variation in particle size.

Comparing the field equation for a magnetic Eq. 3.30 and an electric dipole Eq. 3.21 shows the similarities. In analoguey to the electrostatic case the magnetic dipole field is obtained after the Taylor expansion of the magnetic potential is terminated after the first order. For well separated magnetic particles this approximation and the magnetic dipole-dipole force Eq. 3.32 hold as the higher order terms of the magnetic potential (multipoles) decay inversely with higher order of the distance. If particles are in close proximity the multipole term's influence increases and the actual magnetic force acting between the magnetic particles deviates from the dipole-dipole force. The influence of the multipoles can be included as e.g. Biller *et al.* [17] showed by using a multipole expansion to depict the mutual magnetic interactions of the magnetic particles. Furthermore, one

has to consider that particles mutually influence their magnetization by their generated magnetic fields. This becomes non negligible the closer particles get to each other. This can be taken into account by solving the particle magnetization iteratively as e.g. done by Puljiz *et al.* [134] and will be explained in section 3.3.1.

3.3 Framework of present work

Many simulations and theoretical modeling of MREs are available in literature [16, 18, 19, 36, 37, 49, 94, 131, 134, 171]. The published theoretical work ranges from two particle interaction to multi-particle interaction, from linear to nonlinear elasticity etc.. For the material system presented in this work in modeling had already started in previous collaborations as part of a DFG priority program (SPP 1681), and were validated by experiments of MREs with same constituents as the samples investigated in this work [135]. The theoretical models calculate the magnetization of two paramagnetic nickel particles and their displacements inside the matrix in an external magnetic field. The arising mutual magnetic and elastic forces were solved iteratively. As a result, the calculation provided the inter-particle distance dependency on the external magnetic field strength and showed good qualitative and quantitative agreement with the experimental results. The main equations and assumptions of Puljiz *et al.* [135] are be discussed in the following. Also, the modeling framework of Metsch *et al.* [116] are be mentioned, since experiments presented in this work were used to validate these simulations. In this work, the inter-particle distance of two nickel particles subjected to a rotating homogeneous magnetic field was simulated by calculating the free energy of the system. The free energy is split into a mechanical and magnetic part and respective fields inside the sample are explicitly resolved. For the magnetic part, a SQUID magnetization measurement provided the particle magnetization values. In contrast to [135] the system's mechanical part has been modeled with a nonlinear hyperelastic material model. The experimental part of [116] is discussed in chapter 5.1.

3.3.1 Reversible magnetomechanical collapse

Initially, a single paramagnetic nickel particle is subjected to the external magnetic field. Its magnetization is given by Eq. 3.27. Inserting a second particle near to the first (compare Fig. 3.3 b)), the magnetic dipole field of each particle Eq. 3.30 also contributes to the magnetization of its

neighbor particle. Thus the effective magnetic moment needs to be calculated as [135]:

$$\vec{m}_i = V \frac{\chi}{1 + \frac{\chi}{3}} [\vec{H}_e + \vec{H}_p(r_i)]. \tag{3.35}$$

This equation has to be solved iteratively in combination with Eq. 3.30 to determine the actual magnetic moment of the particles. To start the iteration, the magnetization of a single nickel particle was determined in a first step by fitting an experimentally obtained magnetization curve (vibrating sample magneto-meter, Lake Shore 7407) [135]. The obtained magnetization of the particle at the applied external magnetic field strength $\vec{H}_e$ allowed to calculate the magnetic field $\vec{H}_p$ of the first particle at the position r_i of the second particle. The external field strength and the particle field strength of the first particle sum up and influence the magnetic moment $\vec{m}_i$ of the second particle. This modified magnetic moment is used as input to calculate the magnetic field $\vec{H}_p$ of the second particle which inserted into Eq. 3.35 gives yet a new modified magnetic moment of the first particle. This iteration is repeated until the magnetic moment does not change significantly anymore. The result is the actual magnetic moments of two particles in close proximity. The force acting on the particles can then be calculated straight forward by solving Eq. 3.32 for every particle distance $|r|$.

In the case of Puljiz *et al.* [135] nickel particles were embedded in a PDMS matrix by placing them on a cross-linked PDMS layer with defined distances before another layer of PDMS was poured on top (Fig. 3.4 a)). In one experiment two nickel particles were embedded in a PDMS matrix. The sample was placed in between two permanent magnets and the magnetic field was increased stepwise by decreasing the distance between the two magnets. The magnetic force acting on the particles displaces the particles and thereby distorts the matrix. The matrix was assumed to be homogeneous, isotropic, and incompressible and the displacement matrices were mathematically described in detail in [134]. As basic equations, the linear elastostatic Navier-Cauchy equations were taken. The Navier-Cauchy equations result from the Cauchy-Euler's law of motion for small displacements in combination with the Hooke's law Eq. 3.1 and describe the deformation of elastic materials in the linear elastic regime. Replacing the velocity through displacement fields in the Navier-Cauchy equations Puljiz *et al.* [134] discovered that the solution approach of the hydrodynamic Navier-Stokes equations is applicable.

For simplification, only the underlying idea is given and the reader is referred to [134] for the detailed mathematical description. When particle 1 is displaced it creates a displacement field Fig. 3.4 b). Due to the deformation of the matrix, particle 2 is displaced as well and would be distorted Fig. 3.4 b). Since the particle can be assumed as rigid it opposes distortion with a counter displacement field. This counter displacement field is acting with a restoring force on

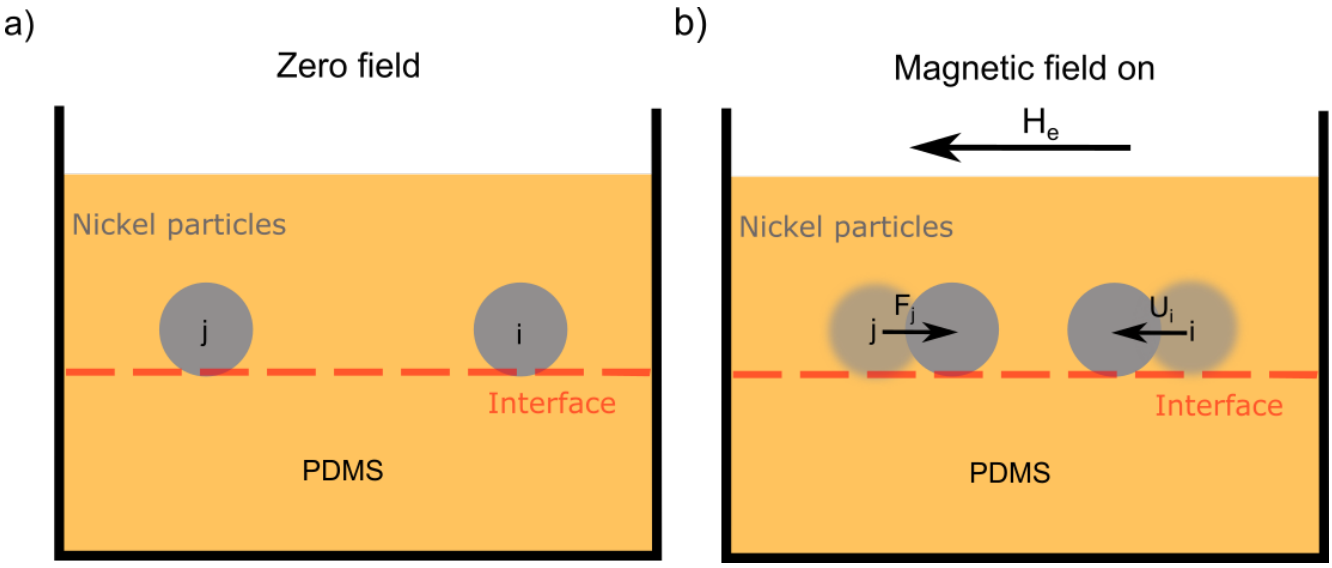

Figure 3.4: a) exemplary two nickel particles are embedded in a PDMS matrix. No magnetic field was applied. As the first PDMS layer is cured before the second layer is poured to allow particle positioning, an interface marked with a dashed red line exists. b) when a magnetic field is applied the particle j is displaced from its original position (blurred gray circle) as a force F_j is acting on it. This displacement is mediated by the matrix causing a displacement field which displaces particle i.

particle 1. An iteration is needed again since the displacement of particle 1 displaces particle 2 and vice versa. Keeping in mind, that the magnetic force is distance depended, meaning that the inter-particle distance affects the magnetic force, the iteration for the displacement, and actual magnetic moments Eq. 3.35 or rather the iteration of the magnetic force need to be combined. After different steps of iterations, the displacement fields are summed up and superimposed with all acting forces resulting in a displaceability matrix (see Eq. 10 in [134]). It can be written in form of [135]:

$$U_i = M_{ii} \cdot F_i + M_{i \neq j} \cdot F_j, \tag{3.36}$$

where $M_{ii}, M_{i \neq j}$ are the displaceability matrices, U_i is the deformation field, F_i is the magnetic forces and $(i, j) \in (1, 2), (2, 1)$ giving the particle number. The mathematical model was applied and solved numerically by iteration [134, 135]. It showed very good agreement with experimental data.

Experimental data, as well as the mathematical model, showed an inter-particle dependence on the magnetic field strength and that at a certain magnetic field strength the particle snapped into contact. At this time, the experimental setup only allowed the stepwise increase of the magnetic field. Thus, the magnetic field strength at which particles separate again could not be resolved experimentally. The theoretical analysis predicts a hysteresis, meaning particles separate at lower magnetic field strength than is needed to let them snap into contact. On one hand, this can be

explained by the relation between magnetic dipole-dipole and elastic force. Since the dipole force scales with the inverse fourth power of the inter-particle distance, for the same external magnetic field strength, particles in contact are governed by a much stronger magnetic dipole-dipole force than particles well separated. Biller *et al.* [17] could show that the total energy, the summation of magnetic and elastic energy, has two minimum. Those two minimum resemble the equilibrium state of particles well separated and particles in contact. With increasing magnetic field strength the system transitions from one minimum to the other. As a result, the transition between the two equilibrium states is by nature hysteretic in the applied field strength. On the other hand finite-element (FE) simulations showed a spatial inhomogeneity of the magnetization inside the particles. When particles are in contact the magnetization is strongly enhanced at the point of contact. Including this spatial inhomogeneity of the magnetization into the calculations, the two particle system shows an even more distinctive hysteresis compared to the sole dipole-dipole model.

3.3.2 Field-induced interactions

The following equations and modeling was conducted by P. Metsch and M. Kästner (TU Dresden) and can be read in detail in [116]. The experiments conducted to provide the input values for the simulation and to validate the simulations will be presented later in the course of this work. The model selected to simulate simplified two, three, and four particle MRE systems was also a microscopic continuum approach. In contrast to the previous explained model of Puljiz *et al.*, the matrix was modeled as a nonlinear hyperelastic material and the dipole approximation assuming a homogeneous magnetization inside the particles was exchanged by calculating the actual (inhomogeneous) magnetization inside the particle. Choosing a low amount of particles reduces the influencing factors to a manageable number and facilitates comparison with experiments. The detailed microscopic continuum model can be found in [112] and here only the essential equations are repeated which was similarly done in [116]. The derivations can be read as well in [112]. Since the matrix material is non-magnetic and the particles are in contrast very stiff the free energy can be split into a mechanical and magnetic contribution:

$$\rho_0\psi(C,H) = \rho_0\psi^{mech}(C) + \rho_0\psi^{mag}(H), \tag{3.37}$$

with ρ_0 the mass density per unit volume. The mechanical part of the free energy describes the properties of the non-magnetizable matrix and only depends on the Cauchy–Green deformation tensor C. Assuming an isotropic and elastic matrix the free mechanical energy ψ^{mech} can be

expressed by the compressible Mooney-Rivlin model in form of the strain energy density function:

$$W = \rho_0 \psi^{mech}(C) = \frac{G}{2}[p(I_1 - 3) + (1-p)(I_2 - 3)] + \frac{K_b}{4}(J_v^2 - 2lnJ_v - 1). \tag{3.38}$$

p denotes a dimensionless parameter that regulates the influence of the first two principal invariants $I_{1,2}$ and J_v is the Jacobi determinant. As described in section 3.1.1, the Moonley-Rivlin model divides the energy into a deviatoric and a volumetric term. Herein, the deviatoric part is interrelated to the shear modulus G and the volumetric to the bulk modulus K_b. To account for the matrix incompressibility the Poisson ratio was set to be 0.49 and to account for the equal contribution of the invariants $p = 0.5$. Thus Eq. 3.38 simplifies to Eq. 3.18 with $G = 4(C_{10} + C_{01})$. Finally, the magnetic free energy of the particles needs to be determined. As a first step, this included the magnetization measurement of a single particle with SQUID. Fitting the curve gives the magnetization $\vec{M}(H)$ for every magnetic field strength. The curve was fitted with a Langevin-function. In contrast to the linearized relation between magnetization and field strength (Eq. 3.25) that is only valid up to a certain field strength, the Langevin-function describes the actual magnetization-field strength relation for superparamagnetic materials. Hereby, the Langevin-formalism sets the orientating force of the external magnetic field in relation to the disorientating effect of thermal motion. Using the magnetization given by the Langevin-function the magnetic free energy can be calculated with:

$$\rho_0 \psi^{mag}(H) = -\frac{\mu_0 M_s}{\alpha} \ln \cosh(\alpha \vec{H}). \tag{3.39}$$

α denotes a scaling factor extracted by fitting the magnetization curve, M_s the saturation magnetization and μ_0 the vacuum permeability.
For the finite element simulation with *FEniCS* the particles were assumed to be spherical and the matrix was modeled as a mesh with *Gmsh* [116]. Comparable to experiments the magnetic field is not instantaneously applied but ramped up to $H = 135.3\,kA/m$ in 10 steps. The magnetic relaxation of the particles occurs on a much faster timescale than the magnetic field variations hence, providing a quasi-static measurement. Considering the experimental measurement on MREs that will be shown later in this work, the following parameters were chosen for the simulation: To account for the incompressibility of the PDMS matrix the Poissons ratio was set to be 0.49. As the Young's modulus could not be defined experimentally it was determined by identifying the smallest error in the particle displacement between experiment and simulation. A comparison between simulation and experimental results will be given in chapter 5.1.

4 Sample fabrication and experimental setup

Chapter 2 introduced the MRE constituents and chapter 3 the basics for mechanical and magnetic modeling needed to understand particle dynamics in MRE. This chapter starts with explaining the sample fabrication method. A distinction between bulk samples, thin samples, and macroscopic magnetic structured samples will be made. To create particle movement, two different types of magnetic fields, a homogeneous and an inhomogeneous gradient field, were used. The homogeneous field was generated by permanent magnets arranged in a so-called Halbach-array. The inhomogeneous gradient field was generated by an electromagnet. When MRE samples are subjected to either of the mentioned magnetic field forces are generated that displace the particles inside the MRE. In the presented work these particle movements are optically detected with an optical setup that is described in the adjacent sections. In the course, the particle tracking process will be explained and errors caused by the magnetic and optical setup will be determined. Concluding, an in situ measurement of the samples Young's modulus is presented.

4.1 Sample preparation method

There are two common preparation methods of MREs. The first method uses a magnetic field during the curing process. MRE samples are subjected to the magnetic field while the carrier matrix has yet to solidify. Depending on the time and strength of the applied magnetic field, more or less extended particle configurations, e.g., chain-like agglomerations form. MREs that were structured during the curing process have a "built-in" anisotropy due to the preferred orientation of these structures along the applied field. In the second method, the samples are crosslinked under zero-field influence. Such MREs are isotropic MREs as the particles are randomly distributed.
Both methods disperse the filler material inside the matrix material before curing. Therefore, the inter-particle distance can only be adjusted indirectly. For isotropic MREs, the volume percentage of added filler material is adapted. For anisotropic MREs, the amount of particles in contact, i.e., the average group size of the particle structures depends significantly on the strength and time of the applied external magnetic field during the crosslinking process [23]. In both methods, the inter-particle distance is not well controlled. To work around this limitation, the conventional fabrication method of MREs that mixes the particles with the carrier material is not used in this thesis. Instead, a process that builds up the samples layer by layer is used, similar to the process

described in [69, 134, 135, 179]. This process offers the possibility to deposit the particles with a specific initial position and, therefore, defined inter-particle distances. This enables to create particle configurations of selected shape like rectangle or hexagonal arrangements. Additionally, a particle selection can be carried out limiting the influencing variables. Concluding, the potential of the fabrication method to produce magnetically structured 3D MREs will be shown.

4.1.1 Bulksystems

Instead of using a readily available polymer kit like Sylgard® 184 from Dow Corning, a strongly diluted functional PDMS is crosslinked by adding a platinum catalyst like in [69, 134, 135]. The first step included preparing a stock amount of the so-called prepolymer mixture. To this end, 90.9 wt % difunctional vinyl-terminated polydimethylsiloxane (DMS-V25, 500 cSt Gelest Inc. with a molecular weight of 17.200 g/mol) were mixed with 9.1 wt % of the SiH-containing methylhydrosiloxane–dimethylsiloxane crosslinker (HMS-151 Gelest Inc.). Within tolerance, the ratio of the prepolymer mixture stayed unaltered for all samples. By adding a platinum catalyst solution consisting of 5 wt% platinum(0)-1,3-divinyl-1,1,3,3-tetramethyldisiloxane complex (SIP6830.1 Gelest Inc.) and 95 wt% trimethylsiloxy-terminated PDMS (molecular weight 770 g/mol, Alfa Aesar) to the prepolymer mixture an elastic, chemically linked PDMS network is created. To obtain swollen PDMS carrier matrices, an intermediate step was required.
A certain weight percentage of prepolymer mixture was added to the low-molecular-weight trimethylsiloxy-terminated PDMS (molecular weight 770 g/mol). This was done prior to starting the crosslinking reaction with a platinum catalyst solution. Thereby, the prepolymer portion only accounts for a small weight percentage, in maximum up to 25 %. The mixture of PDMS and prepolymer mixture is called reactant solution. The reactant solution was always mixed in the volume ratio of 16:1 with the catalyst solution. The actual crosslinking takes place through a hydrosilation reaction, see section 2.2. As the chemical reaction only happens between the prepolymer components, the low-molecular-weight PDMS is only woven in and effectively swells the network. Hence, the Young's modulus of the finished sample is adjustable by the weight percentage of added prepolymer mixture to the chemically inert PDMS. Consequently, a swollen, crosslinked PDMS matrix with adjustable stiffness is obtained. In the following, the crosslinked PDMS matrices are defined by the weight percentage of the added prepolymer. A 25 % PDMS matrix contains thus 25 wt % prepolymer solution. Ingredients were weighted with a scale accurate to the milligram range. Even so, slight fluctuations occur between the mixing ratios of every new batch. Those small fluctuations are in the range of 0.2 % and do not affect the stiffness of the PDMS matrix, significantly, and can be neglected. To circumvent these fluctuations PDMS

matrices could be prepared out of the same stock of reactant solution.
In the following, the term bulk samples will be used for samples with matrix dimensions exceeding the particle extensions by far. Bulk system samples, i.e., samples with total thickness ≥ 3 mm were always prepared according to the following scheme: 320 μl of reactant solution were mixed with 20 μl catalyst solution and cast into square plastic moulds with an edge length of 1.5 cm and height of 1 cm. The mold kept the viscous PDMS in form during crosslinking. As the chemical reaction is temperature dependent and a diffusion driven process, the PDMS network was cured at $60° C$ for 24 hours.
Afterwards, this layer has enough mechanical stability and the magnetic particles can be deposited on the layer. The used particles were carefully selected for a high roundness and a specific diameter. The roundness $Round$ is given by $\left[Round = 4 * \text{particle area}/(\pi * \text{major particle axis}^2)\right]$ such that a perfectly spherical particle's roundness is $Round = 1$. Used nickel particles showed a roundness between 0.91 and 0.99 (extracted by ImageJ). After particle deposition and in order not to harm the matrix, the particles were carefully pushed over the surface with a micro manipulator device until they reached their designated position. This procedure allowed a position accuracy of $\approx \pm 10\,\mu m$ due to the resolution of the used microscope. More limiting factors for the exact positioning of the particles are the PDMS softness and particle surface roughness. Particles deposited on the matrix create a deformation in their surrounding. The softer the PDMS the larger this deformation and hence, particles positioned in a distance smaller than a certain limiting distance snapped together. The exact positioning of the particles also was influenced by their surface roughness. Particles with a high surface roughness were more likely to exhibit a certain equilibrium position due to the edges of the particles.
To fully encapsulate the positioned particles in the cross-linked PDMS matrix material, a second layer of the same crosslinkable PDMS was cast on top (Fig. 4.1 and figure 3 in [133]). It consisted of $320\,\mu l$ reactant solution with the same mixing ratio as the first layer, and $20\,\mu l$ catalyst solution. Another curing period at $60° C$ for 24 hours followed. The crosslinking process then is slowed down to a point at which it ensures a matrix with stable Young's modulus over the time period of the measurements. The final matrix thickness is about 4 mm and exceeds the particle diameters by a factor of > 10. Therefore, the particle movement is well decoupled from the mechanical boundary conditions at the PDMS surface, and matrix boundaries do not influence the particle movement.

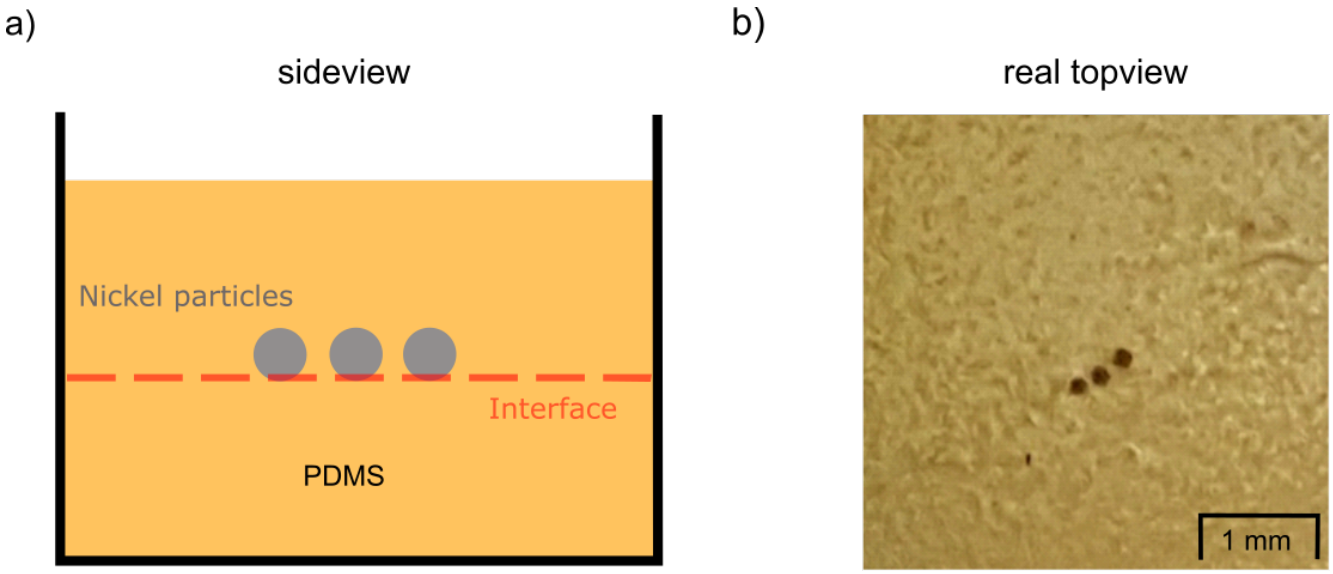

Figure 4.1: a) Side view sketch of an exemplary three particle bulk system. The black rim resembles the plastic mould that keeps the PDMS solution from flowing during crosslinking. A PDMS layer is crosslinked before particle and top layer deposition. The interface between the lower and upper PDMS layer is marked with a red dashed line. b) Top view of a real three particle bulk sample. The particles are the black spots and the yellowish surrounding is the PDMS matrix.

4.1.2 Free-standing layers

In bulk samples, the microscopical particle displacements do not lead to detectable macroscopic matrix deformations. To facilitate macroscopic matrix deformation, the matrix flexibility was enhanced by reducing the sample thickness, i.e., thin free-standing films were prepared. Previously used plastic moulds could not be considered as the adhesion of the PDMS to the plastic was too high to remove the samples from the moulds after crosslinking. Since it is not easy to prepare a thin, free-standing PDMS matrix without support two strategies were used. The first one applied the use of a sacrificial layer. To this end, 10 wt % polyvinylalkohol (PVA, 113000 MW, 90 % hydrolysation) were dissolved in water at $80° C$ under continuous stirring. The obtained solution was cast and dried at room temperature until the water evaporated and a solid film was formed. After solidification, a rim of two component epoxy glue from UHU with dimension 2x2 cm was mounted on top. The glue rim functioned as an enclosure preventing the PDMS solution from spreading. Subsequently, PDMS solutions were mixed with the same ratio as in the previous section only the volume of the reactant solution was reduced to 160 μl. Hence, the bottom matrix layer exhibits a thickness of $\approx 350\,\mu m$. A curing period of 24 hours under $60° C$ was conducted. Afterwards, the deposition and arranging of the particles took place analogue to the bulk system. Encapsulation was done with yet another layer PDMS. Its volume of 160 μl resulted in an overall PDMS matrix thickness of $\approx 700\,\mu m$. Concluding, the PVA substrate was sacrificed by placing the

whole construct into an $80 \circ C$ water bath. This solved the PVA substrate leaving the thin MRE sample free standing only supported by the glue rim. If required, the MRE sample could simply be cut out of the glue rim to be completely unsupported.
An alternative method without sacrificial layers was to use a Teflon^{TM} sheet as substrate. Analogue to the sacrificial layer method, a two component epoxy glue rim with dimension 2x2 cm was attached on top. Same volumes of reactant solution were used resulting in a film thickness of $\approx 700\,\mu m$. Also curing time/temperature and particle selection/deposition/positioning remained the same as for the sacrificial layer method. Instead of dissolving the substrate, it was carefully peeled off. This is possible as the adhesion of the PDMS to Teflon^{TM} is significantly lower than to the plastic moulds. In the end, both procedures lead to thin PDMS films stabilized by a glue rim or if required, completely unsupported MRE samples.

4.1.3 Magnetic coated PDMS spheres

Microparticles made out of PDMS are gaining more and more attention as they have a variety of beneficial properties. They are biocompatible, simple surface modifiable, permeable to a variety of gases and can be used in medical and environmental applications [79, 107]. To create PDMS microspheres/microbeads, two different methods are used. The first is a microfluidic approach where a flow-focusing mechanism is applied. The PDMS solution is injected into an aqueous solution and thereby dispersed into microdroplets [79, 122]. Afterward, these droplets are collected and cured, forming spherical monodisperse microspheres. The second method requires the production of a stable emulsion and is called bulk technique [80, 90, 175, 180]. Both mentioned methods have their challenges.
For the microfluidic method, the channels are often constructed out of PDMS themselves. Hence, the sidewalls are strongly adhesive for the injected PDMS solution. Thus, the sidewalls need to be prepared by complex processes [79]. Furthermore, a surfactant needs to be added to the aqueous solution the PDMS solution is injected into. The process of droplet generation with the flow-focusing mechanism underlies additional influences: The viscosity of the PDMS solution, the interfacial tension and flow rates of the aqueous and PDMS solution [79,122]. The bulk technique's challenge to create stable emulsions in aqueous solution and monodisperse droplets [32, 90, 107]. Creating stable emulsions can be problematic due to surface energy and the high viscosity of common PDMS solutions. To create a stable emulsion, the mixture of water, surfactant, and PDMS requires to be stirred for several hours. To prevent the droplets from aggregating or coalescing, an ultrasonic emulsifier is often used, additionally.
In the following, a production process for PDMS spheres is presented that neither requires high

technical effort nor the use of surfactants or other toxic chemicals. Apart from the PDMS it only uses propan-2-ol (C_3H_8O) and distilled water. Propan-2-ol is widely used in industries and easily attainable and manageable. Furthermore, the fabrication process only requires an Eppendorf pipette. Hence, the fabrication method can be vastly applied without great risks and technical effort.
Distilled water is mixed with propan-2-ol in a glass jar in the ratio of 50/50 volume fraction. After preparing the PDMS solution like in 4.1.1 it is extruded into the propan-2-ol/water solution with an Eppendorf pipette. Thereafter, the density of the propan-2-ol/water solution is adapted carefully to create a density match between propan-2-ol/water solution and PDMS mixture as follows:

1. If the sphere sinks to the bottom of the jar, water is added until the sphere floats again (Fig. 4.2 a) red arrow).
2. If the PDMS forms a layer on the surface of the solution, propan-2-ol is added until a floating sphere forms (Fig. 4.2 a) red arrow).

The integrity of the sphere is not harmed during the matching process. Depending on the PDMS mixing ratio it takes one to five minutes until the PDMS spheres are crosslinked and mechanically stable enough to be removed with tweezers. Compared to typical PDMS solutions like Sylgard

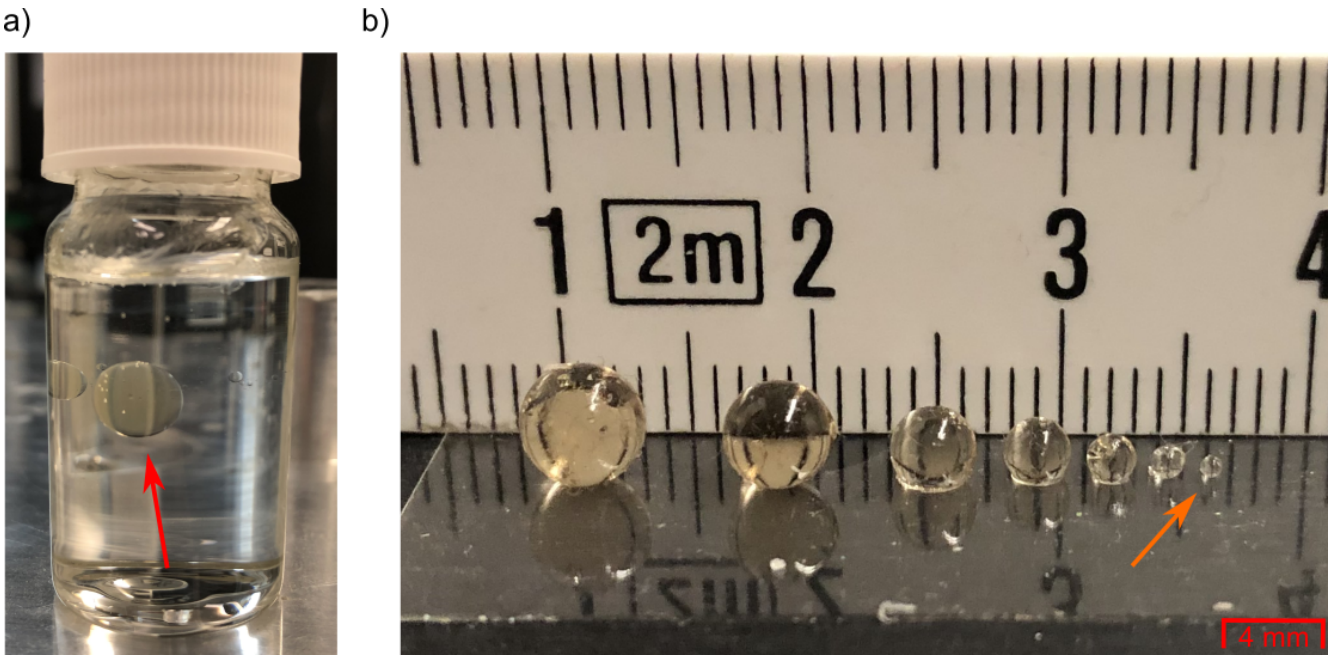

Figure 4.2: a) Glass container containing propan-2-ol and water. The red arrow indicates a floating PDMS sphere. b) Crosslinked PDMS spheres with different sizes in front of a folding rule. The size of the PDMS spheres ranges from a few hundred μm to some mm. The orange arrow indicates a PDMS sphere with a diameter of $\approx 800\,\mu m$.

184 the crosslinking is significantly faster. Since the fabrication method functions without stirring it exhibit high reproducibility concerning the sphere size. By adapting the pipette-ted volume, spheres with radius in the range from a few hundred μm (Fig. 4.2 b) orange arrow) to some *mm* can be produced, Fig. 4.2 b). While the output of spheres per batch compared to the microfluidic and bulk techniques is lower the short curing time of this production method allows for more production batches. Depending on the mixing ratio of the used PDMS solution the sphere´s Young's modulus can be adapted in the range of a few Pa to some kPa. Thus, a method to fabricate PDMS spheres of different sizes and Young's moduli was developed that does not require significant technical or chemical effort. For the measurements presented in this work, only mm size spheres were used as they are easier to handle.
After the preparation of the PDMS sphere, the next step involved the coating of the PDMS sphere with magnetic particles. To this end, the spheres were rolled in a closed vessel containing nickel particles characterized in section 2.1. Thus, a close packed monolayer of particles forms on the sphere's surface. Since the particles are attached by simple adhesion, two strategies to permanently fix them to the PDMS spheres were followed. The first strategy was to embed the sphere in a PDMS layer sample as described in 4.1.1. The second strategy was to coat the sphere with another layer of PDMS. Therefore, the sphere was first mounted on top of a thin needle. Afterwards, PDMS was poured on it while the needle was rotated to ensure a homogeneous distribution. Both methods had to be done with caution in order not to harm the magnetic particle layer. Subsequently, the spheres were cured for 24 hours at $60° C$ to ensure a stable Young's modulus.
With this procedure, it is possible to create either free-standing or embedded magnetic PDMS spheres in various diameters and stiffnesses. It is a fast, simple, and efficient method without significant technical or chemical effort. Its biggest advantage over the microfluidic and bulk technique is the simple but defined adaptability of the sphere size.

4.1.4 Membranes with 2D magnetic layer

This section focuses on the fabrication process of magnetic membranes. Hereby the term membrane stands for thin free-standing PDMS samples containing a monolayer of magnetic particles. Membranes were produced similar to the thin free-standing PDMS samples. First, a 4 cm on 2 cm rectangle glue rim was attached to a Teflon^{TM} substrate. The glue rim consisted of two component epoxy glue from UHU. After preparing the PDMS solution as in 4.1.1 a thin layer of it was cast by pouring 640 μl PDMS inside the rim. Nickel particles were scattered on the layer after its mechanical stability was ensured. The particles were carefully distributed by dragging a thin glass slide over the surface without harming the underlying PDMS film. Hence a close packed

monolayer of particles formed (see the sketch in Fig. 4.3 a)). The thickness of this magnetic layer consequently amounts to one particle diameter. Excess particles did not adhere to the layer and were shaken off. A second layer of 640 μl was poured on top to encapsulate the particles. Different particle patterns could be formed by placing cured epoxy structures on the PDMS layer before distributing the particles. Those epoxy structures could easily be removed after particle distribution. Consequently, the areas covered by the epoxy structure stayed particle free and were, thus, non-magnetic Fig. 4.3 b). Subsequently, the membranes were cured for 24 hours at $60° C$. Afterwards, they were peeled off the Teflon substrate. To get free-standing membranes, they were cut out of the glue rim. The membrane thickness was $\approx$ 1 mm. The membrane stiffness could again be adapted by the PDMS mixing ratio. Therefore, the presented production method allows the preparation of 2D magnetic structured membranes with defined magnetic areas. Furthermore, the size, thickness and stiffness of the membrane is easily adaptable.

4.2 Magnetic setups

In this work, two kinds of magnetic fields were applied to the samples: A homogeneous and an inhomogeneous gradient field. A homogeneous magnetic field was accomplished by a distinctive arrangement of permanent magnets, a Halbach-array. To create an inhomogeneous magnetic field no permanent magnets are used. The field is generated by electrical current passing through

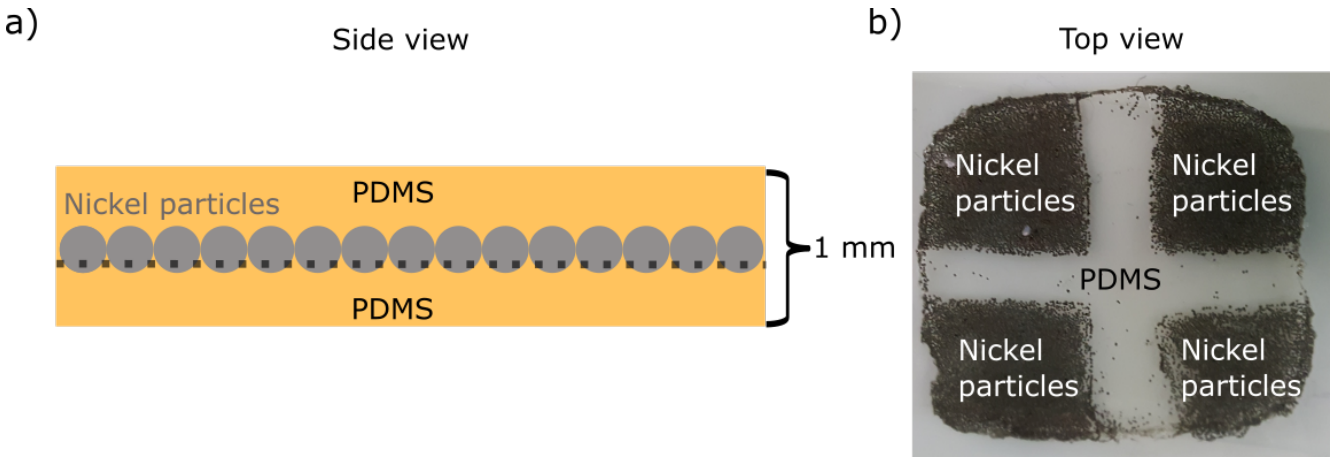

Figure 4.3: a) Sketch of a membrane with a close packed monolayer of particles positioned between two PDMS layers (side view). Particles are distributed on a cross-linked PDMS layer with a thickness of roughly 500 μm. The dashed line marks the interface to the second cross-linked PDMS layer which is deposit after particle distribution. An overall membrane thickness of approximately 1 mm is obtained. b) Top-view image of a 2D magnetic structured cross-linked PDMS membrane. A cross out of solid glue was placed on the first cross-linked PDMS layer before particle deposition ensuring a particle free area.

coils, so-called electromagnets. In the following, the assembly of the two setups will be described. Additionally, the generated magnetic fields and some of their characteristics like field strength, course of the field, etc. will be determined.

4.2.1 Halbach-array

The Halbach-array was configured by Shilin Huang and is described in detail in [69]. In this paragraph important features of the Halbach-array are mentioned and some further measurements are added. The used array consists of 32 NdFeB permanent magnets sourced from AR.ON GmbH. According to the datasheet, they exhibit a remanence of $1.32\,T$. They were arranged on two rings. Each inner ring's magnet size was $8 \times 8 \times 15\,mm$, each outer ring's magnet size was $14 \times 14 \times 15\,mm$ (see sketch Fig. 4.4). The magnetic orientation was altered $45°$ between every adjacent magnet. For magnets lying on the x- receptively y-axis the magnetic orientation shows in the same direction. Inner and outer ring have the same magnetic orientation configuration Fig. 4.4. Both rings can be rotated simultaneously around a cavity of $2.5\,cm$ in diameter. This cavity allows the placement of the Halbach-array around the sample holder and hence the sample can be centered regarding the z-direction inside the Halbach-array. Since inner and outer ring are

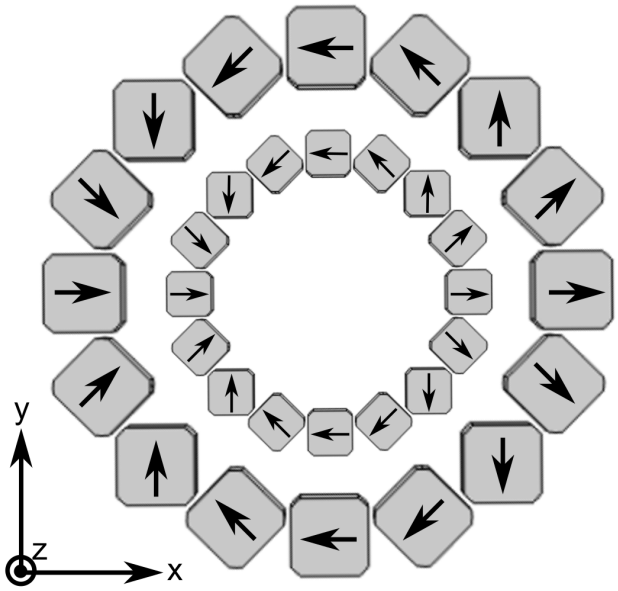

Figure 4.4: Sketch of both Halbach-array rings. The inner and outer ring consist of 16 NdFeB permanent magnets. The magnetic moment of each magnet is depicted with a black arrow. In the shown constellation the field inside the array is at maximum with a flux density of $\approx 216\,mT$ and homogeneous in x and y direction. [Adapted from [151], 2021, ©Springer Nature, CC BY 4.0, [151]]

also rotatable against each other the magnetic field strength can be reduced to a certain degree. At a specific rotation between the inner and outer ring, the magnetic repulsion of the permanent magnets is too strong. As a result, both rings try to separate and can not be kept in the rotated position anymore.

Comsol Multiphysics [121] simulations were carried out by modeling the permanent magnets with the Ampere's law [69]. Other simulation parameters like dimension, position, and remanence of the magnets were taken from the real setup. Only the aluminum housing was not incorporated and assumed to be magnetically inactive. The simulation showed that the magnetic field in the area of $\approx 9\,mm^2$ around the center of the Halbach-array [69] can be assumed as homogeneous, i.e., the small field gradients do not affect the measurement. The simulation was validated by measurements with a Gaussmeter Lakeshore 410. For this thesis, the Gaussmeter Lakeshore 410 measurements were repeated. To this end, the magnetic field probe head was, while centered in the z- and y-axis, moved in $0.1\,mm$ steps along the x-axis. At each step, the magnetic flux density B was measured Fig. 4.5 a). The jumps in the magnetic flux density are due to the Gaussmeter resolution limit of $0.1\,mT$. Subsequently, a second order polynomial fit was applied and its first derivative with respect to x was determined. The derivative provides the gradient of the magnetic field in x-direction Fig. 4.5 b). The gradient shows a linear dependence (slope of $0.4\,mT/mm^2$) on the distance from the center. Since the gradient $3\,mm$ from the center is still close to $1\,mT/mm$ the field can be assumed as homogeneous in the area of observation. This becomes even more apparent when comparing the dipole-dipole force with the force generated by the gradient in the magnetic field. Assuming two nickel particles with a diameter of $200\,\mu m$ and an inter-particle distance of $300\,\mu m$ the dipole-dipole force becomes $\approx 85\,\mu N$. In contrast, assuming a nickel particle with a diameter of $200\,\mu m$ positioned in x-direction $3\,mm$ from the center, the force generated by the gradient is $\approx 4\,\mu N$ and thus, more than 20 times weaker than the dipole-dipole force.

The gradient of the magnetic field along the z-axis was measured in the same way, Fig. 4.5 c) and d). A maximum flux density of $216\,mT$ was measured in the center of the Halbach-array. Since the samples were slightly shifted along the z-axis the actual flux density at the sample position was $180\,mT$. The shift also resulted in a z-gradient. That gradient, however, is too small to negatively affect the measurements (gradient force $\approx$ 7 times weaker than comparable dipole-dipole force) and no particle displacement in z-direction under applied magnetic field was observed. As the magnetic field along the particle plane (x-y plane) can be assumed as homogeneous, the force due to the small gradient in the field can be neglected. Every particle displacement in the x-y plane is a result of magnetic particle interaction.

To determine the magnetic field direction, the external housing was equipped with a scale with

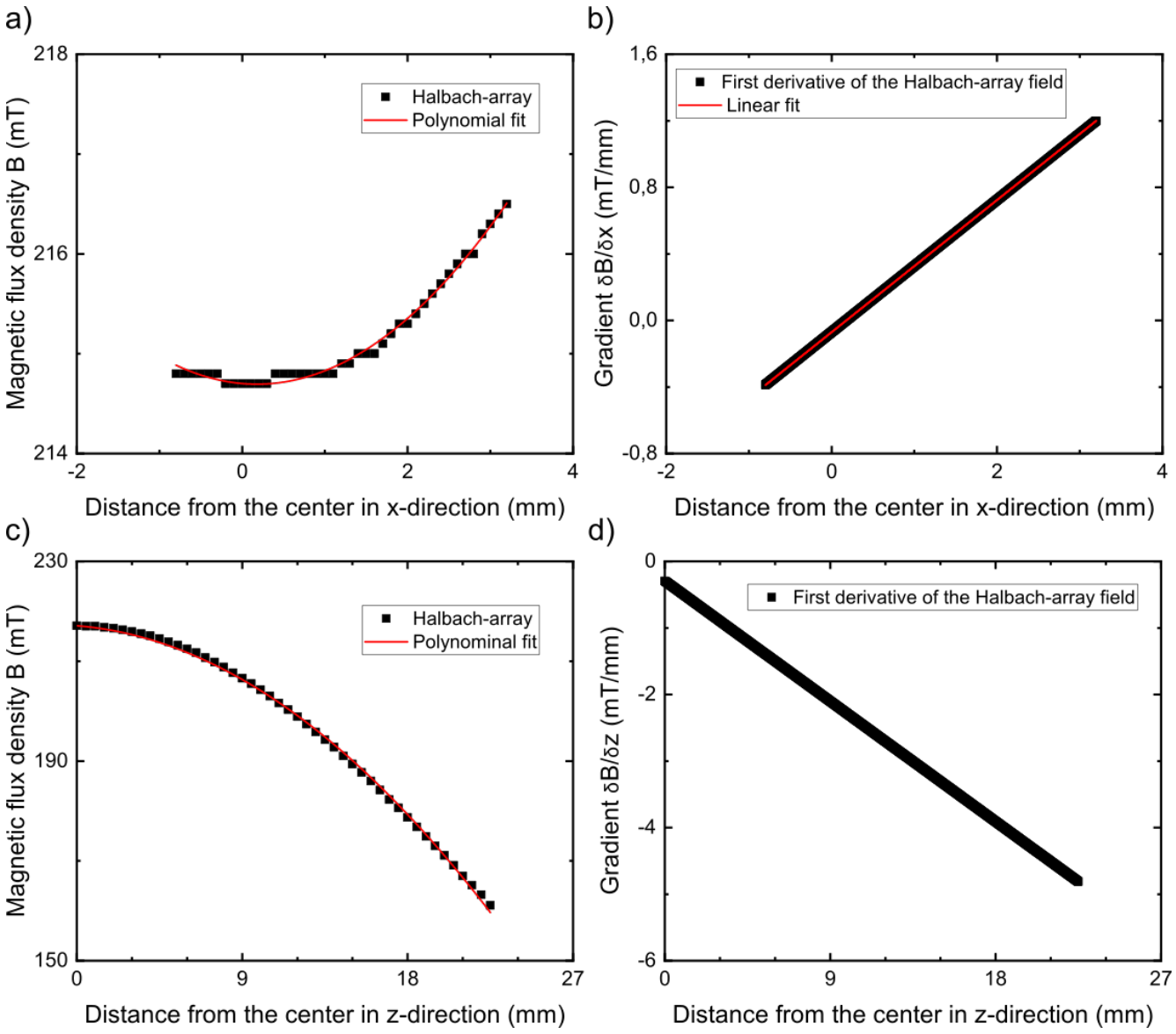

Figure 4.5: The magnetic flux density of the Halbach-array a) in the x direction while the probe head was centered in z and y direction. The steps in the measurement are due to the accuracy of the Gaussmeter. A polynomial fit of second order depicts the trend accurately (red line). b) the gradient of the field in x direction is given by the first derivative with respect to x. It shows a linear dependence with a slope of $0.4\,mT/mm^2$. The magnetic flux density of the Halbach-array c) in z direction while the probe head was centered in x and y direction. A polynomial fit of second order depicts the trend accurately (red line). d) the gradient of the field in the z direction is given by the first derivative with respect to z. It shows a linear dependence with a slope of $-0.2\,mT/mm^2$.

incremental steps of $1°$. The reading error during measurements was estimated to be $\pm 0.5°$. Additionally, a systematic offset to the magnetic field orientation of $\pm 1.5°$ was considered to reflect the error introduced by the determination of the actual magnetic field orientation. Both errors added up and resulted in a total magnetic field orientation error of $\pm 2°$ for every magnetic measurement conducted with the Halbach-array.

4.2.2 Electromagnet

In a homogeneous magnetic field, the displacements of the particles take place because of their mutual magnetic interaction. To create a force on a single particle, the magnetic field has to have a gradient. To obtain gradient fields an electromagnetic setup was used. For this setup, two solenoids were removed from a D-frame DC lifting magnet (Mecalectronic [70]). Their inductance L was measured at $5\,mH$ while the resistance R was determined to be $7.3\,\Omega$. The solenoids were connected parallel and a resistance of $2\,\Omega$ was connected in series. In every solenoid, an ARMCO pure iron core with pointed pole shoes (diameter of $0.66\,cm$) was inserted Fig. 4.6. The distance between both pole shoes was $1.3\,cm$. The iron cores reinforce the solenoid's field which is strongest at the surface of the pole shoes and weakest in the center between both. A dual power supply ($280\,W$, EX354D, Thurlby Thandar Instruments) was used to generate a stable voltage. The dual power supply has two independent and isolated outputs and can supply a maximum voltage of 0 to $35.5\,V$ and a maximum current of 0 to $4\,A$ at each output. With a waveform generator (33220A, Agilent), signals with different frequencies, amplitude, and form were generated. The signals were amplified by a custom-built current-amplifier which was powered by the dual power supply. For low frequencies, the inductance of the solenoids does not play a role but for higher frequencies, the set current strength is not reached before the voltage changes. To avoid the influence of the inductance, only signals with a frequency of $100\,mHz$ (rectangular signal, $2\,V$) were applied. The generated magnetic flux density B at maximum voltage and current of the power supply was measured with a Gaussmeter (Lakeshore 410) by moving the probe head in

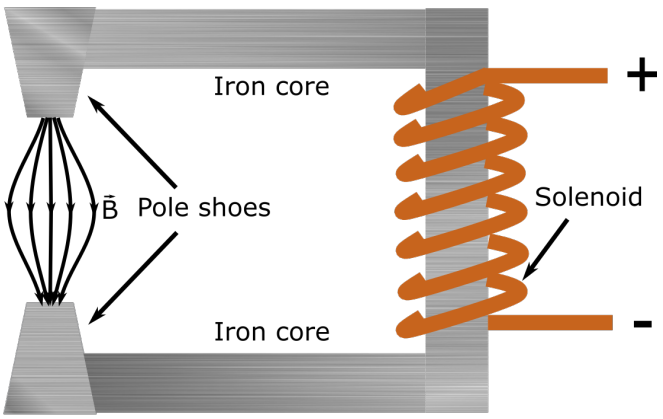

Figure 4.6: For simplicity, the actual two solenoids are depicted only as one in the image (brownish color). An electric current runs through it and creates a magnetic field. The iron core was placed in the center of the solenoid. It ends in pointed pole shoes. The gradient field between the pole shoes is indicated by black arrows.

$0.1\,mm$ steps from the surface of one pole shoe towards the center between both pole shoes Fig. 4.7 a). The error in the step size was estimated to be $0.05\,mm$ and the error of the magnetic flux density due to the resolution limit of the Gaussmeter to be $0.2\,mT$. The trend of the magnetic field B was fitted with an exponential function with four parameters p_{1-4} defined by the fit:

$$y = p_1 e^{\left(\frac{-x}{p_2}\right)} + p_3 + p_4 x. \tag{4.1}$$

The fit converged with a χ^2 tolerance of 1E-14 for $p_1 = (54 \pm 7)\,mT/mm$, $p_2 = (2.4 \pm 0.3)\,mT/mm$, $p_3 = (19 \pm 8)\,mT/mm$ and $p_4 = (2 \pm 1)\,mT/mm$ Fig. 4.7 a) red line. After fitting the field trend and differentiation Eq. 4.1 in respect to x the gradient at each distance from the pole shoe surface is determined, Fig. 4.7 b). The gradient increases the closer one gets to the pole shoe's surface. Near the center between both pole shoes, the gradient becomes quite small because both pole shoes act with roughly the same field strength.

4.3 Optical setup

The optical setup will be exposed to magnetic stray fields. As the magnetic components would

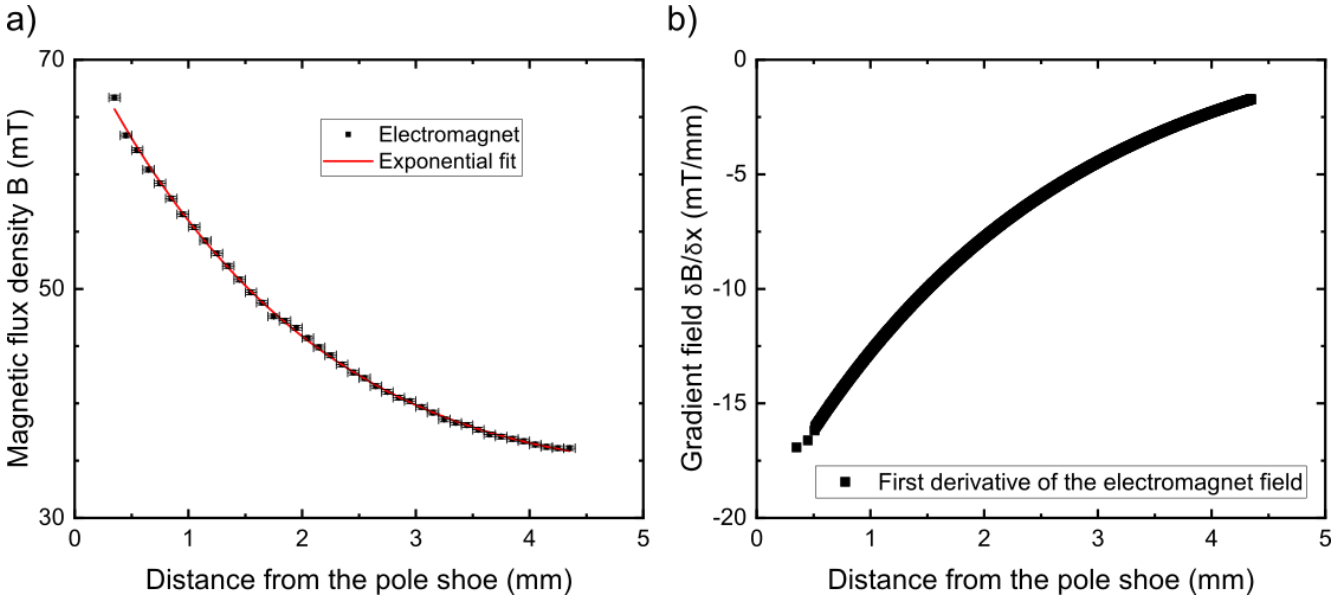

Figure 4.7: a) the magnetic flux density of the electromagnet between its pole shoes. It follows an exponential decline when moving from the pole shoe's surface towards the center. An exponential decay function was fitted to the trend (red line). The error of the distance from the pole shoe is assumed with $0.05\,mm$ and of the flux density with $0.2\,mT$. Deriving the field in respect to the distance determines the gradient of the field b). Near the pole shoe, the gradient is highest decaying to almost zero in the center between the pole shoes.

interfere with the magnetic field at the position of the sample, aluminum with its neglectable magnetization capability was used as the main material for the optical setup design. Any influence on the applied magnetic field by the optical setup itself is negligible. A mounting plate and the sample holder were screwed onto posts on top of a breadboard (Thorlabs GmbH) (Fig. 4.8 a)). This fixation ensures mechanical stability during the measurements. To prevent a relative movement between sample and camera the camera post was screwed onto the breadboard as well. Images were taken from above vertical to the sample plane. It was possible to adjust the distance between the sample and the camera. Thereby, the focus plane could be adapted. Samples were fixed on a cylindrical sample holder to prevent them from being displaced especially between

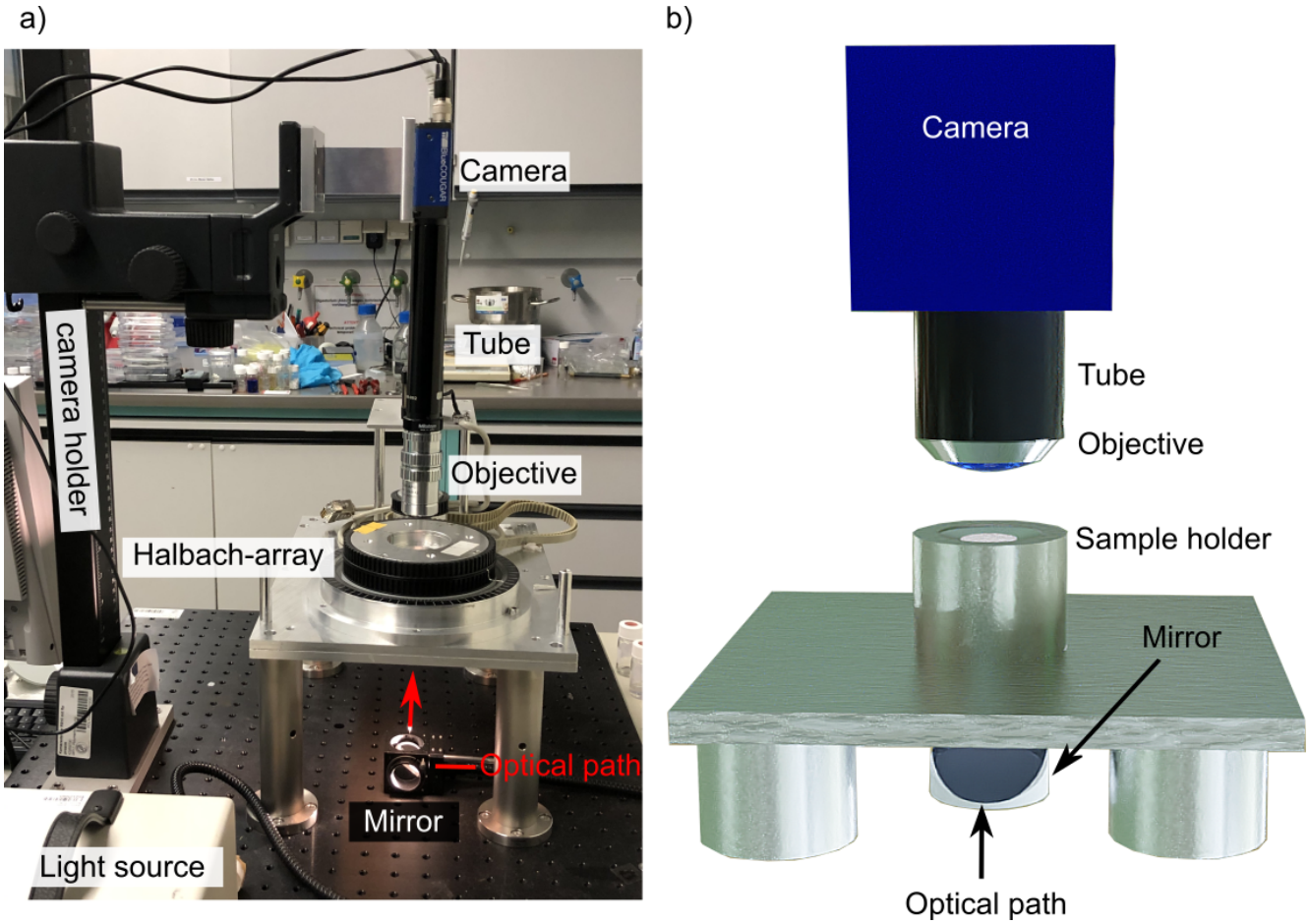

Figure 4.8: a) Real image of the optical setup. The optical setup consists of a CCD camera (mvBlueCOUGAR-S from Matrix Vision GmbH), a tube without magnification to prevent optical aberrations, Mitutoyo objectives, a camera holder, and the sample holder made from aluminum. The Halbach-array is placed around the cylindrical sample holder. For illumination, a LED-light source (Intraled 3, Volpi AG) was used. With the camera holder, the distance between sample and camera could be adapted. b) A sketch of the essential components. For clarity, the Halbach-array is not shown. Samples were placed on a cylindrical elevation with a recess in the middle which allowed the illumination of the samples from below. [Reused from [151], 2021, ©Springer Nature, CC BY 4.0, [151]]

zero-field and field images. The cylindrical sample holder allowed to place the Halbach-array around the samples (Fig. 4.8 a)). Furthermore. it ensures the sample to be near the center of the Halbach-array and thus being subjected to a homogeneous magnetic field. A sketch of the essential parts of the setup but without Halbach-array is shown in Fig. 4.8 b). A round cavity in the cylinder allowed vertical illumination from below. Fixing a translucent glass between the LED-light source (Intraled 3, Volpi AG) and the opening in the cylinder provided a homogeneous illumination of the samples.
Different Mitutoyo objectives could be mounted on top of the CCD camera (mvBlueCOUGAR-S from Matrix Vision GmbH). Inserting a $1\times$ tube of 23 cm length between objective and camera prevents aberrations of the focus plane. A conversion from pixel to μm was done by imaging a micrometer grid. To this end, a line was plotted on the micrometer grid and its length measured. This procedure led to following conversions, Tab. 4.1. Since the particles are not transparent

$\times$ Mitutoyo objectives	Conversion from pixel to μm
2	2.35$\pm$0.03
5	0.94$\pm$0.01
10	0.47$\pm$0.01
20	0.23$\pm$0.02

Table 4.1: Depending on the magnification of the used Mitutoyo objective a different conversion from pixel to micrometer had to be carried out. For the used objectives the conversation factors are listed.

and measured with light transmitted vertically from below, it was only possible to resolve the maximum particle dimension sharply. Hence, the focus plane was adjusted to the maximum particle diameter. To get information about the particle surface that lies outside the maximum dimension, the particle had to be measured in reflecting mode. For the reflective measurement, the sample was illuminated from above. As the PDMS has high transparency for light in the visible range, the light was mostly reflected by the surface of the nickel particles. Consequently, the surface of the nickel particles could be optically dissolved.

4.3.1 Measurement procedure using the Halbach-array

Before the MRE samples were subjected to the magnetic field of the Halbach-array, an image was taken (zero-field case). With the help of the open software TrackMate from ImageJ [165] the particle positions, the x- and y-coordinate of the particles x_i, y_i, were extracted. This is referred to as the initial particle position. The particle position determination was done as follows: At the

start, the inverted grayscale images were loaded into ImageJ [71]. Apart from enhancing the contrast, no further image modifications were applied. To extract the particle's x-y coordinates, the LoG detector (Laplacian of Gaussian) in TrackMate was selected. Applying the LoG detector the image is convolved with a Gaussian kernel and then the Laplacian operator is applied. This results in a strong negative response for bright areas with the size defined by the Gaussian kernel. The detailed mathematics behind the detection process is shown in [104].
In TrackMate it is sufficient to set a mask size which defines the diameter of the particles the algorithm tries to detect, i.e., the algorithm searches for areas and shapes defined by the mask which are bright compared to their surroundings. As the mask is given by the Gaussian kernel only circular shapes with a roundness of 1 are detected. In the presented work the mask size was set always to the diameter of the largest particle in the picture as a mask size smaller than the particle diameter created a larger detection error than a mask size larger than the particle diameter. After the detection algorithm is completed the particle positions can be extracted in form of x- and y-coordinates. By calculating:

$$|r| = \sqrt{(\Delta x)^2 + (\Delta y)^2}, \tag{4.2}$$

with $\Delta x = x_2 - x_1$ the difference in the x-coordinate and $\Delta y = y_2 - y_1$ respectively the difference in y-coordinate of both particles. Thus, the inter-particle distance $|r_{12}|$ is obtained. In the following, the inter-particle distance of samples not subjected to a magnetic field is referred to as initial inter-particle distance.
Subsequently, the samples were centered inside the Halbach-array by placing it around the cylindrical sample holder. Prior to the actual measurement full loading cycles were carried out, i.e., the sample was subjected to the magnetic field of the Halbach-array and subsequent the Halbach-array was rotated in consecutive $360°$ turns around the sample. Those full loading cycles exclude any influence of the pre-loading on the PDMS matrix's stress-strain behaviour, the so-called Mullins effect [43, 120] and reveal if the particle displacement ruptures the matrix.
Continuing with the actual measurement process: After the loading cycles, the Halbach-array was rotated in $5°$ steps, after every step a single image was taken. The system was in an equilibrium state for every field orientation since magnetic moment relaxations or matrix viscosity effects are of a much faster timescale. Therefore dynamics effects play no role in these measurements, implying that the measurements were quasi-static.
For the various magnetic field orientations, an image of the particles does exist and the above introduced detection method of the particle position is applied. The next step was to connect the identical particles in every image. Therefore, connecting parameters between adjacent images needed to be set in TrackMate. Three connecting parameters required to be defined: The maximum

linking distance, which sets the spacial distance range for matching particles between adjacent images, the gap-closing distance, which sets the maximum distance a particle can be linked when not detected in the adjacent image and the gap-closing maximum frame gap, which sets the maximum amount of frames a particle can not be detected and still be linked. In the presented work the gap-closing maximum frame gap was always set to two since no particle vanishes between adjacent images. Since every particle is present in each image also the maximum gap-closing distance could be arbitrarily chosen. Only the maximum linking distance was adapted such that every particle was linked with itself in the adjacent image. Following this procedure, for each particle, a x-y trajectory can be extracted for the various magnetic field orientations.
To determine whether the matrix shows the Mullins effect or is ruptured by particle displacement a measurement of ≈ 40 full loading cycles was conducted with an exemplary two particle sample and the above particle center tracking method was applied Fig. 4.9 a). Since the maximum of the inter-particle distance does not change significantly, it is apparent the sample does not show any signs of Mullins effect or matrix destruction Fig. 4.9 a). If the Mullins effect would arise or the matrix would be ruptured by the particle movement throughout the full loading cycles, the

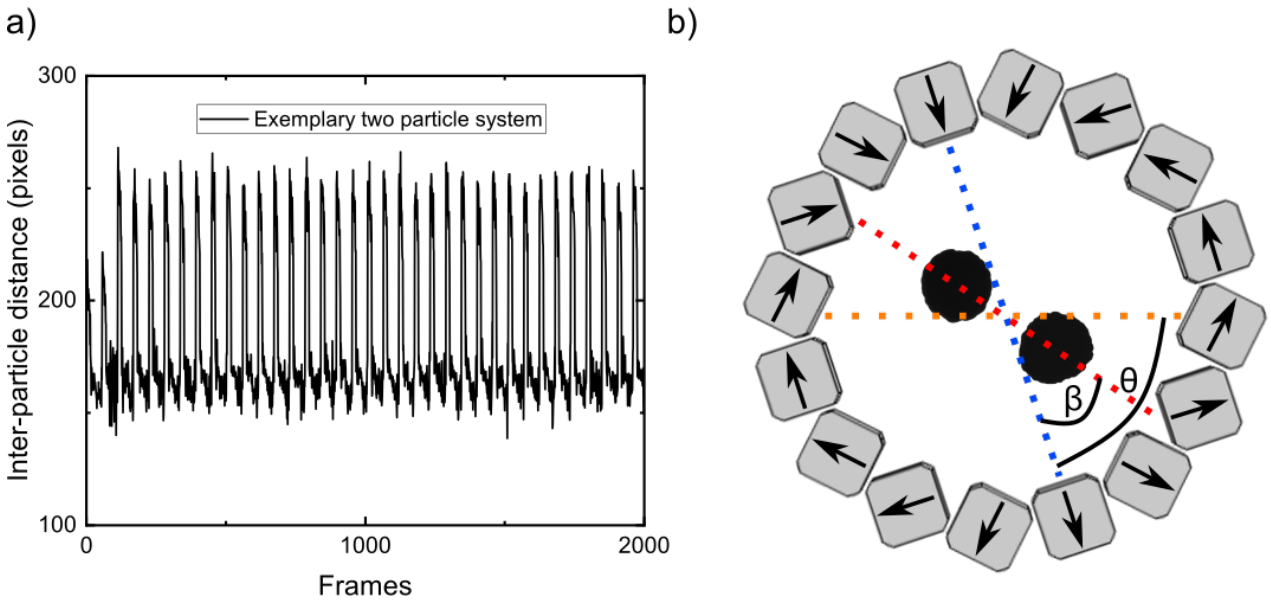

Figure 4.9: a) 40 cycles of $360°$ turns of the Halbach-array were conducted. The inter-particle distance of an exemplary two particle system is shown. b) For simplicity, only one ring of the Halbach-array is depicted (gray rectangular objects) with the magnetic moments of the permanent magnets is indicated by black arrows. The magnetic field orientation is marked with a dashed blue line. Two exemplary nickel particles are inserted. The particle axis is marked with a dashed red line. β denotes the angle between current field orientation and particle axis. θ denotes the angle of the magnetic field orientation compared to the initial position marked with a dashed orange line. [Adapted from [151], 2021, ©Springer Nature, CC BY 4.0, [151]]

restoring elastic force of the matrix would decrease, i.e., the maximum inter-particle distance would decrease and the period between two maxima increase. The small fluctuations of maximum and minimum of the inter-particles visible in Fig. 4.9 a) are due to particle surface roughness and particle rotation around their center.
Furthermore, the particles are assumed as circles (roundness of 1) and detected as such as the particle tracking method uses a LoG (Laplacian of the Gaussian) detection. Due to the surface roughness of the particles the detection with a circular mask can lead to deviation in the detection of the x and y coordinate. To determine the uncertainty in the particle tracking, the image of an exemplary two particle system was rotated in 25, 45, and $90°$ and the particle tracking method was applied. The tracking mechanism does provide nearly identical particle centers for all the images. Thus, it is valid to estimate the error in the particle center detection to be ± 1 pixels in x and y direction. The norm of the center to center vector $|r|$ was calculated with Eq. 4.2 and the error was determined with $\pm 4.68\,\mu m$ for the $2\times$ Mitutoyo objective.
In Fig. 4.9 b), all relevant orientations and angles are summarized: The magnetic field orientation $\hat{B}$ Fig. 4.9 b) (dashed blue line), the center-to-center vector between the particles $\vec{P}$ Fig. 4.9 b) (dashed red line), the initial orientation of the particle pair $\vec{P_0}$ Fig. 4.9 b) (dashed orange line), β the angle between particle axis and the magnetic field orientation and θ the angle of the magnetic field orientation in relation to its starting orientation. Determining the inter-particle distance and the external magnetic field orientation $\hat{B}$, with:

$$\beta = acos\left[\frac{\vec{P}\cdot\hat{B}}{|r|}\right], \tag{4.3}$$

the angle β between particle axis $\vec{P} = \begin{pmatrix}\Delta x\\ \Delta y\end{pmatrix}$ (Fig. 4.9 b) dashed red line) and the magnetic field orientation $\hat{B}$ was calculated Fig. 4.9 b). Consequently, the angle β between particle axis and magnetic field orientation and the inter-particle distance $|r|$ can be extracted to calculate the magnetic dipole-dipole force Eq. 3.32. Furthermore, the dependence of the inter-particle distance on the angle between the particle axis and the magnetic field orientation can be extracted from the measured particle trajectories. During the measurements, a particle displacement in the z-direction (out of the particle axis x-y-plane) was never observed and the particle stayed in focus throughout the measurements.

4.3.2 Electromagnetic measurements

After the electromagnet's characteristics have been explained in section 4.2.2 the subtleties of electromagnetic measurements will be evaluated in this section. Within this work, the electromagnet was used to create magnetic field gradients. The gradient fields were used to macroscopically deform magneto-active membranes. To this end, the membranes were placed on a plastic sample holder Fig. 4.10 (red object) with the magneto-active particle layer orthogonal to the field direction. The sample holder was cut in a way that it supports the membrane at the two edges of the longer side. Hence the membranes were free-standing with the same area between the edge suspension points. This facilitates the deformation evaluation as, independent of the matrix stiffness, the same model for calculating the theoretical deformation can be applied. Additionally, the sample holder contained a horizontal connection between both suspension points to ensure mechanical stability. The front of the sample holder was not connected and ensured a good optical detection of the sample. Images were taken with a high-speed digital camera (NX4-S1, Integrated Design Tools, Inc.) and a macro-zoom objective ($8 - 108\,mm$, F2,5/1) from the front.

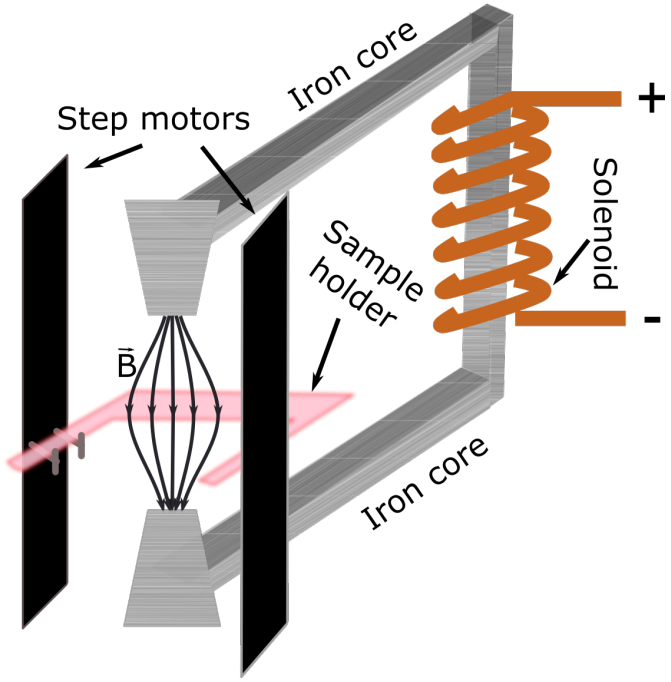

Figure 4.10: For simplicity, the actual two solenoids are depicted only as one in the image (brownish color). A current runs through it and creates the magnetic field. The iron core was placed in the center of the solenoid. It ends in pointed pole shoes. The gradient field between the pole shoes is indicated by black arrows. Step motors to adjusted the height of the sample holder (red sheet) are depicted by the black rectangles. The sample holder is placed on screws that are attached to the step motors (gray).

Illumination was done from above with a LED-light source (intraLED 3, Volpi AG). Stepper motors, used as suspension points for the sample holder, could stepwise move the membrane closer or further away from the surface of one iron pole shoe Fig. 4.10 (black shapes). With that setup, the magnetic force acting on the membrane could be in- or decreased. Exact parameters from the actual measurements are shown in section 6.2.

4.3.3 Rheological measurements

With a rheometer, the mechanical characteristics such as viscosity or elasticity of a liquid, soft-solid or solid can be measured. To determine the Young's modulus of the used polymer matrix, in this case, PDMS, a common choice is a parallel-plate-rheometer. In the rheometer the prefabricated sample is fixed between a stationary, fixed circular flat plate of diameter 25 mm and an opposing rotatable plate of the same size and shape. By oscillating the rotatable plate, a shear deformation is applied to the polymer. To prepare a polymer sample for rheometer measurement, the polymer is cast in a mold on top of the lower, stationary rheometer plate and crosslinked for 24 hours under $60° C$. Afterwards, the sample is restrained by lowering the top plate until it contacts the polymer surface. A normal force of roughly 1 N is applied on top of the sample to ensure good contact between the sample and the plates. The rotatable plate functions as an actuator and exerts a torque with a certain angular frequency on the polymer. The torque is related to the stress and the rotation (displacement) of the sample to the strain.
In the specific rheometer used (HR 3, TA Instruments), either the rotation (strain-controlled) or the torque (stress-controlled) can be preselected while the other value is measured. Concerning the case of a preselected constant torque, the angular frequency is increased in steps and the rotation of the rotatable plate is measured. The rotation can be rheologically evaluated as strain. Thus, to every angular frequency, a corresponding strain is obtained and the shear modulus Eq. 3.6 can be determined for different frequencies. The complex shear modulus consists out of a storage (real part) and loss modulus (imaginary part). For an exemplary 23% PDMS sample, a rheological measurement with a HR 3 rheometer from TA Instruments in plate to plate geometry is depicted in Fig. 4.11 a). Due to the sample fabrication, the surface of the sample is slightly elevated at the edges. This could not be prevented, because, due to capillary forces, the PDMS solution was slightly pulled upwards at the mould's surface. Because of the slightly elevated sample edges, the upper plate was not in perfect contact with the polymer sample and therefore absolute values of the shear modulus can deviate from the actual ones. As the measured polymer can be considered incompressible, its Poisson ratio ν is in good approximation 0.5. Therefore, the Young's modulus can be calculated with 3*G (see Eq. 3.9).

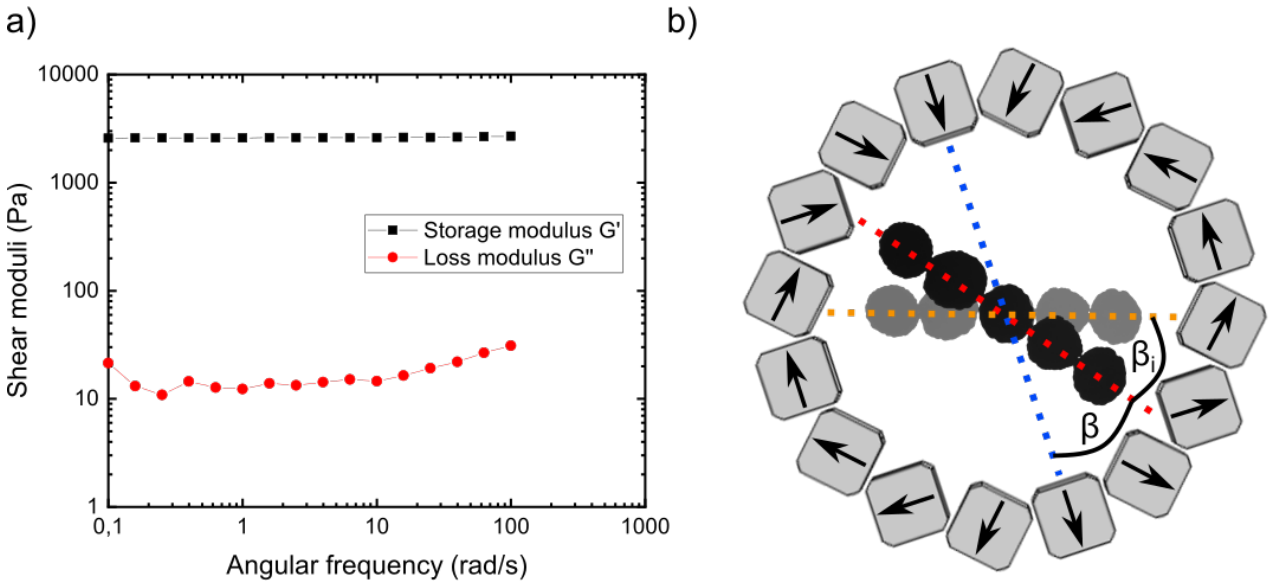

Figure 4.11: a) a plate to plate rheometer measurement was conducted for a cross-linked PDMS with 23 wt% of prepolymer solution. The loss modulus G'' and storage modulus G' were measured for various plate rotation frequencies. The loss modulus is small indicating a negligible viscosity. The storage modulus was determined with $(2.59 \pm 0.01)\, kPa$. b) For simplicity, only one ring of the Halbach-array is shown (gray rectangular objects) with the magnetic moments of the permanent magnets indicated by black arrows. The magnetic field orientation is marked with a dashed blue line. A chain of exemplary 5 nickel particles is inserted. The particle axis is marked with a dashed red line. β denotes the angle between the current field orientation and the chain axis. β_i denotes the angle of the chain axis compared to its initial position marked with a dashed orange line. [Adapted from [151], 2021, ©Springer Nature, CC BY 4.0, [151]]

Another approach to specifying the Young's modulus is an in-situ measurement. The in-situ measurement has the advantage that it considers the exact particle coupling to the matrix. Since the particles are positioned between two not with each other crosslinked PDMS layer, this can be crucial. The in-situ measurement is based on the approach from [172], where the dynamic shear modulus is measured by oscillatory rotating a chain of magnetic particles in a viscoelastic liquid. To make the approach applicable it was adapted to crosslinked polymers by using the Kelvin-Voigt model for viscoelastic solids. Furthermore, the dynamic measurements were converted into static. To start, the fundamental equations are explained and then the experimental realization is described: A particle chain of N paramagnetic particles is assumed. Subjecting the particle chain to a magnetic field, it experiences a torque as long as the magnetic field orientation is not aligned with the chain orientation [69, 110, 172]. Considering only nearest neighbor interaction, the magnetic torque Γ_m becomes:

$$\Gamma_m = \frac{3\mu_0 m^2}{4\pi} \frac{N^2}{2d^3} sin\,(2\beta)\,. \tag{4.4}$$

Herein, β denotes the angle between chain axis and magnetic field orientation Fig. 4.11 b), m the magnetic moment of one particle with diameter d and μ_0 the permeability of free space. Since the chain is deflected from its initial position, an elastic torque arises for the deformation of the polymer matrix, which counterbalances the magnetic torque. Taking the Kelvin-Voigt model (chapter 3.1) and due to the static measurement neglecting dynamical parts in equation Eq. 3.3 which equals the elimination of any dissipative terms, the elastic torque Γ becomes:

$$\Gamma = C * \beta_i \qquad \text{with} \qquad C = \kappa_e V G. \tag{4.5}$$

Herein, β_i denotes the angle of the chain orientation to its initial position Fig. 4.11 b), $V = N * V_p$ the Volume of the rotating object with N the particle amount per chain and V_p the particle volume, G the shear modulus and Γ the elastic torque. κ_e is the geometrical elastic rotation factor that can be calculated by [172]:

$$\kappa_e = \frac{2N^2}{ln(\frac{N}{2}) + \frac{b}{N}}. \tag{4.6}$$

It contains parameter b, which was experimentally determined by [172] to be 2.4. The chain rotates until the elastic torque equals the magnetic torque. Setting $\Gamma = \Gamma_m$ equation 4.5 becomes:

$$\frac{\mu_0 N M^2}{16} sin\,(2\beta) = G\beta_i\kappa_e. \tag{4.7}$$

Here, the substitution $m = M * V_p$ was carried out to get the dependency on the magnetization M of a single particle. Rearranging the equation after the shear modulus G it can be calculated by:

$$G = \frac{\mu_0 N M^2}{16\beta_i\kappa_e} sin[2\beta]. \tag{4.8}$$

Thus, the shear modulus G can be determined from the experimental quantities β_i the angle of the chain to its original position, β the angle between the chain and external magnetic field orientation, N the particle amount per chain and M the magnetization of the chain.
To determine the Young's modulus experimentally, 5 particles were positioned in chain formation between two crosslinked PDMS layers. The sample was prepared according to the bulk sample fabrication introduced in section 4.1.1. Samples for various PDMS mixing ratios were produced, Tab. 4.2. After curing for 24 hours under $60°\,C$ to ensure a constant Young's modulus throughout the measurements, the samples were positioned in a way that the chain was orientated in x-direction inside the Halbach-array. In order to exclude any rupture of the matrix, no full-loading cycle was carried out prior to the actual measurement and the Halbach-array was positioned in a way that the magnetic field orientation and chain orientation were aligned.

After positioning the samples in the center of the Halbach-array, the following procedure was applied: The Halbach magnet was turned clockwise in $5°$ steps. An image was recorded with the Blue Cougar camera at each step. Between every step sufficient time elapsed so any dynamic effects could be excluded. Due to magnetic torque Eq. 4.4 acting on the chain it starts to rotate in the direction of the set magnetic field orientation. As the elastic torque Eq. 4.5 counteracts the chain's deflection, the chain rotation is not of the same magnitude as the magnetic field rotation, i.e., an angle β between the magnetic field and chain orientation arises. Defining the connecting line between the ending particle centers as the chain orientation, the angle between current and initial chain orientation was calculated employing equation:

$$\beta_i = acos\left[\frac{\Delta x_i \Delta x_0 + \Delta y_i \Delta y_0}{\sqrt{\Delta x_i{}^2 + \Delta y_i{}^2} \cdot \sqrt{\Delta x_0{}^2 + \Delta y_0{}^2}}\right]. \tag{4.9}$$

Herein, $\Delta x_{0,i}, \Delta y_{0,i}$ denote the difference between x respectively y coordinate of the edge particles in the zero field and the deflected positions Fig. 4.12. The equation Eq.4.9 is obtained by the scalar product of the connecting vectors of the ending particles $\vec{P_0} = \begin{pmatrix}\Delta x_0 \\ \Delta y_0\end{pmatrix}$ respectively $\vec{P_i} = \begin{pmatrix}\Delta x_i \\ \Delta y_i\end{pmatrix}$ Fig. 4.12 dashed lines.
In a wide angle range θ of the magnetic field orientation, an assumption of a stiff chain is justified while only the end particles are taken into account. The magnetization is extracted by the single

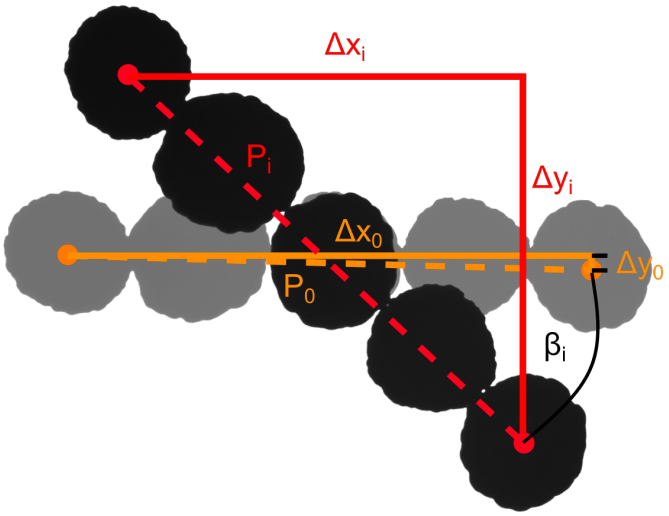

Figure 4.12: An exemplary five particle chain rotated by the angle β_i from its initial (light gray particles) to its current position (black particles). The angle β_i is calculated by calculating the scalar product of the connecting vectors of the ending particles P_0 and P_i (dashed lines). Therefore, the difference in the x and y coordinates $\Delta x_{0,i}$ respectively $\Delta y_{0,i}$ of the ending particles was determined. The centers of the ending particles are marked with a dot.

particle SQUID measurement (chapter 2.1) and hence, for the various magnetic field orientations the shear modulus G can be calculated by Eq. 4.8. To determine a mean value only the values for a magnetic field orientation of $\theta = 5$ to $25°$ were used since for higher magnetic field orientation the assumption of a stiff chain is not justified any-more and errors in the calculated shear modulus due to chain instabilities increase. Furthermore, the model assumes linear elasticity. For magnetic field angles larger than $25°$ this is not valid anymore as the chain deforms the matrix strongly.
Comparing the mean shear modulus of a PDMS with mixing ratio 23 % obtained by the in-situ measurement [$G = (237 \pm 3)\, Pa$] with the result of simulation [$G = (2.9 \pm 0.1)\, kPa$] and rheometer measurement [$G = (2.59 \pm 0.01)\, kPa$] Fig. 4.11 a), one notices an absolute value that is 10 times smaller. Still, the values of the shear modulus for the various PDMS mixing ratios show good agreement with the percolation law. Hence, one can assume a scaling error. The scaling error can not be explained by fluctuations in the PDMS mixture or variation in the fabrication process as the PDMS stock solution and fabrication process was identical for all three measurements. The values for simulation and rheometer measurement show good agreement. Therefore, it is valid to assume that the scaling error lies within the in-situ measurement. As previously mentioned the model used to evaluate the in-situ measurement uses assumptions such as stiff particle chain, linear elasticity, and nearest magnetic particle interaction. The linear elasticity was taken into account as only values for small chain rotations were considered to calculate the shear moduli. During those small chain rotations, the ending particles showed no movement relative to each other and thus, the assumption of a stiff particle chain should hold. Due to the small particle amount considering only nearest magnetic particle interaction should not lead to such large deviations. Furthermore, the particle magnetization and the angle β between the magnetic field and chain orientation was determined quite precisely compared to the geometrical elastic rotation factor κ_e (see Eq. 4.8. Thus, one explanation for the observed strong discrepancy could be the geometrical elastic rotation factor $\kappa_e \approx 35.8$ that was taken from [172]. The data of the rheometer measurement is hence used to calibrate the experiment and a geometrical elastic rotation factor κ_e of 3.26 was determined. This geometrical elastic rotation factor was then used to determine the shear moduli of PDMS of various mixing ratios.
Measurements were executed with a mixing ratio of 8 to 23 wt% . The mean values of the Young's modulus were calculated from the values of the shear moduli in the magnetic field orientation range of $\theta = 5$ to $25°$ and are listed in Tab. 4.2.
To determine the dependence of the Young's modulus on the mixing ratio, the data was plotted and fitted by a power law similar to Eq. 2.3, Fig. 4.13. The power law is given by:

$$G = G_0 \frac{(x - r_c)^v}{r_c}. \tag{4.10}$$

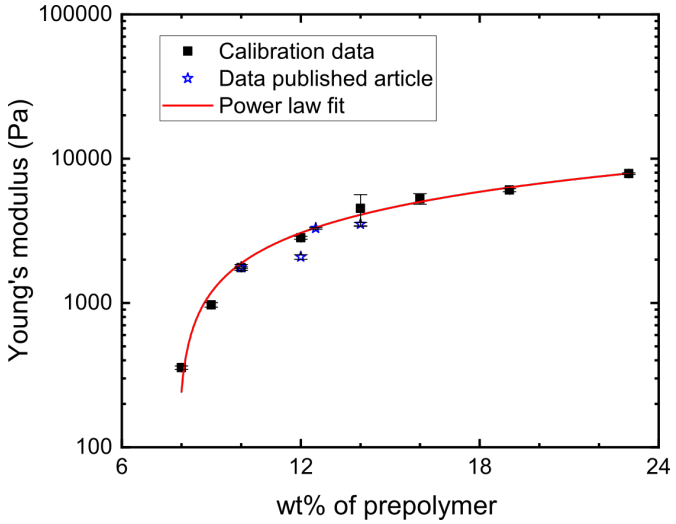

Figure 4.13: Young's modulus dependence on the wt% of prepolymer mixture. A power law (see Eq. 4.10) was fitted at the data set. It is given by the red. Error bars are the standard deviation of the mean values. The standard deviation of the power law fit was extracted with ± 301 Pa.[Adapted from [151], 2021, ©Springer Nature, CC BY 4.0, [151]]

A power law dependency between the Young's modulus and the PDMS mixing ratio is visible for $r_c = 7.9 \pm 0.2$, $G_0 = (8.5 \pm 1.5)\, kPa$ and $v = 0.73 \pm 0.06$ and small deviations from the fit are

PDMS ratio in %	Mean E in kPa	Statistical error of the mean values in kPa
8	0.36	0.01
9	0.97	0.04
10	1.76	0.02
12	2.83	0.06
14	4.5	1.1
16	5.3	0.4
19	6.1	0.2
23	7.9	0.1
PDMS mixing ratio used for measurements presented in chapter 5.2		
PDMS ratio in %	Mean E in kPa for article	Statistical error of the mean values in kPa
10	1.8	0.1
12	2.1	0.1
12.5	3.29	0.05
14	3.5	0.1

Table 4.2: Young's modulus dependence on the PDMS solution mixing ratio. The shear moduli G were measured and the Young's moduli calculated. The mean values were determined from the measured values for the magnetic field orientation of $\theta = 5$ to $25°$. The error of the mean values is given by the statistical error.

explainable by small deviations in the prepolymer mixing ratio as well as the mixing ratio of PDMS and prepolymer solution. For PDMS mixing ratios where the Young's modulus was experimentally determined (see Tab. 4.2) the errors in computing the Young's modulus mean values are given by the statistical errors of the mean values. For PDMS mixing ratios where the Young's modulus was not experimentally determined the absolute value is extracted from the power law fit. The error in the Young's modulus can then be calculated with Gaussian error propagation by considering the errors of the fit parameters r_c, G_0 and v. For example, the absolute value and the error of the Young's modulus of a 15 % PDMS matrix is determined with $(4.6 \pm 0.8)\, kPa$. The power law fit is in the following used as calibration curve and gives the Young's modulus of the cross-linked PDMS matrices.

For the matrices used for the measurement in chapter 5.2 the Young's modulus was again determined with the above in-situ method (blue stars in Fig 4.13). While for the 10%, 12.5%, and 14% mixtures the values match the fit quite well for the 12% a strong discrepancy is observed. Looking at the images of the rotating chain this can be related to the initial chain structure. During the preparation, the particles slightly separated. Only the induced magnetic force pulls the particles together to form a connected chain. Apparently, this causes the model of a rotating chain to be not valid anymore. With help of the power law fit the Young's modulus can be calculated for all PDMS layers created after the procedure explained in the preceding sections.

5 Magneto rheological elastomers with discrete particle distribution

5.1 Field induced interactions in MREs

To get an idea of MRE's macroscopic behaviour, an understanding of the underlying microscopic processes is essential. To this end, it is inevitable to validate simulations via comparison with experimental data. In the following a short summary of the work of Metsch *et al.* [116], for which I conducted the experiments is given. A continuum approach (section 3.3.2), proposed in [112], was used and local magnetic and mechanical fields were accounted. Systems with arbitrary particles distances, shapes and volume fractions can be simulated. To keep the influencing variables at a manageable level and facilitate comparison between simulation and experiment, the samples contained particle configurations of only two, three and four particles, Fig. 5.1. Sample preparation was done as described in 4.1.1. Nickel particles, as characterized in 2.1, were used. Some distinct features of these measurements and the results are mentioned in the following. Particle detection was done with a transmitted light microscope, section 4.3. To ensure a similar magnetic field at the particle positions, it was of utter importance that particle were

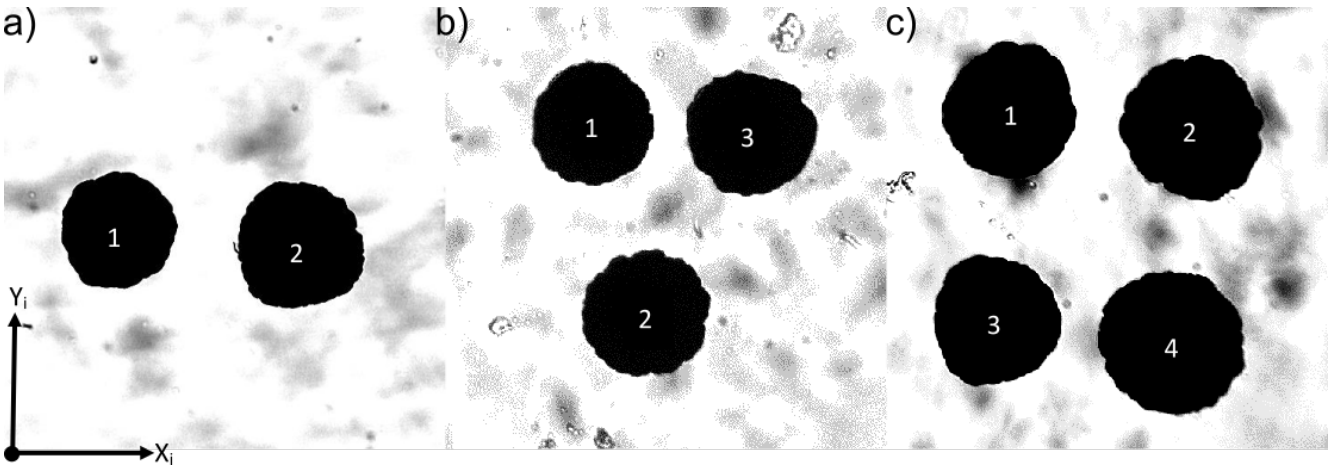

Figure 5.1: Particles in the a) two, b) three and c) four particle configuration without magnetic field. Pictures served to determine particle diameter and initial position. Axes were depicted to show the direction of y- and x-axis but the origin of the coordinate system was defined to be in the center of particle number 1. [Reused from [116], 2020, ©IOP Publishing, CC BY 4.0, [116]]

placed in the same height. As simulations were computed with spherical particles of identical size, particles were selected to show a very good roundness and a similar size. In contrast to Puljiz *et al.* [134] the initial particle distance was decreased to one particle diameter or less and hence an inhomogeneous magnetization occurs. Particles should be prevented from touching, as the simulation can not reliably compute a matrix that strongly deformed. Therefore, the preparation process had to be adapted compared to the previous work of Puljiz *et al.* [134], where particles were prevented from touching by a relative large initial inter-particle distance of more than three particle diameters. To this end, the elastic stability of the surrounding PDMS matrix was increased by adding 20 wt% prepolymer mixture to the low molecular PDMS. Rheology measurements using a plate-to-plate rheometer (section 4.3.3) determined a Young's modulus of $\approx (5.20 \pm 0.01)\, kPa$ for the PDMS matrix. Though due to two reasons, some uncertainties on this value remain: The first reason resulted from the used sample preparation. For the PDMS matrix two PDMS layer were cast and the first PDMS layer was completely crosslinked before the second PDMS layer was cast on top. As a result, these two PDMS layers did not cross-link among each other but were only attached by adhesion. The second reason was the contact of the upper plate in the rheometer measurement. The upper plate did not have perfect contact with the sample due to ridges at the sample edges. Hence for comparison between experimental and simulation data the Young's modulus was determined during simulation to be $\approx 7.2\, kPa$ [116].
Samples were positioned in the setup (see section 4.3) and illuminated from below. For every particle configuration a picture without external magnetic field was taken Fig. 5.1. Thereby, the particle's initial positions and diameters could be determined, see table 5.1, and used as input for the simulations. The origin of the system of coordinates was defined to coincide with the center of the particle number 1. The diameter of each particle was calculated via their projected area by assuming them to be spherical. The numeric simulations required magnetic boundary conditions at the surface of the particles. Considering the experimental realization, a 32-magnet Halbach-array (described in chapter 4.2) was used to create a homogeneous and clearly defined magnetic field with flux density of $\approx 180\, mT$. The Halbach-array consists of permanent magnets and the measurements were quasi static as magnetic relaxation inside the particle occurs significantly faster as field variations. Bearings allow to vary the magnetic field orientation in the sample plane and a step size of $\Delta\theta = 5°$ was chosen. Prior to the actual measurements the Halbach-array was rotated a few cycles to guarantee reproducibility of the particle movements and exclude the Mullins effect (section 4.3.1). Particle movement recording and center tracking is described in chapters 4.3 and 4.3.1. As the magnetic field orientation was rotated stepwise in the particle plane, a change in the inter-particle distance was observe. The values of the inter-particle distance were calculated by Eq. 4.2 after the particle positions were

Particle **i**	$\mathbf{x}_i$ in μm	$\mathbf{y}_i$ in μm	$\mathbf{z}_i$ in μm	$\mathbf{d}_i$ in μm
two particle system				
1	0	0	0	208
2	329	-29	0	223
three particle system				
1	0	0	0	180
2	104	-279	0	182
3	269	-14	0	188
four particle system				
1	0	0	0	200
2	303	-27	0	208
3	-25	-309	0	189
4	275	-344	0	211

Table 5.1: Particles initial position defined by their centers. Values for the two, three and four particle configurations depicted in figure Fig. 5.1. The diameter of each particle was calculated via the area and assumption of spherical shape. Point of origin was positioned in particle number one. As all particles lie on the same layer z-position was taken as equal for all particles. Error in center detection due to optical resolution was estimated with an upper limit of $\pm 4\,\mu m$. [Reused from [116], 2020, ©IOP Publishing, CC BY 4.0, [116]]

extracted, Fig. 5.2. Experimental measurements showed particle attraction, $\Delta d_{12} < 0$, over a wide angle range Fig. 5.2. In agreement with Biller *et al.* [17] in the angle region from $65° \leq \theta \leq 125°$

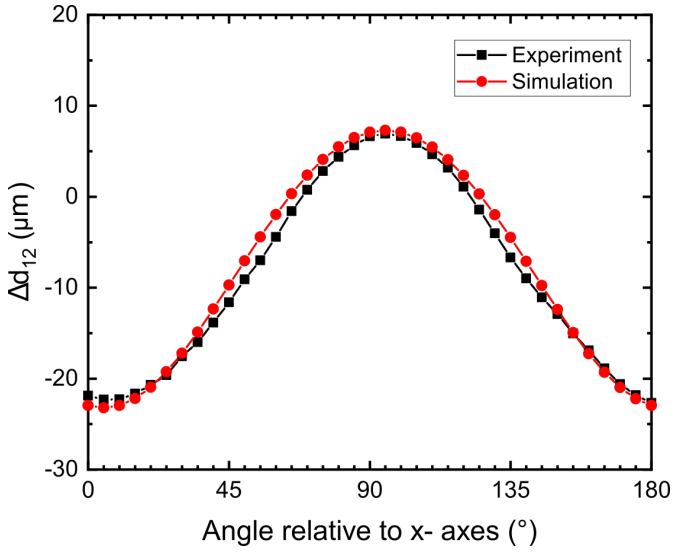

Figure 5.2: Inter-particle distance over the magnetic field angle relative to the x-axis for the two particle configuration depicted in Fig. 5.1. A magnetic attraction is observed except for the angle range of $65° \leq \theta \leq 125°$. In this angle region the particles magnetically repel each other. Particle movement determined by the simulation shows good qualitative and quantitative agreement with the experimental data. [Adapted from [116], 2020, ©IOP Publishing, CC BY 4.0, [116]]

the particles feel magnetic repulsion.
Apart from a maximum deviation of $2.5\,\mu m$ at the transition of attraction to repulsion simulated inter-particle distance accorded qualitatively and quantitatively with the experimental values Fig. 5.2. A 3D simulation was used as a 2D simulation considers only particle motion in the particle plane and would overvalue as out of plane motions were suppressed (see Fig. 6b in [116]). Obviously, apart from material parameters, the particle configurations govern the MRE´s behaviour as the amount of mutual interactions is increased. To identify influences of additional particles on the particle motion and to get an indication about the numerical simulation sensitivity, samples with three and four particle configurations were produced, Fig. 5.1 b) and c). The initial position of the three particle system used as input for simulations are listed in Tab. 5.1. The optimal value for the Young's modulus for the three particle system was determined to be $\approx 6.8\,kPa$. For the three particle system a good match between experiment and simulations for distance of particle 1-3 and 2-3 was observed. But simulation lacked to reproduce the distance of particles 1-2 accurately, Fig. 5.3. However, comparison of experimental and simulation showed a non-negligible effect caused by the initial particle position. A vertical shift in the initial position of particle 2 by $-5\,\mu m$ improved the agreement to the simulation, Fig. 5.3 dashed black line, even though, this represents only a slight modification of 2.7%. Adapting the initial position improved the numerical results, which can be explained by the fact that the real particles are not spherical. Thus, determining their center in the out of particle plane direction (z-direction) experimentally

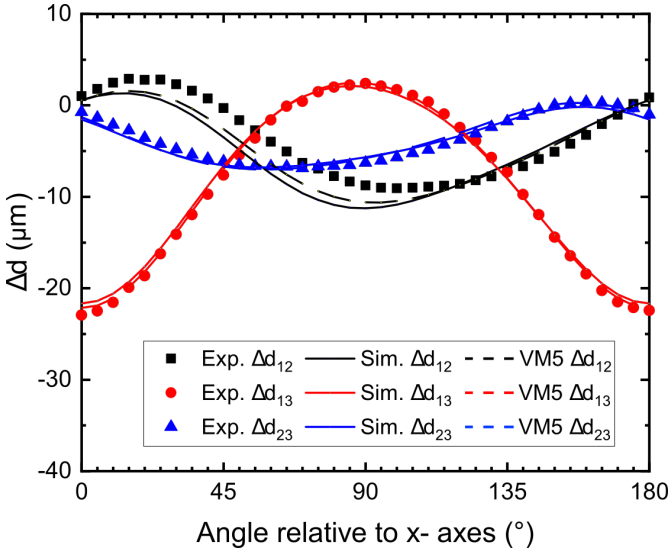

Figure 5.3: Inter-particle distance over the magnetic field orientation in relation to the x-axis for the three particle configuration depicted in Fig. 5.1 b). The experimental data points are depicted for the inter-particle distance of particle pair 1-2, 1-3 and 2-3. Results of the numerical simulation are given by the lines in the identical color as the experiment. The simulation results are more consistent with the experiment if the initial position of particle 2 is vertically shifted by $-5\,\mu m$ (dashed lines). [Adapted from [116], 2020, ©IOP Publishing, CC BY 4.0, [116]]

was only accurate to a certain point. For example, tomographic sample analysis could clear these uncertainties by providing a 3D image of the particles and thus, a more precise particle initial position.

Considering the four particle samples numerical results fit again quantitative and qualitative very well, Fig. 5.4. The Young's modulus was calculated with $\approx 7.3\,kPa$. Most discrepancy shows the inter-particle distance of particle 1 and 4. Whether the deviation of the simulation results to the experimental data can be traced back to the initial particle position or not can only be determined by a full sample analysis e.g. X-ray tomographic imaging. With every particle added, uncertainties increase, as the simulations assume e.g. particle sphericity. Even though, the accuracy of the simulations of the four particle system is comparable to the two and three particle system.

Within the above section, simplified MRE samples comprising two, three and four particles were subjected to a homogeneous magnetic field. The field orientation was rotated in the particle plane and the particle movement optically detected. Using a microscopically continuum model, the magnetic field induced interactions were simulated. Simulations agreed well with the experiments even though, the simulation assume e.g. sphericity of all particles. Hence, the above introduced simulation is a powerful tool to predict the microstructural interactions and thus, the particle movement in MREs.

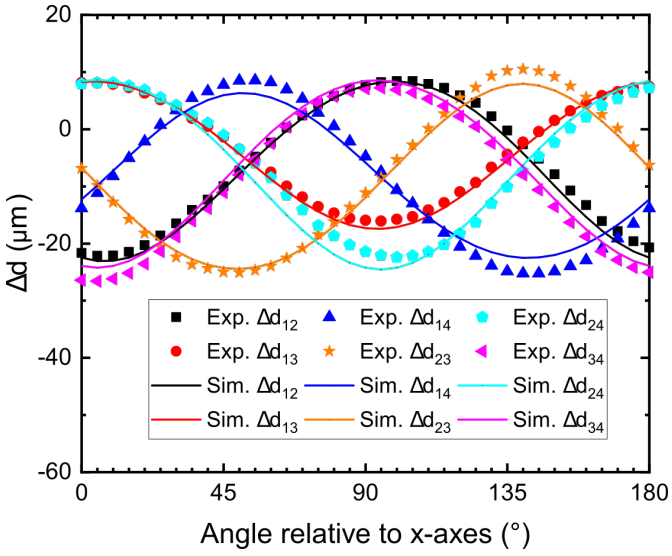

Figure 5.4: Inter-particle distance over the magnetic field orientation in relation to the x-axis for the four particle configuration depicted in Fig. 5.1 c). Simulations show good qualitative and quantitative with the experimental data. The accuracy is comparable to the two and three particle configuration. Whether the slight deviations are due to inaccuracy in the assumed initial particle position only 3D images of the particles can prove. [Adapted from [116], 2020, ©IOP Publishing, CC BY 4.0, [116]]

5.2 New strong magneto-active state

In previous section it was of utter importance to prevent particle from colliding. This was achieved by creating PDMS matrices with a Young's modulus of ≈7 kPa. Also for colliding particles exist quite a few theoretical and experimental results [16, 17, 56, 135, 160]. To my knowledge, particle collision was accomplished by either high magnetic field strength or by increasing the external magnetic field to a certain value at which particles are able to get into contact. In the following a new strong magneto-active state which is switchable by tiny alternations in the magnetic field orientation will be shown. Compared to states switchable with the external magnetic field strength this new magneto-active state is beneficial as a rotation of a constant magnetic field of this strength is more easily to realize. The new strong magneto-active state is investigated with special focus on system parameters like altered initial particle distance, Young's modulus, magnetic field strength and particle configuration.

5.2.1 Two particle system

In order to eliminate as many influencing variables as possible MRE´s including only two magnetic particles were produced. To this end, two nickel particles (section 2.1) were carefully selected to have a high sphericity and very similar size. The selection was carried out under an optical microscope and using tweezers. The selected particles were then placed in the middle between two PDMS layers as described in section 4.1.1. In a first step the initial particle distance was altered while the Young's modulus of the surrounding matrix was kept identical by using the same PDMS solution batch. In order to exclude influences by the particle size experiments were conducted with the exact same particles. Therefore, I extracted them from used samples and cleaned the particles mechanically with tissues before reuse.

Deformation behaviour under alternated initial particle distance

Particles with diameter $186\,\mu m$ and $188\,\mu m$ were deposited in a cross-linked PDMS matrix with mixing ration of 12.5 %. A bulksystem was used (section 4.1.1) to eliminate matrix boundary influences. Determining the Young's modulus with the method described in section 4.3.3 resulted in a Young's modulus of (3.29±0.05) kPa. Pictures without magnetic field were taken to identify the initial inter-particle distance. By the help of a micromanipulating device the initial inter-particle distance was varied from $(230 \pm 5)\,\mu m$ to $(259 \pm 5)\,\mu m$. Particles with initial inter-particle

distance well outside this range did not show the new magneto-active state. Therefore the experiments are not reported here. Based on three representative samples the influences of the initial distance on the particle movement under an applied homogeneous magnetic field will be discussed.

Starting with the smallest initial distance the sample was positioned in the experimental optical setup and the Halbach-array placed around the sample. As a result, the samples were exerted to a homogeneous magnetic field with a flux density of $\approx 180\,mT$. The difference to the maximum flux density of $216\,mT$ was due to the fact that the sample was not perfectly centered inside the Halbach-array but slightly shifted upwards in the z direction. Prior to the actual measurements at least forty consecutive, full loading $360°$ cycles were applied with the Halbach-array as preconditioning step. This made the experiments better reproducible as e.g. the Mullins effect was excluded.

At the beginning of the experiment, the magnetic field was orientated along the particle axis, i.e. in x direction, if not remarked otherwise. Clockwise and couter-clockwise rotations produced consistent results. Therefore, only the results for clockwise rotating magnetic field are depicted, Fig. 5.5 a). The initial inter-particle distance is marked by the dashed lines. The magnetic field orientation is altered in $5°$ steps in clockwise direction. In each step, a picture was taken. Dynamical influence can be neglected as between every rotation step of the Halbach-array enough time elapsed so that the particles could assume a steady state, i.e. elastic and magnetic torque

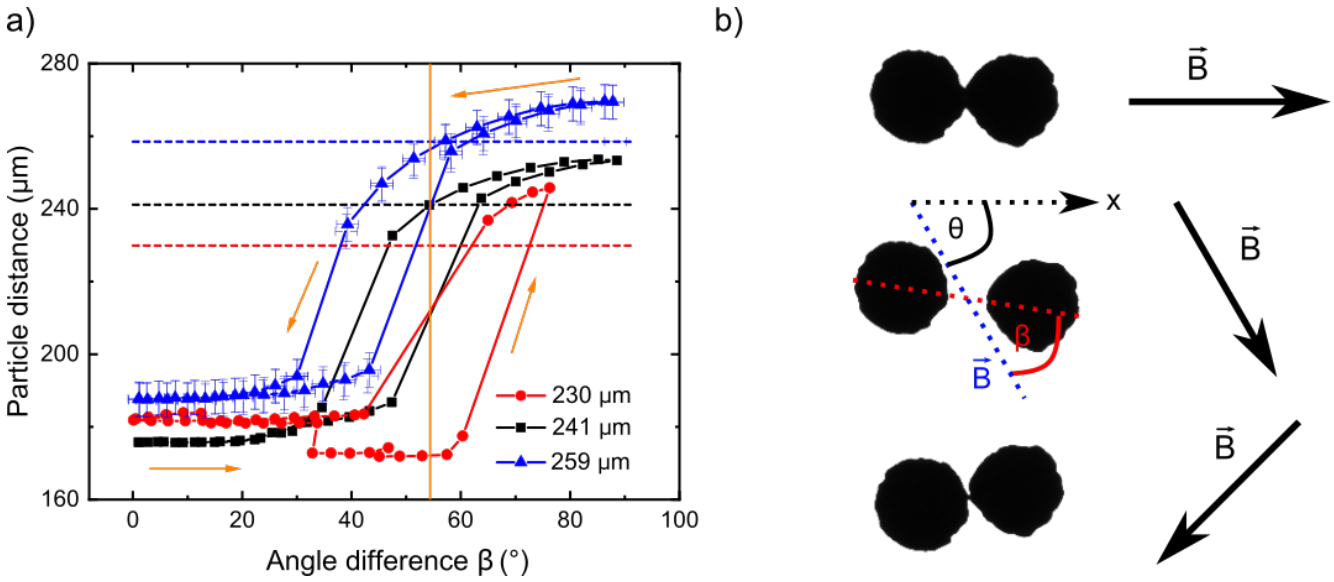

Figure 5.5: Exact same particles with different initial distance (dashed lines, 230, 241, 259 μm). Matrix composition was kept the same for the three samples [Young's modulus of PDMS: (3.29±0.05) kPa]. Orange vertical line indicates the magic angle of $54.7°$. For smaller initial distance particles stay in contact for higher angle difference β. Orange arrows indicate the direction of the experiment. Starting position was $\beta = 0°$. [Reused from [151], 2021, ©Springer Nature, CC BY 4.0, [151]]

matched. Particle tracking was performed with the ImageJ plugin Trackmate [165].
Two main particle configurations were observed: Particles are separated or in contact [Fig.5.5 b)]. Obviously, the particle configuration depends on the angle β between particle axis and magnetic field orientation, Fig.5.5 b). Analyzing the particle movement step by step, starting with the smallest initial inter-particle distance of 230 μm at the magnetic field orientation $\theta = 0 \rightarrow \beta = 0$ [Fig. 5.5 a), red curve]: In this configuration the magnetic dipole-dipole force is strongest and attractive as the induced particle magnetic moments point in the same direction along the connecting vector, the particle axis. The magnetic force is strong enough to overcome the counteracting elastic force that arises by particle movement such as particle displacement or rotation out of the initial position. Consequently, particles collide and get into contact. This collision is associated with a large deformation of the matrix between the particles, i.e. the deformation field diverges locally. Small, locally limited matrix damages are the result. However, as Fig. 4.9 a) showed, these small damages do not affect the particle movement for a large amount of Halbach-array rotation cycles (magnetic field rotation cycles).
Rotating the magnetic field orientation relative to the particle axis increased the angle β as the rotation of the particle pair was counteracted by the elastic matrix, Fig. 5.5 b). Though, the coupled particle rotation was not completely prevented and the magnetic torque acting on the particles leads to a rotation of the particle axis in the direction of the magnetic field orientation, Fig. 5.5 b). Apart from the coupled rotation small variations in the inter-particle distance indicate individual particle rotation around their center, Fig. 5.5 a). This originates from the particle surface roughness. By individual rotation they are able to minimize their center to center distance (inter-particle distance) and thus their magnetic energy.
Disregarding the small changes caused by the individual rotation, the inter-particle distance stays constant for a wide angle range β from $0°$ to at least $(60 \pm 2)°$ (red curve), Fig. 5.5 a). The used nickel particles are paramagnetic and thus, their magnetic moments are orientated along the magnetic field direction. Hence, an increase of β equals a decrease in the magnetic dipole-dipole force, Eq. 3.33, i.e. in a decrease of the attraction between the particle pair. Finally, the elastic forces overcome the attraction and particles separate. Even a repulsion is observable as the inter-particle distance increases beyond the initial distance, Fig. 5.5 a), dashed line. Continuing the cycle, as β decreases particle attraction increases until it was strong enough and particles collided again. A bistability effect between magnetic and elastic force leads to the hysteretic trend in the inter-particle distance, Fig. 5.5 a), which is comparable to Fig. 5 in [17] and Fig. 3 in [135]. This makes the particle configuration strongly magneto-active because two points exist where a tiny alternation in the magnetic field orientation changes the inter-particle distance strongly.
Additionally, the effects of inhomogeneous, nonlinear magnetization is experimentally detectable.

It was already shown by simulations that particles in contact have an increased magnetization at the contact point [135] and theoretical described that the dipole-dipole approximation does not hold [16, 19]. The experiments conducted in this thesis give experimental prove, as particles stay in contact even for angles $\beta_m \geq 54.7°$. This magic angle of $54.7°$ marks the point of sign change in the magnetic dipole-dipole-force, Eq. 3.34, and hence a switch from attraction to repulsion, Fig. 5.5 a), orange vertical line. Errors in specifying the magnetic orientation (see chapter 4.2) or the particle position (see chapter 4.3.1) are systematic and thus, only depicted once in Fig. 5.5 a). To identify how a varied initial inter-particle distance manifest itself in the particle movement, exactly the same particles and matrix solution were used as concurrently the initial inter-particle distance was altered.

Let me start this discussion with the initial distance of $241\,\mu m$, Fig. 5.5 a), black curve. In comparison to the sample with initial inter-particle distance of $230\,\mu m$ the inter-particle distance for the particle couple in contact was smaller. This is a result of the particle surface roughness and even though the identical particles were used the inter-particle distance in contact can vary. Next apparent difference is the angle $\beta = (47 \pm 2)°$ at which the particles separated. The change in the angle β can be interpreted in the following way: Since particles were positioned initially further apart their displacement is larger, when jumping into contact, compared to the $230\,\mu m$ particle pair. As a result the elastic force is increased while the magnetic force is in the starting configuration decreased. Particles with highest initial inter-particle distance, Fig. 5.5 a), blue curve, confirm this analysis and separated at an even smaller $\beta = (42 \pm 2)°$.

Additionally, the shape of the hysteresis changed. It was energetically preferable for the system to increase the elastic energy and to decrease the magnetic energy, i.e, the inter-particle distance became larger than the initial inter-particle distance before it decreased again. The second change was observed at the point just before jumping into contact. The inter-particle distance was smaller than the initial distance and the angle β smaller than for the separation. Those changes indicate the increased elastic forces and thus, the changed ratio between magnetic and elastic forces throughout the measurement. Similar for all three systems was the inter-particle distance just before jumping into contact. This was also validated by Puljiz *et al.* [135] as mentioned in chapter 3.3.1. Their dipole approximation produced a good agreement with the experiments as long as particles were separated.

Overall, for higher initial inter-particle distance, particles stayed apart for a wider range of magnetic field orientations. At an even larger initial inter-particle distance the elastic forces is so strong that the new strong magneto-active state vanishes. Non colliding particle pairs comparable to [116, 134] are observed. For small initial inter-particle distance, particles stayed apart for a smaller range of magnetic field orientations. At even smaller initial inter-particle distance,

particles were not able to separate for any magnetic field orientation. Hence, for particles in the new magneto-active state, a strong inter-particle distance change induced by tiny changes in the magnetic field orientation, is characteristic.
Those changes in the particle displacement are crucial for application in actuators and will be quantified in the following: With increasing initial distance (from 230 to 259 μm) the inter-particle distance changes after particles separate from $68\,\mu m$ (for 230 μm) to 56 μm (for 241 μm) to 60 μm (for 259 μm) and respectively from 53 μm (for 230 μm) to 47 μm (for 241 μm) to 42 μm (for 259 μm) for particles getting into contact. Setting the change in distance equal with the degree of macroscopic deformation, tendency points to the fact that positioning the particles at a certain initial inter-particle distances leads to a maximum deformation. Hereby, a smaller initial distance seems to be preferable.
Finally, as mentioned, the inter-particle distance always depends on the ratio of elastic to magnetic energy because the magnetic force displaces the particles while the elastic force tries to restore the initial configuration. Biller *et al.* [16, 17] could show, that a bistability in the total energy (sum of magnetic and elastic energy) exists, meaning that the collided and separated particles are minima of the total energy. The transition from one minimum to another happens in a hysteretic manner when the external magnetic field strength along the particle axis is increased or decreased. With the experiments presented, it could be shown that this hysteretic transition happens also when varying the angle β between external field and particle axis. Furthermore, it was proven with the presented experiments that only a range r_b for the initial particle distance exists with $r_{min} < r_b < r_{max}$ where the bistability occurs. This was also predicted by Biller *et al.* [16]. The bistability effect also explains why the distance change for particles separating is larger than for colliding. In contrast to Biller *et al.* a significant shape change in the hysteretic transition was observed. Additionally, the collision occurred roughly at the same distance and seems to be independent of the initial inter-particle distance.

Deformation behaviour under alternated Young's modulus

In order for MREs to be used as actuators the mechanical stability plays an important role as well. To this end the Young's modulus of the PDMS matrix was varied by adapting the mixing ration of the PDMS solution from 10 wt %, 12 wt % to 14 wt %. The three samples include exactly the same particles. Under the assumption of spherical shape, the particle diameters were $209\,\mu m$, respectively $201\,\mu m$. Using the method from chapter 4.3.3 the shear modulus G was determined in the magnetic field orientation range from 5 to $25°$. Calculating the mean value of the corresponding data points and using Eq. 3.9 the Young's modulus of the matrices was determined

to be $\approx (1.8 \pm 0.1)\,kPa$, $(2.1 \pm 0.1)\,kPa$, $(3.5 \pm 0.1)\,kPa$. In order to eliminate influences due to deviations in the initial inter-particle distance it was kept roughly equal: $302\,\mu m$, $304\,\mu m$ and $309\,\mu m$. In contrast to the previous measurement with varying initial inter-particle distance the stepsize of the Halbach-array was decreased to $2°$. This allowed to depict the inter-particle distance dependence on the angle β more accurately, Fig 5.6.

Beginning with a qualitative analysis: For all three matrices a clear hysteresis is depicted with nearly identical shape compared to the previous measurement, Fig. 5.5. Particles separate at the angle $\beta = (55, 42, 28)°$, Fig. 5.6. In this case the increase of the Young's modulus has a similar effect on the hysteresis shape like an increased initial inter-particle distance in the previous measurement. A transition to non-colliding particle pairs [116, 134] is observed. This transition starts in the way that the particles do not jump into contact but get into contact by small, step wise decrease of the inter-particle distance (Fig. 5.6 red curve). Concerning the changes of the inter-particle distance provoked by particle separation respectively collision, they were extracted to be $47\,\mu m$, $42\,\mu m$, $25\,\mu m$ for collision respectively $110\,\mu m$, $90\,\mu m$, $76\,\mu m$ for separation. It is quite apparent that a smaller Young's modulus provokes a greater distance change during particle separate or collision when the magnetic orientation is slightly altered. Similar to the alternating distance measurement an asymmetry in the distance changes between particle collision and separation is seen.

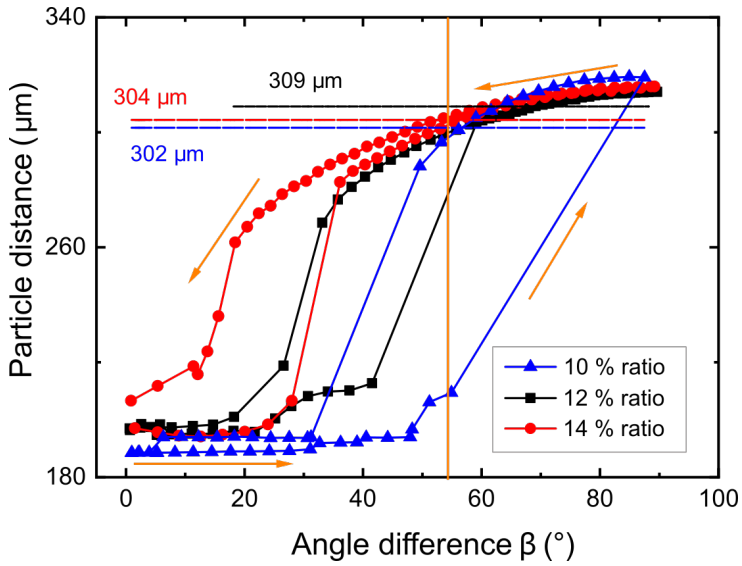

Figure 5.6: Same particles for the three measurements while matrix composition differs. Young's modulus varies from 1.8 to $3.5\,kPa$. The equilibrium distance is marked with dashed lines and was nearly equal for the three measurements as it ranges from 302 to $309\,\mu m$. Orange arrows indicate the direction of the experiment. Orange vertical line indicates the magic angle of $54.7°$. Starting position was $\beta = 0$. [Reused from [151], 2021, ©Springer Nature, CC BY 4.0, [151]]

Deformation behaviour under alternated magnetic field strength

To investigate the influence of the magnetic field strength on the new strong magneto-active state, the MRE sample containing two particles was moved in z-direction out of the center of the Halbach-array. The sample size was such that particles still feel a homogeneous magnetic field in the x-y plane. Due to an increased gradient in z direction particles might be pulled downwards thought. As this force acts on both particles equally, they were still positioned in the same plain. A PDMS solution with mixing ration of 10 % was poured for the matrix and particles with diameter of $209\,\mu m$, respectively $199\,\mu m$, were placed with initial inter-particle distance of $302\,\mu m$. Decreasing the magnetic flux density from $180\,mT$ to $40\,mT$ the system transitions to non-colliding particles and the hysteresis vanishes, Fig. 5.7. Compared to the previous measurements as function of the Young's modulus or initial inter-particle distance, the decrease of the magnetic flux density had not much influence on the angle at which particles separate. For $180\,mT$ to $100\,mT$ the angle diminished from $54.9°$ to $54.1°$ so the change is smaller than the tolerance in the angle resolution. The independence of the separation angle on the magnetic flux density from $180\,mT$ to $100\,mT$ can be explained as a change of the magnetic flux density, i.e. in the magnetization of the particles, only affects the magnetic dipoe-dipole force with the second power. Also the distance changes induced by particle separation or collision differs only slightly (see table Tab. 5.2). Consequently, the new strong magneto-active state is not as strongly affected by a change in initial distance or external magnetic field strength like it is by a change of the Young's modulus. This new state is strongly dependent on the ratio between elastic and magnetic force and thus, only stable for a

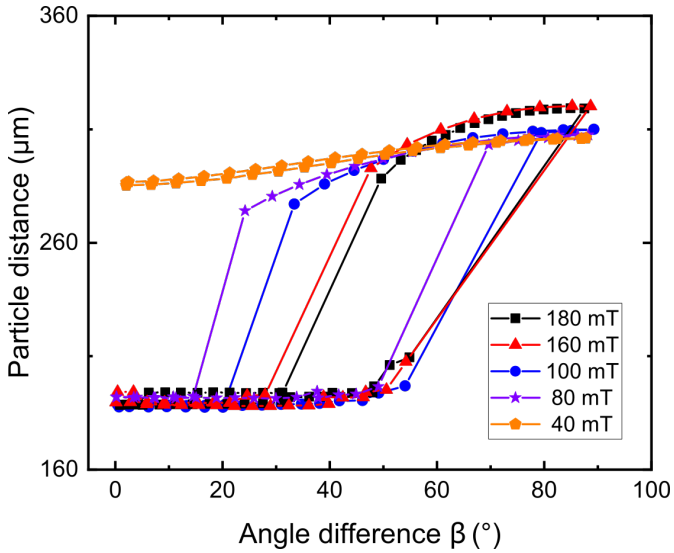

Figure 5.7: Same MRE sample containing two particles while the magnetic flux density was decreased from $180\,mT$ to $40\,mT$. At $40\,mT$ the new strong magneto-active state does not exist anymore.

defined range of initial inter-particle distance, Young's moduli of the PDMS matrices and magnetic field strength.

B in mT	Δd in μm (separation)	Δd in μm (colliding)
180	110	94
160	112	100
100	111	92
80	106	82

Table 5.2: An exemplary two particle MRE sample was subjected to various magnetic flux densities by shifting the sample out of the Halbach-array center. The distance changes induced by particles separating or colliding are extracted from Fig. 5.7.

5.2.2 Three particle system

In the previous section, two particle MREs showed a new strong magneto-active state. It is characterized by a strong change in the inter-particle distance by a few degree alternation of the external magnetic field orientation. At larger initial inter-particle distance, higher Young's moduli and/or weaker magnetic field strength the new strong magneto-active state transitions to non-touching particles. In contrast, for smaller initial distances and/or lower Young's moduli particles never separate. In order for MREs to be used in applications they need to contain a notable volume amount of magnetic filler particles. To gain more insight in the effects of increasing particle numbers, the system was expanded by a third particle, Fig. 5.8 a). This enables to investigate the mutual interactions between elasticity and magnetization and how the new strong magneto-active state is influenced by the presence of a third particle.
Therefore, three particles with roughly the same diameter (Tab. 5.3) were embedded in a 12.5 % PDMS matrix with Young's modulus of $\approx (3.29 \pm 0.05)\, kPa$. In order to eliminate symmetry influences, it was the aim to achieve the same initial distances between particle 1&2 and 2&3 (Tab. 5.3). The used sample preparation method facilitates particle positioning but still, due to particle roughness, same initial inter-particle distances were only achievable to a certain degree. The sample was subjected to a homogeneous magnetic field of $180\, mT$ by placing it in the center of the Halbach-array. The particle axis is in the following defined as the center-to-center vector between two adjacent particles, i.e. for the three particle system, Fig. 5.8 a), between particles 1&2 and 2&3.
Starting with the magnetic orientation aligned along both particle axis all three particles formed a contacting particle chain. Beginning at $\beta = 0°$ and continuing the rotation cycles separation

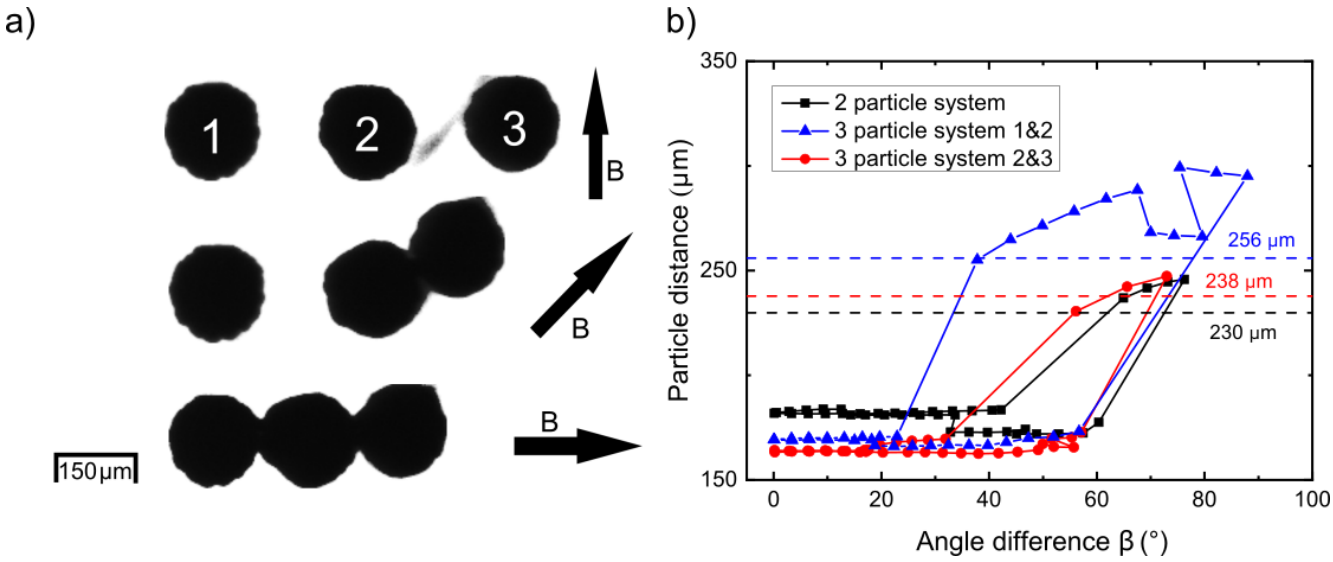

Figure 5.8: a) Three particles in a row. Magnetic field direction is indicated by the black arrow. b) Particle distance over angle difference. Dashed lines mark the equilibrium distance of the two respectively three particle system. The samples had the same Young's modulus of $3.29 \pm 0.05\,kPa$. [Reused from [151], 2021, ©Springer Nature, CC BY 4.0, [151]]

Particle i	Diameter in μm	Initial Δr to i particle in μm
1	161	i=2 Δr=256 ; i=3 Δr=494
2	165	i=1 Δr=256 ; i=3 Δr=238
3	158	i=1 Δr=494 ; i=2 Δr=238

Table 5.3: Particles numeration, their diameter and the initial inter-particle distance to the neighbor particles. The inter-particle distance is defined from particle center to particle center. Values are for the three particle in line configurations depicted in figure 5.8 a). The diameter of each particle was calculated via the area and assumption of spherical shape. Error in the inter-particle distance determination due to optical resolution was estimated with an upper limit of $\pm 4.68\,\mu m$.

and collision events occur comparable to the two particle system Fig. 5.8 a). Minor deviation in particle size and initial distance cause systematically the particle pair with higher initial distance to separate first. Even though the angle $\beta \approx (57 \pm 2)°$ at which separation takes place is equal for both particle pairs within the limits of the error. While the hysteresis shape of the closer particle pair 2&3 is nearly identical to the two particle system, the hysteresis for 1&2 shows some distinct new features Fig. 5.8 b).

First of all, a comparison between particle pair 2&3 with the two particle system with initial distance of $230\,\mu m$, Fig. 5.8 b) black dots, was done. This is possible, as parameters such as Young's modulus (12,5 % PDMS mixture), initial inter-particle distance etc. were nearly identical. Only a slight difference in the initial inter-particle distance (two particle system: $230\,\mu m$) has to be considered. Based on the dependence of the hysteresis shape on parameters such as Young's

modulus or initial inter-particle distance, section 5.2.1, the observed shape changes are mostly in agreement. As expected the angle at separation was smaller for the 2&3 particle pair $\beta = 57°$ compared to the two particle system $\beta = 60°$. Then again, the distance changes for particle collision and separation of $61\ \&\ 74\,\mu m$ were higher compared to the two particle system ($54\ \&\ 71\,\mu m$). These higher distance changes differ from previous observed tendency as the measurement with varying initial inter-particle distance showed decrease for larger initial inter-particle distance. This differences could be connected to the influence of the third particle. If so, the influence of the third particle seems beneficial and consequently the new strong magneto-active state exists in the three particle system as well.

Comparing the hysteresis shape of 1&2, Fig. 5.8 b), with the two particle system with initial distance of $259\,\mu m$, clear significant changes are depicted. The area the hysteresis encloses is much larger for the particle pair 1&2 and after separation particles attain their highest inter-particle distance. At an angle $\beta = (57 \pm 2)°$ particles separated. Regarding the shape and separation angle β, the hysteresis of particle pair 1&2 shows much more similarities with the hysteresis of particle pairs with smaller initial inter-particle distance. Three data points show a sudden and significantly distance decrease, Fig. 5.8 b). This decrease can be related to the behaviour of particle 2&3 and occurs when 2&3 are in the separated state. Hence, this proves that the inter-particle distance of particle pair 1&2 is strongly affected by the movement of the neighboring particle pair which is in good agreement with the theoretical prediction of matrix mediated interaction [133, 135]. Also the magneto-active state is enhanced and distance changes of $122\,\mu m$ (separation) respectively $84\,\mu m$ (collision) were extracted. Those exceed by far the distance changes of the particle pair 2&3 ($74\,\mu m$ and $61\,\mu m$) and of the two particle system with similar initial distance ($60\,\mu m$ and $42\,\mu m$).

To get a better understanding of the particle movements, a more detailed analysis of the acting forces will be performed. All quantities to calculate the magnetic dipole-dipole force were given, i.e. the magnetic moment of the particles was obtained from their volume and the SQUID magnetization curve (section 2.1) and the position for every magnetic field orientation by the particle tracking. While particles lie along the x-axis, the magnetic field was orientated along the y-axis in the starting configuration. Thus, all particles were separated and magnetic forces minimized. When starting to rotate the magnetic orientation, the magnetic force changes from repulsive to attractive. Once the attraction is stronger than the restoring elastic force, particles jumped into contact and a jump in the magnetic net force was observed, Fig. 5.9 a) (marked, e.g. once with a purple arrow). For the separation of the particles similar jumps in the magnetic net force are visible, Fig. 5.9 a) (marked, e.g. once with a dark red arrow). Furthermore, forces on particle 1 and 3 show a similar trend, Fig. 5.9 b). They differ mainly due to the fact that

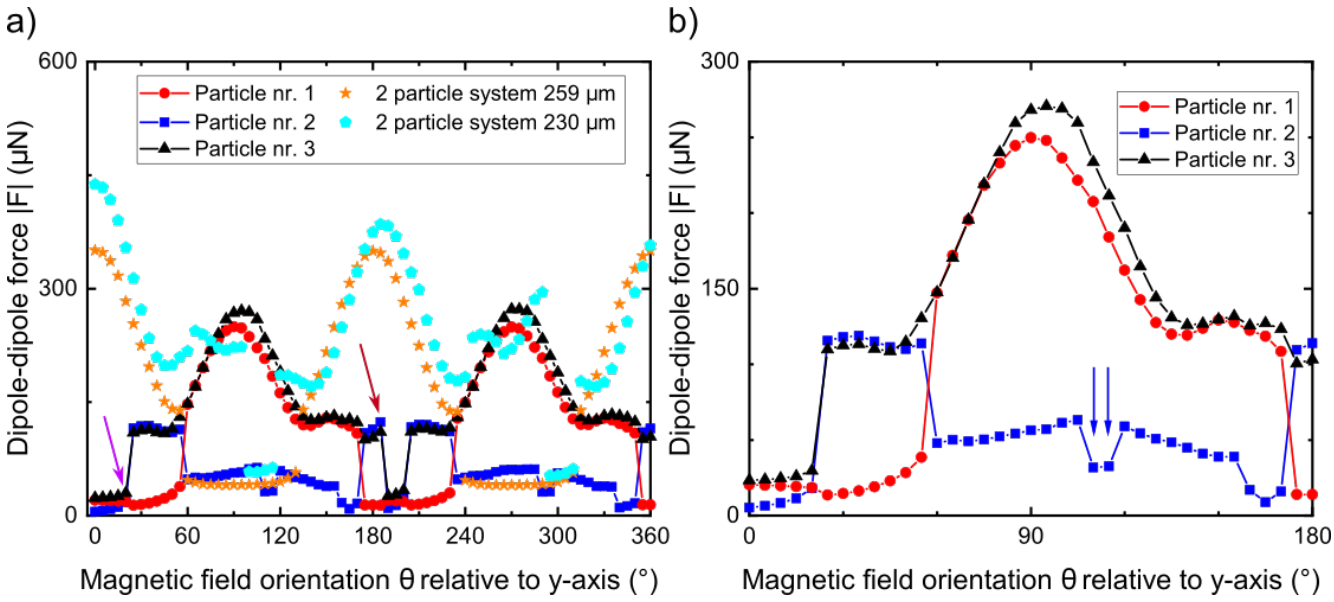

Figure 5.9: a) Magnetic dipole-dipole force over the magnetic field orientation for each oft the particles in the three particle system and for the particles in the two particle system with initial inter-particle distance of 230 and 259 μm. The purple arrow marks a point just before collision. The dark red arrow a point just before separation. Clear jumps in the magnetic net force are visible. b) The magnetic dipole-dipole force dependence on the magnetic field orientation for each oft the particles in the three particle system. Blue arrows mark rotations of particle 1 and 3 around their center.

particle 2 collides, for symmetry reasons, first with particle 3. The force curve of particle 2 shows huge deviations. Here the collision with particle 1 minimizes the net force as it is directed in the opposite direction of the force particle 3 exerts, Fig. 5.9 b). Small symmetrically reoccurring jumps marked in Fig. 5.9 b) with blue arrows occur because once particle 3 and then particle 1 rotate around their center creating a sudden distance change. Comparison with the two particle systems of nearly equal initial distance reveals also a qualitative similar trend. Magnetic force is mostly altered for particle 2 while particles were in contact. Maximum values were larger for the two particle system. This can be connected to the larger particles used in the two particle system. Comparing the increase, respectively decrease, of the magnetic net force at the collision and separation points of the two and three particle system, no clear trend could be determined. Hence, considering only the change in the magnetic force when the inter-particle distance changes can not explain the enhanced magneto activity of particle 1&2. Unfortunately, the elastic interaction is much more complex to calculate and is not included in this discussion.

Finally, the distance between particle 1 and 3 indicates if a long range new magneto-active state exists, Fig. 5.10. Here, also the new magneto-active state is visible and a distance change of 174 μm respectively 160 μm is achieved. But it occurs stepwise as not all particles collide or separate at once. Such the overall distance can only be stepwise adapted but also empowers to

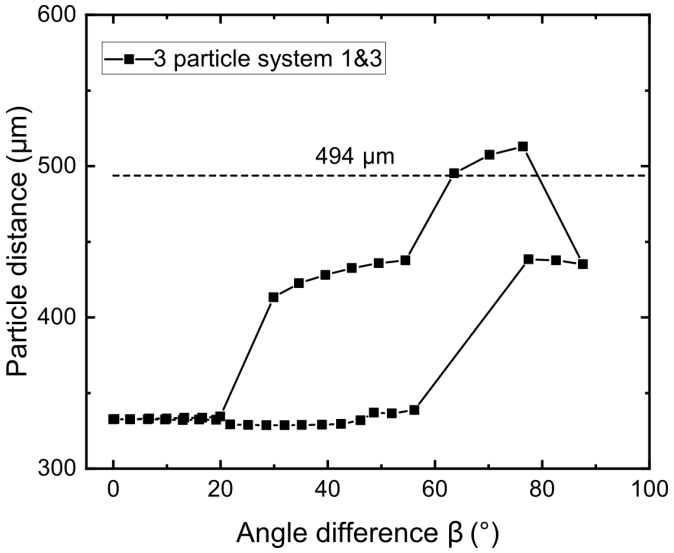

Figure 5.10: Three particle system. The particle distance between particle 1 and 3 for corresponding angles β between particle axis and magnetic field orientation. Particle 1 and 3 had an initial inter-particle distance of $494\,\mu m$, marked with a dashed line. For three angles β all three particles are separate.

assume an intermediate contraction.

5.2.3 14 particle system

The previous analyzed three particle system showed major changes in the inter-particle distance caused by tiny magnetic field orientation alternation. This relation is characteristic for the new strong magneto-active state. The particle pair with the smaller initial distance was nearly unaffected in its movement by the third particle. In contrast the particle pair with higher initial distance revealed an enhanced magneto-active configuration, i.e. the inter-particle distance change for separating and colliding particles was enhanced. Locally the system acted according to a two particle system, global distance changes, i.e. distance change between the edge particles, were only reached over an intermediate particle distance step. For actuators especially global distance changes are essential to create an overall deformation. To investigate how the overall kinetics of colliding and separating particles is influenced by further magnetic and elastic interactions, the system was expanded to fourteen particles, Fig. 5.11 a). In order to link particle distance changes to macroscopic matrix deformation the system is thinned as described in section 4.1.2. The thinning increases the matrix flexibility and thus, might makes the deformations surface accessible.

Samples were centered in the Halbach-array with particles aligned along the x-axis and the magnetic field was orientated in y-direction for starting configuration. Here already two particle

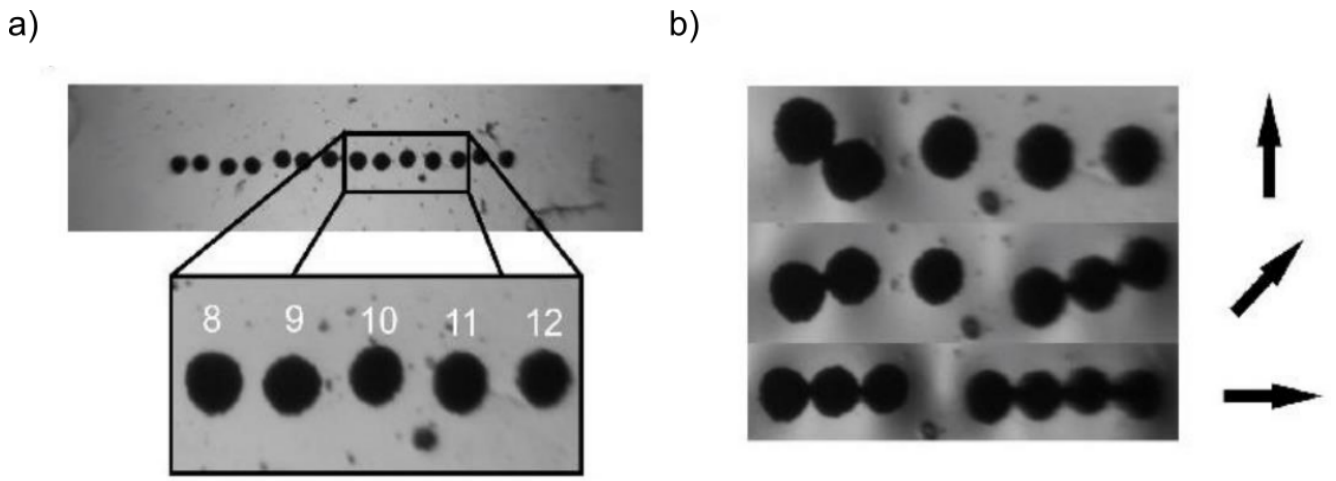

Figure 5.11: a) fourteen particles in a row. Particles 8 to 12 are highlighted. The image was taken under zero magnetic field. b) Particle formation of particle 8 to 14 for different magnetic field orientations (black arrow). In the top image starting from the left particle 8 to 12 is visible. In the middle image particle 13 and in the lower image also particle 14 appear. [Reused from [151], 2021, ©Springer Nature, CC BY 4.0, [151]]

pairs have collided. They did not separate for any magnetic field orientation hence were not in a magneto-active state. When the magnetic field was orientated along the x-axis the attractive magnetic force between the particles was strongest and more particles were able to get into contact. Particle groups of two, three and four particles evolved. Apparently, for no magnetic field orientation a chain forms that contains all particles. Instead particles formed well separated particle groups with varying particle number, exemplarily shown for particle 8 to 14 for different magnetic field orientations, Fig. 5.11 b).

In section 5.2.1, the sensitivity of the new magneto-active state to the initial inter-particle distance was shown. Analyzing the initial distances between neighboring particles provides hence first indication which particle pairs could be in the magneto-active state. Prior to the actual magnetic measurements a picture under zero magnetic field was taken. Their initial position is determined and depicted as colored circles in Fig. 5.12. Particles that were able to get in contact are marked in identical color. The field-free distances with the next neighbor particle were calculated and are plotted as data points in the middle between the particle positions, Fig. 5.12 black squares. When linking the initial inter-particle distance with the particle group formation, it was observed that small initial inter-particle distance lead particles to collide first, Fig. 5.12 black arrows. Additionally, particle groups that stay well separated show a high initial particle distance indicated by the peaks in Fig. 5.12. At the example of the three particle group (Fig. 5.12 magenta) and four particle group (Fig. 5.12 red) it was observed, that an initial distance smaller than at least one neighbor particle pair was crucial for particles to get into contact. To get a better understanding of the particle movement a closer analysis of the kinetics is carried out.

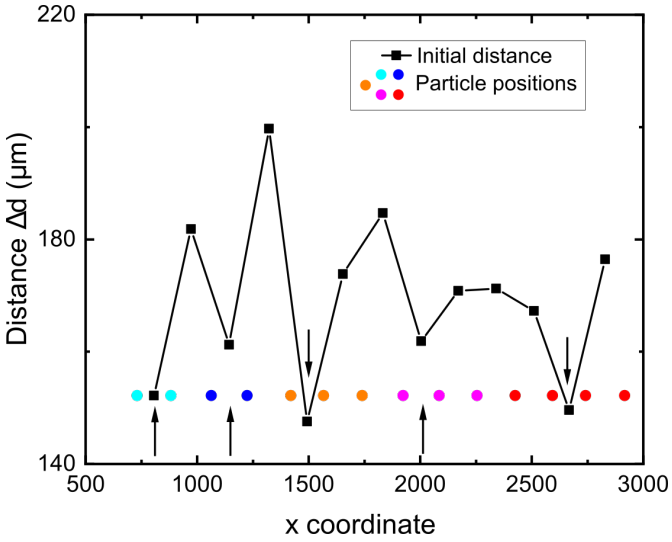

Figure 5.12: Initital inter-particle distance of the fourteen particles in row configuration. The initial inter-particle position between adjacent particles is shown by the black dots connected with a black line. The initial position of the particles is indicated by the colored circles. Circles of the same color are used for particles that were able to get into contact.

To this end, the five particles marked in Fig. 5.11 a) are investigated more closely. Concerning the particle configuration for different magnetic field orientations, groups consisting of three and even four particles were observed, Fig. 5.11 b). Particles of both groups were in the magneto-active state comparable to the two and three particle systems which were previously characterized, section 5.2.1 and 5.2.2. In order to get an idea why these particle groups stayed well separated, especially the edge particles 10 and 11 need to be investigated. This is done in regards to their inter-particle distance and the magnetic force acting on either of them. As the matrix mediates the particle displacements, the particle movement of the adjacent particles 9 and 12 were considered as well, Fig. 5.13.

Taking a closer look at the inter-particle distance of particle pairs 9&10, 10&11 and 11&12, some significant distance changes are visible. The distance changes marked with a orange arrow occurred due to collisions or separations of adjacent particles (8 or 13), the distance changes marked with blue and red arrows were the particle collision of the addressed particle pairs, Fig. 5.13. The particle pairs 8&9 and 12&13 did not significantly matrix mediate their distance changes to the particle pair 10&11. Quite the contrary was observed for the distance changes between particle pairs 9&10 and 11&12. Their distance changes are clearly depicted in the distance between particle pair 10&11, Fig. 5.13 black arrows. The distance changes marked with purple arrows indicate rotations of particle 10 or 11. How those distance changes between particle 10 and 11 affect their magnetic interaction will be discussed in the following.

By means of Eq. 3.32 the magnetic net force and its direction acting on the particles 10 and 11

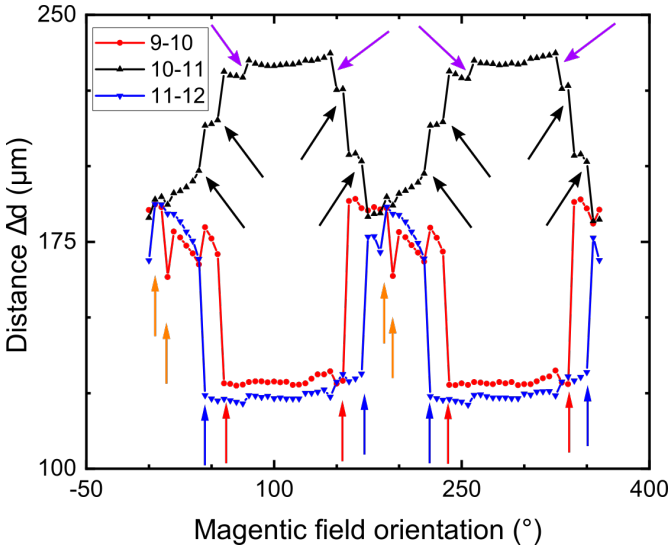

Figure 5.13: Particle distance between particle pairs 9&10, 10&11 and 11&12. Clear jumps are visible. Jumps induced by adjacent particle 8 or 13 are marked with an orange arrow. Separation and collision of particle pair 9&10 and 11&12, marked with blue and red arrows, induced a significant distance change between particle 10 and 11, marked with black arrows. Smaller distance changes between particle 10 and 11, marked with purple arrows, are caused by particle rotations of particle 10 and 11. [Adapted from [151], 2021, ©Springer Nature, CC BY 4.0, [151]]

was calculated for every magnetic field orientation. Only the interaction with the two nearest neighbor particles was considered. Using the particle position as starting point, the magnetic force was plotted for every position the particles occupied during one full $360°$ cycle of the magnetic field, Fig. 5.14. Only small attractive magnetic forces along the particle axis between 10&11 were observed. On the one hand, these small magnetic forces were due to the large particle distance between particle 10 and 11. On the other hand by the strong magnetic force from their neighboring particles acting in the opposing direction, i.e. the net force along the particle axis between 10&11, was small in comparison to the surrounding particles. The strongest attractive force occurs when particle 10 was in contact with particle 9, opposing the force between particle 10 and 11. Same counts for particle pair 11&12. Hence, the splitting into particle groups can be described as follows: The particle distance 10&11 was initially slightly larger than between 9&10 and 11&12. This was sufficient that particles 9&10 and 11&12 collide primarily. Those collision increase the distance between particle 10 and 11. As a result the attractive magnetic force between particle 10 and 11 was small compared to the surrounding particles and particle pair 10&11 was not in the magneto-active state. Thus, the particle groups stayed separated for every magnetic field orientation.

The fourteen particle system has some similarities with the model and simulation of Goh *et al.* [56]. A comparison will be carried out though. For a detailed description can be found in [56]. Goh, *et al.*, used a dipole-spring model to simulate the particle dynamic of a particle chain consisting

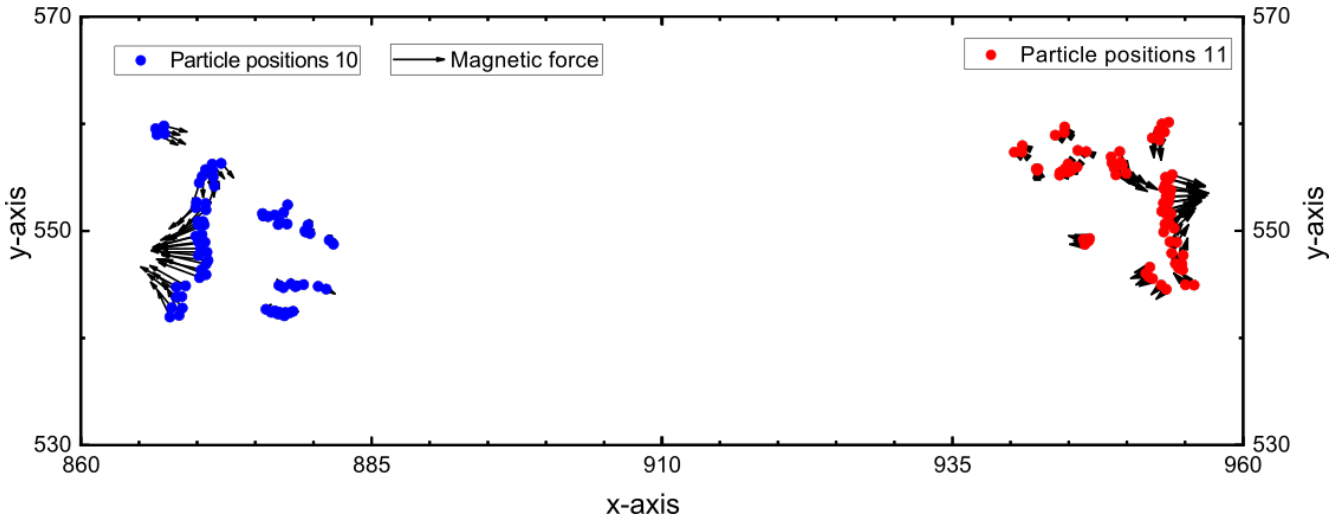

Figure 5.14: Particle position of particle 10 and 11 during a full $360°$ cycle of the external magnetic field. The particle positions of particle 10 are marked with blue points and the positions of particle 11 are marked with red points. Black arrows indicate the strength and direction of the acting magnetic force.

of N spherical particles. The total energy of the chain is given as follows: Harmonic springs with stiffness k and length a account for the elastic interactions. The magnetic dipole–dipole interaction was calculated taking nearest neighbor interaction into account and assuming identical magnetic moments for each particle. Finally, to prohibit a collapse of the chain a steric repulsion was introduce. All those contributions were summed up to obtain the total energy of the system. Since only the contributions of adjacent particles were considered the total energy was written in form of a pairwise energy *e(r)*, where the individual contributions only depend on the distance r to the nearest neighbors.

Different scenarios for the touching/separation dynamics along the chain were presented for various regimes of the pairwise energy *e* of the chain system. Using two independent control parameters, the particle's magnetic moment $\vec{m}$ and the initial distance between adjacent particles, the pairwise energy landscape could be adapted (one minimum, two minima etc. see Fig. 2 in [56]). The energy landscape could be divided according to the value and sign of the first derivative e^1 and second derivative e^2 of the pairwise energy function with respect to r. Equilibrium particle configurations correspond thereby to $e^1(r) = 0$ and the relaxation dynamics was governed by the second derivative. In contrast to the simulations the experimental measurements were quasi static. Hence, the immediate particle dynamics such as simple relaxation or shock-wave propagation after an instantaneous magnetic field was applied could experimentally not be observed [56]. Experimentally, the equilibrium configuration of the particles were investigated and not the relaxation dynamics of the particle chain.

Out of the emerging scenarios of Goh, *et al.* [56], one, where particle pair building is a stable

condition, is used to make a comparison to my fourteen-particle system. In the article of Goh, *et al.* [56], the authors observed particle pair formations for a moderate magnetic moment and an initial distance between adjacent particles where $e^{(2)} < 0$. Beside the two particle configuration near $e^{(2)} = 0$ also particle configurations with more particles per group were observed during the simulations. These heterogeneous states were stable and no uniform equilibrium configuration was observed. Similarly, the fourteen particle system formed particle groups and not an overall connected particle chain. Observed particle groups consist of two particles to four particles. This would indicated, that the experimental system was in the parameter range leading to these heterogeneous state, i.e. in the pairwise energy regime of $e^{(2)} \leq 0$ [56].
Concerning the relaxation dynamics, the results of the fourteen particle system is difficult to compare to the simulations as the magnetic field is not instantaneous applied and the particle motion is not time resolved. During the stepwise rotation of the magnetic field orientation, pair formation does not necessarily start at the edge particles as shown in the simulation. But as a no homogeneous particle distribution existed in the experimental system, Fig. 5.12, particle group formation starts with particles with smallest initial inter-particle distance. This was mentioned in [56] as well. They stated, that heterogeneity in the initial particle distance leads to different initiation spots of the formation processes. Considering the results, the experimental fourteen particle system seem to be, regarding the dynamics and equilibrium state, in the bistable energy regime, i.e. $e^{(2)} \leq 0$, described by Goh *et al.* [56].
Finally, scenarios described in [56] were strongly governed by the pairwise energy. Since the pairwise energy depended on the magnetic moment $\vec{m}$ of the particles and the initial particle distance between adjacent particles the fourteen particle system can be adapted. The initial particle distance remains identical but by shifting the sample to a higher z position in the Halbach-array the magnetic moment $\vec{m}$, was varied. By varying the magnetic field strength between 170 and $45\,mT$, i.e. decreasing the magnetic moments $\vec{m}$ of the particles, the particle group size was analyzed. To this end, the magnetic orientation was altered from 0 to $360°$ in $5°$ steps and an image was taken after each step. Afterwards, the number of particle groups with n particles per group was counted for every magnetic field orientation and summed up, Fig. 5.15. For the small magnetic fields, magnetic moments were small and the system transitions to the uniform equilibrium state described in [56]. In this scenario, no particle pairs formed because elasticity forces predominate. Increasing the magnetic field up to it´s maximum of $170\,mT$ a clear tendency to building particle pairs was observed. In summation over all magnetic field orientations, still a group size of two particles is preferred but also groups with higher particle numbers form. Maximum group size was four particles. Therefore, for even higher magnetic moments a transition to the uniform case where all particles form a chain is assumed.

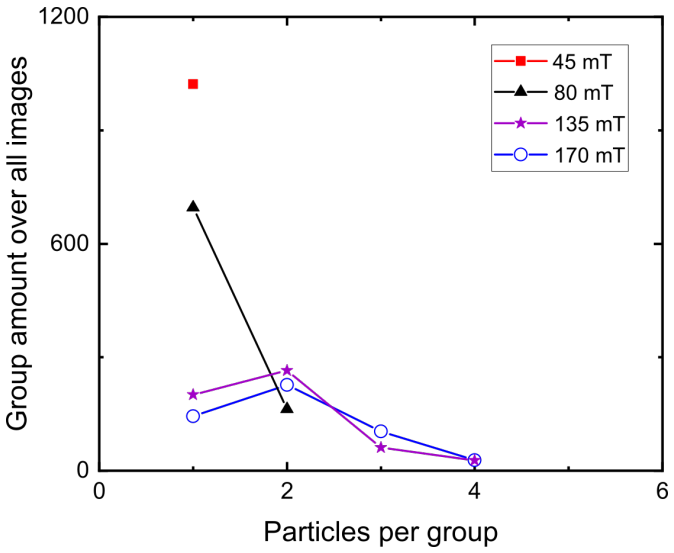

Figure 5.15: Group amount of particle groups with n particles for all corresponding magnetic field directions. For small magnetic flux densities the particles stayed separated. With increasing magnetic flux density the particle number per group increased. At a magnetic flux density of $170\,mT$ particle groups of four particles formed. [Adapted from [151], 2021, ©Springer Nature, CC BY 4.0, [151]]

As describe at the beginning of this section, locally particles were still in the magneto-active configuration, similar to the two and three particle system. But as shown for particles 10 and 11, interaction with adjacent particles prevents a collision. This also affected the distance change between the ending particles 1 and 14. Apart from small distance jumps that only alternated the overall distance by $\approx 1\%$, a smooth sinus-like change is shown, Fig. 5.16 a). Maximum and minimum distance between particle 1 and 14 differ by $\approx 4.5\%$. The transition from the minimum to the maximum can not be generated by a small alternation in the external magnetic field orientation, Fig. 5.16 a).

Compared to the two and three particle samples, where matrix thickness was significantly higher than the particle movements, the samples used for the fourteen particle system was much thinner and showed some macroscopic deformations. In the resulting particle images clear dark and bright areas were visible for different particle configurations, Fig. 5.16 b). Particle collision pushes the incompressible matrix between the particles out. This deformed also the surface and thus, causing light to diffract differently compared to zero magnetic field configuration, leading to bright and dark areas in the images, Fig. 5.16 b). But unfortunately a quantification of the surface deformation could not be achieved so far.

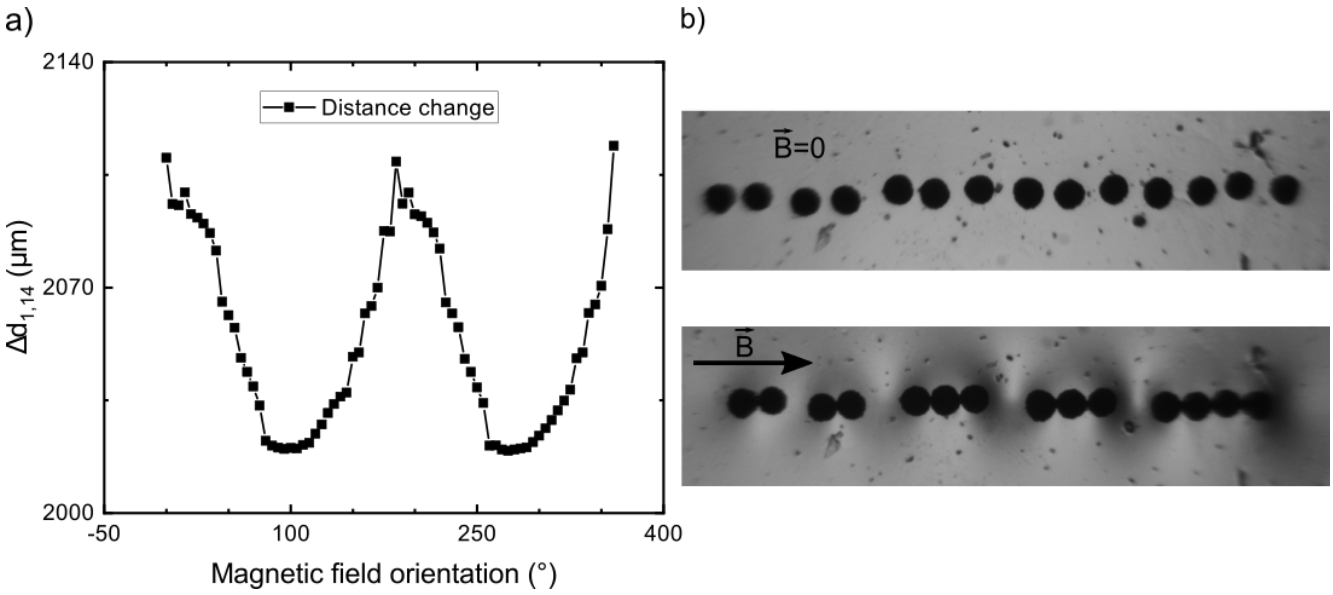

Figure 5.16: a) Particle distance of the ending particles 1 and 14 for the corresponding magnetic field orientations. Only small jumps in the distance are visible. The difference between maximum and minimum distance is $\approx 4.5\%$. b) Real images of the fourteen-particle system. The upper image was taken at zero field. The lower image was taken with the magnetic field orientated along the particle axes. Clear dark and bright areas are visible in the magnetic field image.

5.3 Particle lattices

In numerous theoretical as well as experimental investigations of MREs it was shown, that the spatial particle distribution effects strongly the magnetically created deformations (magnetostriction) [34, 38, 72–74, 82, 113, 148, 181]. Theory approaches are in most cases based on either the macroscopic continuum-mechanics or microscopic dynamics. While the macroscopic approach neglects the discrete particle position and instead uses a demagnetization shape factor the microscopic approach considers the exact local particle allocation. With the microscopic theoretical approach it was calculated that the magnetic field inside a MRE depends on the local particle distribution and thus, the behaviour of MREs. Experiments revealed various reactions of MREs which depended on the internal particle structure. Particle formations such as chains inside the MRE caused a contraction of the system along the field while an isotropic particle distribution on the contrary leads to an elongation [34, 38, 82, 181]. In previous studies it was shown that particles in MREs with isotropic particle distribution rearrange into chain-like formation when subjected to a magnetic field [160]. Additionally, the wavy-chain model of Han *et al.* [66] showed that it is important to consider the particle alignment in order to describe the mechanical response of a MRE accurate.

In the previous sections system with well defined particle distribution of up to fourteen particles

were evaluated. They showed vast particle movements and particle distance could be change by tiny alternation of the external magnetic field orientation. Apart from the initial distance also the number of particles influenced the behaviour of their movement. Thus particles in the fourteen particle samples resided only locally in the magneto-active configuration. But for large systems, no sudden distance changes were observed. How the spatial distribution influences the magneto-active configuration and particle group formations, shall be investigated in the following. To this end, the systems were expanded to a five by five lattices. Focus was on the particle group formation process. Particle group formation was analyzed regarding symmetry aspects and number of particles per particle groups. Finally, the group formation was connected to changes in the area the edge particles surround.

5.3.1 Particle groups formation

In order to create vast matrix deformation, particles need to be displaced over large distances. In the previous sections, a promising magneto-active particle state with particles changing their distance due to a tiny alternation of the magnetic field orientation was observed. Fourteen particles positioned in a line revealed only locally deformation as groups of particles form. This inhibited a large global deformation and the end-to-end distance changed only slightly ($\approx$4.5%) in a sinus like form as a function of the magnetic field orientation. In the following the system was expanded to a two dimensional three by three, four by four and five by five particle lattice and particle group formation was analyzed in respect to the lattice regularity.
All samples were produced according to chapter 4.1. In the following only specifications like mixing ratio, sample thickness etc. are mentioned. I will compare lattices prepared in the same way and discuss their differences and variability. Starting with the smallest system, a thin PDMS layer was cast with mixing ratio of 12.5%, Young's modulus of $(3.29 \pm 0.05)\, kPa$ and nine particles were positioned in a three on three square (compare, e.g., the lattice in Fig. 5.17 a)). After particles were encapsulated with yet another layer the sample was exposed to a homogeneous magnetic field of $180\, mT$ by placing it in the center of the Halbach-array. Beginning with the field orientated along the x axis, particle groups with three particles orientated along the field direction form. While rotating the field orientation clockwise in 5° steps, particle groups first follow this rotation, but with a diminished amplitude compared to the external magnetic field. At around 55°, the interaction of magnetic and elastic force causes the particles to rearrange. The former particle groups decay, building new groups with up to five particles. When the field is orientated initially in y direction, a similar picture arises. Particle groups of three particles form with direction in y. But due to an irregularity in the initial particle distance along the y direction, as will be shown

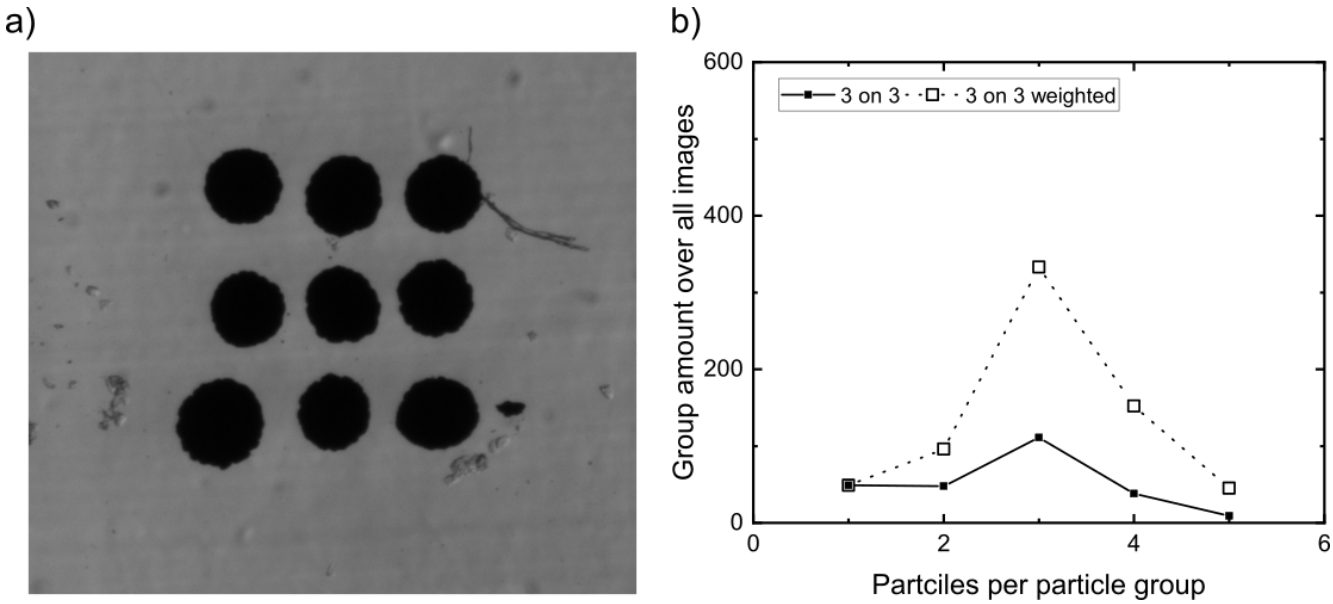

Figure 5.17: a) Exemplary three on three particle lattice. The PDMS matrix had a mixing ratio of 12.5%. b) Particle group amount detected for all corresponding magnetic field orientations in relation to the particle number per group. A clear tendency to form particle groups with three particles is shown.

later, only two of the three rows are fully connected. One row splits into one single particle and a particle pair. Similar to the fourteen-particle sample, the jump in contact of the particles caused a deformation of the matrix that induced darker and brighter areas around the particles. Particle rearrangement happens instantaneous and changes the location of the darker and brighter areas of the image. It shows that the particle group formation deforms the matrix. Comparison of a zero field picture before and after exertion to the magnetic field showed unchanged particle positions. In conclusion, the matrix seems to stay intact in spite of the multitude of particle displacements. After describing the particle group formation qualitatively, the particle group distribution will be analyzed in relation to the magnetic field orientation and group size. Therefore, particle positions were tracked and particle center to center distances calculated. Whether particles could be regarded as touching or not was identified by setting a limit value for the inter-particle distance in the size of the particle diameter. As a result, the number of particles per particle group could be assigned and the particle groups with exact same number of particles could be counted. This gives the dependence of particle group size on the external magnetic field orientation. Summing up the number of groups over all magnetic field orientations, a tendency is depicted. Apparently, the three by three particle lattice forms in average groups with three particles per groups. This is depicted through the peak in Fig. 5.17 b) black squares and even better when the number of groups is weighted with the particle number per group Fig. 5.17 b) black open squares. Additionally, a maximum group of five particles is forming for a field orientation of 145 to $160°$ and 325 to $340°$.

As it is not observed for a magnetic field orientation of $55°$ or $235°$ relative to the x-axis, the irregularity in the initial inter-particle distance along the lattice diagonal could play a roll.
In order to get any indication whether the irregularity in the initial inter-particle distance influences the number of particles per particle group, the lattice was separate in particle squares of four particles Fig. 5.18 a). Hence, only nearest neighbor particles were taken into account. For a perfect square of identical particles, particles would be positioned in a $90°$ angel on the axis and with identical inter-particle distance. This would imply particles positioned on the diagonal to have an angle of $45°$ to the corners and a distance of $\sqrt{2}$ times the particle distance on the axis. By extracting the particle coordinates, all angles and distances in each of the divided four particle squares could be determined. In Fig. 5.18 b)-e) an exemplary four particle square is depicted and all calculated particle distances and angles to identify the regularity of the lattice were marked. Proceeding systematically, the lattice was first analyzed along the x direction. To this end, all left upper angles of the square, marked with φ in Fig. 5.18 c), were computed and set in correlation to the adjacent particle distance marked in Fig. 5.18 b) with x_1. The mean value and standard derivation were calculated from all four particle squares the lattice was divided in Fig. 5.18. For a full characterization, also the facing angle marked with θ in Fig. 5.18 c) was taken into account. In that case it was correlated with the distance x_2, Fig. 5.18 b). Hence for the x direction two mean values were determined. Subsequent for the diagonal and y direction the mean values were calculated in similar manner. In y direction the angles φ an δ were assigned with distances y_1 and y_2, Fig. 5.18 b), c). Respectively for the diagonal the angles β and ε with the distances dia_1 and dia_2, Fig. 5.18 b), d), e).
Plotting the mean angles over the mean distances, Fig. 5.19, the deviation from a perfect square lattice can be analyzed. The orange line marks the angle of $90°$ degree and the magenta line of $45°$. In the case of a perfect lattice, data points would lie on those lines. At first sight it is apparent that particles have a greater overall initial distance in the y direction as in x direction. In addition,

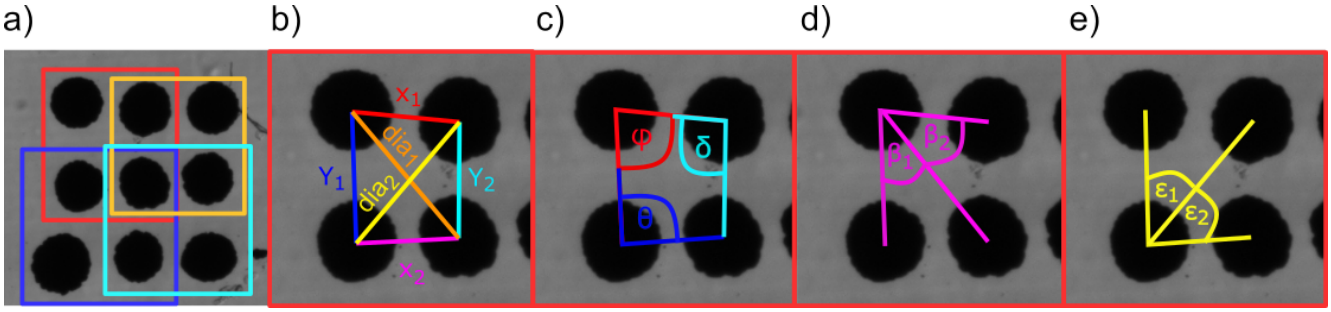

Figure 5.18: a) The particle lattice was divided in squares of four particles in order to determine the initial inter-particle distances and angles. b) Definition of the initial inter-particle distances in x, y and the diagonal direction $dia_{1,2}$. c) Definition of the angles between particles in the x and y direction. d) and e) Definition of the angles for particles positioned on the lattice diagonal.

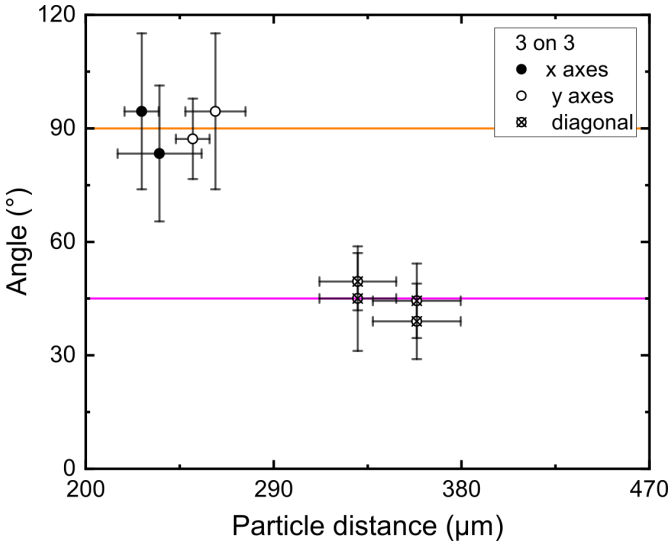

Figure 5.19: Mean initial inter-particle distances and angles of the three by three lattice. Therefore, the mean initial distances in x, y and diagonal direction were connected to the corresponding angles, 5.18. The orange line marks the angle of $90°$ and the magenta line marks the angle of $45°$. For a perfect square data points would lie on those lines.

particles in y direction lie closer to a rectangular position than in x direction. Concerning the diagonals, the plot shows that along one diagonal direction the particles are further apart as along the other. For both diagonal direction particles along one axis lie in a nearly $45°$ angle, while for the other axis the angle is smaller respectively larger.

When the lattice was orientated with its edges along the x and y direction particles exert strongest magnetic interaction for magnetic field orientation along these axes and thus, it was observed that chains of three particles form in the same direction. As the dipole force scales with $\frac{1}{|r|^4}$ (Eq. 3.34), in y-direction one particle row is interrupted due to the high initial inter-particle distance. Considering the initial mean inter-particle distance along the axes, a small difference is observed. This small difference cause particles along the x-direction $x_{1,2}$ to stay in contact for more magnetic field orientations as along the y-direction $y_{1,2}$. A result, already observed for the three particle system in the line configuration. Due to the larger particle number an increased number of mutual magnetic and elastic interactions is generated. This, though, does not affect the particle group formation along the axes.

Analyzing the particle group formation for magnetic field orientations along the diagonal direction dia_2 of the lattice, a chain size of up to five particles was observed. These chain sizes were observed for field orientations of 145 to $160°$ and 325 to $340°$. However, for the other diagonal direction dia_1, i.e., orientations of $55°$ or $235°$ a chain size of maximum four particles was detected. Linking the chain size to the initial inter-particle distance along the diagonal direction, an inverse relation than along the axes was observed. Along the diagonal dia_1 with the smaller initial inter-particle

distance the chain size of maximum four particles was formed. Hence, for chain formation along the diagonal the initial inter-particle distance seems not to be the regulating factor. This is supported by the observation, that a direct connection of the diagonal particles did not occur but via a particle positioned on one of the axes. Hence, ε and β, the angle between the particle positioned on the diagonal and the particle positioned on one of the axes [Fig. 5.18 d), e)], could be a determining factor for the particle group size along the diagonal direction. β was $(45 \pm 6)^\circ$ respectively $(49 \pm 3)^\circ$ and ε was $(44 \pm 4)^\circ$ respectively $(39 \pm 4)^\circ$. In the diagonal direction dia_2 particles positioned on one of the axis were positioned in a smaller angle to the diagonal direction. This creates a particle configuration in which the particles on the diagonal direction and on the axes are more likely to magnetically attract each other and thus, more likely to form a chain.
Before continuing with larger lattices a short recapitulation: For the particle group formation along the axes $x_{1,2}$ and $y_{1,2}$ the mean initial inter-particle distance is the determining factor. A smaller initial inter-particle distance was beneficial and particles stayed in contact for more magnetic field orientations. For particle group formation along the diagonal directions $dia_{1,2}$ an inverse relation to the initial inter-particle distance was observed. Particles along the diagonal with larger initial inter-particle distance dia_2 formed a larger chain than along the diagonal dia_1 with smaller initial inter-particle distance. Here, $\varepsilon_{1,2}$ and $\beta_{1,2}$, the angle between a particle positioned on the axis and the diagonal particle were significant. A smaller angle creates a particle configuration where it is more likely that particles simultaneously attract each other. In order to investigate the influence of both parameters in systems with more mutual magnetic and elastic interaction, a four by four and five by five particle lattice was prepared and analyzed identical to the three by three lattice.

Four by Four particle lattice

The samples were prepared as described in chapter 4.1 and the identical PDMS batch as for the three by three lattice used. On the interface between the PDMS layers, a sixteen particle lattice was configured. The sample was centered in the Halbach-array. The Halbach-array was rotated a full 360° turn and the chain size analyzed, Fig. 5.20 a). In contrast to the three by three particle lattice, no peak is observed at the lateral size of the lattice. The chain with maximum particle number contained five particles and though more particles were present, maximum particle number did not increase compared to the three by three lattice.
In order to link the initial inter-particle distance and the inter-particle angles to the group formation process, the lattice regularity was analyzed as for the three by three lattice, Fig. 5.20 b). Beginning with the magnetic field orientated along the x or y lattice direction, instead of chains with four particles smaller particle cluster form. Comparable to the fourteen-particles in a line

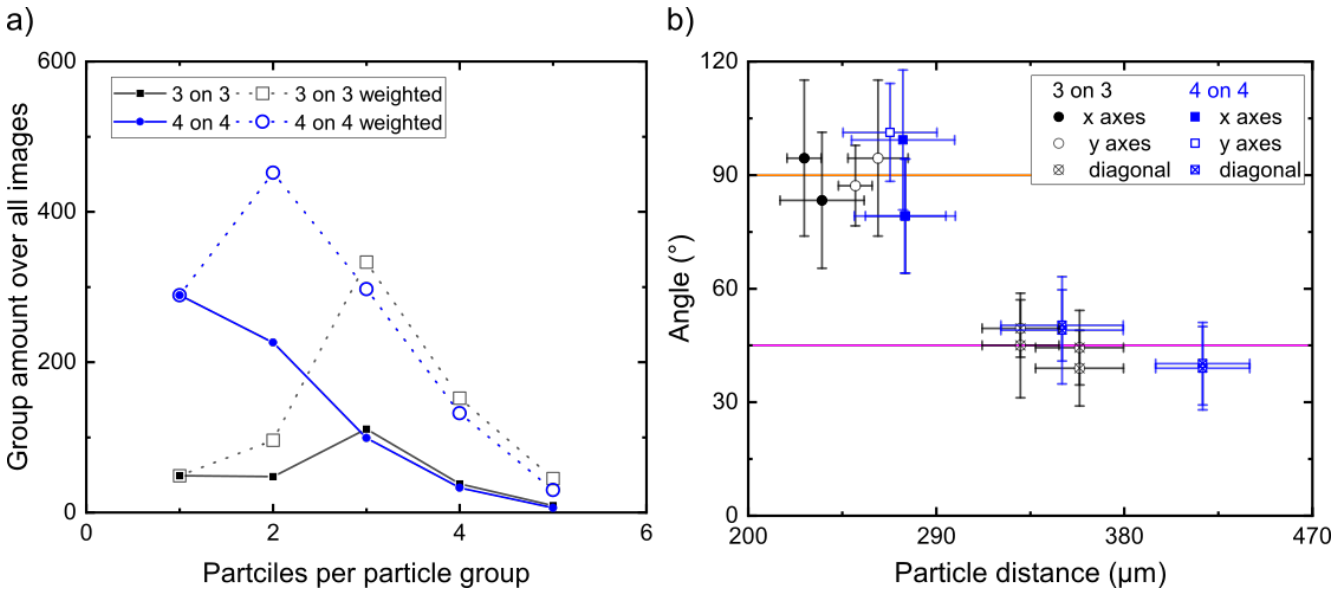

Figure 5.20: a) Particle number per group in relation to the number of groups with same particle number detected for all corresponding magnetic field orientations. In contrast to the three by three lattice the four by four lattice forms mostly particle groups of two particles. b) Mean initial inter-particle distances and angles of the three by three and four by four lattice. The four by four lattice shows larger initial distances.

configuration, section 5.2.3, a splitting into particle groups with one, two or three particles was observed. Considering the regularity of the lattice, Fig. 5.20 b), blue points, this can be directly linked to the large mean initial-inter particle distances in x and y direction. It is even larger than the mean initial inter-particle distance in y-direction of the three by three lattice. The mean initial inter-particle distance in x- and y-direction was roughly the same and scattered less than the mean initial inter-particle distance of the three by three lattice. Also the statistic of the group size was identical, i.e., for the x as well for the y direction same number of groups with particle number of one, two and three were identified. Considering the mean angles the lattice differs from a perfect square. The deviation from the $90°$ is larger than for the three by three lattice. Despite the angle entering the magnetic dipole-dipole force, this influence can be neglected compared to the impact of a variation in the inter-particle distance, which scales with inverse fourth power. Though, it locally might result in larger elastic restoring forces.

For field orientations along the diagonal direction, the highest particle number per chain was extracted as previous for the three by three particle lattice. This time the higher particle number was identified along the diagonal dia_1 with smaller mean initial inter-particle distance and higher angle between the diagonal and axes particles. Since for the three by three lattice quite the inverse dependence between chain size and mean initial inter-particle distance respectively angles along the diagonals was observed, local variations in the initial inter-particle distance, particle size and inter-particle angles need to be considered. These three parameters can be determining whether

the magnetic force is large enough to overcome the restoring elastic forces and thus, whether the particle chain is a state of minimal energy comparable to the two particles in contact (section 5.2.1 and [17]].

Five by Five particle lattice

Next, the system was expanded to a five by five lattice. Sample preparation and characterization was conducted identical to the three by three and four by four particle lattice. Analyzing the chain size no peak was observed for five particles per chain, but chains with up to eight particles were observed. If weighted with the particle number per group, groups containing two or three particles were mostly represented, Fig. 5.21 a). Starting the discussion with the magnetic field orientated along the axes, compared to the three by three particle lattice slightly larger mean initial inter-particle distance, Fig. 5.21 b) red points, caused the particles to disintegrate into small clusters. The more particles are involved in the group formation process the higher the generated restoring elastic force and the system becomes more and more sensitive to the mean initial inter-particle distance and local distance variances.
The mean initial distance along the lattice axes did not differ significantly, even though, the

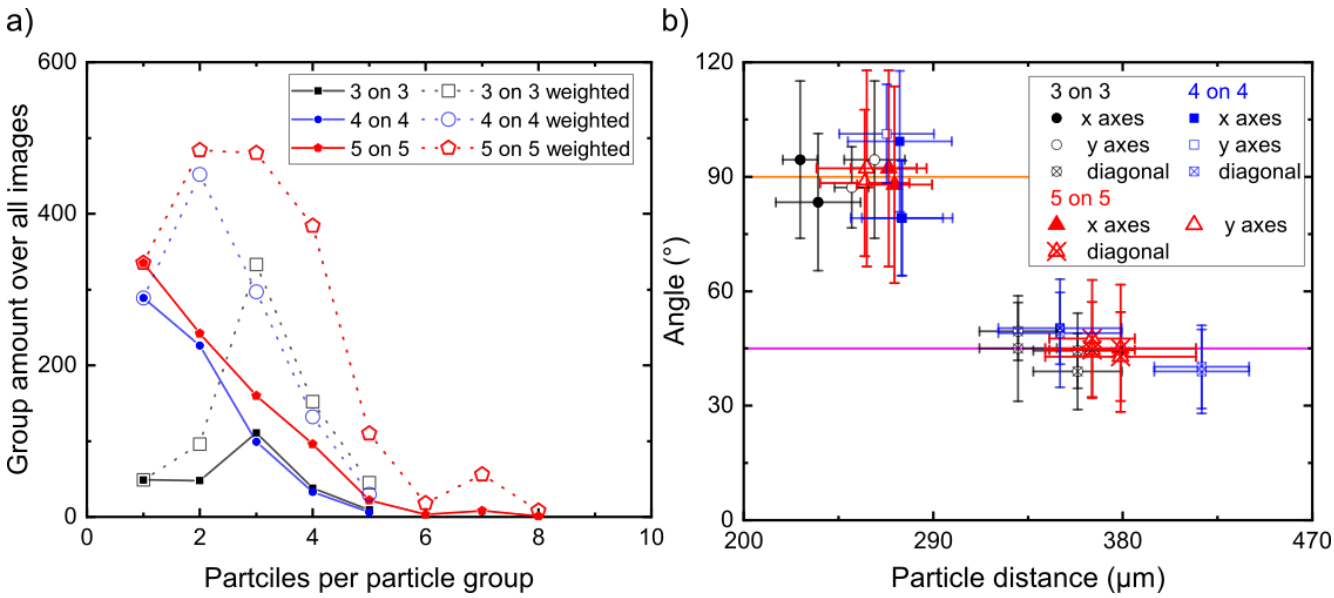

Figure 5.21: a) Particle number per group in relation to the amount of groups with same particle number detected for all corresponding magnetic field orientations. The five by five lattice forms mostly particle groups with two and three particles. A small peak shows that also particle groups of seven particles were formed. b) Comparison of the mean initial inter-particle distances and angles.

resulting group formation did. For the magnetic field orientated in the y-direction particle connection occurred only in this direction. Whereas for the magnetic field orientated in the x-direction particle connection also occurred in y-direction. This can only be explained by local fluctuations in the inter-particle distance and inter-particle angles. As the mutual magnetic forces are reduced on particle positioned at the edge of the lattice, they are more sensitive to local irregularities.
Additionally, for magnetic fields directed along the diagonals of the lattice, different particle formations were observed. This cannot be explained by variances in the mean initial distances or mean angles. Hence, local lattice imperfection (variances in angles and inter-particle distances) as nucleation factor for particle group formations need to be considered. As the magnetic field orientation was altered while the field was still applied not only the initial particle positions play a role, but also the magnetic history of the sample. Hence, the more particles a system contains the less significant the initial particle distances become and the more important the local magnetic and elastic fields, i.e. the magnetic history of the sample. Therefore, in the following the focus will be put on the particle group formation process in relation to lattice imperfections and magnetic history.

5.3.2 Lattice imperfections and magnetic history

For a lattice containing few particles such as the three by three lattice, the system formed particle chains expanding over the whole system. For lattices with larger particle number, such long chains are impeded by the multitude of long range elastic and magnetic forces acting on the particles. So whereas for the three by three particle lattice the mean initial inter-particle distance was still linkable to the particle group size, for systems containing more particles the influence of local imperfections and magnetic history increases.
In order to connect local imperfections, such as variances in the initial inter-particle distance, with the particle chain formation process, distances between nearest neighbor particles were calculated as in previous sections, Fig. 5.22 a). The solid lines mark the mean initial distance in x (red line), y (black line) and diagonal (blue line) lattice direction. The dashed lines in the same color indicate a deviation of 5% from the absolute mean value. All data points lying outside these dashed lines show a strong deviation in initial inter-particle distance and represent imperfections of the lattice. Particle pairs with an initial inter-particle distance smaller than the dashed lines were connected with a blue line and those with a larger initial inter-particle distance with a red line, Fig. 5.22 b). Both lattice imperfections can function as nucleation points for group formation processes as follows: Particles with smaller initial inter-particle distance generate in comparison to their surrounding particles higher magnetic forces, i.e. were more likely to overcome the elastic

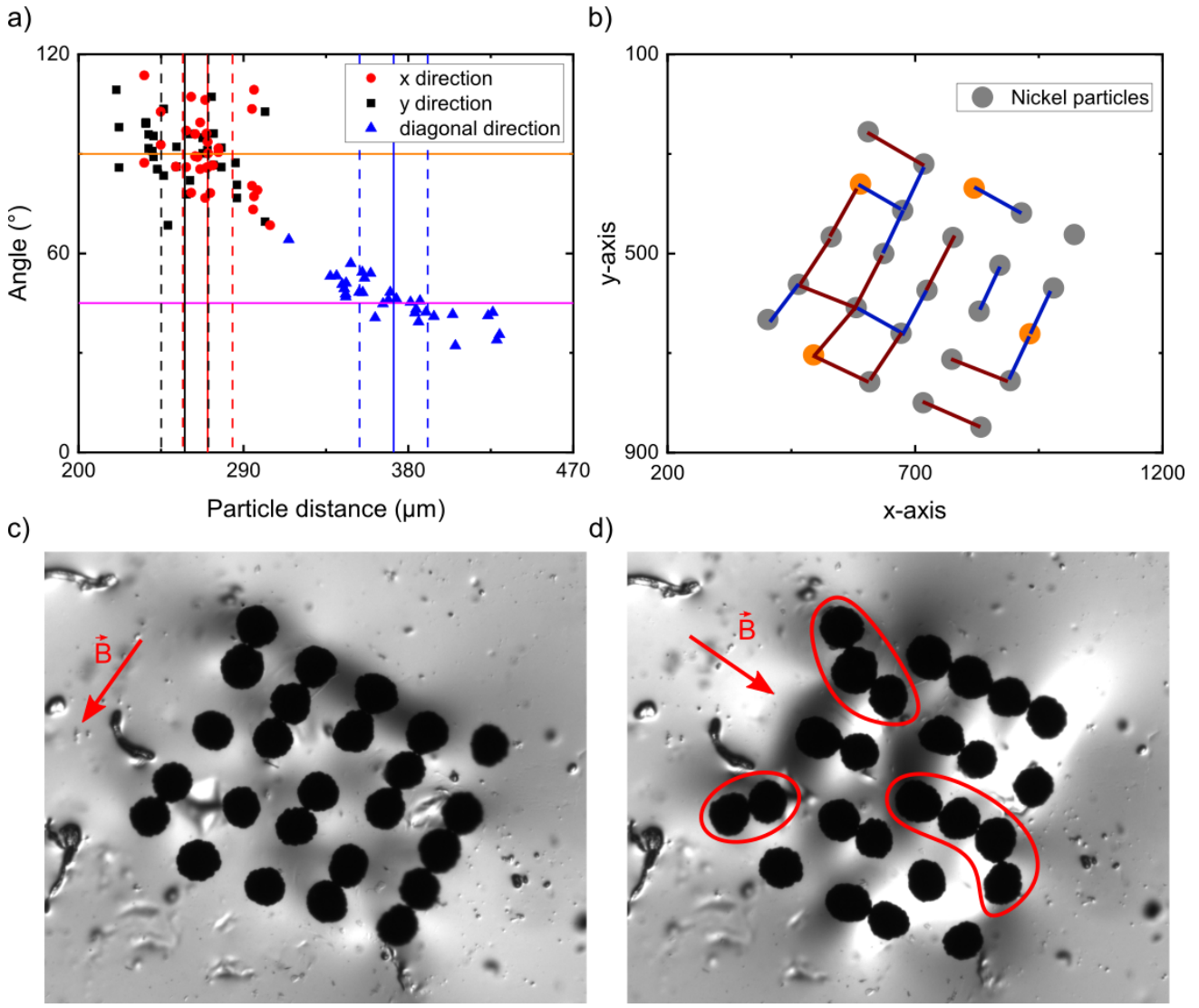

Figure 5.22: a) Initial inter-particle distances of all particle pairs in the five on five lattice. The solid lines mark the mean value and the dashed lines mark a 5% deviation from the absolute mean value. b) A five on five particle lattice. Particles that are comparably large are colored orange. Particle pairs that show an initial distance larger than 5% of the absolute mean value are connected with a red line and particle pairs that show an initial distance smaller than 5% of the absolute mean value are connected with a blue line. c) Real image of the five on five lattice depicted in b). The red arrow indicates the magnetic field orientation. Nickel particles are the black spots. d) Real image of the five on five lattice depicted in b). The red arrow indicates the magnetic field orientation. Nickel particles are the black spots. The red circled particle groups are connected at an angle to the magnetic field.

restoring forces. Particles with higher initial inter-particles distance generate weaker magnetic forces and thus, were more likely to get in contact with surrounding particles. Therefore, it is crucial to consider both kind of variances.

With the magnetic field aligned along the y edge of the lattice well separated particle groups of maximum four particles formed, Fig. 5.22 c). Comparing the lattice imperfections, Fig. 5.22 b),

with the particle group formation a good agreement was observed. All particle pairs exhibiting an initial inter-particle distance 5% or more above the average distance, marked with a red line in Fig. 5.22 b), stayed separated. All particle pairs exhibiting an initial inter-particle distance 5% or more below the average distance, marked with a blue line in Fig. 5.22 b), got into contact. Hence, the identification of variances (lattice imperfections) in the initial inter-particle distance provides a good understanding of the particle group formation for magnetic fields orientated along the edge of the lattice. For magnetic field orientated along the x edge of the lattice a similar group formation process was observed. Particle pairs with initial distance 5% or smaller as the absolute mean value were able to get into contact whereas particle pairs with initial distance 5% or larger as the absolute mean value stayed separated. For particle pairs that showed no strong deviation from the mean value a prediction was more difficult. In that case, the initial distance of the surrounding particles, particle size and angle between the particles decided whether particles collided or stayed separate. High aberrations of the angle from $90°$ in combination with a small initial distance in y direction could also be the explanation that particle groups formed at an angle to the applied field orientation, Fig. 5.22 d) red loops.
As the dark and bright areas in the images, Fig. 5.22 c) and d), indicate the matrix was strongly deformed by the particle displacements. Those displacements generate matrix mediated interactions. Hence, the particle's current positions need to be considered, i.e. the particle system is in kind of "preloaded state". The influence of the preloading becomes more significant for magnetic fields orientated at an angle to the lattice edges as the different particle axes take various orientations in relation to the magnetic field direction. Tiny alternations in the magnetic field orientation lead then to local changes in the ratio between elastic and magnetic force, i.e. particle groups separate and regroup. Depending on the current particle positions, i.e. the current deformation fields and magnetic forces, the regrouping can lead to particle groups with particle numbers exceeding the lattice edge length. Thus, it is also difficult to link parameters such as initial inter-particle or angles to the formation of those larger particle groups. These parameters are less significant and the magnetic history becomes more important. This is supported when comparing the particle groups for the same magnetic field orientation but different direction of rotation, Fig.5.23. Even so the magnetic field orientation is similar different group formations are visible, Fig. 5.23.

5.3.3 Statistic on particle group formation

In order to identify parameters that influence the group size of particles nine PDMS samples with a five by five particle lattice were prepared as in section 4.1.2. To keep the various possible influences at a manageable amount, the identical PDMS solution with a mixture of 12%, i.e. a

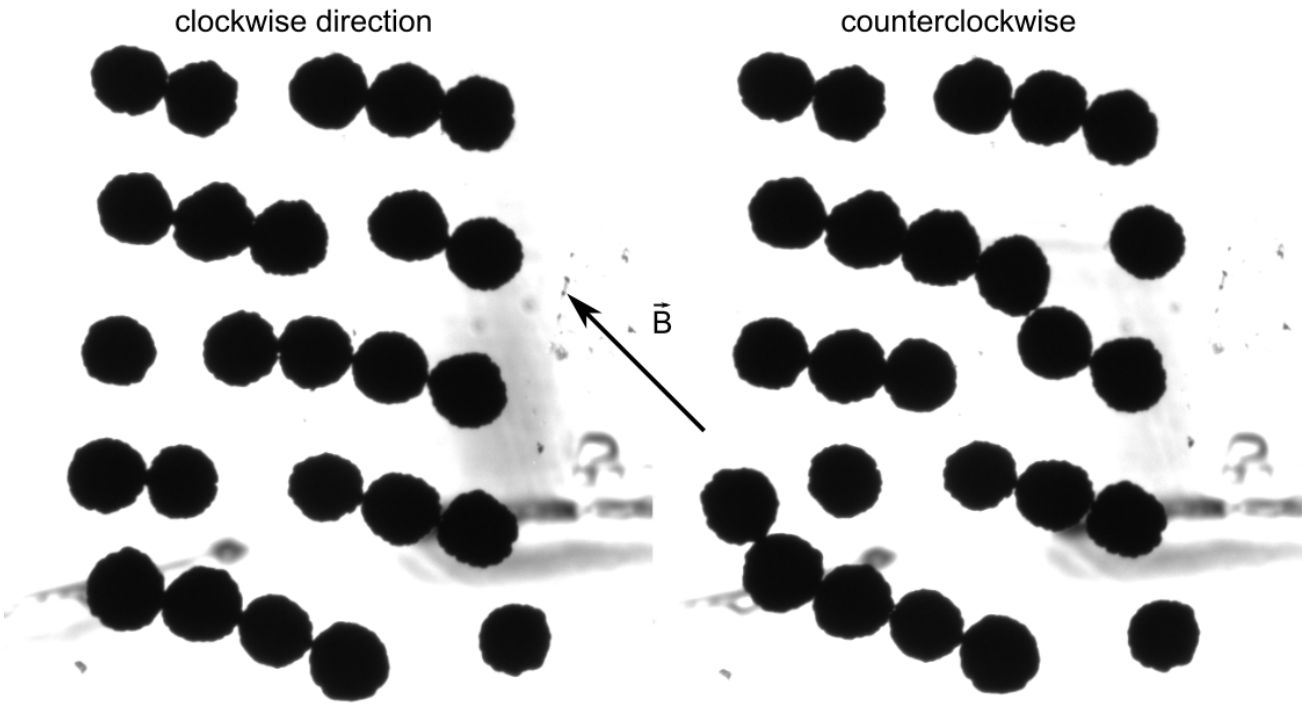

Figure 5.23: Image of the identical particle lattice. Ones the field was turned clockwise and ones counterclockwise. For the same magnetic field orientation, black arrow, different particle groups form.

Young's modulus of $(3.1 \pm 0.6)\, kPa$, was used for every sample. Slight variations in the sample dimension, i.e. in the sample thickness could not be excluded. The used sample preparation facilitated a particle positioning, regardless imperfections in the lattice could not be prevented. In the following the influence of local lattice imperfection on the particle group formation process is analyzed in more detail.

Samples were centered inside the Halbach-array and the Halbach-array rotated a full $360°$ cycle. Every $5°$ an image was taken. After detecting the particle position with TrackMate [165] the particle group size was determined, i.e it was evaluated if particles touch. In this way, the particle number per particle group was determined for every corresponding magnetic field orientation. Summing up the number of groups with n particles per group, it could be identified whether the lattice tends to form large particle groups (particle number $n \geq 4$) or not, Fig. 5.24. The group size was weighted with the number of particles per group. Three clear features could be distinguished, Fig. 5.24: Lattices 2, 6, 9 showed large particle groups while lattice 7 showed a shoulder at particle groups consisting of four and five particles and lattice number 4 did not form large groups at all. Lattice 6 showed the least scattering in the mean initial inter-particle distance and was taken as reference. In the following, lattices number 2, 4, 7 and 9 were compared with it. Starting the discussion with lattice 2, the angle and particle distances were determined as in

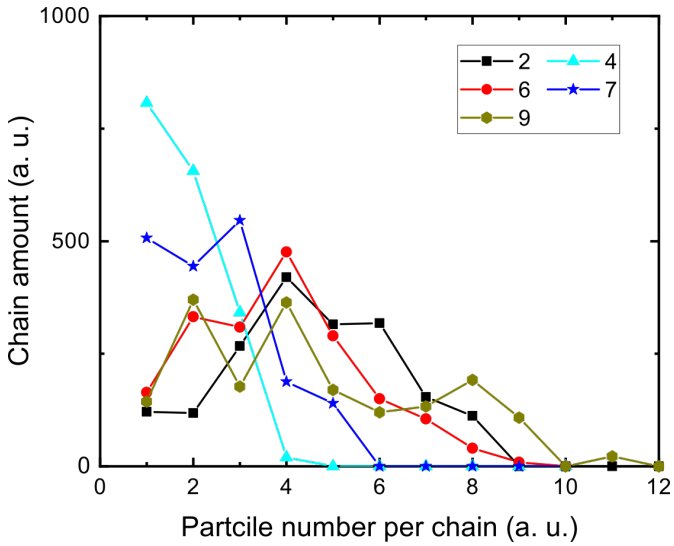

Figure 5.24: Amount of particle groups with the particle number of n for the five on five lattices 2, 4, 6, 7, 9. Lattice 2, 6, 9 show particle groups with particle number of more than five particle. Lattice 7 shows a small shoulder at particle groups of four and five particles. Lattice 4 did not form large particle groups.

section 5.3.1 by dividing the lattice in squares containing four particles. Thereafter, the mean value of the initial distance and its 5% tolerance was calculated. The mean value was marked with a solid line, a black line for the y- and a red line for the x-direction of the lattice and the 5% tolerance with a dashed line of same color, Fig. 5.25. Comparing it with lattice number 6 at first sight it is apparent that lattice number 2 had a smaller mean initial distance in x- [(271 ± 21) to $(283 \pm 17)\,\mu m$] as well as in y-direction [(243 ± 17) to $(281 \pm 21)\,\mu m$]. For fields directed along the lattice axes more particle were able to touch in lattice 2, especially in y-direction where the mean initial distance is much smaller. Overall the lattice 2 shows the tendency to form larger particle groups. This might be due to the smaller initial distance in lattice 2. Considering the lattice imperfections, lattice 6 was more regular as the scattering in the initial inter-particle distances was smaller in lattice 6 compared to lattice 2. Particle pairs with significantly smaller or larger initial distance than the mean value were less represented in lattice 6. Therefore, lesser nucleation points for group formation exist for lattice 6 and thus, even so the initial distances are larger compared to lattice 2 explain the similar group size of both lattices.
Continuing with lattice 4: In contrast to lattice number 6 no groups with particle number of more than five were formed and also the amount of groups with four and five particles was considerable lower than for lattice 6, Fig. 5.24. Considering the mean initial distance, only a small differences in y-direction of $10\,\mu$, which was below the typical scattering of this distance, and no significant difference in x-direction was observed, Fig. 5.26. Also the lattice imperfections were nearly identical. Counting the particle pairs that show a deviation more or less than 5% from the absolute

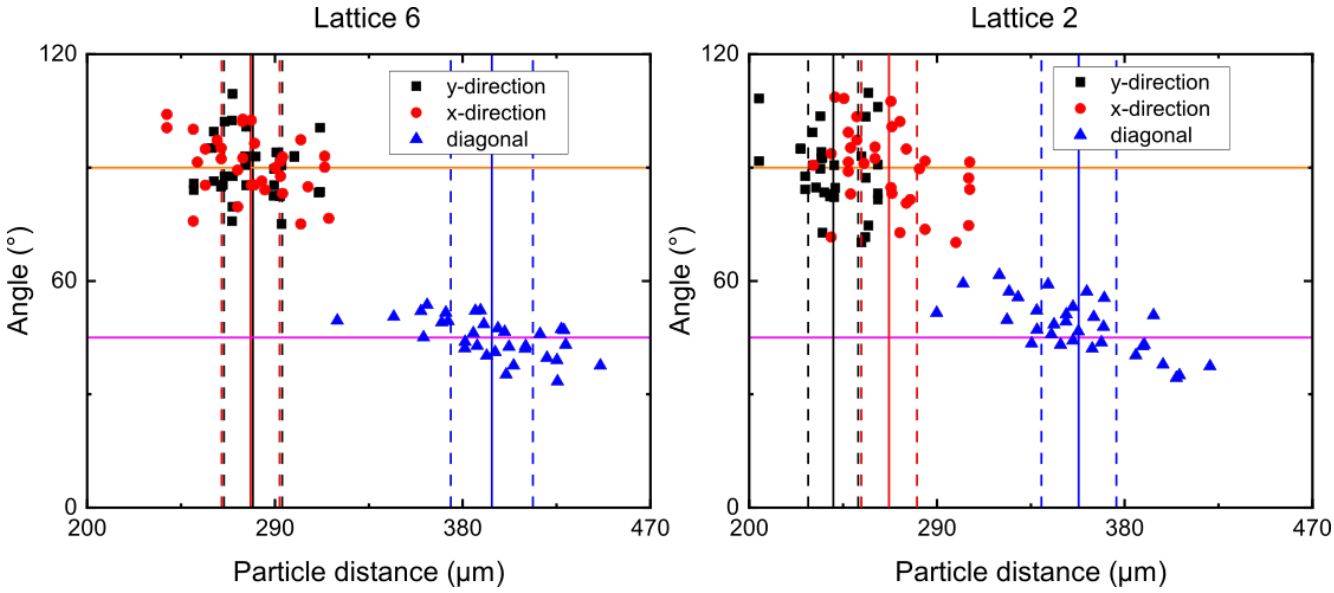

Figure 5.25: On the left side the mean initial inter-particle distances for each particle pair of the lattice 6 is shown. The solid line mark the mean values. The dashed lines mark a 5% deviation from the absolute mean value. On the right side the mean initial inter-particle distances for each particle pair of the lattice 2 is shown. The solid line mark the mean values. The dashed lines mark a 5% deviation from the absolute mean value.

mean value, no difference is obtained, i.e. both particles are similarly irregular. Hence, a closer look of the lattice imperfection and there position in relation to each other was done, Fig. 5.27 a)

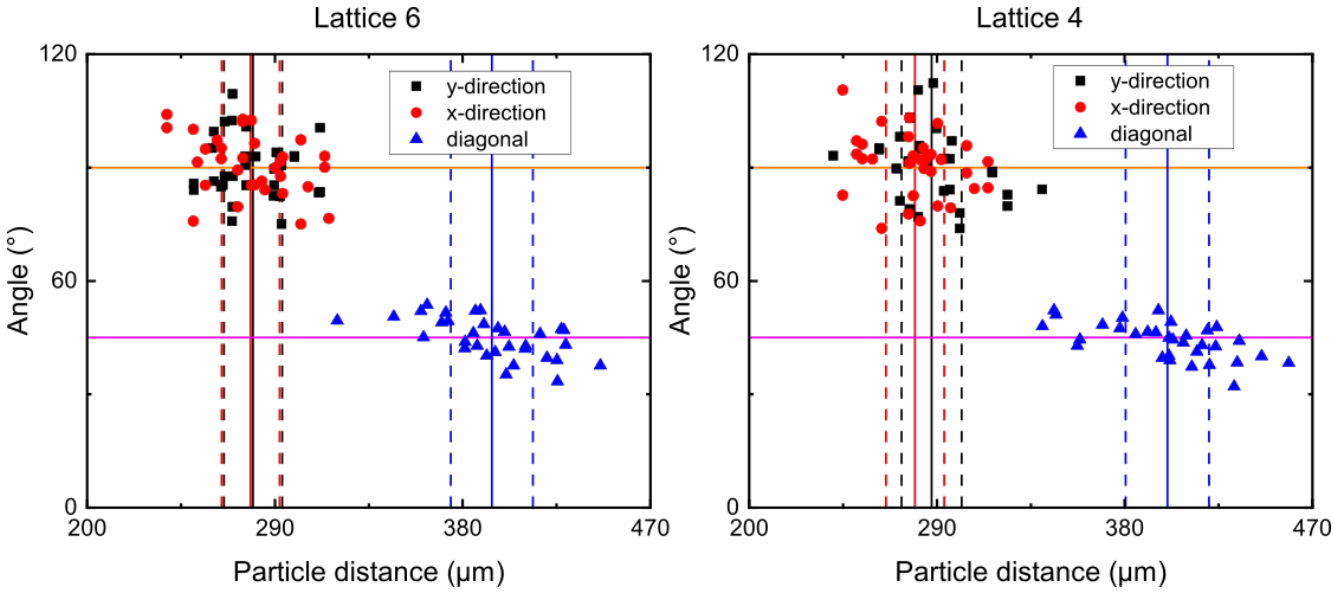

Figure 5.26: On the left side the mean initial inter-particle distances for each particle pair of the lattice 6 is shown. The solid line mark the mean values. The dashed lines mark a 5% deviation from the absolute mean value. On the right side the mean initial inter-particle distances for each particle pair of the lattice 4 is shown. The solid line mark the mean values. The dashed lines mark a 5% deviation from the absolute mean value.

and c). Initial distances that were 5% or more larger than the mean value were marked with a red connection line whereas shorter ones were marked with a blue connection line. In order to get a tendency, how those imperfections influence particle group formation, particle position without field, Fig. 5.27 a) and c), and particle position at the field direction, Fig. 5.27 b) and d) (the

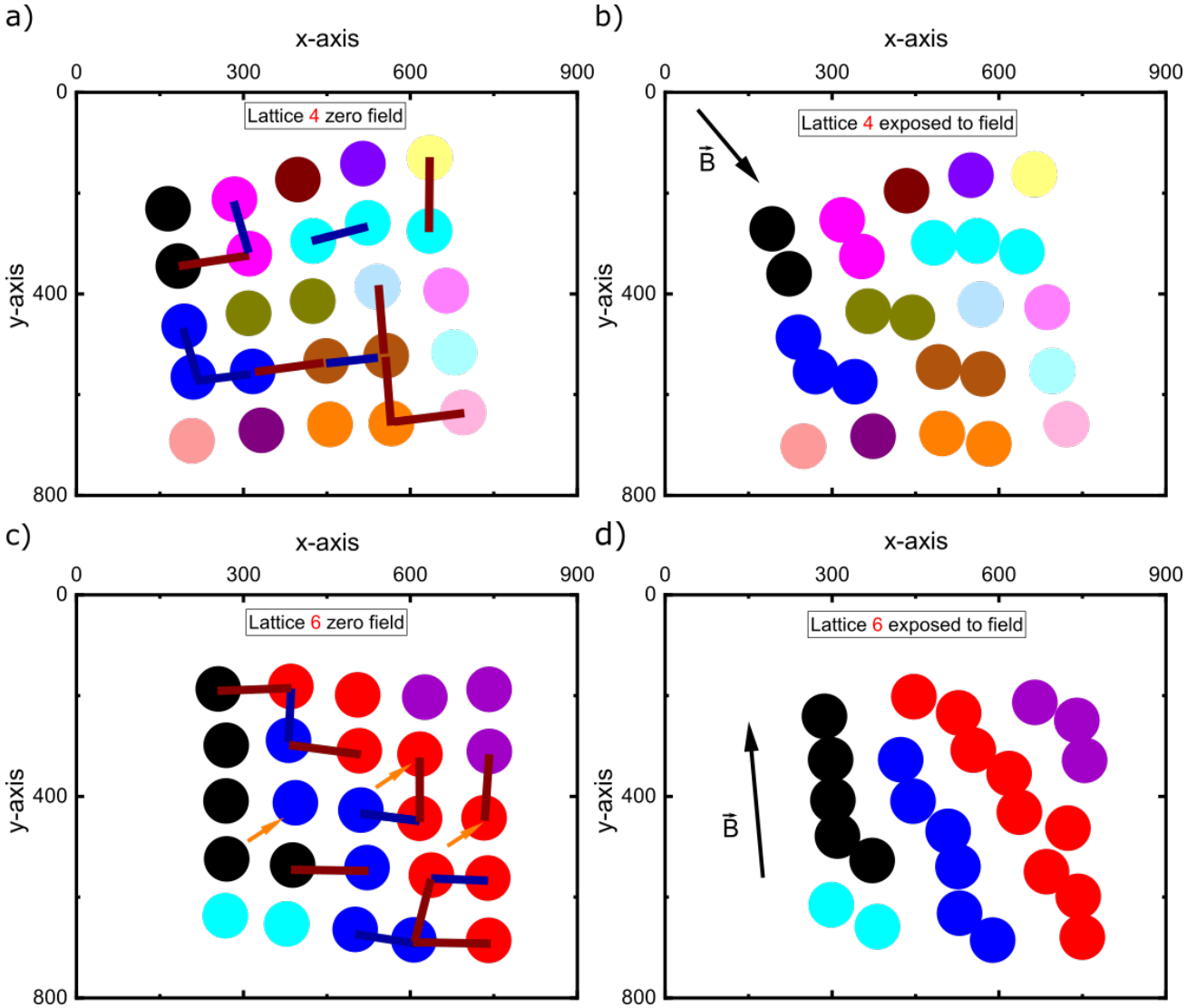

Figure 5.27: Particle positions of the lattice 4 and 6. a) The particle positions of lattice 4 at zero field. Red respectively blue lines mark particle pairs that show an initial value deviating of more or less than 5% from the absolute mean value. b) Lattice 4 subjected to a magnetic field. The field orientation is indicated by a black arrow. Particles that got into contact are marked with the same color. c) The particle positions of lattice 6 at zero field. Red respectively blue lines mark particle pairs that show an initial value deviating of more or less than 5% from the absolute mean value. Particles indicated with an orange arrow have a larger than average diameter. d) Lattice 6 subjected to a magnetic field. The field orientation is indicated by a black arrow. Particles that got into contact are marked with the same color.

magnetic field direction is indicated by the black arrows), for which largest group formation was

observed, were plotted. Particles that touch when the samples were subjected to the magnetic field were identically colored in the plot with zero field as well as for the plot with magnetic field. In the case of the lattice number 4, particles with 5% larger initial distance as the mean value stayed separated unlike particles with 5% smaller initial distance as the absolute mean value that were able to get into contact. A slight different situation was observed for lattice number 6. Here also particles with 5% larger initial distance as the absolute mean value were still able to get into contact. Additionally, more particle pairs that did not show a significant deviation to the mean initial distance got into contact. That particle pairs that showed an initial distance 5% larger as the mean value were able to get into contact can be explained with a larger particle size of some particles [marked with orange arrows in Fig. 5.27 c)]. The particles marked had a larger diameter of roughly $20\,\mu m$ and therefore stronger magnetic interaction with their surrounding particles. Even so particle diameter was in average $175\,\mu m$ for lattice 4 and $179\,\mu m$ for lattice 6, i.e. quite similar for both lattices. Comparing the image before and after a $360°$ rotation cycle of the magnetic field another aspect that accounts for the larger particles groups formed by the lattice 6 was observed. In the lattice 6 particles changed their initial position either by a rotation around their center and by being displaced in the particle plane. Hence, particles of lattice 6 had a higher mobility than particles of lattice 4 and thus, formed larger particle groups. The multitude of particle regrouping damage the matrix of sample 6 irreversible.

Proceeding with lattice number 7: The number of groups with more than three particles was less than for lattice 6, Fig. 5.24. Nevertheless, groups of four and five particles formed resulting in a small shoulder shape at the right side of the plot in Fig. 5.24 blue line. Analyzing the scattering plot of the initial particle distances and angles a strong irregularity between x- and y-direction was observed, Fig. 5.28. In x-direction a mean initial distance was determined with $(251 \pm 20)\,\mu m$ whereas in y-direction it was $(302 \pm 22)\,\mu m$. So while, compared to lattice number 6, the particles in x-direction lie in closer approximation in y-direction they were positioned further apart. This explains why unlike for a field orientated along the y-direction in x-direction particles were able to touch and the group number with four and five particles was increased in contrast to lattice 4. Similar to lattice 4 the lattice imperfections determine mostly which particles were able to get into contact and which not. Comparing the image before and after a $360°$ rotation cycle of the magnetic field lattice 7 showed no particle position changes, i.e. no matrix damages. This explains that unlike lattice 6 no particle groups were formed exceeding the particle number of five.

Concluding with a comparison to lattice 9: Lattice 9 showed out of all lattice the highest number and largest particle groups. An determination of the mean initial particle distance for lattice 9 provided values of $(286 \pm 15)\,\mu m$ in y direction and $(315 \pm 30)\,\mu m$ in x direction. So in both

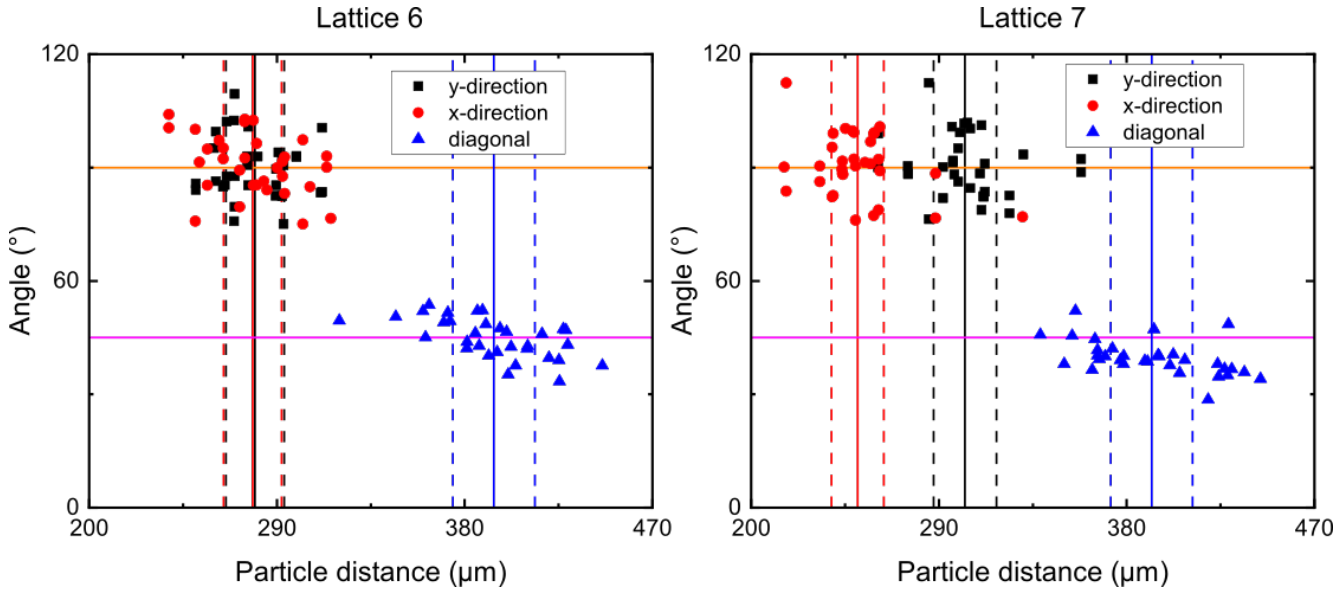

Figure 5.28: On the left side the mean initial inter-particle distances for each particle pair of the lattice 6 is shown. The solid line mark the mean values. The dashed lines mark a 5% deviation from the absolute mean value. On the right side the mean initial inter-particle distances for each particle pair of the lattice 7 is shown. The solid line mark the mean values. The dashed lines mark a 5% deviation from the absolute mean value.

direction larger initial distances than lattice 6,Fig. 5.29. Additionally the discrepancy between x- and y-direction was greater. So both factors that might facilitate particle group formation did indicate that lattice 9 should form only small particle groups. An explanation was identified by looking at the lattice before and after a full loading magnetic field cycle of $360°$. In case of lattice 9 nearly every particle changed its original position. The particle displacement largely damaged the surrounding matrix leading to a larger particle mobility and hence particle groups with a high number of particles formed. Such changes in the particle positions was also observed for lattices embedded in a bulk sample, i.e. the difference in layer thickness was not the cause for higher particle mobility and/or the large matrix damages. It is more likely that the multitude of regrouping when particles form large particle groups destroys locally the PDMS matrix. Why some lattices showed matrix damage while others stayed completely intact might depend on the particle size, shape and surface roughness.

To sum the section up: Three distinctive particle group formation processes occurred in five by five particle lattices. First one was that only small groups with particle amount smaller than five particles formed (lattice number 4). Second scenario was, that also groups with a higher number of particles formed especially with particle number of the size of the lattice edge length (lattice number 7). Last formation process distinguished through particle groups with particle numbers higher than the lattice edge length (lattice 2, 6 , 9). Since the elastic modulus of the PDMS matrix was identical throughout the samples the interplay of two factors mainly dominated

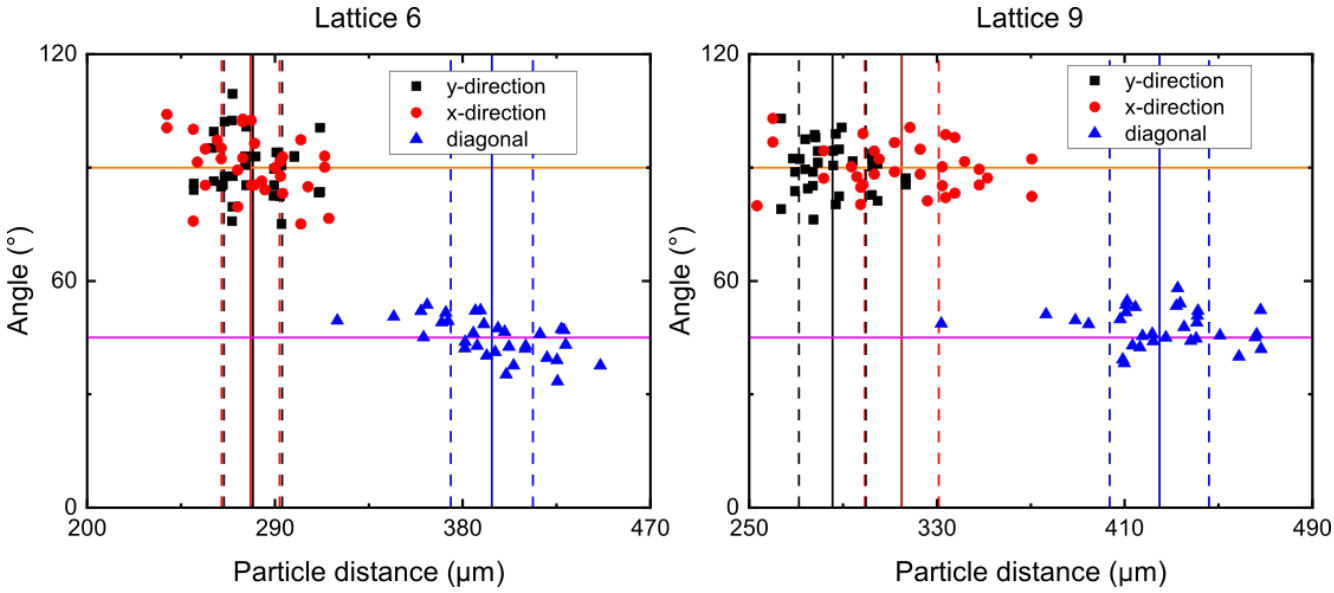

Figure 5.29: On the left side the mean initial inter-particle distances for each particle pair of the lattice 6 is shown. The solid line mark the mean values. The dashed lines mark a 5% deviation from the absolute mean value. On the right side the mean initial inter-particle distances for each particle pair of the lattice 9 is shown. The solid line mark the mean values. The dashed lines mark a 5% deviation from the absolute mean value.

the formation tendency: The initial particle distance and lattice imperfections such as strong variances in the initial inter-particle distance. The mean initial distance in the x or y direction was determining the group formation for fields orientated along the lattice edges. For small enough initial distances groups of five particles formed along the lattice edge direction and produced a shoulder like shape in the plot of the group amount, Fig. 5.24. Lattice imperfection provided for all lattices an indication which particle pairs stay separated or got into contact. Nevertheless, the imperfections could not explain the group formation of large particle groups. This was explained by an increased particle mobility and matrix destruction. A irreversible particle movement, i.e. matrix destruction was also reported by Gundermann *et al.* [61], for iron particles (average diameter $35\,\mu m$) randomly distributed in a PDMS matrix, after $4\,s$ respectively $6.5\,s$ exposure to a field of $270\,mT$. The higher mobility and matrix damage was identified by comparing images before and after the rotation of the Halbach-array. Samples that showed large particle groups also showed a change of the particle positions after the rotation of the magnetic field.

5.3.4 Field induced changes in the lattice area

In the previous section the tendency of particle lattices to form particle groups and the driving factors were analyzed. This section aims to connect the mean number of particles per chain to

the area particles inhabit. The particle area will not be directly connected to the quantity of macroscopic deformations of the PDMS matrix, but indicates if the matrix was compressed or elongated. Hence, a trend of the matrix´s magnetostriction can be implied. The lattices number 2, 4, 6, 7, 9 were taken and were analyzed as follows.
From the obtained particle positions, the edge particles were identified. Marking those in the real image and comparing it with the tracked particle positions provides a good agreement Fig. 5.30 a) and b). Afterward the enclosed polygon area, marked with the yellow line in Fig. 5.30 a) and b), was calculated. Therefore the areas underneath every edge particle with its adjacent edge particles were determined and added up:

$$A = \sum_{i=0}^{n-1} A_{i,i+1} \tag{5.1}$$

with

$$A_{i,i+1} = \frac{(x_i - x_{i+1})(y_i + y_{i+1})}{2} \tag{5.2}$$

Hereby, n denotes the number of edge particles, x and y the particle coordinates and $A_{i,i+1}$ the trapeze area between the x axis and two adjacent edge particles. A is the final polygon area the edge particles encircle, Fig. 5.30. In order to connect the area to the number of particles

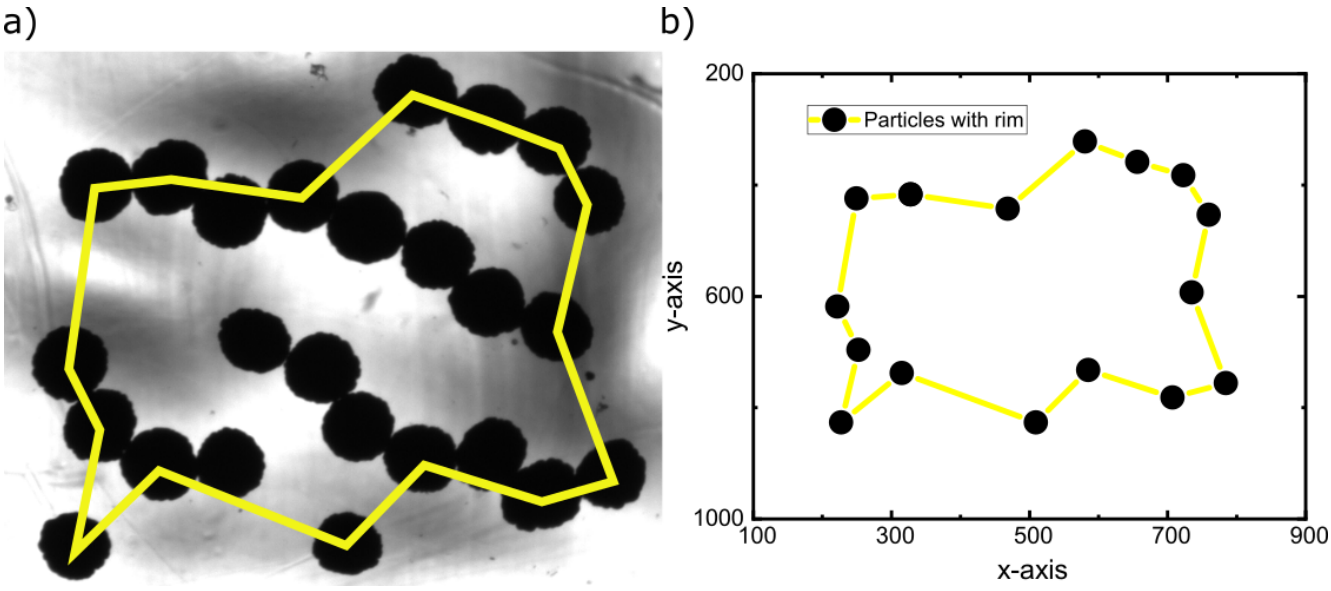

Figure 5.30: a) Real image of the particle lattice. The particle lattices was subjected to a magnetic field. With the yellow line the edge particles are connected and the enclosed polygon area is calculated. b) Tracked particle position of the edge particles of the lattice in a). The yellow line connects the edge particles and the enclosed polygon area is calculated.

per group, the mean particle number of the particle groups for the corresponding magnetic field orientations was calculated:

$$\bar{x}_{mea} = \frac{25}{\sum_n^{25} i_n} \tag{5.3}$$

Herein, n denotes the particle number per chain and i the incidence of the particle group with n particles was detected. To determine whether any correlation between average particle group size and the encircled area exists, both trends were plotted for the five selected lattices, Fig. 5.31. Thereby, the area was normalized to the area at zero field, i.e. gives the area in percent of the zero field area.

Apparently, all lattices decrease their area in comparison to the zero field case, Fig. 5.31 blue curves. The matrix seems to be always compressed by applying a magnetic field. Due to the in-compressibility of the matrix the compression in the particle plane leads to an expansion in the perpendicular direction. Furthermore, area variations of up to 10% were created by the rotation of the external field. A strong dependency on the mean particle number per particle group was observed. This was validated by comparing the area, Fig. 5.31 blue curves, with the mean particle number per group, Fig. 5.31 black curves. The more particles in average were connected the smaller the area the particles enclose. As a result, the lattice number 4, Fig. 5.31 b), with smallest average particle amount per chain showed also the smallest change in the area for the application of the field, $\approx$ 10% variation, as well as for the rotation of the field, $\approx$ 4% variation. The lattices 6 and 7, Fig. 5.31 c) and d), decreased their area in relation to the zero field case more significantly. A rotation of the field induced particle group formation and led to area variations of $\approx$ 6% which was not significantly higher than for the lattice 4. For lattice 2, Fig. 5.31 a), at least 8% were reached. For lattice 9 a clear matrix damage is visible as the lattice area continuously decreases, i.e. the mean particle number continuously increases over the magnetic field rotation cycle. In contrast, lattices that exhibit no matrix damage (lattice 4 and 7) are symmetrical around $180°$ regarding the magnetic field orientation.

All particle lattices showed a tendency to compression the matrix when subjected to the external magnetic field. This was indicated by the decreased area the edge particles enclose, Fig. 5.31 blue curves. Especially if the lattice tends to form large particle groups, the orientation in which the magnetic field was applied played a significant role as the area particles enclose was directly related to the geometric mean group size: The more particles were in average connected, the smaller the area the rim particles enclosed. Except for lattice 9, which showed significant matrix destruction, all curves were quite symmetric around $180°$ magnetic field orientation. The incompressibility of the matrix implies that the compression of the matrix in the particle plane leads to an expansion of the matrix perpendicular to the particle plane.

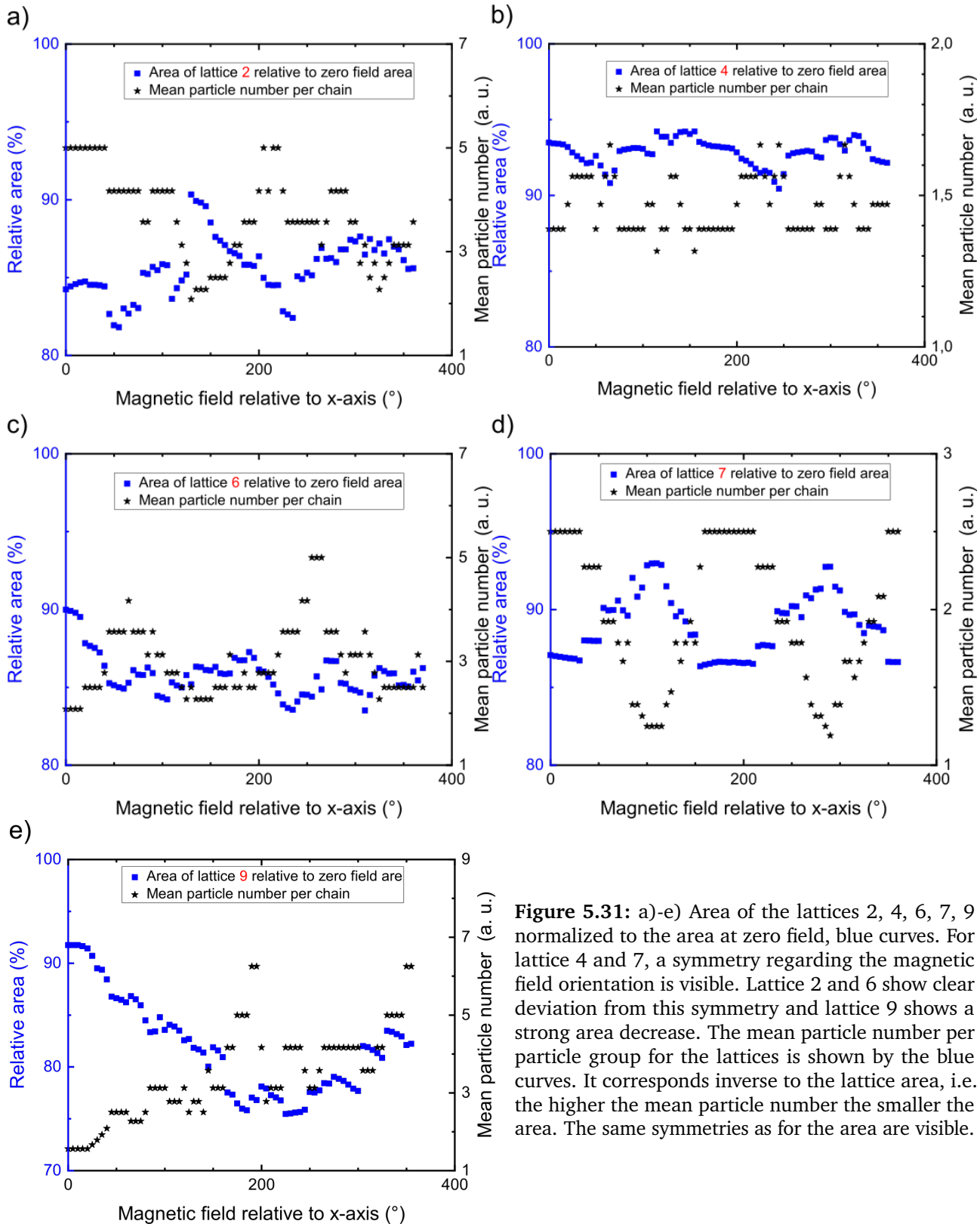

Figure 5.31: a)-e) Area of the lattices 2, 4, 6, 7, 9 normalized to the area at zero field, blue curves. For lattice 4 and 7, a symmetry regarding the magnetic field orientation is visible. Lattice 2 and 6 show clear deviation from this symmetry and lattice 9 shows a strong area decrease. The mean particle number per particle group for the lattices is shown by the blue curves. It corresponds inverse to the lattice area, i.e. the higher the mean particle number the smaller the area. The same symmetries as for the area are visible.

5.4 Strategies to prepare larger lattices

In the previous chapter deformations of a five by five particle lattice were investigated. To be able to study larger particle arrangements particle alignment was performed. This also safes time and simplifies the particle positioning compared to 5.3. Additionally the influence of particle size distribution should be eliminated. Thus spherical polystyrene-ironoxide-particles with diameter of $(4.69 \pm 0.20)\,\mu m$ (Microparticles GmbH, PS-MAG-RhB-S2538) were purchased.

5.4.1 Particle alignment

Two main alignment procedures were carried out. One used convective/capillary forces while the other used magnetic forces in order to align the particles in the designated structures. Structures were produced either by creating an imprint from a photolitographic structured SU8 surface or a structured silicon wafer. Therefore, Sylgard® 184 was poured over the structured surfaces. After the Sylgard® 184 is crosslinked it can be pulled of and has imprinted the negative structure of the SU8 or silicon wafer. This process is known as "replicated from a master".
The first alignment process used convective/capillary forced to align the particles. This process was performed in collaboration with Patrick Probst and carried out at the Leibniz institute in Dresden. Detailed information on the experimental setup can be found in [63] (and its supporting information: Template-assisted colloidal self-assembly). Here, only the essential steps for the particle alignment are mentioned. Prior to the alignment procedure particles were washed to eliminate any stabilizing surfactants and as the contact angle plays an important role the wettability of the PDMS substrate was increased by plasma activation with a plasma cleaner for two minutes. Afterwards, a water droplet containing 5 vol% fluorescent labeled, spherical polystyrene-ironoxide-particles with a diameter of $(4.69 \pm 0.20)\,\mu m$ (Microparticles GmbH, PS-MAG-RhB-S2538) was positioned on the structured substrate. Subsequently, the droplet was clamped between the substrate and a parallel aligned glass slide by decreasing the gap size between them (gap≈500 μm). The substrate was then moved laterally with a velocity of typically $1\,mm/s$ and the droplet was dragged over the surface. By adapting the gap size in combination with the moving speed of the substrate, forces such as capillary can be adapted in a way that particles aligned in the structures 5.32 a). For a detailed analysis of the forces acting during the alignment procedure and how they are affected by parameters like the gap size the reader is referred to [108, 124].
The second process exploited the magnetism of the particles. A permanent magnet was attached to the bottom of the structured substrate. Particles were not washed and a 5 μl droplet from the

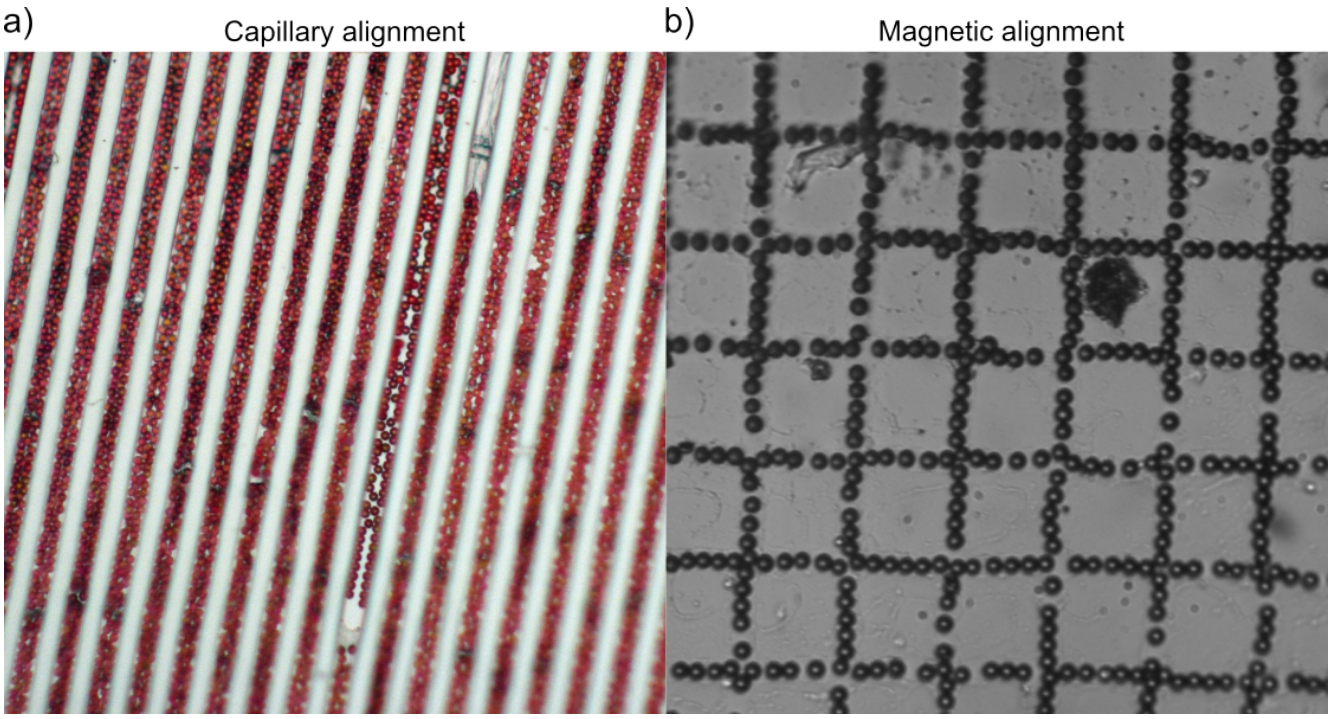

Figure 5.32: a) particle alignment with convective/capillary forces. Exemplary the particle alignment in 10 μm broad lines is depicted. The fluorescent labeled particles are red. b) particle alignment with magnetic force. The particles were aligned in squares with line thickness of 5 μm. Image was taken with a 20$\times$ Mitutoyo objective mounted on the mvBlueCOUGAR-S camera from Matrix Vision GmbH while the sample was illuminated from below.

particle solution purchased from Microparticles GmbH was deposit on the substrate. The droplet was moved with a glass slide by pulling it manually over the substrate at an angle of $\approx 45°$ to the substrate. Continuing this procedure until the droplet was dried resulted in nearly perfect particle selectivity inside the structures 5.32 b). Due to the simplicity and higher efficiency of this second method it was preferred over the first one to align the magnetic particles.

5.4.2 Transfer process

After the possibility to align the particles in every structure that was available, the obtained arrangements needed to be transferred to the actual PDMS matrix material. Therefore a layer of PDMS with mixing ratio of 6 wt% was cast over the structured template. After crosslinking a lift off process was started by pulling the cross-linked PDMS layer of the template. Though, due to mechanically instability the PDMS layer ruptured during the lift of process. Adapting the matrix mechanical stability and making it more stable by increasing the Young's modulus lead to the point that the lift of process was successfull. The matrix stiffening was accompanied by suppression of particle movement as the magnetic forces acting on the particles were to small to

overcome the elastic forces.
To further facilitate the lift-off process a sacrificial layer was used. This sacrifical layer could be dissolved after the PDMS was crosslinked on top. To this end, master structure was replicated in PVA by pouring a PVA solution on top of the silicon wafer or SU8. The PVA solution consisted of 10 wt% polyvinylalkohol (PVA, 113000 MW, 90% hydrolysation) solved in water at $80° C$ (compare section 4.1.2). After 24 hours at room temperature the PVA solution solidified and was peeled off, leading to the negative structure imprinted. Afterwards, particle alignment was carried out with the previous introduce magnetic alignment process 5.4.1. A nearly perfect selectivity was observed (see Fig 5.32 b)). The next step included the casting of a layer of PDMS with mixing ratio of 6 wt% on top. After waiting until the PDMS was sufficiently crosslinked at $60° C$ for 24 hours the PVA template was solved in a 80° C water bath. But either the forces crated during the desolving or the subsequent drying (water evaporation) destroyed the PDMS again. Even using BREAK-THRU® S 240 (EVONIK) a non-ionic surfactant to reduces the water surface tension significantly and consequently decreases the capillary forces during the drying process did not improve the result. One alternative available would be to use stronger magnetic particles. This would lead to the possibility to use stiffer matrices and thus circumvent described matrix destruction.

6 Macroscopic deformable MREs

The particle displacement of the previously measured samples with defined particle positions was generated by magnetic particle interaction. So far, the particle amount was quite small due to the micro-structuring process. Nevertheless, the bottom up sample preparation by stacking PDMS layers consecutively, allows preparing larger samples with defined particle and particle free areas, i.e. a magnetic texture. To this end, 3D PDMS spheres were created and coated with magnetic nickel particles. Magnetic membranes containing a mono layer of dense packed magnetic nickel particles were also produced. In the following both system are analyzed in relation to their capabilities.

6.1 Magnetically coated PDMS spheres

Previous research on PDMS spheres investigated for example their surface buckling or wrinkling [27, 78, 101, 175, 180]. Investigated magneto-active spheres consisted of polymer spheres filled with a certain amount of magnetic filler particles [51, 52, 57, 140, 141, 184]. In the following, the production process described in 4.1.3 was used to create novel "magnetically hollow" spheres. This reduces the number of magnetic particles aiming to facilitate a theoretical description as the magnetic structure is reduced to a monolayer of magnetic particles. The Young's modulus and the size of the spheres could be easily adapted. In order to identify if the spheres can be used to build heterogeneous, large magneto-active materials or function themselves as actuator, the deformation of the spheres under the influence of a stepwise rotated magnetic field was investigated while the spheres were enclosed by different materials such as PDMS or water.
PDMS spheres were produced as described in chapter 4.1.3. Their size was between a couple hundred micrometers to a few millimeters in diameter. The spheres were coated with nickel particles with a diameter between $125\,\mu m$ and $160\,\mu m$. The PDMS solution had a mixing ratio of 14% which corresponds to a Young's modulus of $(4.1 \pm 0.8)\,kPa$ extracted from the power law fit in Fig. 4.13. After the crosslinked PDMS spheres were coated with the magnetic mono layer, they were included in a two layer bulk matrix. Therefore, a glass vial with diameter of $0.9\,cm$ was filled with $800\,\mu l$ of a 14% PDMS solution and after the first layer was mechanically stable enough the PDMS sphere was positioned on top. Yet another PDMS layer with identical mixing ratio and a volume of $1600\,\mu l$ ensured that the sphere was fully encapsulated. Curing for 24 hours under

$60° C$ provides a stable Young's modulus throughout the measurement.
In order to resolve the particle movement under the influence of a magnetic field x-ray tomographic measurements were performed [130,152–155,168,173]. The tomographic measurements were done by Malte Schümann in Dresden (Chair of Magnetofluiddynamics, Measurement and Automation Technology, Dresden). To this end, the samples were centered in the tomographic setup [155]. First an image was taken without external magnetic field Fig. 6.1 a). This allowed to determine the initial particle positions. Apparently, the sphere did not possess a perfect mono layer of magnetic particles. During the casting of the second PDMS layer some magnetic particles had been removed from the surface of the sphere and the sphere had been subjected to the magnetic field of the Halbach-array, prior to the x-ray tomographic measurement. Otherwise the magnetic layer was densely packed.
In the next step the encapsulated sphere was subjected to a $250\,mT$ magnetic field which was orientated along the z axis, Fig. 6.1 b). The spherical caps orthogonal to the magnetic field direction are the sphere's poles, while the spherical surface directed along the magnetic field orientation is defined as the sphere's equator, Fig. 6.1 b). The tomographic image revealed a deformation of the sphere along the orientation of the magnetic field. A particle detachment at the poles seems to have taken place. Comparing the image with and without magnetic field the deformation is better visible Fig. 6.1 c). In x-direction the sphere decreased its diameter from ≈ 821 to 805 pixels which was roughly a relative decrease of $\approx 2\%$ compared to the original length. In contrast the diameter in z direction increased from ≈ 819 to 861 pixels and corresponded with a increase

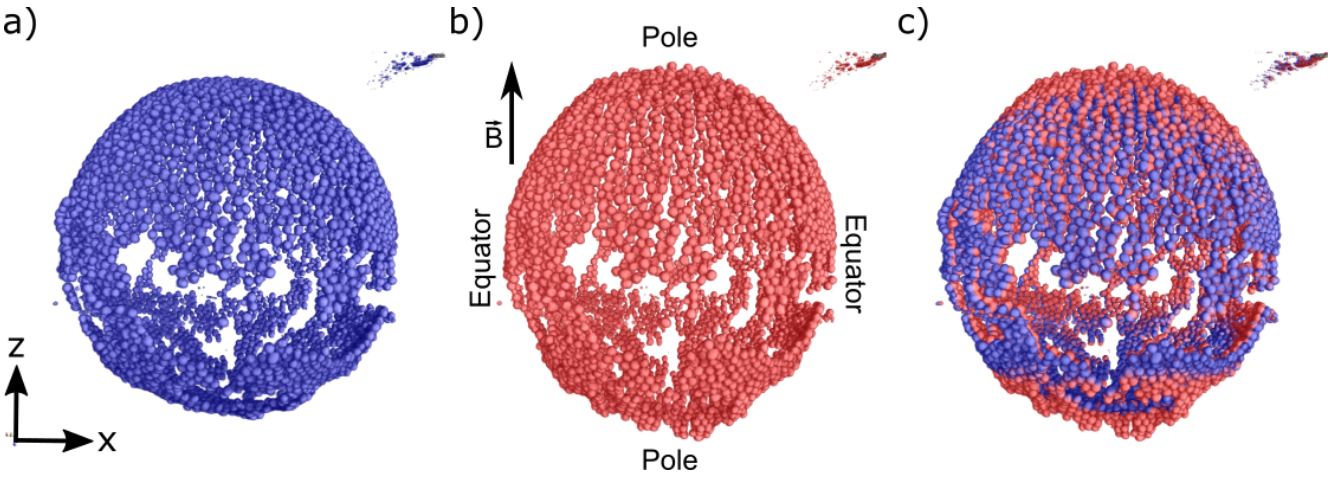

Figure 6.1: Tomographic images of a PDMS sphere coated with magnetic nickel particles. The PDMS sphere was embedded in a PDMS matrix of same mixing ratio. a) The particle position at zero field (blue dots). Apart from small areas the particles form a dense mono layer. b) A magnetic field was applied in z-direction. The particle position is depicted (red dots). A particle detachment at the sphere poles is visible. c) Comparison of the sphere with (red) and without field (blue). An elongation in z-direction is visible.

in length of $\approx 5\%$ compared to the original length. As the PDMS matrix is incompressible the volume should remain unchanged. Calculating the spheroid volume for zero field and magnetic field a good agreement was observed. The deviation was only about 1% and thus the changes in the diameters are considered valid.
Although the particles were not tracked themselves, they clearly formed chains along the z-direction. Distinguishing between the sphere's equator and poles, particles at the poles showed relative strong particle displacement along the x- and y- direction while particles at the equator formed chains along the magnetic field direction. This chain formation might contribute to the elongation of the sphere in the direction of the applied magnetic field. In order to determine the sphere's elongation and corresponding particle displacement (microscopic view) that can be induced by the magnetic deformation effect [140, 141, 161, 182, 183], i.e. the deformation a homogenous magnetic spherical shell experiences in an uniform magnetic field, the sphere was measured at various magnetic field orientations and environments.
Above, the deformation of the sphere could be linked to a particle movement due to the magnetic field applied. Tomographic imaging is relatively time consuming compared to measurements with a Halbach-array. For improved efficiency the deformation behaviour at different magnetic field orientations therefore was run with a Halbach-array. To get an idea how those deformation proceed with varying magnetic field orientations yet another PDMS sphere with mixing ratio of 12.5 % $(3.3 \pm 0.6)\, kPa$ was embedded in a PDMS matrix of identical mixing ratio (similar to Fig. 6.2 a)) and placed in the center of the Halbach-array. Thus, the sphere was subjected to a magnetic flux density of $\approx 172\, mT$. In contrast to the X-ray tomographic measurement not the single particles were resolved. Instead, the sphere was illuminated from below and images taken from above (compare chapter 4.3). Thus, only the whole sphere was depicted as dark circle on bright background, Fig. 6.2 b).
The diameter of the sphere in the x and y direction was detected as follows: The images were loaded in ImageJ and converted to black and white images. Subsequently a line profile was drawn in x-respectively y-direction. Along the line profile the brightness values of the pixels can be extracted. As the images are black and white pixel can only attain values of 0 or 255. A sudden change from dark to bright, i.e., change from 255 to 0 marked the edges of the sphere. Subtracting the x- respectively y- coordinates of the two pixels with value 255 before the value changes to 0, results in the x- respectively y-diameter.
In order to get the initial sphere diameter, prior to the magnetic measurement, a picture from the sphere at zero field was taken. In the following, all elongation in relation to the initial sphere diameter are specified as ε_i^x in x and ε_i^y in y direction and the ratio between minimum and maximum diameter are specified as ε_r^x and ε_r^y, respectively. Fifty full loading cycles, i.e. fifty $360°$

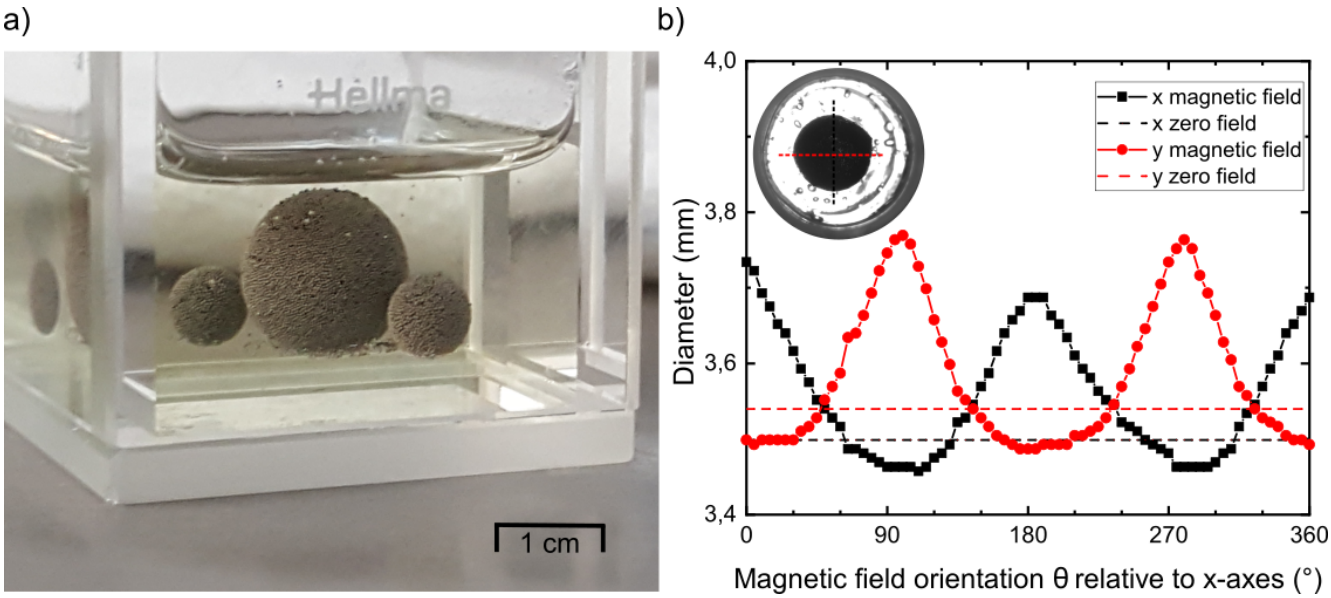

Figure 6.2: a) Three magnetic coated PDMS spheres embedded in a PDMS matrix. b) Diameter in x and y direction of a single PDMS sphere embedded in a PDMS matrix with identical mixing ratio. The dashed lines indicate the initial diameter, i.e., at zero magnetic field. The dots connected by a solid line show the diameter in x and y direction for the corresponding magnetic field orientations at a magnetic flux density of $\approx 172\,mT$. A real image of a sphere is shown -in the inset as example. Dashed lines mark the line plots to determine the diameter.

turns of the Halbach-array were carried out before the actual measurement was started. The measurements always started with the magnetic field orientated in the x direction. Subsequently, the orientation was turned in $5°$ steps until a $360°$ turn was completed. As described above the diameter of the sphere was determined for all the magnetic field orientations. Plotting the x and y diameter of the sphere in relation to the magnetic field orientation, an oscillating curve was observed, Fig. 6.2 b). Thereby, the largest diameter in x and y direction was achieved when the field was orientated along the x and y axis, respectively, Fig. 6.2 b).

The diameter in x and y direction behaved anticyclical, i.e., when the x diameter was largest y diameter was smallest and vice versa. Along the y direction a greater maximum sphere diameter was determined as along the x direction. This is a consequence of the slight aspherical form of the sphere, Fig. 6.2 b), dashed lines. Comparing the initial sphere diameter, Fig. 6.2 b), dashed lines, with the size when subjected to the magnetic field, it is observed that the elongation was not symmetrical around the initial sphere diameter. This indicates a compression of the sphere in z direction. The compression was a consequence of the elongation in x- and y direction (magnetic deformation effect) and of the force generated by the field gradient in z-direction. At the top of the sphere the gradient of the field was $\approx 4.4\,mT/mm$. Considering the incompressibility of the PDMS matrix the volume of the sphere remained unchanged during the deformation. Hence, with the assumption of an unchanged volume the ratio of the sphere's diameter in z direction before

and after the deformation was calculated with ≈ 0.95, i.e. the sphere was compressed 5% in z direction.
Concerning the diameter at applied magnetic field in relation to the initial sphere diameter only a reduction of $\varepsilon_i^x = 1.2\%$ and of $\varepsilon_i^y = 1.5\%$ occurred while a stretch of 5.4% and 6.5% was determined. This is a similar deformation as determined with the tomographic measurements even so a larger magnetic field strength and Young's modulus was used. As a sine fit did not provide a good agreement the minima and maxima of the diameter in x and y direction were read out. In case of the x diameter the maximum at $185°$ was taken. For both direction a change of $\varepsilon_r^x = 6.6\,\%$ or rather $\varepsilon_r^y = 8.1\,\%$ between minimum and maximum diameter was calculated. Comparing the reduction of the z diameter with the reduction of $\varepsilon_i^x = 1.2\%$ and of $\varepsilon_i^y = 1.5\%$ the compression induced by the gradient seems to be larger as the magnetic deformation effect induced by the homogenous field. The deviation between ε_r^x and ε_r^y indicates a stronger elasticity in the x direction of the sphere. This could be either caused by a slight difference in the particle monolayer, i.e. slight difference in the acting magnetic forces, or by the determination of the sphere diameter as the diameter included the particle monolayer where a rotation or movement of a particle could lead to such variances. When the sphere was subjected to a magnetic field, elongations were generated. In the case of the Halbach-array measurement, elongation direction of the sphere was continuously altered by rotating the external field.
In order to connect the elongation with the alternating particle displacement (microscopic view), particles needed to be resolved. This was achieved by illuminating the sphere from the top and taking reflection images Fig. 6.3. As the focus depth was smaller than the sphere dimension once the sphere at the equator [Fig. 6.3 a), b)] and once the particle at the boundary (poles) [Fig. 6.3 c), d)] were resolved. Still the particles can be clearly distinguished as such. Comparing the images for the magnetic field orientated along the x and y direction, a clear elongation along the field direction is visible. Due to the spatial resolution single particle tracking is not possible, but no clear particle chain formation or movement was visible at the equator of the sphere, Fig. 6.3 a), b) enlarged pictures. Particles at the poles in contrast seem to have moved, Fig. 6.3 c), d) blue and red boxes. Comparing these qualitative results with the tomographic measurement the particle movement at the poles was similar but a chain formation process at the equator could not be observed. This could be due to the dense packing of the particle monolayer. Hence, the magnetic deformation effect seems, on the microscopic scale, to mostly affect the particles at the poles and particle interaction plays a minor role.
The deformation of the sphere was impeded by the encapsulation with PDMS. In the following, free standing spheres were investigated. For following measurements a sphere was used that was coated with an additional layer of crosslinked PDMS. The extra PDMS layer fixed the magnetic

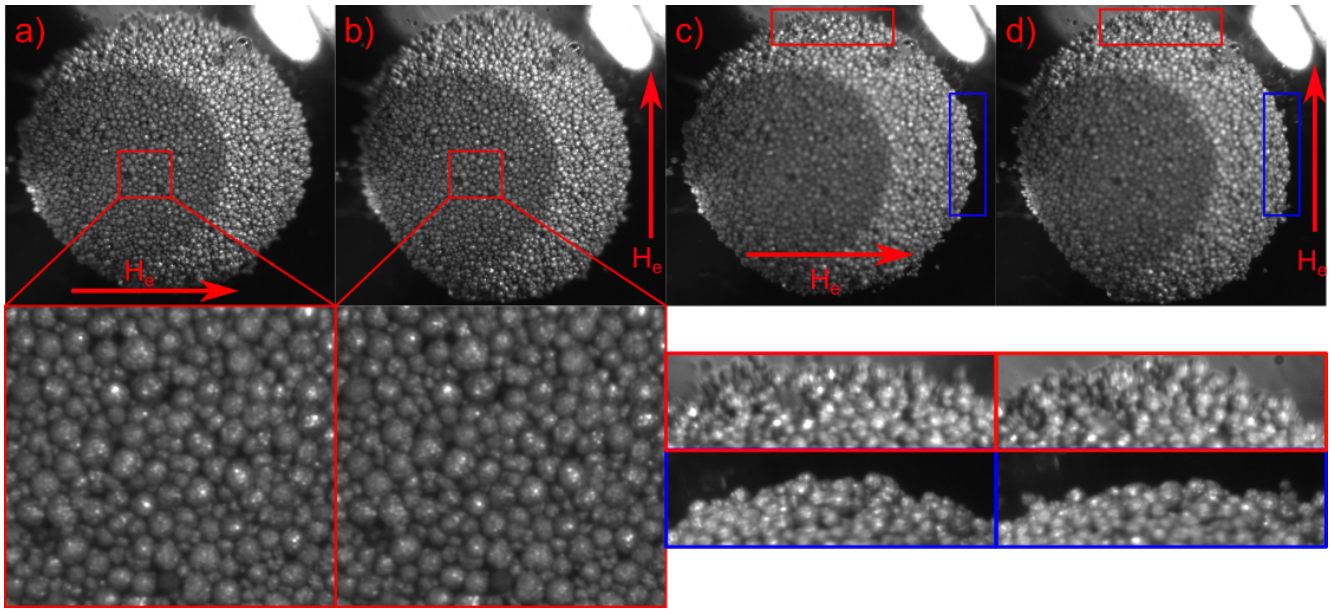

Figure 6.3: Reflective images of magnetic coated PDMS spheres. The sample was illuminated at an angle from above. The nickel particles are distinguishable. a) Focus is on the pole of the sphere. The magnetic field (black arrow) is orientated in x direction. b) Focus is on the pole of the sphere. The magnetic field (red arrow) is orientated in y direction. c) Focus is on the boundaries (maximum sphere dimension). The field is orientated in x direction. d) Focus is on the boundaries (maximum sphere dimension). The field is orientated in y direction.

particles and prevented them from detachment. A sphere with mixing ratio of $12.5\,\%$ was glued to the bottom of a glass flask with two component epoxy glue. Hence, the sphere is mainly surrounded by air. Afterwards, measurement and evaluation were conducted like describe above. Starting with the magnetic field orientated along x direction an elongation in x direction was observed with a ratio of x-length/y-length$= 1.1$ Fig. 6.4 a). During the rotation of the magnetic field the change in diameter was sinusoidal, similar to the sphere embedded in PDMS. A sine fit (Fig. 6.4 a) orange line) showed that at the magnetic field angle relative to the x axis of $107°$ y-elongation and at $10°$ x elongation reached its maximum. This can be explained by a starting configuration where the magnetic field was not exactly orientated in x direction and by a slight offset from the center when the line plots were used to determine the diameter. Comparing the initial diameter of the sphere, Fig. 6.4 a) dashed lines, a small asphericality, the ratio of x to y initial diameter is 1.02, is present. In x direction a maximum elongation $\varepsilon_r^x = 6.4 \pm 0.1\,\%$ and in y direction $\varepsilon_r^y = 8.0 \pm 0.2\,\%$ was reached, Fig. 6.4 a). These elongations were of the same magnitude as the one for the sphere encapsulated in PDMS. Thus, the oscillating change in diameter did not strongly couple to the surrounding matrix, i.e. was not influenced by the sphere's environment. This could indicate that the magnetic-deformation effect depends on the particle movement. In order to fixate the particle monolayer on the sphere surface a thin PDMS layer ($\approx$ one particle diameter) was cast onto of the sphere. This thin layer seems not to affect the particle movement.

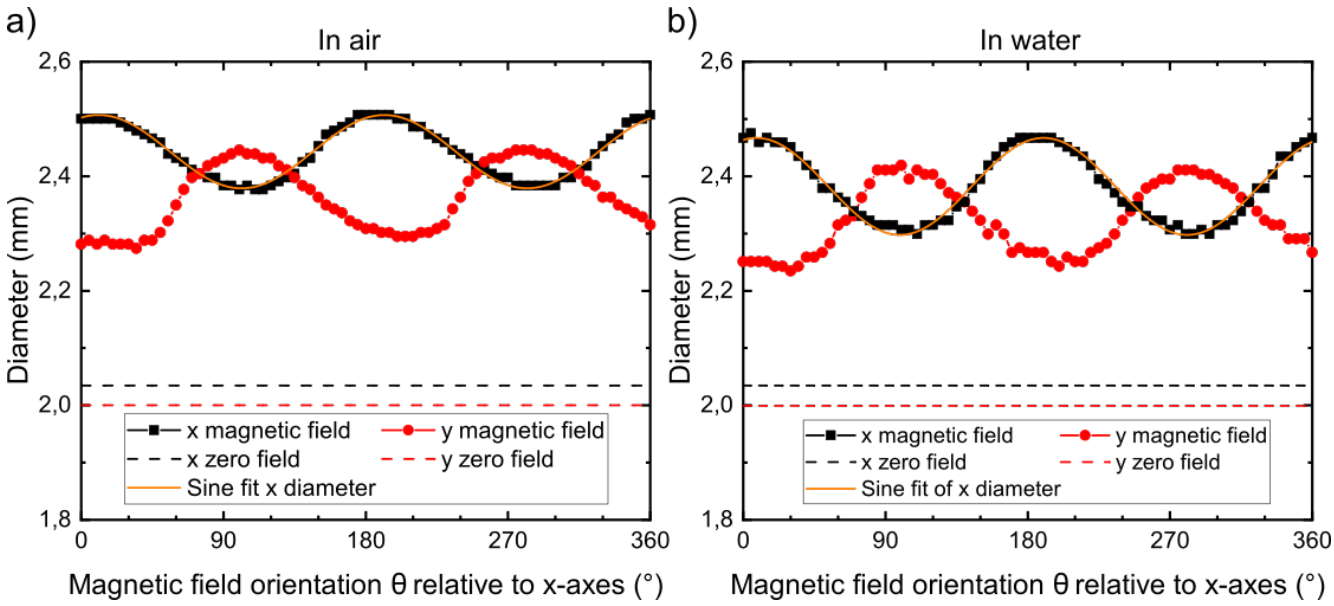

Figure 6.4: a) Diameter of a magnetic coated PDMS sphere surrounded by air. Dashed lines indicate the initial (zero magnetic field) diameters. The diameter of the sphere is strongly increased by the subjection to the magnetic field. A rotation of the magnetic field orientation leads to an alternation of the diameter along the axes. b) Diameter of a magnetic coated PDMS sphere surrounded by water. Dashed lines indicate the initial (zero magnetic field) diameters. The diameter of the sphere is strongly increased by the exposure to the magnetic field. A rotation of the magnetic field orientation leads to an alternation of the diameter along the axes.

The oscillating change in the sphere diameter was solely generated by the magnetic-deformation effect as the gradient, i.e. the compression in z-direction was independent from the magnetic field orientation.

The deformation was significantly stronger when comparing the field-free configuration to the one under applied field. With a sine fit of the x and y diameter a stretch of the sphere by a maximum of $\varepsilon_i^x = 23.2\%$ and by a maximum of $\varepsilon_i^y = 22.3\%$, Fig. 6.4 a), was determined. These huge deformations were not caused by the magnetic-deformation effect and corresponding re-arrangement of the particles but rather by the gradients of the magnetic field. Considering the spheres dimension ($\approx 2\,mm$) the Halbach-array has a nearly homogeneous magnetic field in x and y direction. Whereas, considering the particle at the equator of the sphere, the gradient in z direction generates a force that flattens the sphere by pulling the particle in the direction of the center. Considering that the gradient leads to an elongation of the sphere diameter in the complete x-y-plane the deformation induced by the gradient had a higher coupling to the surrounding matrix as the deformation induced by the magnetic deformation effect. Especially, as the sphere was only surrounded by air the elastic force opposing the gradient induced deformation was weak compared to the encapsulated sphere. The magnetic deformation effect leads to an elongation in the direction of the magnetic field and thus should depend mainly on the elasticity of the PDMS

sphere. The deformation changes between $\varepsilon_r^x \approx 6.4\%$ and $\varepsilon_r^y \approx 8.2\%$ show good agreement with Raikher *et al.* [140] who predicted an elongation in the range of 10% for a ferroelastic sphere with a shear modulus of $\approx 1\,kPa$ and a particle volume percentage of 5%.
Both elongation mechanisms enable the spheres to act as an active element for example as a valve. Thereby a gradient in the magnetic field could be used to deform the sphere on a large scale while a homogenous field could be used to change the magnetic-deformation effect, i.e. change the direction of the elongation. In the following the sphere is surrounded by water in order to see the effect of the surrounding medium on the large deformation.
To this end, the glass flask was filled with distilled water and measurements repeated as described above. Analysis of the diameter in x and y direction showed again a sinus like change while the magnetic field orientation was varied Fig. 6.4 b). A ε_r^y of $8.2 \pm 0.2\,\%$ and ε_r^x of $8.5 \pm 0.1\,\%$ was determined by fitting the curves with a sine function. The values for air and water were in good agreement and only tiny differences were observed. Those tiny difference were due to a different initial sphere orientation and show the influence of the magnetic monolayer on the magnetic-deformation effect. The large elongations were in good agreement, too. An ε_i^y of 23.8% and an ε_i^x of 21.3% was determined, Fig. 6.4 b). This tested material shows potential for use is active elements also in fluids. Observed elongations were by a magnitude larger than previously reported ones [51, 57].
Finally, comparing all three situations, spheres encapsulated in PDMS, spheres in water and spheres in air: All systems confirm unambiguously that the mechanism elongating the spheres can be generated either in a homogeneous or in a gradient magnetic field. In a homogeneous magnetic field the magnetic deformation effect occurs and mainly particles at the poles rearranged on microscopical scale. This resulted in diameter changes between $\approx 6\,\%$ and $8\,\%$. The elongation was orientated along the magnetic field orientation. Thus, a change in the orientation of the magnetic field changed the direction of elongation. Compared to the deformations induced by magnetic-deformation effect large deformations were induced by a field gradient in z direction. The field gradient generates a force compressing the sphere by pulling the particle on the poles in direction of the sphere's center. In these cases the environment of the sphere significantly influenced the magnitude of the deformations. For a sphere encapsulate in PDMS the compression in z direction was still observed but compared to the spheres in water and air quite small as for the encapsulated sphere the surrounding matrix opposes the compression strongly. Some theoretical models exist to calculate the deformation of a magnetic sphere or ellipsoid when subjected to a uniform magnetic field [52, 140, 141, 143, 161, 182, 185]. These models use a magnetic particle distribution inside the sphere. Nevertheless, Raikher *et al.* [140] predicted an elongation in the range of 10% for a ferroelastic sphere with a shear modulus of $\approx 1\,kPa$ and a particle volume

percentage of 5% which is roughly in the same order of the above measured magnetically hollow spheres. Furthermore, a model to calculate the stress distributions within a spherically isotropic hollow sphere under compression exists [176]. This model might be adaptable to the magnetically hollow spheres.

6.2 Membranes with 2D magnetic layer

In the previous chapter the same approach was used to produce PDMS spheres with a dense packed mono layer of magnetic nickel particles. Subjected to a magnetic gradient field the spheres largely deformed. Now, the bottom up approach was used to create magneto-active membranes. Thereby, magnetic membranes consist of a monolayer of dense packed nickel particles embedded between two thin PDMS layers of identical mixing ratio. The entire structure is free standing and only supported at its rim, compare section 4.1.4. In the subsequent sections magneto-active membranes are analyzed regarding their resonance frequency and bending deformation. Using the Uflyand-Mindlin theory for bending plates an effective Young's modulus of the membranes can be determined once by their resonance frequency and once by their maximum deformation. Finally, a potential application of the membrane to be used as a droplet selector is shown.

6.2.1 Resonance frequency and beam bending theory

Membranes were produce as described in section 4.1.4. In the following the results with membranes with dimension of $(19.5 \pm 0.1)\,mm$ on $(38.3 \pm 0.1)\,mm$ and thickness of $(1.0 \pm 0.1)\,mm$ are presented. Membranes with various PDMS mixing ratio could be produced. In the following the determination of the membrane's resonance frequency will be explained exemplary with a $25\,\%$ PDMS mixture with an elastic modulus of $(8.7 \pm 1.6)\,kPa$ for the PDMS gel. As the particle monolayer is rigid compared to the PDMS layer and enhances the membrane's stiffness, its effective Young's modulus has to be determine. In this section the effective Young's modulus of the membrane will be calculated from its resonance frequency.
The membrane had a weight of $m_m = (1.3 \pm 0.1)\,g$ and thus a density of $\rho = \frac{m_m}{V} = (1740.6 \pm 0.2)\,\frac{kg}{m^3}$ wherein V denotes the volume of the membrane. Consequently, the membrane has a density between pure PDMS ($965\,\frac{kg}{m^3}$) and pure nickel ($8090\frac{kg}{m^3}$), i.e. a particle volume of $\approx 11\%$. The membrane was placed on the plastic sample holder [see Fig. 6.5 a), b)]. The membrane was supported at its both smaller sides leaving its long ends to be free. Depending on the PDMS mixing ration the membranes were thus more or less bended in the center due to gravity. To

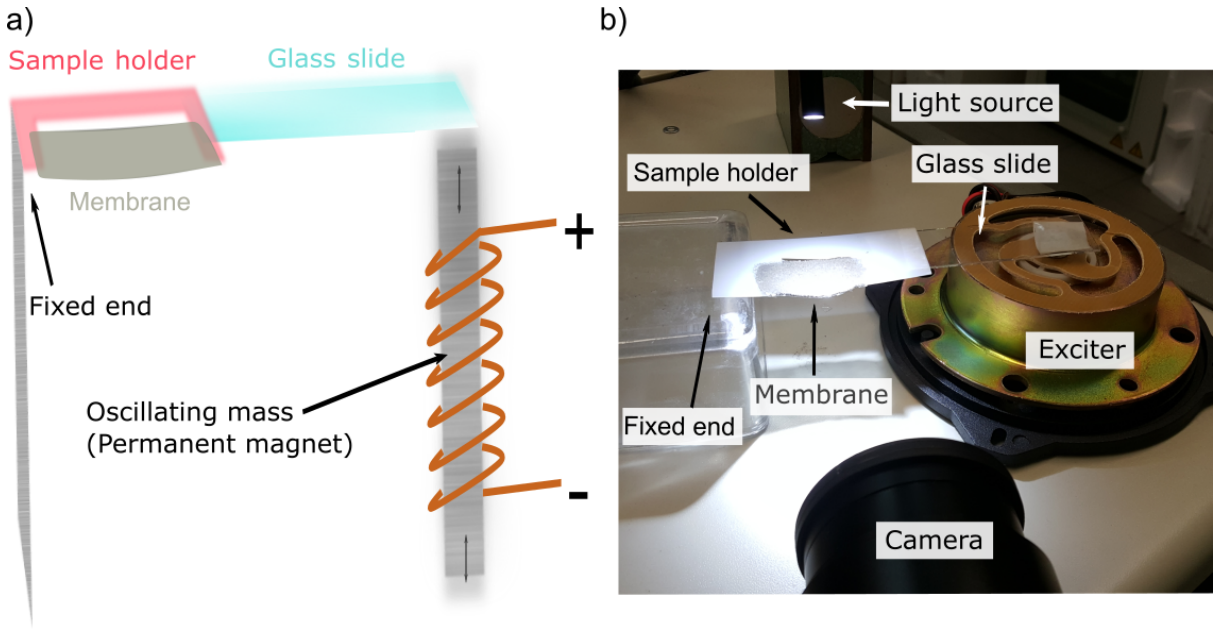

Figure 6.5: a) Sketch of the setup used to excite the membrane and determine its resonance frequency. The membrane is place on a sample holder and only two edges are simply supported. To ensure a good coupling to the exciter, the sample holder is on the left side fixed to a stable foot and on the right side on a glass slide. The glass slide is fixed on the permanent magnet of the exciter. Passes an alternating current through the coil of the exciter the permanent magnet begins to oscillate and with it the membrane. b) Real image of the setup used to excite the membrane. A NX4-S1 camera was used to detect the motion of the membrane.

excite the membrane, the sample holder was fixed with one end on a solid non-movable foot and with the other end on a $1.1\,mm$ thick glass slide. The glass slide was connected to an exciter [6.5 a) and b)]. The exciter was purchased from Visaton (BS 130 - 4 Ohm) and consists of a permanent magnet that is pulled against a spring when a current runs through the coil. On top of that permanent magnet the glass slide was stably fixed. Using the glass slide as spacer between membrane and exciter ensured that the magnetic stray fields of the permanent magnet and the coil did not affect the magnetic membrane.

Similar to the electromagnetic setup, the power supply EX354D (Thurlby Thandar Instruments) was used to generate a stable voltage of $12\,V$ and stable current of $0.4\,A$ at an amplifier from Basetech (AP-2100). The voltage and current at the power supply remained constant throughout the measurement. With a waveform generator (33220A, Agilent), signals with different frequencies, amplitudes and forms could be generated. The signals were amplified by an amplifier from Basetech (AP-2100) and transmitted to the exciter. For the resonance measurement, a sinus wave is set at the waveform generator and the excitation mass moves up and down. From the exciter the movement was transmitted from one side into the membrane, Fig. 6.5 a). As the glass slide and sample holder were quite stiff, the exciter and membrane are coupled well and the membrane starts to oscillate with the set frequency. In order to determine the resonance frequencies of the

membranes, the input frequencies were varied and the deformation of the membranes tracked as follows.

The membrane was illuminated at an angle from above and the membrane excite. Images from the unsupported membrane side were taken with the NX4-S1 camera at 1000 frames per second Fig. 6.6 a). Using ImageJ, the edges of the membrane were detected with the process "Find Edges" in ImageJ Fig. 6.6 b). To detect the displacement of the membrane, a line was placed in the center of the membrane [point with maximum displacement, red line in Fig. 6.6 a), b)] and the macro plot profile in ImageJ applied. This provides the brightness value of the pixels along the line. Pixels can obtain values of 0 for white or 255 for black. Defining the lower edge of the membrane as the sudden transition from white to black a detection of the membrane's edge position was possible. Tracking the edge position over a certain period of time depicts the membrane's displacement. The detected displacement of the membrane is exemplary depicted for an excitation frequency of 22 Hz, Fig. 6.7 a).

After detecting the displacement it was fitted with a sine function:

$$y = y_0 + A_T \, sin \left[\pi \left(\frac{t - t_c}{T} \right) \right]. \tag{6.1}$$

Herein y_0 denotes the shift around the central oscillation point, A_T the amplitude of the oscillation, t_c the phase shift and T half the oscillation period. From the period the membrane oscillation frequency can be calculated by $f_m = \frac{1}{2*T}$. Comparing the calculated oscillation frequency with the excitation frequency gives an indication of how well the determination of the membrane movement worked. The amplitude of the oscillation gives the maximum displacement of the membrane. y_0 and t_c are in this case purely fitting parameters and not relevant in the following. In order to determine the resonance frequency, the excitation frequency was altered from 20 to

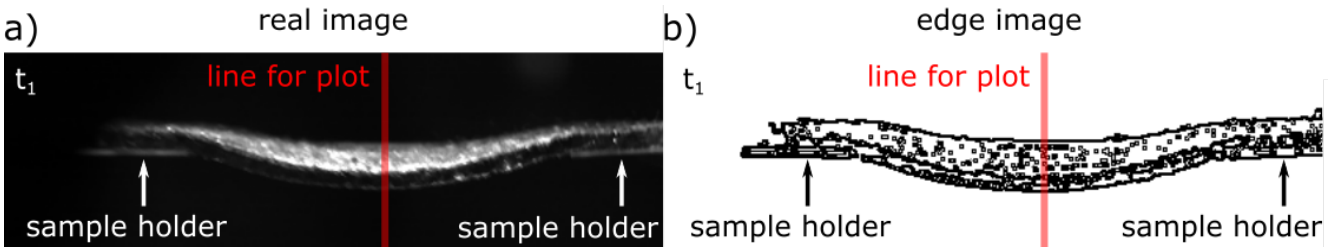

Figure 6.6: a) Real image of a magneto-active membrane at an unspecific time t_1. On the left and right side the sample holder is distinguishable. The long sides of the membrane are unsupported and illumination takes place at an angle from above. The red line marks the point of maximum displacement of the membrane. b) Edge image of the magneto-active membrane. The image is obtained after processing the real image a) in ImageJ and shows the edges of the membrane. The red line marks the line profile for determining the brightness values of the pixels along the line.

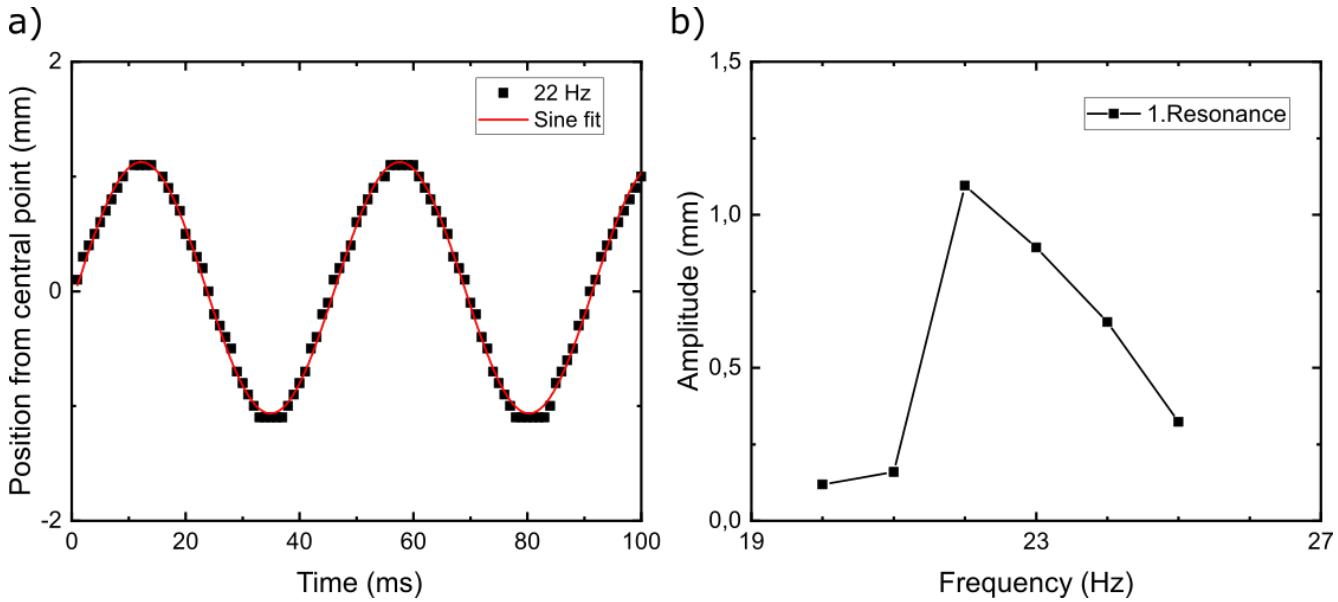

Figure 6.7: a) The membrane was excited with a frequency of 22 Hz and its movement detected. As can be seen, the membrane oscillates around a center point. The oscillation was fitted with a sine function (red line). With the sine fit the amplitude of the oscillation was determined. b) Amplitude dependency on the excitation frequency. Around 22 Hz a clear peak is observed. Due to the asymmetry the curve could not be fitted. The peak marks the first order resonance frequency of the membrane.

25 Hz in 1 Hz steps and the displacement of the membrane detected. The extracted oscillation frequencies f_m were in good agreement with the excitation frequencies f, Tab. 6.1, and supports a good determination of the membrane movement. Uncertainties of the oscillation frequencies are given by the statistical error of the sine fit, Tab. 6.1. Plotting the amplitude A_T over the excitation frequency f results in Fig. 6.7 b). A clear peak at roughly 22 Hz can be identified, marking the 1. resonance frequency of the membrane. Compared to the amplitude dependence of a forced damped harmonic oscillator (see Fig. 11.22 of [41], slightly asymmetric around the resonance), the curve in Fig. 6.7 b) clearly shows a different shape. This might be a result from the

f in Hz	T in ms	standard error of T in ms	f_m in Hz
20	25.00	0.02	20.00±0.02
21	23.78	0.04	21.03±0.04
22	22.70	0.03	22.03±0.03
23	21.81	0.04	22.93±0.04
24	20.84	0.01	23.99±0.01
25	20.01	0.01	24.99±0.01

Table 6.1: Applied excitation frequency to determine the resonance frequency of the membrane. The oscillation of the membrane was detected and fitted. From the fit the half oscillation period T is extracted and listed. The standard errors of T are given by the fits. Frequencies of the membrane f_m are calculated from the half oscillation period T.

experimental setup.The glass slide and sample holder can be assumed as quite stiff compared to the membrane, even though, the system presents a coupled oscillator system. Due to the coupling of different oscillators, the resonance peak is not shaped like an damped harmonic oscillator and a fitting with a Lorentz or Gauss peak function was not possible.
A system like the membrane can exhibit more than one resonance frequency. Higher resonance frequencies are in general weaker in amplitude and thus, harder to resolve. In order to determine the 2. resonance the excitation frequency was altered from 36 to $42\,Hz$ in $1\,Hz$ steps. Evaluation was similar to the 1. resonance case. Since the second resonance has the shape of a full sine wave two lines were used, one at the point of minimum displacement, Fig. 6.8 a), b) blue line, and one at the point of maximum displacement of the membrane, Fig. 6.8 a), b) red line. Fitting the displacement of the membrane at both points with the sine fit of Eq. 6.1, Fig. 6.9 a), two amplitude dependencies were obtained Fig. 6.9 b).The amplitude of the center reduces to nearly zero at the resonance frequency, while the displacement of the point in the middle between center and suspension point is at its maximum. Consequently, a 2. resonance at roughly 42 Hz was extracted. Knowing the resonance frequencies of the membrane the effective Young´s modulus of the membrane can be calculated. Therefore, beam bending theories will be used.
For the bending beam two main models exist: The Euler-Bernoulli beam theory and the Timoshenko beam theory [59]. While the Euler-Bernoulli beam theory is used for rigid beams, the Timoshenko beam theory allows for rotation bending as well as shear deformation. As the Timoshenko theory is an extension of the Euler-Bernoulli theory, the Euler-Bernoulli theory will be introduced first. A detailed derivation of both theories can be found e.g. in Gross *et al.* [59].

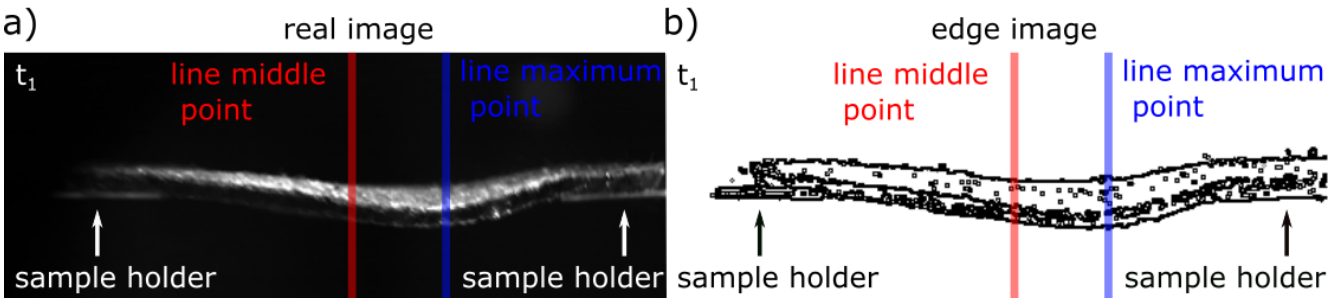

Figure 6.8: a) Real image of a magneto-active membrane at an unspecific time t_1. On the left and right side the sample holder is distinguishable (white arrows). The long sides of the membrane are unsupported and illumination takes place at an angle from above. The blue line marks the point of maximum displacement and the red line the point of minimum displacement of the membrane. b) Edge image of the magneto-active membrane. The image is obtained after processing the real image a) in ImageJ and shows the edges of the membrane. The red and blue line mark the line profiles for determining the brightness values of the pixels along the line.

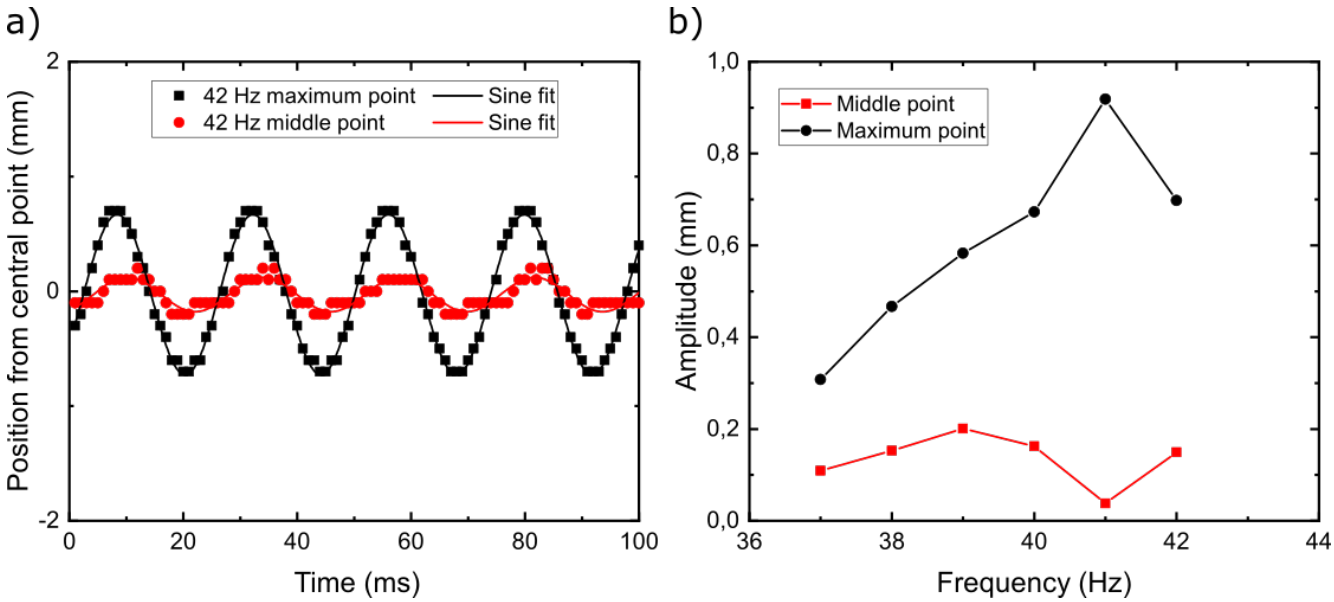

Figure 6.9: a) The membrane was excited with a frequency of 42 Hz and its movement detected. As can be seen, the membrane oscillates around a maximum point and rests nearly in the middle point. Both movements were fitted with a sine function (red and black line). For both movements an amplitude was extracted b) Amplitude dependency on the excitation frequency. Around 41 Hz a clear peak is observed in the amplitude of the maximum point (black line). Simultaneously, for this frequency the middle point shows smallest amplitude (red line). The second order resonance frequency was determined with 41 Hz.

To begin with, the equation of motion for a rigid beam is given with [59]:

$$\frac{\partial^4 W}{\partial x^4} - \kappa^4 W = 0 \quad \text{with} \quad \kappa^4 = \omega^2 \frac{\rho A}{EI}. \tag{6.2}$$

Herein W denote a general solution function, ω the angular frequencies, I the axial geometrical moment of inertia, A the area, ρ the density and E the Young's modulus. Depending on the specific initial and boundary conditions, the natural frequencies ω_k of the beam can be calculated. In the experiment setup the edges of the membrane were not clammed. Therefore, it is valid to assume, as in literature defined [59], simply supported edges. For this type of mounting, the boundary conditions require a vanish momentum and displacement at the mounted edges of the membrane. The natural frequencies of the membrane can hence be calculated with [59]:

$$\omega_k = \kappa^2 \sqrt{\frac{EI}{\rho A}} = k^2 \pi^2 \sqrt{\frac{EI}{\rho A l^4}} \quad \text{with} \quad \kappa l = k\pi \quad \text{and} \quad k = 1, 2, 3..... \tag{6.3}$$

while $\kappa l = k\pi$ follows from the boundary conditions with l the length of the beam [59]. Equation Eq. 6.3 gives the natural frequencies of a Bernoullie beam with simply supported edges and k defines the order of the natural frequency.

To obtain equation Eq. 6.3 the assumption $GA_s \to \infty$ (rigid beam, $G =$ shear modulus, $A_s =$cross-sectional area) and $\rho I \to 0$ (negligible rotation inertia) have been used but Eq. 6.3 can be expanded by allowing bending and shear deformation. This gives the natural frequencies of a Timoshenko beam with:

$$\omega_t = \left[1 - (1+\tau)\left(\frac{k\pi i}{l}\right)^2\right]\omega_k \quad \text{with} \quad \tau = \frac{EA}{GA_s} \quad \text{and} \quad i^2 = \frac{I}{A}. \tag{6.4}$$

Comparing Eq. 6.4 and Eq. 6.3 shows that the Timoshenko beam theory differs from the Bernoullie beam theory just by the term in square brackets. The correction by the Timoshenko beam theory becomes relevant for $l/k \geq t_b$ with t_b the height of the beam, i.e. the length is much larger as the cross sectional area. In the case of the membrane it gives only a correction of 0.3% for the first resonance frequency. For a detailed derivation of the Timoshenko beam theory the reader is again referred to Gross *et al.* [59]. Rearranging the equation Eq. 6.4 to evaluate the Young's modulus E gives:

$$E = \frac{\omega_t^2 \rho A l^4}{k^4 \pi^4 I \left[1 - (1+\tau)\left(\frac{k\pi i}{l}\right)^2\right]^2} \tag{6.5}$$

Considering, the membrane's rectangular shape $A_s = 5/6\ A$. Additionally taking the incompressibility of the membrane into account by setting the Poisson ration to 0.5, $\tau = \frac{18}{5}$. Above, the first resonance frequency of the membrane with mixing ration of 25% was determined with $f_m = \omega_t/2\pi = 22\,Hz$. Inserting the extracted variables such as A_s, τ, ω_t etc. the Young's modulus E of the membrane was calculated with equation Eq. 6.5 to be $224\,kPa$. Extracting the Young's modulus for a pure matrix membrane with $25\,\%$ mixture, a value of $(8.7 \pm 1.6)\,kPa$ is obtained. As a result the membrane shows a Young's modulus more than 25 times larger than its pure PDMS matrix. The added nickel particles are orders of magnitude stiffer than the PDMS and should contribute to the larger Young's modulus of the membrane. In order to determine the order of magnitude this contribution accounts for, the by Batchelor derived model [12,15] for homogenous composites was considered. It describes the dependence of the Young's modulus on the volume fraction of the filler particles. The altered Young's modulus can be calculated with:

$$E_s \approx E_m(1 + 2.5\phi + 5.2\phi^2), \tag{6.6}$$

where ϕ denotes the particle volume fraction and E_m the modulus of the pure matrix material. At the beginning of this chapter the density of the membrane was calculated and with it that the particle volume fraction inside the membrane amounts to $\approx 11\%$. Inserting this particle volume

fraction in the Batchelor model results in a Young's modulus of $\approx 11.6\,kPa$ for the membrane. This is still small compared to the $224\,kPa$ determined with the beam theory. So, in the case of the membrane a model that estimates the reinforcement of an elastomer matrix with homogenous particle distribution does not provide accurate values for the effective Young's modulus .
Another explanation for the Young's modulus of $224\,kPa$ could be the limitation of the beam theory considering the membrane's geometry. In the following, the membrane's Young's modulus will be calculated by using Kirchhoff and Uflyand-Mindlin plate theories as the plate theories consider that the membrane is a extended area.

6.2.2 Resonance frequency and plate theory

Similar to the bending beam, a description of rigid $(GA_s \to \infty)$ and non-rigid plates exists. The theory that describes rigid plates is called Kirchhoff theory and the theory that describes non-rigid Uflyand-Mindlin theory. Similar to the Timoshenko beam theory, the Uflyand-Mindlin theory is an expansion of the Kirchhoff theory by considering shear deformation. Since the solution of the Uflyand-Mindlin theory are just a small extension of the Kirchhoff theory, the Kirchhoff theory will be induced first.
To begin with, the equation of motion of a two dimensional plate with size a and b is given with [59]:

$$\Delta\Delta W - \kappa^4 W = 0 \quad \text{with} \quad \kappa^4 = \frac{\rho t_p \omega^2}{K} \quad \text{and} \quad K = \frac{E t_p^3}{12(1-\nu^2)}. \tag{6.7}$$

W denotes a general solution function, ρ the plate density, t_p the plate thickness, ω the angular frequency, K the plate stiffness, ν the Poisson ratio and E the Young's modulus. Using a separation approach, it can be shown, that [59]:

$$W(x,y) = F\,sin(\alpha x)sin(\beta y), \tag{6.8}$$

is a solution of the motion equation Eq. 6.7 with F a dimensionless parameter. α and β denote the eigenvalue which have yet to be determined using the boundary conditions. Implementing Navier boundary conditions, $W = 0$ and $\Delta W = 0$ at the membrane edges, the natural angular frequencies become [59]:

$$\omega_{m,n} = \kappa^2 \sqrt{\frac{K}{\rho t_p}} = \left(\alpha^2 + \beta^2\right) \sqrt{\frac{E t_p^2}{12\rho\left(1-\nu^2\right)}} \quad \text{with} \quad \alpha = \frac{m\pi}{a}, \beta = \frac{n\pi}{b}, \tag{6.9}$$

with m, n=1,2,... giving the order of the resonance frequencies in x respectively y direction. The solutions of equation Eq. 6.9 give the resonance frequencies of a Kirchhoff plate simply supported on all edges.
Expanding the model to include rotary inertia and shear deformation one obtains the Uflyand-Mindlin theory. The exact derivation can be found in [4, 47, 98, 117]. Here, just the expansion coefficient λ for the natural frequencies is given [4]:

$$\lambda = \frac{\sqrt{1 + \varsigma_r^2 + \varsigma_s^2 \pm \sqrt{\left(1 + \varsigma_r^2 + \varsigma_s^2\right)^2 - 4\varsigma_r^2\varsigma_s^2}}}{\sqrt{2}\varsigma_r\varsigma_s}. \tag{6.10}$$

ς_r, ς_s denote the correction coefficient for including the effect of rotary inertia respectively shear deformation and are given by:

$$\varsigma_r^2 = \frac{t_p^3}{12}(\alpha^2 + \beta^2) \quad \text{and} \quad \varsigma_s^2 = \frac{t_p^2}{5\,(1-\nu)}\left(\alpha^2 + \beta^2\right). \tag{6.11}$$

Consequently, the natural frequencies become:

$$\omega_{u_{m,n}} = \omega_{m,n}\lambda. \tag{6.12}$$

Inserting Eq. 6.9 in Eq. 6.12, after rearranging the Young's modulus is defined by:

$$E = \frac{9\,\omega_{u_{m,n}}^2\rho}{\lambda^2(\alpha^2 + \beta^2)^2 t_p^2} \tag{6.13}$$

Coming back to the resonance frequency measurement of the membrane. As stated in the beginning of this chapter the membrane's dimension were $a = 38.3\,mm$, $b = 19.5\,mm$ and thickness $t_p = 1.0\,mm$. To facilitate a calculation of the Young's modulus by using the Uflyand-Mindlin theory the boundary conditions of the experimental setup had to be adapted. Instead of only supporting two membrane edges the membrane was placed on a sample holder where all four edges were simply supported. Thus the membrane's active area reduced to 14.5 on $24.5\,mm$. Otherwise the experimental setup did not change to previous resonance frequency measurement. Images of the membrane's center were taken while the excitation frequency was varied in $1\,Hz$ steps from 29 to $42\,Hz$ Fig. 6.10 a). By inverting the images and using the process "Find Edges" in ImageJ, an edge image is obtained, Fig. 6.10 b). In the edge image the membrane's edges are well distinguishable from the background. Inserting a vertical line at the center of the membrane [red line Fig. 6.10 a), b)] the brightness values of the pixels along the line can be evaluated. Hereby, a

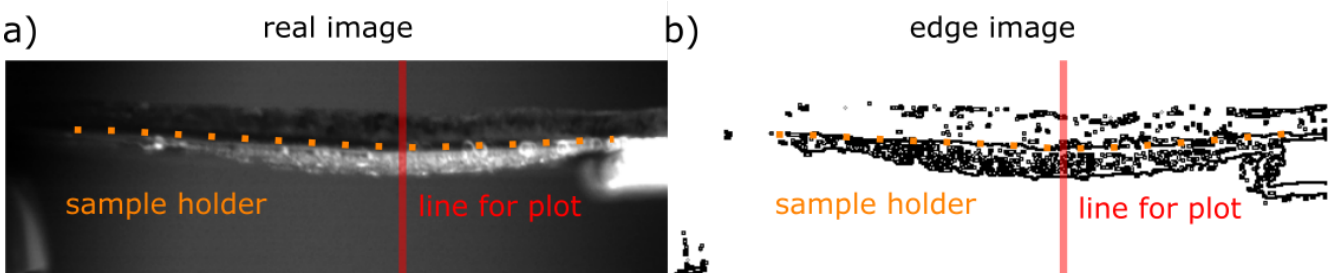

Figure 6.10: a) Real image of a membrane place on the sample holder with all four edges simply supported. Illumination was done at an angle from above. A dashed orange line marks the sample holder. Along the vertical red line the brightness values of the pixels were extracted. b) Edge image of the real image in a). It was obtained by using the process "Find Edges" in imageJ. A dashed orange line marks the sample holder. Along the vertical red line the brightness values of the pixels were extracted.

change from dark to white pixel marks the position of the membrane's edge. The membrane's edge position was tracked, mirroring the membrane's movement and a sine fitting (Eq. 6.1) was conducted Fig. 6.11 a). The fitted frequency was in good agreement with the excitation frequency. Subsequently, the amplitudes of the membrane oscillation are determined for the various frequencies. Plotting the maximum amplitude over the applied excitation frequencies a resonance is extracted for $(33.3 \pm 0.3)\,Hz$ Fig. 6.11 b). A two peak Gauss fit can be applied giving a second peak at $(39.2 \pm 0.9)\,Hz$ Fig. 6.11 b). The $33.3\,Hz$ belong to the first order resonance frequency in both direction (m=1, n=1). Calculating the Young's modulus by using the Uflyand-Mindlin theory Eq. 6.13 a value of $E = 154\,kPa$ is obtained. Inserting the Young's modulus of $154\,kPa$ into Eq. 6.13 and solving it for the next higher order resonance frequency (m=2, n=1) a resonance frequency of $58\,Hz$ is determined. This frequency significantly deviates from the second fit peak at 39.6 Hz. Therefore, the second peak does not give the second resonance but is probably an effect of the asymmetry in the resonance of the coupled system.

To summarize: The membrane with a PDMS mixture of 25% was excite from the right edge with defined frequencies. The experimentally setup only supported the two shorter membrane edges leaving the long edges free. Tracking the membrane movement a first order resonance frequency of $22\,Hz$ could be determined. Using the Timoshenko beam theory with the boundary conditions in form of two simply supported edges, a Young's modulus of $224\,kPa$ could be calculated. Comparing this value with the Young's modulus of a the sole PDMS matrix $(8.7 \pm 1.6\,kPa)$ the membrane shows a significantly increased Young's modulus. Considering the reinforcement of the elastomer by particle addition, the by Batchelor derived model gives an estimation for the membrane's Young's modulus in relation to the particle volume fraction.But the value calculated with this model was still of orders smaller, i.e. a model assuming a homogeneous particle distribution could not give accurate values for the membrane's Young's modulus. In order to account for the membrane's geometry more precise the Young's modulus was calculated by using the Uflyand-

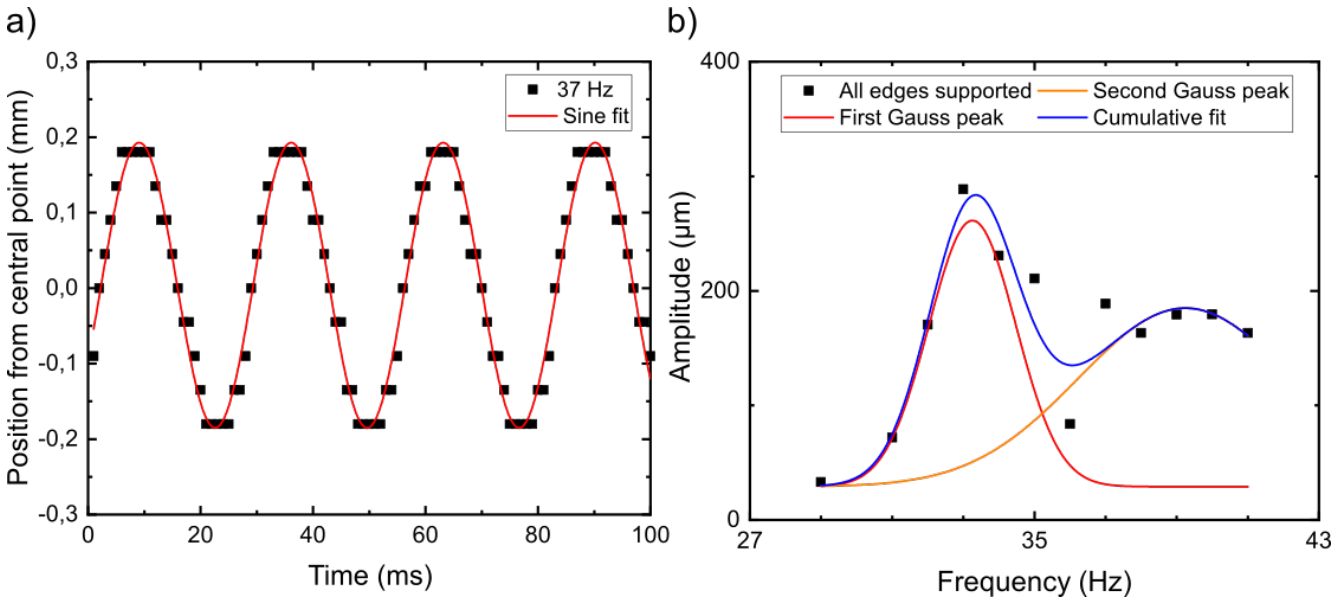

Figure 6.11: a) The membrane was excited with a frequency of 37 Hz and its movement detected. As can be seen, the membrane oscillates around a center point. The oscillation was fitted with a sine function (red line). An amplitude of $0.19\,mm$ was extracted. b) Amplitude dependency on the excitation frequency. Around 32 Hz a clear peak is observed. Fitting the curve with two Gauss peaks (red, orange lines) results in the depicted cumulative fit (blue line). The Gauss peaks are positioned at 33.3 and 39.2 Hz. The Gauss peak at 33.3 Hz marks the firs order resonance frequency of the membrane.

Mindlin plate theory. Therefore, the experimental boundary conditions needed to be adapted and the membrane was placed on a sample holder with all four edges simply supported. Repeating the resonance frequency measurement a first order resonance frequency of $(33.3 \pm 0.3)\,Hz$ could be identified. Inserting the resonance frequency into Eq. 6.13 a Young's modulus of $154\,kPa$ was calculated. Compared to the Timoshenko beam theory this is a $\approx 30\%$ smaller value showing that the approximation of the membrane as a beam leads to large deviations of the calculated Young's modulus. Hence, the particle arrangement in a monolayer strongly stiffens the membrane.

6.2.3 Deformation and plate bending theory

In order to verify the Young's modulus determined by the resonance frequency measurement and corresponding plate theory, another way to determine the effective elastic modulus of the membrane was used. Therefore, the membrane needed to be actively deformed. As the membrane is magneto-active the deformation can be induced by a magnetic field, i.e. the membrane was placed orthogonally between the poles of the electromagnet, compare Fig. 4.10. The acting magnetic force causes the membrane to deflect until the elastic force equals the magnetic force. Assuming a rectangular load of area A_l, applied at the center (a/2, b/2) of the membrane, the

deflection can be represented by the double Fourier series as follows [77]:

$$d_z = \sum_{m=1,3,5..} \sum_{n=1,3,5..} d_{nm} \left[1 + \frac{t_p^2}{2.5} \left(\left(\frac{m\pi}{a} \right)^2 + \left(\frac{n\pi}{b} \right) \right) \right] sin\left(\frac{m\pi}{2} \right) sin\left(\frac{n\pi}{2} \right). \tag{6.14}$$

Herein, d_{nm} denote the deflection coefficients and t_p the plate thickness. The deflection coefficients are defined by the boundary conditions and become [77]:

$$d_{nm} = \frac{16\Lambda_0}{\pi^6 A_l K} \frac{sin\left(\frac{m\pi}{2}\right) sin\left(\frac{n\pi}{2}\right) sin\left(\frac{m\sqrt{A_l}\pi}{2a}\right) sin\left(\frac{n\sqrt{A_l}\pi}{2b}\right)}{mn\left[(\frac{m}{a})^2 + (\frac{n}{b})^2\right]^2}, \tag{6.15}$$

for a plate with all edges simple supported. Λ_0 is the applied load and K is the plate stiffness which was already defined in Eq. 6.7. Substituting Eq. 6.15 into Eq. 6.14 the deflection dependency on the Young's modulus is obtained. Rearranging Eq. 6.14 after E gives the Young's modulus of the plate with:

$$E \approx \frac{144\Lambda_0}{\pi^6 A_l d_z t_p^3} \frac{1}{\left[\left(\frac{1}{a}\right)^2 + \left(\frac{1}{b}\right)^2\right]^2} \left[1 + \frac{t_p^2}{2.5} \left(\left(\frac{\pi}{a} \right)^2 + \left(\frac{\pi}{b} \right) \right) \right]. \tag{6.16}$$

In this case the summation in Eq. 6.14 was cut off after $m, n = 1$ since terms of higher order are much smaller and converge fast against zero [59]. Consequently, by measuring the deflection the Young's modulus can be calculated.

Getting back to the experimental realization: The membrane ($25\,\%$) with length $a = (38.3 \pm 0.1)\,mm$, width $(b = 19.5 \pm 0.1)\,mm$ and thickness $t_p = (1.0 \pm 0.1)\,mm$ was place on the sample holder with all four sides supported. Subsequently, the pole shoes of the electro magnet were placed orthogonally to the membrane's plane, Fig. 4.10. A rectangular signal of $2\,V$ and $100\,mHz$ was applied to the electro magnet (maximum voltage and current at the power supply). For this setting, the magnetic field and its gradient had been measured with the gaussmeter Lakeshore 410 (section 4.2.2).

Subjecting the membrane to the magnetic field a magnetic force acts on the magnetic nickel particles due to the field gradient. This magnetic force deflects the membrane. To optically detect the deflection, the illumination was done at an angle from above, images were taken with the camera NX4-S1 (1000 frames per second). Evaluation of the membrane deflection was conducted similar to the resonance measurement, i.e., the real image was inverted in Image J and the edges detected with the process "Find Edges". A vertical line was plotted through the center of the membrane and the pixel's brightness values along this line extracted [compare Fig. 6.10 a), b)]. A change from white to black determines the position of the membrane's edge. By additionally detecting the pole shoe surface the distance between membrane and pole shoe surface can be

extracted Fig. 6.12 a). In Fig. 6.12 a) the onset of the magnetic field is clearly visible in form of the sudden distance change. It took the membrane $\approx 75\,ms$ to reach the displaced state. The membrane remained in the displaced state as long as the magnetic force was applied. In this state the magnetic and elastic forces were equal. The deflection of the membrane is given by Eq. 6.14. In the case of the experiment the load Λ_0 is defined by the magnetic force acting on the membrane. The acting magnetic force was calculated as follows.
The magnetic force on one particle is given by:

$$F_m = \frac{1}{\mu_0}\Delta\chi V_p (B \cdot \nabla)B. \tag{6.17}$$

$\Delta\chi$ denotes the difference between particle susceptibility and surrounding medium, V_p the particle Volume, μ_o the vacuum permeability and $B, \nabla B$ the magnetic flux density respectively the gradient of the magnetic flux density at the particle position. Assuming a homogeneous field in x-y-direction over the area of the pole shoe the scalar product $(B \cdot \nabla)B$ simplifies to $B_z \frac{\partial B}{\partial z}$. Inhomogeneous fields outside the pole shoe area will be neglected as gradients were comparably small and forces generated were directed either to the membrane's center or along the z-direction.

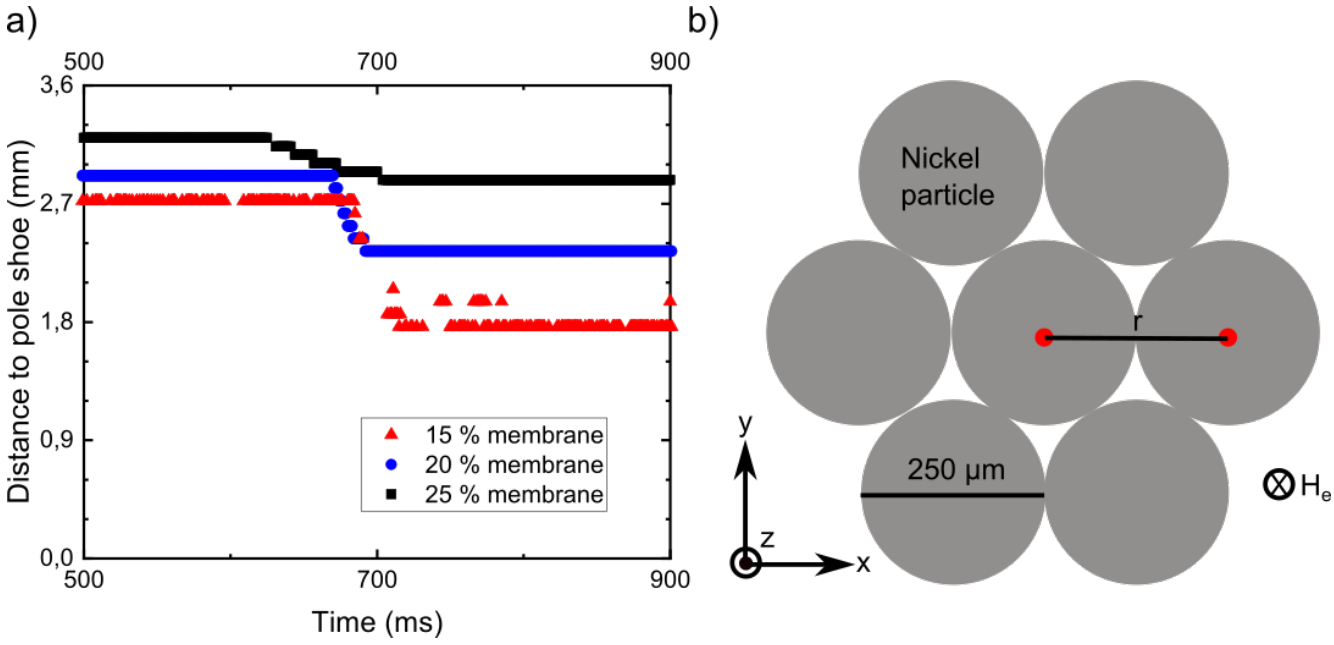

Figure 6.12: a) Displacement measurement of the membranes with PDMS mixing ratio of 15, 20 and 25 %. The membranes were placed horizontally between the pole shoes of the electromagnet. A magnetic force displaces the membranes. Optical detection allowed to extract the distance between the pole shoe and the membrane's edge. The onset of the magnetic force is clearly depicted by the distance change. b) Particles are assumed to form a hexagonal lattice. The particle size is assumed to be $250\,\mu m$. A center particle is surrounded by six neighbor particles. All neighbor particles have the same distance of $r = 250\,\mu m$ to the center particle.

As a magnetic field was applied to deform the membrane, the particles inside the membrane were magnetized and generated a magnetic dipole field. This dipole field counteracts the external magnetic field, decreasing the effective magnetic field acting on the particles. Hence, the stray fields of the particles need to be considered. Assuming a hexagonal dense packed particle layer and only treating nearest neighbor interaction, the fields of six surrounding particles act on the center particle [Fig. 6.12 b)]. Particles were positioned in the same plane as the central particle and due to the symmetry of the hexagonal positioning had the same distance r of one particle diameter $d = 250\,\mu m$ to the central particle. Thus the stray field of the nearest neighbor particles at the center particle becomes:

$$B(d) = -6\frac{\mu_0 M_p V_p}{4\pi d^3}. \tag{6.18}$$

M_p and V_p denote the magnetization respectively the volume of the particle and μ_0 the vacuum permeability. Comparable to section 3.3.1, Eq. 3.35, the demagnetization field of Eq. 6.18 needs to be solved iteratively.

This iteration procedure starts with the undisturbed external magnetic flux density at the position of the deflected membrane. From the deformation measurement Fig. 6.12 a), a distance of 2.9 mm to the pole shoe is extracted for the $25\,\%$ membrane. Adding half the thickness of the membrane (0.5 mm) in order to obtain the particle position, the particles rest at a distance of 3.4 mm from the pole shoe surface. At this distance the electromagnet generates a magnetic flux density of $38.3\,mT$ (section 4.2.2). At this flux density the nickel particles have a magnetization M_p of $\approx 62\,kA/m$ (SQUID measurement, section 2.1). Subsequently, using equation Eq. 6.18, the magnetic flux density of the 6 surrounding particles at the center of the center particle was calculated and subtracted from the external applied flux density. Consequently, the particles are subjected to a reduced magnetic flux density and their magnetization reduces as well. The resulting magnetization at the reduced magnetic flux density is extracted and the previous calculation is repeated. After several iteration steps the effective magnetic flux density of $26.7\,mT$ is obtained. Apparent, by taking the magnetization of the neighbor particles into account the particle is only subjected to approximately 70% of the external flux density and thus, also only to 70% of the field gradient. The adaption of the magnetic flux density was done equally for the 15% and 20% membrane.

In order to assess the magnetic force the number of particles in which the magnetic force is acting needs to be roughly estimated. Assuming a hexagonal particle arrangement, 211 particles fit in the area of the pole shoe. With Eq. 6.17 and under consideration of the effective flux density at the particle position, the magnetic force acting on a single particle can be calculated. Multiplying Eq. 6.17 with the particle amount gives the overall magnetic force acting on the membrane.

With the extracted membrane displacement and determined magnetic force the Young's modulus

for a 15%, 20% and 25% membrane can be calculated using Eq. 6.16. The obtained Young's moduli are listed in Tab. 6.2: Comparing the value of the 25 % membrane with the value obtained

PDMS ratio in %	15	20	25
Young's modulus in kPa	149	153	158

Table 6.2: Young's modulus for a 15%, 20% and 25% membrane. The values were obtained by deflecting the membrane with a magnetic gradient field and using plate bending theory.

by resonance frequency measurement and corresponding plate theory, they are in good agreement. Considering the various assumption, such as that the magnetic force acts only in the area of the pole shoe, the deviation between resonance and deflection measurement is negligible small. Comparing the Young's modulus of the 15%, 20% and 25% membrane only a small influence of the matrix stiffness on the membrane's Young's modulus shows.
To summarize this section: The membrane was subjected to the magnetic field of the electromagnet (section 4.2.2). Due to the gradient in the magnetic field a force is acting on the magnetic nickel particles. This displaces the membrane until elastic and magnetic force are equal. Using plate deflection theory, the effective Young's modulus of the membrane could be calculated. Therefore, the defelction of the membrane was optically determined and the magnetic force calculated by assuming that the magnetic force only acts in the area of the pole shoe. The stray fields of nearest neighbor particles were considered. When comparing the obtained Young's modulus of the membrane with the value obtained with resonance measurement and corresponding plate theory a good agreement was observed. The small deviation can be easily explained by the various assumption used in determining the Young's modulus. Comparing membranes of different PDMS mixing ratios only a small influence of the PDMS mixing ration on the membrane's Young's modulus is observed. This was due to the membrane's stack structure of PDMS layer-particle monolayer-PDMS layer. The particle monolayer was significantly more rigid than the PDMS layer, i.e. determined the stiffness of the membrane.

6.2.4 magneto-active valves

In the previous section, the membranes were characterized regarding their Young's modulus and resonance frequencies. It was shown that the particle monolayer significantly increases the membrane's stiffness. The following section focuses on how membrane deformations (magnetostriction) can be used to create a magneto-active valve.
Membranes were produce like described in section 4.1.4 and a PDMS with mixing ration of 20%

was used for the PDMS layers. After 24 hours at $60° C$ the membrane was cut out off the glue rim. Then a cross ($1\,cm \times 1\,cm$) was cut in the center of the membrane, Fig. 6.13 a) inset. Placing the membrane horizontal over the pole shoe of the electromagnet, Fig. 4.10, the magnetostriction was tested, i.e., whether the cut can be opened and closed with the magnetic field. To this end, a rectangular signal with $2\,V$ peak to peak voltage and a frequency of $100\,mHz$ was applied to the electromagnet (maximum current and voltage at the power supply). The low frequency ensured a constant magnetic field as the inductive reactance of the electromagnet could be neglected. By decreasing the distance between membrane and pole the gradient and thus the magnetic force on the membrane could be increased. In the case of the 20 % membrane at a distance of $3.6\,mm$ the magnetic force was sufficient and the cut opened when the magnetic field was applied and was closed again by the restoring elastic forces at zero field.
In order to test if the cut can control liquid flow and drop motion, water droplets were positioned on top of the cut. For a drop volume of $16\,\mu l$ at zero magnetic field, it was observed that the droplet stays on top of the membrane Fig. 6.13 a). So, when the cut was closed, the drop of water did not pass through. Due to the membrane´s hydrophobic nature the water droplet did not spread. Applying a 2 V peak to peak voltage with a rectangular shape and frequency of $100\,mHz$ to the electromagnet, the cut opened, Fig. 6.13 b). The droplet was already slightly sunken into the cut. In image Fig. 6.13 c) the fully open cut, framed withe orange, was visible and the droplet

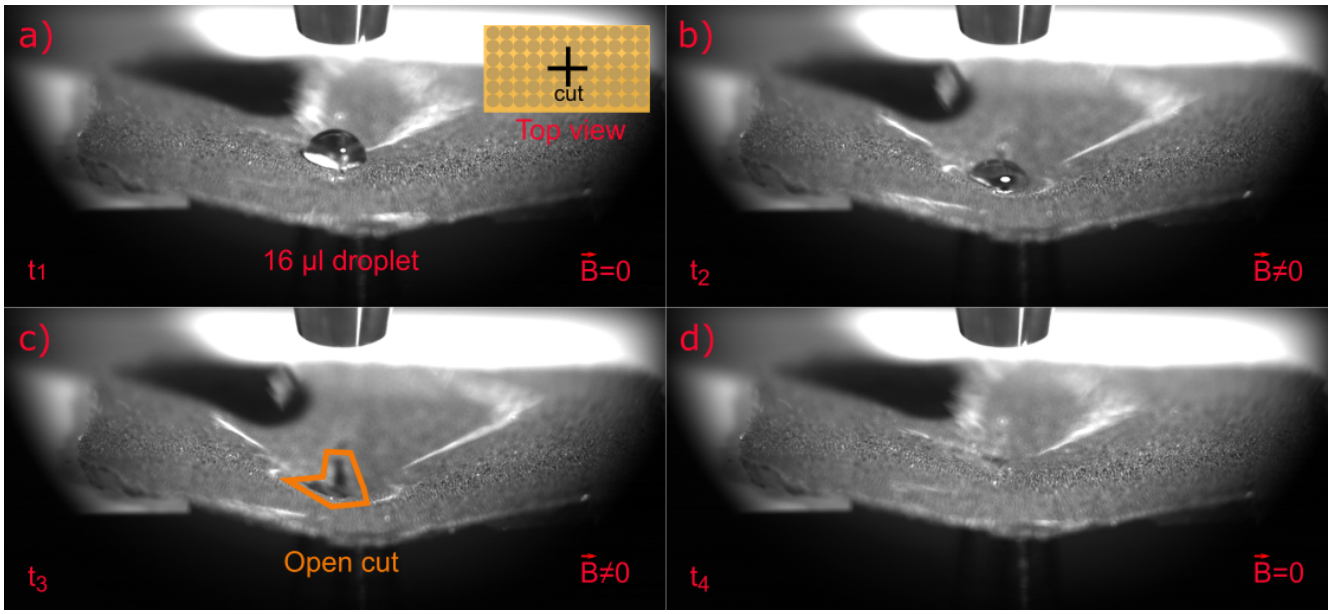

Figure 6.13: $16\,\mu l$ drop placed on a magnetic membrane. The membrane had a cut in the center which could be opened and closed by a magnetic field. a) Zero field. The drop keeps its shape and size. b) The cut opens and the drop starts to sink into the cut. c) The drop has passed the cut. The open cut is encircled (orange). d) The drop has passed the cut and the cut was closed again.

has vanished. It fully passed through the cut. For zero field the cut was able to close again as can bee seen in Fig. 6.13 d). Hence, the cut in the membrane can be opened and closed to let water droplets pass. By placing droplet after droplet on the membrane this process can be repeated. Though, so far it was unclear if the flow of water can also be stopped by closing the cut.
In order to test a use as a magnetic controllable valve the drop size was increased. Water drops with volume of 24, 120 and $300\,\mu l$ were positioned on top of the cut. All drop volumes produced the identical results: Hence, the results are discussed exemplarily for the $120\,\mu l$ drop. At zero field, the droplet remains its drop shape and did not spread on the membrane Fig. 6.14 a). Neglecting evaporation, the system was stable for hours and the water droplet did not pass through the cut. Similar to previous measurement a signal with $2\,V$ peak to peak voltage, rectangular shape and frequency of $100\,mHz$ was applied to the electromagnet. The cut opened, marked with the orange arrow, and the drop sank slightly into the open cut Fig. 6.14 b). But the drop did not pass through the cut. It remained unchanged regarding shape and volume even after the cut closed again, Fig. 6.14 c). Shape and size of the drop were, within the scope of the resolution, identical to the starting drop. Frequently repeating of the opening and closing cycle did not provide a different result Fig. 6.14 d). So the drop's surface tension and the membrane´s hydrophobic nature prevented the water drops with volume of 24 to $300\,\mu l$ to pass through the open cut.

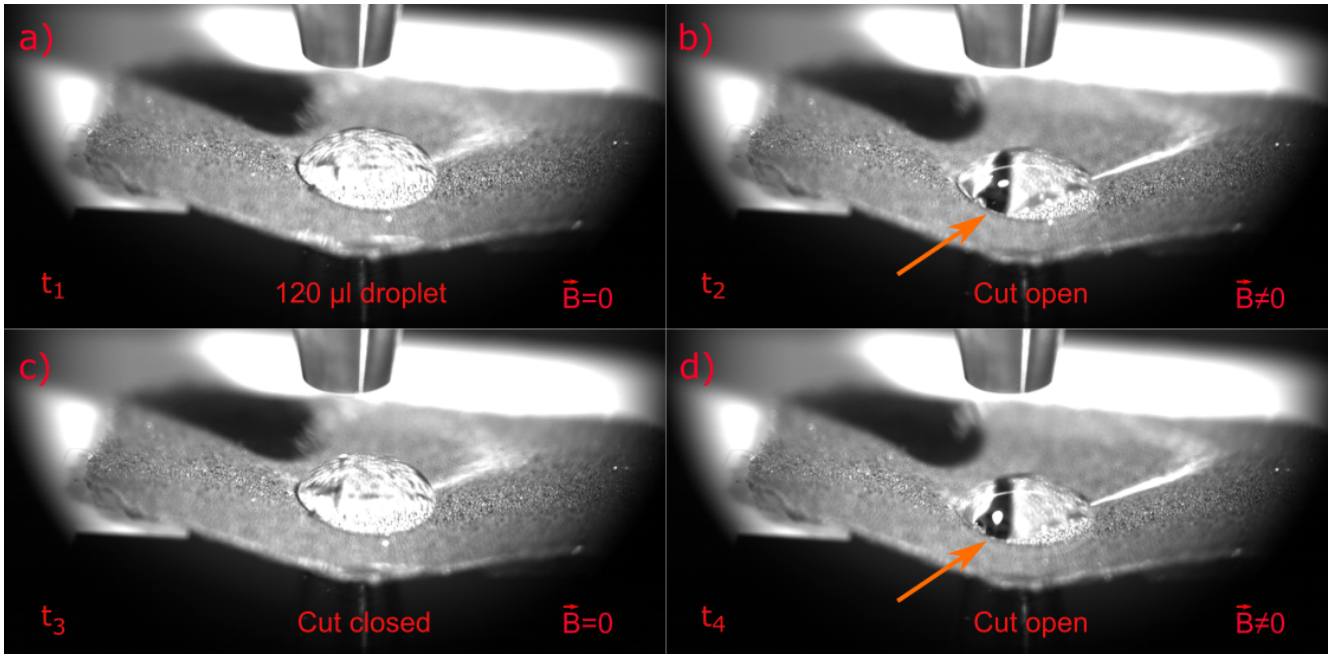

Figure 6.14: $120\,\mu l$ drop placed on a magnetic membrane. The membrane had a cut in the center which could be opened and closed by a magnetic field. a) Zero field case. The drop keeps its shape and size. b) The cut opens and the drop starts to sink into the cut. An orange arrow marks the open cut. c) Even though the cut was opened and closed the drop did not pass. d) After repeated opening and closing cycles the drop still stayed on top of the membrane.

Finally a water drop of $600\,\mu l$ was used: Without a field gradient the drop rests on top of the membrane in its equilibrium state, Fig. 6.15 a). Applying the same magnetic field gradient as in the previous measurements the cut in the membrane opens up. Similar to the other volume sizes the drop began to sink into the cut Fig. 6.15 b). Unlike for the $16\,\mu l$ drop the cut was not large enough for the drop to pass with complete integrity of its shape and the drop starts to flow Fig. 6.15 c). This was due to the larger gravity force acting on the droplet and thus, the increased volume ensured a flow of water through the cut. At the time the gap was closed again, the drop had completely passed the cut Fig. 6.15 d). This showes, that for a sufficient volume of water the application of a magnetic field gradient can start a flow of water. Still the stopping of the water flow was an issue that was more subtle than in the $16\,\mu l$ case.
In order to close the cut while water was still passing through the cut, the frequency was increased to $1\,Hz$. Thereby it was observed, that even though the cut tried to close the water drop was not stopped from flowing Fig. 6.16 a-d). One assumption was that the nickel particles at the cut´s edges form a hydrophilic channel preserving the water flow even for closed cuts. Another explanation was, that the restoring elastic forces were not strong enough to stop the liquid flow. To exclude the issue of a hydrophilic channel, the membrane was structured by using a glue cross (see chapter 4.1.4) and preventing particles to lie at the cut's edges. Repeating the previous measurement with a $600\,\mu l$ droplet revealed that the water droplet once in motion still passes

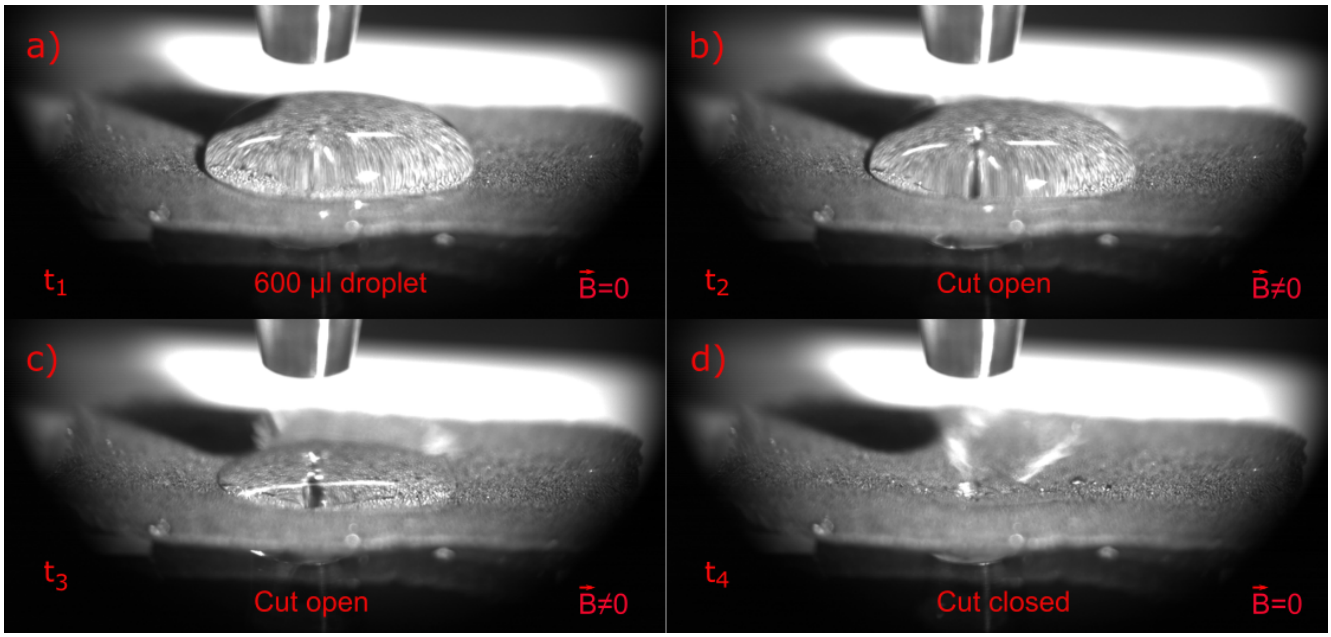

Figure 6.15: $600\,\mu l$ drop placed on a magnetic membrane. The membrane had a cut in the center which could be opened and closed by a magnetic field. a) Zero field case. The drop keeps its shape and size. b) The cut opens and the drop starts to sink into the cut. c) The drop flows through the cut. d) The drop has passed the cut and the cut was closed again.

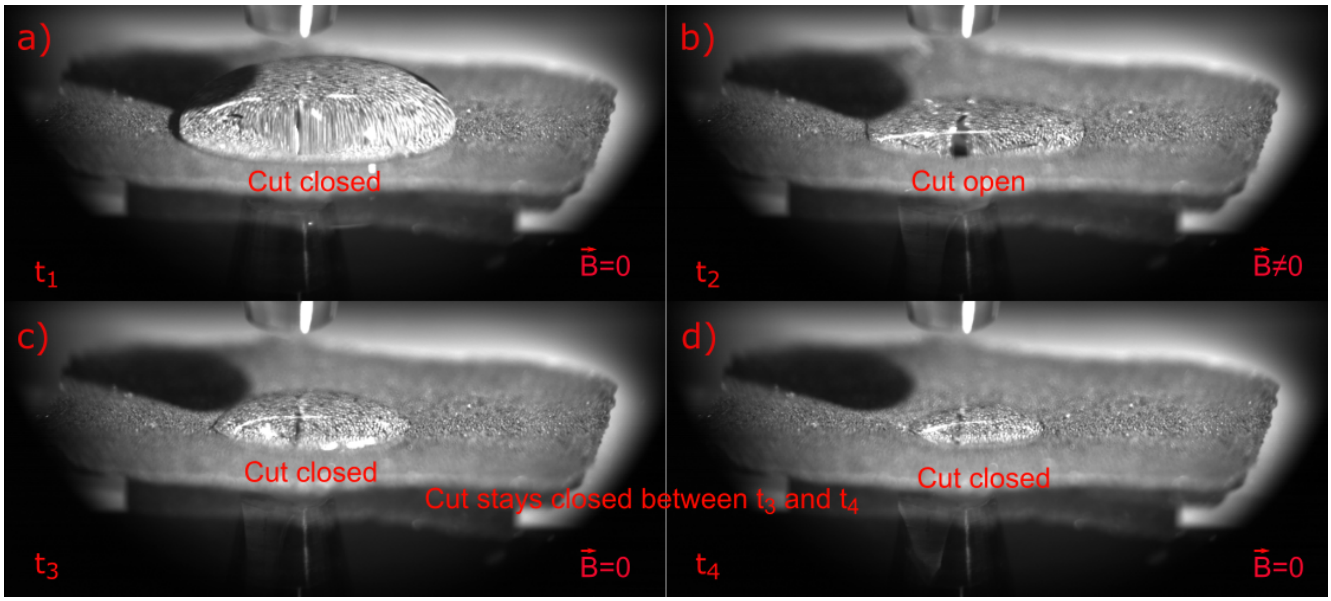

Figure 6.16: $600\,\mu l$ drop placed on a magnetic membrane. The membrane had a cut in the center which could be opened and closed by a magnetic field. a) Zero field case. The drop keeps its shape and size. b) The cut opens and the drop starts to sink into the cut. c), d) Even though the cut was closed the drop still flows.

after the cut was closed. Hence, the force of the running water (surface tension, capillary force) was stronger than the restoring elastic force of the membrane.
In order to increase the elastic restoring forces the Young's modulus of the membrane could be adapted by using a PDMS with higher mixing ratio. Since this would also increase the required field strength required to open the cut, another approach was used. The cut's edges were coated with lubricating grease in order to increase the hydrophobicity and seal the cut more efficiently at zero fields, i.e. seal tiny gaps that were created by mechanically cutting the membrane. This increased the drop volume that could stay on the membrane to $2400\mu l$ so for times more as to previous measurement. Drops exceeding this volume started flowing again once the cut was opened by the magnetic field and were not stopped from flowing once the cut closed. Hence, the following mechanism could be determined: The hydrophobicity of the cut influenced the drop volume that was possible to stay on top of the membrane. Once the drop volume exceeds a limit the gravity force acting on it was strong enough to overcome the repelling hydrophobicity and the drop started to flow as soon as the cut in the membrane opened. To stop the liquid flow though, the hydrophobicity of the cut had no influence. Also tiny gaps that were created by cutting the membrane and remained for zero fields could be excluded. This supports the assumption that the restoring elastic forces were to weak to stop the liquid flow. Increasing the Young's modulus should clear this uncertainty. Unfortunately, a larger Young's modulus results in stronger magnetic fields required to open the cut which could not be realized with the used electromagnetic setup.

To summarize this section: The magnetic structured membranes can function as a droplet selector. To show this, a cross ($1\,cm \times 1\,cm$) was cut into the membrane that opens when the membrane was subjected to a magnetic field and closes after the field was turned off. Subsequently, water droplets with volume from 16 to $600\,\mu l$ were placed on top of the membrane. Opening and closing the cut showed that a certain volume range exists for which the drops are not able to pass the cut. Droplets with smaller or larger volume could pass. Once the drop had started to flow through the cut a closing of the cut could not stop the liquid flow. Increasing the hydrophobicity of the cut by coating the edges with lubricating grease allowed for a higher droplet volume to remain on the membrane but could not stop the liquid flow as well. So the ratio between hydrophobicity and gravity force on the droplet determines whether the droplet flows or not. In contrast, to stop the liquid flow a larger elastic restoring force is required. This could be achieved by a larger Young's modulus of the membrane and will be subject of future investigations.

7 Conclusion

Within this work, MRE samples with defined inter-particle distance and particle arrangement were analyzed to link their particle motion to the magnetostriction effect, i.e. linking microscopical, field induce particle movements to macroscopic deformations of the sample. To this end, MRE samples were prepared similar to [133, 135], i.e. as stacked PDMS layers, section 4.1. This preparation method allowed to place the particles on a crosslinked PDMS layer and facilitated a defined particle arrangement with quite precise inter-particle distance. To induce particle displacement, MRE samples were centered in the Halbach-array, section 4.2.1, and thus subjected to a homogenous magnetic field of $\approx 180\,mT$. The induced particle movement was optically detected and evaluated by tracking of the particle position with TrackMate [165]. Thus, also the inter-particle distance changes could be analyzed.
In a quantitative comparison to simulations, to keep the influencing variables at a manageable level, MRE sample comprised at first two, in maximum up to four, superparamagnetic nickel particles with a inter-particle distance of roughly one particle diameter. As a comparison with simulation was aspired, particles were prevented from getting into contact by using PDMS layers of a Young's modulus of $7.2\,kPa$. Preventing particles from touching was crucial, since touching particles create a diverging deformation of the elastic matrix between the particles, which is difficult to simulate. Particle displacement was induce by a homogenous magnetic field and the inter-particle distance was determined for various magnetic field orientations. In order to predict the particle movement, Metsch *et al.* conducted finite element simulations using a three-dimensional fully coupled continuum model. For all samples, a good agreement between experiments and simulation was observed. Thus, their novel approach to predict particle movement by modeling the particles magnetization, was validate. Consequently, the three-dimensional fully coupled continuum model seems to be applicable to even complexer systems. Furthermore, a high sensitivity to the initial particle position was observed, highlighting the importance of detailed knowledge of the underlying particle distribution as it determines the actual particle displacement.
To allow a comparison between simulation and experiments, the particles were prevented from touching by using a stiff PDMS matrix. Adapting the PDMS mixing ratio, a touching of particles was enabled. A novel strong magneto-active state was observed in MRE samples comprising two nickel particles. The strong magneto-active state was characterized by a major change in the inter-particle distance, i.e. a switch from touching to separated particles or vice versa, which was

induced with a small change in the magnetic field orientation. The change in the inter-particle distance ranged up to one particle diameter and showed a hysteresis loop in relation to the angle β between particle axis and magnetic field orientation. The hysteretic nature of this inter-particle distance change is a consequence of the bistability in the total energy (sum of elastic and magnetic energy). A similar bistability effect was theoretically described by Biller, *et al.* [16, 17], for an increasing magnetic field strength. The presented work showed that the bistability also exists as a function of the magnetic field orientation.

The sensitivity of the magneto-active configuration on the initial inter-particle distance, matrix stiffness and magnetic field strength was determined. A range of $r_{min} < r_b < r_{max}$, with r_b the initial inter-particle distance, was determined for which the magneto-active state was stable. For $r_b < r_{min}$ particles never separated while for $r_b > r_{max}$ particles never touched. Furthermore, particles with small initial inter-particle distance separated at angles $\beta > 54.7°$, which experimentally supports the assumption that dipole-dipole approximation does not hold for particles in contact. As the bistability in the total energy can be influenced either by the elastic or by the magnetic energy, a change in the Young's modulus of the PDMS matrix leads to a similar change in the inter-particle distance change as the change in the initial distance. For too stiff PDMS matrices particles never touched while for too weak PDMS matrices particles never separated. Overall though, the magneto-active state was more sensitive to the Young's modulus.

The magnetic force can also been governed by the magnetic field strength and hence, the same trend was observed with increasing or decreasing magnetic field strength. This new magneto-active state was strongly dependent on the ratio between elastic and magnetic force and thus, only stable for a defined range of initial inter-particle distance, Young's moduli of the PDMS matrices and magnetic field strength. It endured at least forty $360°$ rotations of the magnetic field. The magnetic field orientation can be altered more easily than the magnetic field strength. This makes the novel magneto-active state highly appealing to be used in actuators.

Rarely, a MRE only consists of two particles. To gain more insight in the effects of increasing particle numbers, the system was expanded by a third particle. Since the used preparation method only allows to define the initial inter-particle distance and particle size to a certain precision, some scattering of the particle positions was unavoidable. Therefore, also the magnetic interaction shows some scattering . This leads to the fact, that systematically the particle pair with higher initial inter-particle distance was first to separate. Consequently, while the magneto-active configuration of the particle pair with smaller initial inter-particle distance resembled the one of a sole particle pair, the hysteresis for the other particle pair altered. Apparently, the matrix mediated the displacement of the closer particle pair and changed the inter-particle distance of the neighboring particle pair. Thus, a third particle altered the over all magneto-active configuration due to arising

asymmetries in the magnetic interaction.
The samples were thinned to make the generated deformations more accessible and the particle number was increased to fourteen particles. Under an applied magnetic field, a disintegration into particle groups was observed, i.e. no continuous particle chain formed. A strong dependence on the initial inter-particle distance was identified and particles with a smaller initial inter-particle distance as at least one neighboring particle pair, got into contact. Thereby, the distance to adjacent particles was increased and inevitable the magnetic force was not strong enough to overcome the elastic force, i.e. particle groups formed. Therefore, the change in the end-to-end distance of the particle line was significantly smaller as for the two and three particle system. Furthermore, the images showed darker and lighter areas while the particles were displaced. This could indicate, that the surface of the thin layer was deformed and macroscopic deformations emerged. Future measurements need to be conducted in order to quantize these surface deformations.
Introducing further particles into the system, magneto-activity particle lattices with five by five particles were prepared. Three characteristic particle group formation process could be identified:

1. Only small particle groups form (up to three particles)
2. A peak at particle groups containing five particles
3. Large particle groups (particle number>five)

Lattice imperfections, such as variations of the initial inter-particle distance from the mean value, predicted quite precisely the particle group formation for magnetic fields orientated along the lattice edges. Smaller distances than the mean value lead particle pairs to get into contact. In contrast, larger distances than the mean value lead in general to separate particle pairs. To show a peak at particle groups containing five particles, the initial inter particle distance needed to be small enough so that particle chains along the field direction formed. To form particle groups comprising more than five particles the field was directed at an angle to the lattice edges. Then particles connected in a "wavy" chain like structure along the magnetic field. As a consequence of those various particle displacements, the lattice showed more or less matrix damage. After the magnetic field rotation, particle rested not at their initial position. The average particle group size was correlated to the area the rim particles of the lattice enclosed. It applies, the larger the average group size, the smaller the area was. Furthermore, for all lattices an area decrease between zero field and magnetic field was observed. Hence, to generate larger matrix deformation a particle group formation of large groups was beneficial. Thereby though, one has to consider that the multitude of particle displacements can lead to a matrix damage.
Finally, the preparation method was used to create MRE samples containing a monolayer of dense packed particles like magnetically hollow PDMS spheres. To this end, the PDMS solution was

crosslinked in a density matched solution of water and propan-2-ol and then coated with nickel particles. Afterwards, the magnetically hollow PDMS spheres were either completely encapsulated in a PDMS matrix or glued to the bottom of a glass container and surrounded by air or water. Centering the spheres inside the Halbach-array and varying the field orientation in $5°$ steps lead to following observations: The spheres elongated along the magnetic field direction while in orthogonal direction a reduction of the sphere diameter was determined, i.e. the spheres showed a magnetic deformation effect [52, 140, 141, 143, 161, 182, 185]. This elongation changed its direction according to the magnetic field orientation and a change in the diameter between $\approx 6\%$ and $\approx 8.5\%$ was extracted. From a microscopic view, a particle movement mostly at the poles accompanied the magnetic deformation effect. On top of the magnetic deformation effect a second deformation was observed. It was generated by a magnetic field gradient that effectively compressed the sphere from the top. Therefore, the second deformation was in contrast to the magnetic deformation effect strongly influenced by the surrounding media. While the sphere embedded in PDMS increased its diameter not significantly compared to its initial diameter, the sphere surrounded by air or water increased its diameter up to $\approx 24\%$. Combining those two deformations makes the spheres interesting for application as, on one hand, large deformations can be created and, on the other hand, the deformation direction can be switched by alternating the magnetic field direction.

Freestanding magneto-active membranes, i.e. a dense packed particle monolayer positioned in between two thin PDMS layer were prepared. To determine the effective Young's modulus of the membrane, resonance frequency and deformation measurements were conducted. Using the Uflyand-Mindlin plate theory a Young's modulus of $154\,kPa$ (resonance frequency measurement) respectively $158\,kPa$ (deformation measurement) was calculated. Considering the approximations used for both calculations the values are in good agreement. Hence, with both independent measurements a Young's modulus was obtained that exceeds the Young's modulus of the sole PDMS layers by far. As the particle monolayer was rigid compared to the PDMS layer the special arrangement of PDMS layer- particle monolayer -PDMS layer ensured a large stiffening of the membrane. Thereby only a small influence of the PDMS mixing ratio on the membrane stiffness was observed.

Cutting a cross of $1\,cm \times 1\,cm$ into the membrane, its magneto activity could be used to open and close the cut with an external magnetic gradient field, e.g., to allow drops to pass through. A correlation between the drop volume and its behaviour at opening and closing of the cut, was observed. Water droplets smaller than a certain volume passed through the open cut while keeping their shape integrity. Water droplets larger than a certain volume started flowing once the cut was opened. Water droplets with volumes in between remained in their drop shape for

numerous opening and closing cycles of the cut. Hence, whether a water droplet passes through the cut depended strongly on the ratio between hydrophobicity and gravity acting on the drop. After the water started flowing it could not be stopped by closing the cut. The restoring elastic force was not enough to overcome the surface tension and capillary forces of the liquid flow.

7.1 Outlook

The results of the present thesis showed that a precise positioning of the magnetic particles is important for an optimized magneto activity of the sample. In order to allow for an efficient preparation of larger samples, I tested different strategies. Particle alignment with magnetic force and structured template was shown. Future work need to focus on achieving a particle transfer process between the template and the PDMS matrix. Using spherical particles of identical size in combination with the alignment them in the MRE samples would further decrease influencing variables such as lattice imperfection on the particle group formation. This could lead to a more detailed understanding of particle group formation in microscopically structured MRE samples. Creating large particle groups which expand over the whole sample can be essential to generate tailored deformations. Thereby, possible matrix damages need to be considered.
Preparing membranes with larger Young's modulus can be the key to increase the elastic restoring force and thus, stopping actively a liquid flow. Therefore, also stronger magnetic field strength are required to open the cut. The preparation method used in the presented work has huge potential and can be used to prepare MRE samples with beneficial and novel deformation.

List of Tables

List of Figures

Glossary

Symbols in chapter 2

Symbol	Units	Meaning
G	Pa	Shear modulus
G_0	Pa	Fitting parameter in the power law fit
$\vec{H}$	A/m	Magnetic field strength inside the particle
$\vec{H}_d$	A/m	Demagnetization field
$\vec{H}_e$	A/m	External, i.e., applied Magnetic field strength
$\vec{m}$	Am^2	Magnetic moment
$\vec{M}_s$	A/m	Saturation magnetization
$\vec{M}_p$	A/m	Particle magnetization
p	%	Percentage of reacted bonds
p_c	%	Percentage of reacted bonds at the percolation point
r	%	Mixing ratio
r_c	%	Critical mixing ratio
t		Fitting exponent
V_p	m^3	Particle volume
μ_r		Relative permeability
ς	m/A	Fitting parameter
γ_d		Demagnetization factor

Symbols in chapter 3

Symbol	Units	Meaning
a	m	Position of point charges
$\vec{B}$	T	Magnetic flux density
β	$^\circ$	Angle between magnetic field and particle axis
β_m	$^\circ$	"Magic angle"
$C_{j,k}$		Material parameter of the hyperelastic material model
χ		Magnetic susceptibility
χ_e		Electric susceptibility
d	m	Thickness of the sheared sample
D	As/m^2	Electric flux density
D_k		Material parameter of the hyperelastic material model
E	Pa	Young's modulus (elastic modulus)
$\vec{E}$	V/m	Electric field strength
$\vec{E}_p$	V/m	Electric field strength of electric dipole
η	$Pa\,s$	Viscosity
ϵ_0	As/Vm	Electric vacuum permeability
$\vec{F}_m$	N	Magnetic dipole-dipole force
G	Pa	Shear modulus
$G*$	Pa	Complex shear modulus
G'	Pa	Storage modulus (real part of $G*$)
G''	Pa	Loss modulus (imaginary part of $G*$)
γ		Strain
$\boldsymbol{\gamma}$		Strain tensor
$\dot{\gamma}$		Shear rate
γ_0		Strain amplitude
$\gamma_{i,j}$		Components of strain tensor
γ_d		Demagnetization factor
$\vec{H}$	A/m	Magnetic field strength inside the particle
$\vec{H}_p$	A/m	Magnetic field strength of a magnetic dipole
$\vec{H}_d$	A/m	Demagnetization field
$\vec{H}_e$	A/m	External, i.e., applied Magnetic field strength
$I_{1,2,3}$		Invariants of the hyperelastic material
J_v		Jacobian determinant
K_b	Pa	Bulk modulus (compression modulus)

λ	Pa	Lamé coefficient
$\lambda_{stretch}$		Principal stretches of the hyperelastic material model
$m_{0,1,2,...}$		Coefficient generalized Kelvin-Voigt model
$\vec{m}$	Am^2	Magnetic moment
$\hat{m}$	Am^2	Unity vector of the magnetic moment
$\|m\|$	Am^2	Norm of the magnetic moment
$M_{ii,i\neq j}$		Displacability matrices
$\vec{M}$	A/m	Magnetization
$\vec{M}_p$	A/m	Particle magnetization
μ	Pa	Lamé coefficient
μ_0	N/A^2	Magnetic vacuum permeability
$n_{0,1,2,...}$		Coefficient generalized Kelvin-Voigt model
ν		Poisson ratio
ω	Hz	Angular frequency
ψ	J	Free energy
ψ^{mag}	J	Magnetic part of the free energy
ψ^{mech}	J	Mechanical part of the free energy
$\vec{p}$	Ams	Electric dipole moment
$\vec{P}$	As/m^2	Electric polarization
q	C	Electric point charge
$\vec{r}$	m	Distance
$\hat{r}$	m	Unity vector of the distance
$\|r\|$	m	Norm of the distance
ρ	kg/m^3	Mass density per unit volume
σ	Pa	Stress
$\boldsymbol{\sigma}$		Stress tensor
σ	Pa	Stress
$\sigma_{i,j}$	Pa	Components of stress tensor
t	s	Time
t_0	s	Starting time of the applied stress
τ	s	Viscoelastic relaxation time
Θ_p	V	Electrostatic potential
U	m	Shift of the sheared sample
U_i		Deformation fields
V	m^3	Volume

V_p	m^3	Particle volume
W	J/m^3	Elastic energy density
W_{diss}	J/m^3	Dissipative energy density
W_d	J/m^3	Deviatoric part of the elastic energy density W
W_V	J/m^3	Volumetric part of the elastic energy density W

Symbols in chapter 4

Symbol	Units	Meaning
b		Fit parameter
$\vec{B}$	T	Magnetic flux density
β	$^\circ$	Angle between magnetic field and particle axis
β_i	$^\circ$	Angle between initial and deflected particle axis
χ^2		Tolerance of the fit
d	m	Particle diameter
G	Pa	Shear modulus
G_0	Pa	Fit parameter
Γ	Nm	Elastic torque
Γ_m	Nm	Magnetic torque
κ_e		Geometrical elastic rotation factor
$\vec{m}$	Am^2	Magnetic moment
$\hat{m}$	Am^2	Unity vector of the magnetic moment
$\|m\|$	Am^2	Norm of the magnetic moment
μ_0	N/A^2	Magnetic vacuum permeability
N		Number of particles
$\vec{P}_{0,i}$	m	Particle's center to center vector
$p_{1,2,3,4}$	T/m	Fit parameters of the exponential fit
$\vec{r}$	m	Distance
$\hat{r}$	m	Unity vector of the distance
$\|r\|$	m	Norm of the distance
r_c	%	Fit parameter
R	Ω	Resistance
$Round$		Roundness of the particles
θ	$^\circ$	Angle of the magnetic field in respective to x- or y-axis
V	m^3	Volume
V_p	m^3	Particle volume
v		Fit parameter
$x_{0,i}$	m	x-coordinate
$y_{0,i}$	m	y-coordinate

Symbols in chapter 5

Symbol	Units	Meaning
a		Length of the harmonic springs
$\vec{B}$	T	Magnetic flux density
β	$^\circ$	Angle between magnetic field and particle axis
$\beta_{1,2}$	$^\circ$	Lattice diagonal angle
β_m	$^\circ$	Magic angle: Magnetic interaction switches from attraction to repulsion or vice versa
d_i	m	Particle diameter
$dia_{1,2}$	m	Diagonal lattice direction
Δd_{12}	m	Inter-particle distance change
δ	$^\circ$	Lattice angle
$\epsilon 1, 2$	$^\circ$	Lattice diagonal angle
e	J	Pairwise energy
e^1		First derivative of the pairwise energy
e^2		Second derivative of the pairwise energy
k		Stiffness of the harmonic springs
$\vec{m}$	Am^2	Magnetic moment of the particle
N		Number of particles per chain
r_b	m	Range of initial inter-particle distance
r_{min}	m	Lower limit of initial inter-particle distance
r_{max}	m	Upper limit of initial inter-particle distance
θ	$^\circ$	Magnetic field angle relative to the x axis

Symbols in chapter 6

Symbol	Units	Meaning
α, β		Eigenvalues
a, b	m	Edge length of the membrane
A	m^2	Area of the beam or membrane
A_l	m^2	Area of load
A_s	m^2	Cross-sectional area of the beam or membrane
A_T	m	Amplitude of the oscillation
$\vec{B}$	T	Magnetic flux density
χ		Magnetic susceptibility
d	m	Particle diameter
d_z	m	Membrane deflection
$d_{m,n}$		Deflection coefficients
E	Pa	Young's modulus
E_s	Pa	Effective Young's modulus
E_m	Pa	Young's modulus of pure matrix material
$\varepsilon_i^{x,y}$	%	elongation in relation to the initial sphere diameter
$\varepsilon_r^{x,y}$	%	ratio between minimum and maximum sphere diameter
f	$1/s$	Excitation frequency
f_m	$1/s$	membrane oscillation frequency
F_m	kgm/s^2	Magnetic force
G	Pa	Shear modulus
$\vec{H}_e$	A/m	External magnetic field strength
I	kgm^2	Axial geometrical moment of inertia
i	kgm^2	Rotational inertia
κ, k		Order of the natural frequencies
K	Pa	Plate stiffness (Bulk modulus)
l	m	Length of the beam or membrane
λ		Correction coefficient Uflyand-Mindlin theory
Λ_0	kgm/s^2	Applied load
m_m	kg	Membrane weight
$\vec{M}_p$	A/m	Particle magnetization
μ_0	N/A^2	Vacuum permeability
ν		Poisson ratio
ω	$1/s$	Angular frequency

ω_k	$1/s$	Natural frequencies (resonance frequencies)
ω_t	$1/s$	Natural frequencies (resonance frequencies) of a Timoshenko beam
$\omega_{u_{m,n}}$	$1/s$	Natural frequencies (resonance frequencies) of a Uflyand-Mindlin plate theory
ρ	kg/m^3	Membrane density
ς_r		Correction coefficient for rotation inertia
ς_s		Correction coefficient for shear deformation
T	s	Half the oscillation period
t	s	Time
t_b	m	Height (thickness) of the membrane (plate) or beam
t_c		Phase shift of the oscillation
θ	$^\circ$	Magnetic field orientation relative to the x-direction
Θ	%	Particle volume fraction
τ		Correction factor natural frequencies (resonance frequencies) Timoshenko beam
V	m^3	Membrane volume
V_p	m^3	Particle volume
W		General solution functions
y		Sine fit function
y_0		Shift around the central oscillation point

Abbreviations

Abbreviation	Long-name
C_3H_8O	Propan-2-ol
DMS-V25	Difunctional vinyl-terminated polydimethylsiloxane
HMS-151	SiH-containing methylhy-drosiloxane–dimethylsiloxane crosslinker
MRE	Magneto-rheological elastomer
MRF	Magnetorheological fluids
MR-effect	Magnetorheological effect
PDMS	Polydimethylsiloxan
PVA	Polyvinylalcohol
SiH	Silyl group
SQUID	Superconducting quantum interference device
VSM	Vibrating sample magnetometer

Bibliography

[1] Chemiedidaktik uni wuppertal. https://chemiedidaktik.uni-wuppertal.de/fileadmin/Chemie/chemiedidaktik/disido/de/info/m_fact/crossmod.htm.

[2] Wacker Chemie AG. Solid and liquid silicone rubbermaterial and processing guidelines. Technical report, Wacker Chemie AG, https://www.wacker.com/h/medias/6709-EN.pdf, 2019.

[3] Raju Ahamed, Seung-Bok Choi, and Md Meftahul Ferdaus. A state of art on magneto-rheological materials and their potential applications. *Journal of Intelligent Material Systems and Structures*, 29(10):2051–2095, 2018.

[4] Johannes Altenbach, Holm Altenbach, and Konstantin Naumenko. *Schubelastische Platten mit kleinen Durchbiegungen*, pages 289–314. Springer Berlin Heidelberg, Berlin, Heidelberg, 1998.

[5] Eyvazian Arameh, Hamouda Abdel Magid, Tarlochan Faris, Mohsenizadeh Saeid, and Dastjerdi Ali Ahmadi. Damping and vibration response of viscoelastic smart sandwich plate reinforced with non-uniform graphene platelet with magnetorheological fluid core. *Steel and Composite Structures*, 33(6):891–906, December 2019.

[6] Günter K. Auernhammer. Magnetorheological gels in two and three dimensions: understanding the interplay between single particle motion, internal deformations, and matrix properties. *Archive of Applied Mechanics*, 89(1):153–165, January 2019.

[7] A. K. Bastola, M. Paudel, and L. Li. Dot-patterned hybrid magnetorheological elastomer developed by 3d printing. *Journal of Magnetism and Magnetic Materials*, 494:165825, January 2020.

[8] A. K. Bastola, M. Paudel, and L. Li. Line-patterned hybrid magnetorheological elastomer developed by 3d printing. *Journal of Intelligent Material Systems and Structures*, 31(3):377–388, November 2020.

[9] A.K. Bastola, M. Paudel, and L. Li. Development of hybrid magnetorheological elastomers by 3d printing. *Polymer*, 149:213 – 228, 2018.

[10] Anil K. Bastola and Mokarram Hossain. A review on magneto-mechanical characterizations of magnetorheological elastomers. *Composites Part B: Engineering*, 200:108348, November 2020.

[11] Anil Kumar Bastola, Milan Paudel, Lin Li, and Weihua Li. Recent progress of magnetorheological elastomers: a review. *Smart Materials and Structures*, 2020.

[12] G. K. Batchelor and J. T. Green. The determination of the bulk stress in a suspension of spherical particles to order c2. *Journal of Fluid Mechanics*, 56(3):401–427, 1972.

[13] Alireza Beheshti, Ramin Sedaghati, and Subhash Rakheja. Finite deformation analysis of isotropic magnetoactive elastomers. *Continuum Mechanics and Thermodynamics*, June 2020.

[14] C. BELLAN and G. BOSSIS. Field dependence of viscoelastic properties of mr elastomers. *International Journal of Modern Physics B*, 16(17n18):2447–2453, 2002.

[15] Jörgen S. Bergström and Mary C. Boyce. Mechanical Behavior of Particle Filled Elastomers. *Rubber Chemistry and Technology*, 72(4):633–656, 09 1999.

[16] A. M. Biller, O. V. Stolbov, and Yu. L. Raikher. Mesoscopic magnetomechanical hysteresis in a magnetorheological elastomer. *Phys. Rev. E*, 92:023202, Aug 2015.

[17] Anastasiya Biller, O Stolbov, and Yuriy Raikher. Modeling of particle interactions in magnetorheological elastomers. *Journal of Applied Physics*, 116:114904–114904, 09 2014.

[18] Anastasiya Biller, O Stolbov, and Yuriy Raikher. Bistable magnetomechanical behavior of ferromagnetic particles in an elastomer matrix. *Computational Continuum Mechanics*, 8:273–288, 01 2015.

[19] Anastasiya Biller, O Stolbov, and Yuriy Raikher. Dipolar models of ferromagnet particles interaction in magnetorheological composites. *Journal of Optoelectronics and Advanced Materials*, 17:1106–1113, 07 2015.

[20] Anastasiya Biller, O Stolbov, and Yuriy Raikher. Elastic properties of magnetorheological elastomer: description with the two-particle mesoscopic model. *IOP Conference Series: Materials Science and Engineering*, 208:012007, 06 2017.

[21] Anastasiya Biller, O Stolbov, and Yuriy Raikher. Two-particle element of a magnetorheological elastomer under a cyclic magnetic field. *Journal of Physics: Conference Series*, 994:012001, 03 2018.

[22] Anna Boczkowska, Stefan F. Awietjan, Stanisław Pietrzko, and Krzysztof J. Kurzydłowski. Mechanical properties of magnetorheological elastomers under shear deformation. *Composites Part B: Engineering*, 43(2):636–640, March 2012.

[23] Dmitry Borin. Targeted patterning of magnetic microparticles in a polymer composite. *Philosophical Transactions of the Royal Society A: Mathematical, Physical and Engineering Sciences*, 378(2171):20190256, 2020.

[24] Dmitry Borin, Stefan Odenbach, Larisa Iskakova, and Andrey Zubarev. Non-ergodic tube structures in magnetic gels and suspensions. *Soft Matter*, 14:8537–8544, 2018.

[25] Dmitry Borin, Gennady Stepanov, Anton Musikhin, Andrey Zubarev, Anton Bakhtiiarov, and Pavel Storozhenko. Magnetorheological effect of magnetoactive elastomer with a permalloy filler. *Polymers*, 12(10), 2020.

[26] D.Yu. Borin, S. Odenbach, and G.V. Stepanov. Stress induced by the striction of hybrid magnetoactive elastic composites. *Journal of Magnetism and Magnetic Materials*, 470:85 – 88, 2019. International Baltic Conference on Magnetism: focus on functionalized magnetic structures for energy and biotechnology.

[27] Derek Breid and Alfred J. Crosby. Curvature-controlled wrinkle morphologies. *Soft Matter*, 9:3624–3630, 2013.

[28] Dengke Cai and Andreas Neyer. Cost-effective and reliable sealing method for pdms (polydimethylsiloxane)-based microfluidic devices with various substrates. *Microfluidics and Nanofluidics*, 9(4):855–864, October 2010.

[29] M. Asun Cantera, Majid Behrooz, Ronald F. Gibson, and Faramarz Gordaninejad. Modeling of magneto-mechanical response of magnetorheological elastomers (mre) and mre-based systems: a review. *Smart Materials and Structures*, 26(2):023001, January 2017.

[30] S. W. Chen, R. Li, Z. Zhang, and X. J. Wang. Micromechanical analysis on tensile modulus of structured magneto-rheological elastomer. *Smart Materials and Structures*, 25(3):035001, February 2016.

[31] Naziha Chirani, L'Hocine Yahia, Lukas Gritsch, Federico Motta, Soumia Chirani, and Silvia Farè. History and applications of hydrogels. *Journal of Biomedical Sciences*, Vol. 4:13–23, 12 2015.

[32] Yo Han Choi, Kwang Hyo Chung, Hyo Bong Hong, and Woon Seob Lee. Production of pdms microparticles by emulsification of two phases and their potential biological application.

International Journal of Polymeric Materials and Polymeric Biomaterials, 67(11):686–692, 2018.

[33] Dominique Collin, Günter K. Auernhammer, Odile Gavat, Philippe Martinoty, and Helmut R. Brand. Frozen-in magnetic order in uniaxial magnetic gels: Preparation and physical properties. *Macromolecular Rapid Communications*, 24(12):737–741, 2003.

[34] E. Coquelle, G. Bossis, D. Szabo, and F. Giulieri. Micromechanical analysis of an elastomer filled with particles organized in chain-like structure. *Journal of Materials Science*, 41(18):5941–5953, September 2006.

[35] M. D. Cowley and R. E. Rosensweig. The interfacial stability of a ferromagnetic fluid. *Journal of Fluid Mechanics*, 30(4):671–688, 1967.

[36] P. Cremer, H. Löwen, and A.M. Menzel. Tailoring superelasticity of soft magnetic materials. *Applied Physics Letters*, 107(17), 2015. cited By 20.

[37] Peet Cremer, Hartmut Löwen, and Andreas M. Menzel. Superelastic stress–strain behavior in ferrogels with different types of magneto-elastic coupling. *Phys. Chem. Chem. Phys.*, 18:26670–26690, 2016.

[38] K. Danas, S.V. Kankanala, and N. Triantafyllidis. Experiments and modeling of iron-particle-filled magnetorheological elastomers. *Journal of the Mechanics and Physics of Solids*, 60(1):120 – 138, 2012.

[39] S.K. De, J.R. White, and Rapra Technology Limited. *Rubber Technologist's Handbook*. Number Bd. 1 in Rubber Technologist's Handbook. Rapra Technology Limited, 2001.

[40] P.G. de Gennes, P.P.G. Gennes, and Cornell University Press. *Scaling Concepts in Polymer Physics*. Cornell University Press, 1979.

[41] Wolfgang Demtröder. *Mechanische Schwingungen und Wellen*, pages 327–386. Springer Berlin Heidelberg, Berlin, Heidelberg, 2015.

[42] Huaxia Deng, Guanghui Han, Yuanyuan Wang, Jialei Deng, Jin Zhang, Mengchao Ma, and Xiang Zhong. Interface modeling of magnetorheological elastomers subjected to variable working strain. *Soft Matter*, 15:5574–5584, 2019.

[43] Julie Diani, Bruno Fayolle, and Pierre Gilormini. A review on the mullins effect. *European Polymer Journal*, 45(3):601 – 612, 2009.

[44] G. Diguet, E. Beaugnon, and J.Y. Cavaillé. Shape effect in the magnetostriction of ferromagnetic composite. *Journal of Magnetism and Magnetic Materials*, 322(21):3337 – 3341, 2010.

[45] Issam Doghri. *Mechanics of Deformable Solids*. Springer Berlin Heidelberg, 2000.

[46] Rani Elhajjar, Chiu-Tai Law, and Alessandro Pegoretti. Magnetostrictive polymer composites: Recent advances in materials, structures and properties. *Progress in Materials Science*, 97:204 – 229, 2018.

[47] I.E. Elishakoff. *Handbook On Timoshenko-ehrenfest Beam And Uflyand- Mindlin Plate Theories*. World Scientific Publishing Company, 2019.

[48] Randall M. Erb, Joshua J. Martin, Rasam Soheilian, Chunzhou Pan, and Jabulani R. Barber. Actuating soft matter with magnetic torque. *Advanced Functional Materials*, 26(22):3859–3880, 2016.

[49] John Douglas Eshelby and Rudolf Ernst Peierls. The determination of the elastic field of an ellipsoidal inclusion, and related problems. *Proceedings of the Royal Society of London. Series A. Mathematical and Physical Sciences*, 241(1226):376–396, 1957.

[50] J.P. Joule Esq. Xvii. on the effects of magnetism upon the dimensions of iron and steel bars. *The London, Edinburgh, and Dublin Philosophical Magazine and Journal of Science*, 30(199):76–87, 1847.

[51] Genoveva Filipcsei and Miklos Zrínyi. Magnetodeformation effects and the swelling of ferrogels in a uniform magnetic field. *Journal of Physics: Condensed Matter*, 22(27):276001, jun 2010.

[52] Lukas Fischer and Andreas M. Menzel. Magnetostriction in magnetic gels and elastomers as a function of the internal structure and particle distribution. *The Journal of Chemical Physics*, 151(11):114906, 2019.

[53] Eva Forster, Matthias Mayer, Raman Rabindranath, Holger Böse, Günther Schlunck, Gareth J. Monkman, and Mikhail Shamonin. Patterning of ultrasoft, agglutinative magnetorheological elastomers. *Journal of Applied Polymer Science*, 128(4):2508–2515, 2013.

[54] Evan Galipeau and Pedro Ponte Castañeda. The effect of particle shape and distribution on the macroscopic behavior of magnetoelastic composites. *International Journal of Solids and Structures*, 49(1):1 – 17, 2012.

[55] D Günther, D Yu Borin, S Günther, and S Odenbach. X-ray micro-tomographic characterization of field-structured magnetorheological elastomers. *Smart Materials and Structures*, 21(1):015005, dec 2011.

[56] Segun Goh, Andreas M. Menzel, and Hartmut Löwen. Dynamics in a one-dimensional ferrogel model: relaxation, pairing, shock-wave propagation. *Phys. Chem. Chem. Phys.*, 20:15037–15051, 2018.

[57] Christian Gollwitzer, Alexander Turanov, Marina Krekhova, Günter Lattermann, Ingo Rehberg, and Reinhard Richter. Measuring the deformation of a ferrogel sphere in a homogeneous magnetic field. *The Journal of Chemical Physics*, 128(16):164709, 2008.

[58] David J. Griffiths. *Introduction to Electrodynamics*. Cambridge University Press, 4 edition, 2017.

[59] Dietmar Gross. *Technische Mechanik 4 : Hydromechanik, Elemente der Höheren Mechanik, Numerische Methoden*. Springer Berlin Heidelberg, Berlin, Heidelberg, 10th ed. 2018 edition, 2018.

[60] Xinchun Guan, Xufeng Dong, and Jinping Ou. Magnetostrictive effect of magnetorheological elastomer. *Journal of Magnetism and Magnetic Materials*, 320(3):158–163, February 2008.

[61] T. Gundermann and S. Odenbach. Investigation of the motion of particles in magnetorheological elastomers by x-$^{\mu}$CT. *Smart Materials and Structures*, 23(10):105013, sep 2014.

[62] Fei Guo and Zhiguang Guo. Inspired smart materials with external stimuli responsive wettability: a review. *RSC Adv.*, 6:36623–36641, 2016.

[63] Vaibhav Gupta, Patrick T. Probst, Fabian R. Goßler, Anja Maria Steiner, Jonas Schubert, Yannic Brasse, Tobias A. F. König, and Andreas Fery. Mechanotunable surface lattice resonances in the visible optical range by soft lithography templates and directed self-assembly. *ACS Appl. Mater. Interfaces*, 11(31):28189–28196, August 2019.

[64] Robert M. Hackett. *Hyperelasticity Primer*. Springer International Publishing, Cham, 1st ed. 2016 edition, 2016.

[65] Abdollah Hajalilou. *Field Responsive Fluids as Smart Materials*. Engineering Materials. Springer Singapore, Singapore, 1st ed. 2016 edition, 2016.

[66] Yi Han, Wei Hong, and LeAnn E. Faidley. Field-stiffening effect of magneto-rheological elastomers. *International Journal of Solids and Structures*, 50(14):2281 – 2288, 2013.

[67] Yi Han, Akshi Mohla, X. Huang, W. Hong, and L. Faidley. Magnetostriction and field stiffening of magneto-active elastomers. *International Journal of Applied Mechanics*, 07:1550001, 2015.

[68] Joachim Heintze. *Lehrbuch zur Experimentalphysik Band 3: Elektrizität und Magnetismus*. Springer Berlin Heidelberg, Berlin, Heidelberg, 1st ed. 2016 edition, 2016.

[69] Shilin Huang, Giorgio Pessot, Peet Cremer, Rudolf Weeber, Christian Holm, Johannes Nowak, Stefan Odenbach, Andreas M. Menzel, and Günter K. Auernhammer. Buckling of paramagnetic chains in soft gels. *Soft Matter*, 12:228–237, 2016.

[70] Hubmagnet. https://de.rs-online.com/web/p/hubmagnete-kabelausfuhrung/3073657/.

[71] imagej. https://imagej.net/Fiji.

[72] D. Ivaneyko, V. Toshchevikov, D. Borin, M. Saphiannikova, and G. Heinrich. Mechanical properties of magneto-sensitive elastomers in a homogeneous magnetic field: Theory and experiment. *Macromolecular Symposia*, 338(1):96–107, 2012.

[73] Dmytro Ivaneyko, Vladimir Toshchevikov, Marina Saphiannikova, and Gert Heinrich. Mechanical properties of magneto-sensitive elastomers: unification of the continuum-mechanics and microscopic theoretical approaches. *Soft Matter*, 10:2213–2225, 2014.

[74] Dmytro Ivaneyko, Vladimir P. Toshchevikov, Marina Saphiannikova, and Gert Heinrich. Magneto-sensitive elastomers in a homogeneous magnetic field: A regular rectangular lattice model. *Macromolecular Theory and Simulations*, 20(6):411–424, 2011.

[75] John David Jackson. *Classical electrodynamics; 2nd ed.* Wiley, New York, NY, 1975.

[76] Roland Jakel. Analysis of hyperelastic materials with mechanica – theory and application examples –. Technical report, PRETECH Predictive Design Technologies GmbH, http://www.pretech.de/jcms/images/pretech/vpb/201004_RJakel_Analysis_of_Hyperelastic_Materials_with_MECHANICA.pdf, 2010.

[77] Maan H. Jawad. *Bending of Simply Supported Rectangular Plates*, pages 1–38. Springer US, Boston, MA, 1994.

[78] Youngdo Jeong, Yu-Cheng Chen, Merve K. Turksoy, Subinoy Rana, Gulen Yesilbag Tonga, Brian Creran, Amitav Sanyal, Alfred J. Crosby, and Vincent M. Rotello. Tunable elastic modulus of nanoparticle monolayer films by host–guest chemistry. *Advanced Materials*, 26(29):5056–5061, 2014.

[79] Kunqiang Jiang, Peter C. Thomas, Samuel P. Forry, Don L. DeVoe, and Srinivasa R. Raghavan. Microfluidic synthesis of monodisperse pdms microbeads as discrete oxygen sensors. *Soft Matter*, 8:923–926, 2012.

[80] Leah M. Johnson, Lu Gao, C. Wyatt Shields IV, Margret Smith, Kirill Efimenko, Kevin Cushing, Jan Genzer, and Gabriel P. López. Elastomeric microparticles for acoustic mediated bioseparations. *Journal of Nanobiotechnology*, 11(1):22, June 2013.

[81] I D Johnston, D K McCluskey, C K L Tan, and M C Tracey. Mechanical characterization of bulk sylgard 184 for microfluidics and microengineering. *Journal of Micromechanics and Microengineering*, 24(3):035017, feb 2014.

[82] Mark R. Jolly, J. David Carlson, Beth C. Muñoz, and Todd A. Bullions. The magnetoviscoelastic response of elastomer composites consisting of ferrous particles embedded in a polymer matrix. *Journal of Intelligent Material Systems and Structures*, 7(6):613–622, 1996.

[83] Richard G Jones, Edward S Wilks, W. Val Metanomski, Jaroslav Kahovec, Michael Hess, Robert Stepto, and Tatsuki Kitayama, editors. *Compendium of Polymer Terminology and Nomenclature*. The Royal Society of Chemistry, 2009.

[84] Josmin P. Jose and Kuruvilla Joseph. *Advances in Polymer Composites: Macro- and Microcomposites – State of the Art, New Challenges, and Opportunities*, chapter 1, pages 1–16. John Wiley & Sons, Ltd, 2012.

[85] Karl A. Kalina, Philipp Metsch, and Markus Kästner. Microscale modeling and simulation of magnetorheological elastomers at finite strains: A study on the influence of mechanical preloads. *International Journal of Solids and Structures*, 102-103:286 – 296, 2016.

[86] Karl Alexander Kalina, Jörg Brummund, Philipp Metsch, and Markus Kästner. Microscale modeling and simulation of magnetorheological elastomers. *PAMM*, 17:27–30, December 2017.

[87] Karl Alexander Kalina, Jörg Brummund, Philipp Metsch, and Markus Kästner. Modeling and simulation of hysteresis effects in magnetorheological elastomers. *PAMM*, 18:e201800319, 12 2018.

[88] Karl Alexander Kalina, Jörg Brummund, Philipp Metsch, Markus Kästner, Dmitry Borin, Julia Linke, and S. Odenbach. Modeling of magnetic hystereses in soft mres filled with ndfeb particles. *Smart Materials and Structures*, 26, 07 2017.

[89] Karl Alexander Kalina, Philipp Metsch, Jörg Brummund, and Markus Kästner. Development of a macro-model for magnetorheological elastomers based on microscopic simulations. *PAMM*, 19, 11 2019.

[90] Abdullah Kamit, M. Ashrul Asbollah, Siti Norliza S. A. Rahman, Fairuzeta Ja'afar, Hartini M. Yasin, Jonathan Hobley, and Anwar Usman. Facile fabrication of PDMS microspheres with and without fluorescent dye doping. *International Journal of Engineering Research & Science*, 5(8):27–34, August 2019.

[91] Sung S. Kang, Kisuk Choi, Jae-Do Nam, and Hyoung J. Choi. Magnetorheological elastomers: Fabrication, characteristics, and applications, 2020.

[92] PA Kelly. Mechanics lecture notes: An introduction to solid mechanics. http://homepages.engineering.auckland.ac.nz/ pkel015/SolidMechanicsBooks/index.html, 2021.

[93] Khalil Khanafer, Ambroise Duprey, Marty Schlicht, and Ramon Berguer. Effects of strain rate, mixing ratio, and stress-strain definition on the mechanical behavior of the polydimethylsiloxane (pdms) material as related to its biological applications. *Biomedical Microdevices*, 11(2):503, December 2008.

[94] Sangtae Kim and Nhan Phan-Thien. Faxén relations and some rigid inclusion problems. *Journal of Elasticity*, 37(2):93–111, January 1994.

[95] Yoonho Kim, Hyunwoo Yuk, Ruike Zhao, Shawn A. Chester, and Xuanhe Zhao. Printing ferromagnetic domains for untethered fast-transforming soft materials. *Nature*, 558(7709):274–279, June 2018.

[96] Slavko Kralj and Darko Makovec. Magnetic assembly of superparamagnetic iron oxide nanoparticle clusters into nanochains and nanobundles. *ACS Nano*, 9(10):9700–9707, October 2015.

[97] Uwe Krey and Anthony Owen. *Electrostatics and Magnetostatics*, chapter 17, pages 119–144. Springer Berlin Heidelberg, Berlin, Heidelberg, 2007.

[98] K. KrishnaBhaskar and K. MeeraSaheb. Effect of aspect ratio on large amplitude free vibrations of simply supported and clamped rectangular mindlin plates using coupled displacement field method. *Journal of Mechanical Science and Technology*, 31(5):2093–2103, May 2017.

[99] J. G. Ku, X. Y. Liu, H. H. Chen, R. D. Deng, and Q. X. Yan. Interaction between two magnetic dipoles in a uniform magnetic field. *AIP Advances*, 6(2):025004, 2016.

[100] M. D. Lechner. *Makromolekulare Chemie : Ein Lehrbuch für Chemiker, Physiker, Materialwissenschaftler und Verfahrenstechniker, 4. überarbeitete und erweiterte Auflage*. Birkhäuser Basel, Basel, 4th ed. 2010 edition, 2010.

[101] Qiaoyuan Li, Xue Han, Jing Hou, Jian Yin, Shichun Jiang, and Conghua Lu. Patterning poly(dimethylsiloxane) microspheres via combination of oxygen plasma exposure and solvent treatment. *J. Phys. Chem. B*, 119(42):13450–13461, October 2015.

[102] W H Li and M Nakano. Fabrication and characterization of PDMS based magnetorheological elastomers. *Smart Materials and Structures*, 22(5):055035, apr 2013.

[103] Yancheng Li, Jianchun Li, Weihua Li, and Haiping Du. A state-of-the-art review on magnetorheological elastomer devices. *Smart Materials and Structures*, 23(12):123001, November 2014.

[104] Tony Lindeberg. Feature detection with automatic scale selection. *International Journal of Computer Vision*, 30(2):79–116, November 1998.

[105] Yongyu Lu, He Zhou, Henan Mao, Shousheng Tang, Lei Sheng, Hu Zhang, and Jing Liu. Liquid metal-based magnetorheological fluid with a large magnetocaloric effect. *ACS Appl. Mater. Interfaces*, 12(43):48748–48755, October 2020.

[106] Ruslan Yu. Lukin, Aidar M. Kuchkaev, Aleksandr V. Sukhov, Giyjaz E. Bekmukhamedov, and Dmitry G. Yakhvarov. Platinum-catalyzed hydrosilylation in polymer chemistry. *Polymers*, 12(10), 2020.

[107] Baoguang Ma, Jens Henrik Hansen, Søren Hvilsted, and Anne Ladegaard Skov. Polydimethylsiloxane microspheres with poly(methyl methacrylate) coating: Modelling, preparation, and characterization. *The Canadian Journal of Chemical Engineering*, 93(10):1744–1752, 2015.

[108] Laurent Malaquin, Tobias Kraus, Heinz Schmid, Emmanuel Delamarche, and Heiko Wolf. Controlled particle placement through convective and capillary assembly. *Langmuir*, 23(23):11513–11521, November 2007.

[109] James E. Martin, Robert A. Anderson, Douglas Read, and Gerald Gulley. Magnetostriction of field-structured magnetoelastomers. *PRE*, 74(5):051507, November 2006.

[110] Sonia Melle, Gerald G. Fuller, and Miguel A. Rubio. Structure and dynamics of magnetorheological fluids in rotating magnetic fields. *Phys. Rev. E*, 61:4111–4117, Apr 2000.

[111] A.M. Menzel. Tuned, driven, and active soft matter. *Physics Reports*, 554:1–45, 2015. cited By 94.

[112] P. Metsch, K. A. Kalina, J. Brummund, and M. Kästner. Two- and three-dimensional modeling approaches in magneto-mechanics: a quantitative comparison. *Archive of Applied Mechanics*, 89(1):47–62, January 2019.

[113] Philipp Metsch, Karl A. Kalina, Christian Spieler, and Markus Kästner. A numerical study on magnetostrictive phenomena in magnetorheological elastomers. *Computational Materials Science*, 124:364 – 374, 2016.

[114] Philipp Metsch, Karl Alexander Kalina, Jörg Brummund, and Markus Kästner. A quantitative comparison of two- and three-dimensional modeling approaches for magnetorheological elastomers. *PAMM*, 18:e201800179, 12 2018.

[115] Philipp Metsch, Dirk Romeis, Marina Saphiannikova, and Markus Kästner. Modeling and simulation of magnetorheological elastomers: A comparison of continuum and dipole approaches. *PAMM*, 17:527–528, 12 2017.

[116] Philipp Metsch, Henrik Schmidt, Dirk Sindersberger, Karl Alexander Kalina, Jörg Brummund, Günter Auernhammer, Gareth Monkman, and Markus Kästner. Field-induced interactions in magneto-active elastomers - a comparison of experiments and simulations. *Smart Materials and Structures*, 05 2020.

[117] R.D. Mindlin and N.N. Eshel. On first strain-gradient theories in linear elasticity. *International Journal of Solids and Structures*, 4(1):109 – 124, 1968.

[118] Nima Mirkhani, Michael G. Christiansen, and Simone Schuerle. Living, self-replicating ferrofluids for fluidic transport. *Adv. Funct. Mater.*, 30(40):2003912, November 2020.

[119] M. Mooney. A theory of large elastic deformation. *Journal of Applied Physics*, 11(9):582–592, 1940.

[120] L. Mullins. Softening of Rubber by Deformation. *Rubber Chemistry and Technology*, 42(1):339–362, 03 1969.

[121] COMSOL Multiphysics. https://www.comsol.de/.

[122] B. N. Muñoz-Sánchez, S. F. Silva, D. Pinho, E. J. Vega, and R. Lima. Generation of micro-sized pdms particles by a flow focusing technique for biomicrofluidics applications. *Biomicrofluidics*, 10(27042245):014122–014122, February 2016.

[123] Joseph L. Neuringer and Ronald E. Rosensweig. Ferrohydrodynamics. *The Physics of Fluids*, 7(12):1927–1937, 1964.

[124] Songbo Ni, Lucio Isa, and Heiko Wolf. Capillary assembly as a tool for the heterogeneous integration of micro- and nanoscale objects. *Soft Matter*, 14:2978–2995, 2018.

[125] Stefan Odenbach. Ferrofluide — ihre grundlagen und anwendungen: Magnetische flüssigkeiten kontrollieren. *Physik in unserer Zeit*, 32(3):122–127, 2001.

[126] Stefan Odenbach, editor. *Colloidal Magnetic Fluids : Basics, Development and Application of Ferrofluids*. Lecture Notes in Physics. Springer Berlin Heidelberg, Berlin, Heidelberg, 1st ed. 2009 edition, 2009.

[127] P. Oswald. *Rheophysics: The Deformation and Flow of Matter*. Cambridge University Press, 2014.

[128] S. S. Papel. Low viscosity magnetic fluid obtained by the colloidal suspension of magnetic particles, 1965.

[129] Horst Parisch. *Festkörper-Kontinuumsmechanik : Von den Grundgleichungen zur Lösung mit Finiten Elementen*. Teubner Studienbücher Technik. Vieweg+Teubner Verlag, Wiesbaden, 1st ed. 2003 edition, 2003.

[130] Giorgio Pessot, Malte Schümann, Thomas Gundermann, Stefan Odenbach, Hartmut Löwen, and Andreas M Menzel. Tunable dynamic moduli of magnetic elastomers: from characterization by x-ray micro-computed tomography to mesoscopic modeling. *Journal of Physics: Condensed Matter*, 30(12):125101, feb 2018.

[131] Nhan Phan-Thien. Rigid spherical inclusion: the multipole expansion. *Journal of Elasticity*, 32(3):243–252, September 1993.

[132] Nina Prem, Dirk Sindersberger, and Gareth J. Monkman. Mini-extruder for 3d magnetoactive polymer printing. *Advances in Materials Science and Engineering*, 2019, 2019.

[133] M. Puljiz, M. Orlishausen, W. Köhler, and A.M. Menzel. Thermophoretically induced large-scale deformations around microscopic heat centers. *Journal of Chemical Physics*, 144(18), 2016. cited By 2.

[134] Mate Puljiz, Shilin Huang, Günter K. Auernhammer, and Andreas M. Menzel. Forces on rigid inclusions in elastic media and resulting matrix-mediated interactions. *Phys. Rev. Lett.*, 117:238003, Nov 2016.

[135] Mate Puljiz, Shilin Huang, Karl A. Kalina, Johannes Nowak, Stefan Odenbach, Markus Kästner, Günter K. Auernhammer, and Andreas M. Menzel. Reversible magnetomechanical collapse: virtual touching and detachment of rigid inclusions in a soft elastic matrix. *Soft Matter*, 14:6809–6821, 2018.

[136] Mate Puljiz and Andreas Menzel. Displacement field around a rigid sphere in a compressible elastic environment, corresponding higher-order faxén relations, as well as higher-order displaceability and rotateability matrices. *Physical Review E*, 99, 05 2019.

[137] Mate Puljiz and Andreas M. Menzel. Memory-based mediated interactions between rigid particulate inclusions in viscoelastic environments. *Phys. Rev. E*, 99:012601, Jan 2019.

[138] J. Rabinow. The magnetic fluid clutch. *Electrical Engineering*, 67(12):1167–1167, Dec 1948.

[139] Yu. L. Raikher and O. V. Stolbov. Magnetodeformation effect in a ferroelastic material. *Technical Physics Letters*, 26(2):156–158, February 2000.

[140] Yu. L. Raikher and O. V. Stolbov. Deformation of an ellipsoidal ferrogel sample in a uniform magnetic field. *Journal of Applied Mechanics and Technical Physics*, 46(3):434–443, May 2005.

[141] Yu.L. Raikher and O.V. Stolbov. Magnetodeformational effect in ferrogel objects. *Journal of Magnetism and Magnetic Materials*, 289:62 – 65, 2005. Proceedings of the 10th International Conference on Magnetic Fluids.

[142] S Ramakrishna, J Mayer, E Wintermantel, and Kam W Leong. Biomedical applications of polymer-composite materials: a review. *Composites Science and Technology*, 61(9):1189 – 1224, 2001.

[143] Felix A. Reich, Wilhelm Rickert, Oliver Stahn, and Wolfgang H. Müller. Magnetostriction of a sphere: stress development during magnetization and residual stresses due to the remanent field. *Continuum Mechanics and Thermodynamics*, 29(2):535–557, March 2017.

[144] Rheometer. https://wiki.anton-paar.com/de-de/grundlagen-der-rheologie/.

[145] Zvi Rigbi and Leif Jilkén. The response of an elastomer filled with soft ferrite to mechanical and magnetic influences. *Journal of Magnetism and Magnetic Materials*, 37(3):267 – 276, 1983.

[146] R. S. Rivlin and Geoffrey Ingram Taylor. Large elastic deformations of isotropic materials. i. fundamental concepts. *Philosophical Transactions of the Royal Society of London. Series A, Mathematical and Physical Sciences*, 240(822):459–490, 1948.

[147] Sangchul Roh, Lilian B. Okello, Nuran Golbasi, Jameson P. Hankwitz, Jessica A.-C. Liu, Joseph B. Tracy, and Orlin D. Velev. 3d-printed silicone soft architectures with programmed magneto-capillary reconfiguration. *Advanced Materials Technologies*, 4(4):1800528, 2019.

[148] Dirk Romeis, Vladimir Toshchevikov, and Marina Saphiannikova. Elongated microstructures in magneto-sensitive elastomers: a dipolar mean field model. *Soft Matter*, 12:9364–9376, 2016.

[149] R.E. Rosensweig. Magnetic fluids. *Int.Sci. Tech.*, 1966.

[150] Ronald E. Rosensweig. Fluid dynamics and science of magnetic liquids. In L. Marton, editor, *Advances in Electronics and Electron Physics*, volume 48 of *Advances in Electronics and Electron Physics*, pages 103 – 199. Academic Press, 1979.

[151] Henrik Schmidt, Benedikt B. Straub, Dirk Sindersberger, Ulrich Bröckel, Gareth J. Monkman, and Günter K. Auernhammer. Collision and separation of nickel particles embedded in a polydimethylsiloxan matrix under a rotating magnetic field: A strong magneto active function. *Colloid and Polymer Science*, January 2021.

[152] M Schümann, D Y Borin, S Huang, G K Auernhammer, R Müller, and S Odenbach. A characterisation of the magnetically induced movement of NdFeB-particles in magnetorheological elastomers. *Smart Materials and Structures*, 26(9):095018, aug 2017.

[153] M. Schümann, Th. Gundermann, and S. Odenbach. Microscopic investigation of the reasons for field-dependent changes in the properties of magnetic hybrid materials using x-ray microtomography. *Archive of Applied Mechanics*, 89(1):77–89, Jan 2019.

[154] M. Schümann and S. Odenbach. In-situ observation of the particle microstructure of magnetorheological elastomers in presence of mechanical strain and magnetic fields. *Journal of Magnetism and Magnetic Materials*, 441:88 – 92, 2017.

[155] Natalia Shevchenko, Stefan Boden, Sven Eckert, Dmitry Borin, Michael Heinze, and Stefan Odenbach. Application of x-ray radioscopic methods for characterization of two-phase

phenomena and solidification processes in metallic melts. *The European Physical Journal Special Topics*, 220(1):63–77, March 2013.

[156] D. Sindersberger, A. Diermeier, N. Prem, and G.J. Monkman. Printing of hybrid magneto active polymers with 6 degrees of freedom. *Materials Today Communications*, 15, 2018.

[157] Rasam Soheilian, Hamed Abdi, Craig E. Maloney, and Randall M. Erb. Assembling particle clusters with incoherent 3d magnetic fields. *Journal of Colloid and Interface Science*, 513:400 – 408, 2018.

[158] D. Stauffer and A. Aharony. *Introduction To Percolation Theory*. Taylor & Francis, 1994.

[159] Dietrich Stauffer, Antonio Coniglio, and Mireille Adam. Gelation and critical phenomena. In Karel Dušek, editor, *Polymer Networks*, pages 103–158, Berlin, Heidelberg, 1982. Springer Berlin Heidelberg.

[160] G V Stepanov, D Yu Borin, Yu L Raikher, P V Melenev, and N S Perov. Motion of ferroparticles inside the polymeric matrix in magnetoactive elastomers. *Journal of Physics: Condensed Matter*, 20(20):204121, 2008.

[161] Oleg Stolbov and Yuriy Raikher. Large-scale shape transformations of a sphere made of a magnetoactive elastomer. *Polymers*, 12(12), 2020.

[162] Oleg V. Stolbov and Yuriy L. Raikher. Magnetostriction effect in soft magnetic elastomers. *Archive of Applied Mechanics*, 89(1):63–76, January 2019.

[163] Oleg V. Stolbov, Yuriy L. Raikher, and Maria Balasoiu. Modelling of magnetodipolar striction in soft magnetic elastomers. *Soft Matter*, 7:8484–8487, 2011.

[164] Andrea Stoll, Matthias Mayer, Gareth J. Monkman, and Mikhail Shamonin. Evaluation of highly compliant magneto-active elastomers with colossal magnetorheological response. *Journal of Applied Polymer Science*, 131(2), 2014.

[165] Jean-Yves Tinevez, Nick Perry, Johannes Schindelin, Genevieve M. Hoopes, Gregory D. Reynolds, Emmanuel Laplantine, Sebastian Y. Bednarek, Spencer L. Shorte, and Kevin W. Eliceiri. Trackmate: An open and extensible platform for single-particle tracking. *Methods*, 115:80 – 90, 2017. Image Processing for Biologists.

[166] A. Tomanek. *Silicone & Technik: ein Kompendium für Praxis, Lehre und Selbststudium*. Hanser, 1990.

[167] P. Tordjeman, C. Fargette, and P. H. Mutin. Viscoelastic properties of a cross-linked polysiloxane near the sol–gel transition. *Journal of Rheology*, 45(4):995–1006, 2001.

[168] Mikhail V. Vaganov, Dmitry Yu. Borin, Stefan Odenbach, and Yuriy L. Raikher. Mesomagnetomechanics of hybrid elastomer composites: Magnetization of elastically trapped particles. *Journal of Magnetism and Magnetic Materials*, 499:166249, 2020.

[169] Alex M. van Silfhout, Hans Engelkamp, and Ben H. Erné. Colloidal stability of aqueous ferrofluids at 10 t. *J. Phys. Chem. Lett.*, 11(15):5908–5912, August 2020.

[170] Dieter Wagner. *Einführung in die Theorie des Magnetismus*. Vieweg+Teubner Verlag, Wiesbaden, 1st ed. 1966 edition, 1966.

[171] L. J. Walpole. A rotated rigid ellipsoidal inclusion in an elastic medium. *Proceedings of the Royal Society of London. Series A: Mathematical and Physical Sciences*, 433(1887):179–207, 1991.

[172] C. Wilhelm, J. Browaeys, A. Ponton, and J.-C. Bacri. Rotational magnetic particles microrheology: The maxwellian case. *Phys. Rev. E*, 67:011504, Jan 2003.

[173] J. Winger, M. Schümann, A. Kupka, and S. Odenbach. Influence of the particle size on the magnetorheological effect of magnetorheological elastomers. *Journal of Magnetism and Magnetic Materials*, 481:176 – 182, 2019.

[174] Marc P. Wolf, Georgette B. Salieb-Beugelaar, and Patrick Hunziker. Pdms with designer functionalities—properties, modifications strategies, and applications. *Progress in Polymer Science*, 83:97 – 134, 2018.

[175] Fan Xu, Shichen Zhao, Conghua Lu, and Michel Potier-Ferry. Pattern selection in core-shell spheres. *Journal of the Mechanics and Physics of Solids*, 01 2020.

[176] Lintong Yan and Xuexia Wei. An analytical solution for the stress distribution within a spherically isotropic hollow sphere under diametrical compression. *Mathematics and Mechanics of Solids*, 24(5):1256–1278, 2019.

[177] Kar W. Yung, Peter B. Landecker, and Daniel D. Villani. An analytic solution for the force between two magnetic dipoles. *Magnetic and Electrical Separation*, 9:079537, January 1900.

[178] Jingyi Zhang, Haoming Pang, Yu Wang, and Xinglong Gong. The magneto-mechanical properties of off-axis anisotropic magnetorheological elastomers. *Composites Science and Technology*, 191:108079, May 2020.

[179] Xianzhou Zhang, Suili Peng, Weijia Wen, and Weihua Li. Analysis and fabrication of patterned magnetorheological elastomers. *Smart Materials and Structures*, 17(4):045001, may 2008.

[180] Shaodi Zheng, Shilin Huang, Lian Xiong, Wei Yang, Zhengying Liu, Banghu Xie, and Mingbo Yang. Tunable wrinkle structure formed on surface of polydimethylsiloxane microspheres. *European Polymer Journal*, 104, 05 2018.

[181] G Y Zhou and Z Y Jiang. Deformation in magnetorheological elastomer and elastomer–ferromagnet composite driven by a magnetic field. *Smart Materials and Structures*, 13(2):309–316, feb 2004.

[182] M. Zrínyi, L. Barsi, and A. Büki. Deformation of ferrogels induced by nonuniform magnetic fields. *The Journal of Chemical Physics*, 104(21):8750–8756, 1996.

[183] M. Zrínyi, L. Barsi, and A. Büki. Ferrogel: a new magneto-controlled elastic medium. *Polymer Gels and Networks*, 5(5):415 – 427, 1997.

[184] Andrey Yu. Zubarev. On the theory of the magnetic deformation of ferrogels. *Soft Matter*, 8:3174–3179, 2012.

[185] A.Yu. Zubarev and Ashraf S. Elkady. Magnetodeformation and elastic properties of ferrogels and ferroelastomers. *Physica A: Statistical Mechanics and its Applications*, 413:400 – 408, 2014.

Danksagung

Das "Weiße zwischen den Worten" [1] sind all die Menschen, die mir auf unterschiedlichster Art und Weise geholfen haben. Ihnen allen möchte ich danken, dass ich diese Arbeit so anfertigen konnte, wie sie nun vorliegt.

Ich danke Dr. Günter Auernhammer dafür, dass er mir es ermöglicht hat, auf meinem Thema zu promovieren. Besonders wertvoll waren die zahlreichen fachlichen Diskussionen, die er mit mir geführt hat, und die mich wissenschaftlich weitergebracht haben. Prof. Hans-Jürgen Butt danke ich dafür, dass er es mir ermöglicht hat, meine Promotion am Max-Planck-Institut für Polymerforschung in Mainz anzufertigen.
Ich bin dankbar für meine fantastischen Arbeitskollegen, wie Benedikt Straub, Alexander Saal, Alexander Klaasen, Philipp Baumli, Amelie Axt, Ilka Hermes etc. und vielen mehr, die es mit Sicherheit auch verdient hätten, namentlich erwähnt zu werden. Ich danke ihnen für die motivierenden Worte, die fachlichen Diskussionen und die tollen gemeinsamen Erlebnisse sowohl im Institut als auch außerhalb. Besonders danke ich Benedikt Straub, der mir immer mit Rat und Tat zur Seite gestanden hat, mit dem ich einige erinnerungswerte Geschichten erlebt habe und ohne den die Zeit während der Promotion nicht so einzigartig geworden wäre.
Außerdem danke ich der gesamten mechanischen Werkstatt und dem Elektroniklabor des Max-Planck-Institut für Polymerforschung in Mainz für ihre Unterstützung.
Ein Gruß und ein riesen großes Dankeschön gehen an Soenke und Susan Petersen in die USA dafür, dass sie mir geholfen haben, mein English more native klingen zu lassen. Ich danke all meinen Freunden, die mich während meiner Promotion begleitet haben. Ich danke ihnen für die schönen Erlebnisse abseits der Arbeit, die mir einen guten Ausgleich zu manchmal langen und frustierenden Tagen gegeben haben. Von Herzen danke ich meiner Freundin Désirée, die mich immer unterstützt hat und mir in jeder Lage zur Seite stand. Zum Schluss möchte ich meinen Eltern und meiner Schwester herzlich danken. Ohne sie hätte ich nicht die Möglichkeit zu dieser Promotion gehabt. Ihre Unterstützung in jederlei Hinsicht hat mich von Anfang an begleitet und mir die Kraft gegeben, meine Träume zu verwirklichen.

[1] Frisch, M., Tagebuch 1946-1949, Suhrkamp Verlag